University of Strathclyde

Department of Naval Architecture, Ocean and Marine Engineering

Potential Flow and CFD-Based Hydrodynamic Analyses of Mono- and Multi-Hull Vessels

Tahsin Tezdogan

A thesis presented in fulfilment of the requirements for the degree of Doctor of Philosophy

2015

This thesis is the result of the author's original research. It has been composed by the author and has not been previously submitted for examination which has led to the award of a degree.

Signed: Date:

Acknowledgements

Without a doubt, I have spent three very productive and enjoyable years during my studies in Glasgow. I would like to thank everyone who contributed to this, and helped me towards completing my PhD with their advice, assistance and friendship.

To start with, I would like to express the deepest appreciation to my primary supervisor, Professor Atilla Incecik, who has been a tremendous mentor for me during the last three years. I have benefited from his boundless experience and guidance in both my academic and private life. Professor Incecik has always been a perfect example to me, with his everlasting energy and outstanding academic career. If he had not believed in me, I would have not achieved this. I aspire to become a lecturer like him in the near future. In addition, I would like to acknowledge the valuable support and help of my second supervisor, Professor Osman Turan.

Also, I would like to thank the Rector of Izmir Katip Celebi University, Professor Galip Akhan, for his continuous help and support to me. I am indebted him for his understanding and precious advice. Moreover, I gratefully acknowledge the sponsorship of Izmir Katip Celebi University in Turkey, for giving the Turkish Council of Higher Education PhD Scholarship to fully support my PhD research at the University of Strathclyde, Glasgow.

I would also like to thank the University of Strathclyde Faculty of Engineering for provision of the ARCHIE-WeSt high performance computing facilities. The CFD results were obtained using the EPSRC funded ARCHIE-WeSt High Performance Computer (www.archie-west.ac.uk), EPSRC grant no. EP/K000586/1.

I would like to thank our department's research secretary, Mrs. Thelma Will, for all of her assistance and great support. Every department needs a Thelma to help PhD students solve all of their administrative problems.

Additionally, I would like to thank my colleagues and friends who assisted me during my PhD and helped me to spend three fantastic years in Glasgow: Kurt Mizzi, Matthias Maasch, Saishuai Dai, Elif Oguz, Paula Kellett, S. Anil Gunbeyaz and Volkan Arslan. I would like to thank my colleague, my flatmate, my best friend and

my fellow PhD student, Yigit Kemal Demirel, for his encouragement and for listening to details of my successes and difficulties during my PhD research. I am also indebted to his mother, Huriye Acar Hanimefendi, for looking after us by visiting us in Glasgow from time to time.

Last, but definitely not least, I would like to thank the very understanding and supportive Holly Yu. I gratefully acknowledge her continuous help with the final proofreading of this thesis and my papers. Without her support and motivation, I would not have completed this thesis work on time. I hope she can be awarded her PhD degree soon after me.

And finally, I would like to thank my self-sacrificing mother and brother for always supporting my decisions and for believing in me. I would like to remember my deceased father, who passed away on 4th January, 2014. I very much wish he could see me now I have completed my PhD!

Contents

List of Figures

List of Tables

Abstract

The majority of current techniques used for predicting ship motions rely on assumptions from the potential flow theory. However, this approach is not ideal, since potential flow theory ignores important effects such as breaking waves, turbulence and viscosity, which are significant in problems involving high Froude numbers, those involving large amplitude motions, shallow water problems and problems involving multi-hull ships. These effects should therefore be included in seakeeping and resistance calculations. Reynolds-Averaged Navier-Stokes (RANS) approaches are excellent alternatives to potential flow theory, as they can directly account for viscous effects in their calculations.

Towing tank tests are used widely around the world, giving very accurate results. However, these may be costly and time-consuming. Towing tank experiments are also hampered by a limited availability of suitable facilities. Computational simulations offer a fast, low cost alternative to towing tank experiments. Continued technological advances offer ever-increasing computational power, which can be harnessed for viscous flow simulations to solve the Navier-Stokes equations. Computational Fluid Dynamics (CFD) methods are rapidly gaining popularity for naval architecture, ocean and marine engineering applications. The application of CFD techniques to seakeeping problems allow designers to assess the seakeeping performance of a vessel whilst it is still being designed, enabling any necessary corrective action to be taken before the vessel is actually built.

This work mainly aims to perform hydrodynamic analyses of mono- and multi-hull ships, and to develop a CFD-based unsteady RANS numerical model to predict the hydrodynamic performance of these ships. This model will cover seakeeping and resistance calculations in both deep and shallow water regions.

Firstly, a detailed literature review of the existing numerical methods which have been developed to solve seakeeping problems of ships is performed. This review also looks in detail at the differences between seakeeping analysis techniques; the reasons for these differences are investigated.

Following this, unsteady RANS simulations are performed for various seakeeping and resistance applications. In each specific study, the results obtained using a commercial RANS solver are compared to the results obtained using a potential flow theory code and the available towing tank experiments.

Finally, the results drawn from each chapter of this thesis are summarised and discussed, and recommendations are made for future research.

1. INTRODUCTION

To begin with, this chapter will provide an insight into the issues covered in this thesis. Following this, it will list the motivations behind each chapter of the thesis. Next, it will present individual research aims and objectives, and finally, the chapter will provide an overview of the structure and layout of this thesis.

1.1 General Perspectives

The vast majority of the available techniques to predict ship motions, as well as the added resistance due to waves, rely on assumptions from the potential flow theory, including free surface effects. However, effects which are ignored in potential flow theory, such as breaking waves, turbulence and viscosity, are the most significant for shallow water problems and should therefore be included in the numerical codes. In addition to this, many previous studies, such as Schmitke (1978), have shown that viscous effects are likely to be the most significant, particularly in high amplitude waves and at high Froude numbers (Fn). In addition, Beck and Reed (2001) state that vertical plane motions in catamarans undergo significant viscous damping. Reynolds-Averaged Navier-Stokes (RANS) approaches, on the other hand, are very good alternatives to potential flow theory as they can directly account for viscous effects in their calculations (Tezdogan et al., 2015).

Without a doubt, computers have revolutionised the study of fluid flow. The use of computers to solve complex fluid mechanics equations is a strategy used by around a third of fluid mechanics researchers, with the proportion ever increasing. This field of study is known as Computational Fluid Dynamics (CFD) (Ferziger and Peric, 2002).

Towing tank tests are widely used around the world, for a variety of research purposes. These experiments include, but are not limited to, resistance tests for powering, self-propulsion tests, flow visualisation tests, hull optimisation studies, open water propeller tests, wake field measures, seakeeping tests, and so on. However, such experiments may be difficult and costly to carry out. Also, their usage

is dictated by the availability of such facilities. A further issue is that some measuring equipment may disturb the flow, and some parameters may be measured with inadequate accuracy. Scaling may also be another issue for these experiments. Attempts to maintain a satisfactory similarity between the non-dimensional parameters (such as Reynolds and Froude numbers) associated with a full-length ship and its model can be almost impossible. A compromise is therefore made, as only similarities in the Froude numbers can be achieved in practice (Xiao, 2012).

CFD techniques, on the other hand, may be good alternatives to experimental fluid dynamics (EFD). CFD-based techniques are advantageous in that analyses can be conducted at any time, without the need to plan and set up time-intensive towing tank tests. Further, CFD methods can give very detailed results, animations, and videos which lead to a better interpretation of the results. Also, for an unsteady problem, a set of detailed information related to any time-step can be readily obtained. In addition to this, as opposed to EFD, CFD does not use any consumables. For this reason, it can be easily employed for solving a problem numerous times. It therefore enables the user to perform their exploratory studies with much less expense than the analogous experimental studies. To give an example, at a towing tank, if a mistake was detected in a ship model, this would require the replacement of the ship model, leading to a waste of time, material and hence money. However, such a mistake would not cause such a big problem for a CFD-user. In this case, they would simply import and re-mesh the revised ship model, losing significantly less time compared to the time that would have been lost in a physical towing tank experiment.

As mentioned in Xiao (2012), a typical CFD task consists of three main stages: pre-processing, solving, and post-processing. Pre-processing covers three elements: *i)* the identification of the problem, *ii)* setting the appropriate governing equations, and *iii)* generation of mesh. In the 'solving' stage, as the name implies, the governing equations are solved. Three main theories can be adopted in this stage: finite volume, finite element and finite difference. Each theory includes the discretisation of the governing equations and the solution of algebraic equations. The obtained results are analysed in the 'post-processing' stage of a CFD process. Post-processing covers

geometry and mesh display, visualisation and plotting of scalar and vectoral quantities, and making animations and videos.

Continued technological advances offer ever-increasing computational power. This can be utilised for viscous flow simulations to solve Navier-Stokes equations in the time domain. CFD methods are rapidly gaining popularity for naval architecture, ocean and marine engineering applications, some of which are listed below:

a. Ship hydrodynamics, including resistance and seakeeping
b. Slamming load and green water incidence predictions
c. Performance of marine renewable energy and energy saving devices
d. Propeller efficiency and cavitation
e. Ship noise and acoustics
f. Bio-mimetic robotic swimming fish
g. Bio-fouling and roughness effects
h. Performance of autonomous underwater vehicles
i. Studies on offshore platforms

Specifically, the applications of CFD in seakeeping problems have the distinct advantage of allowing designers to assess the seakeeping performance of a vessel during the design stages, therefore allowing any corrective action to be taken promptly, before the vessel is actually built (Tezdogan et al., 2014a, Tezdogan et al., 2015). As also discussed by the International Towing Tank Conference (ITTC) (2011c), advances in numerical modelling methods and increases in computational power have made it possible to carry out fully nonlinear simulations of ship motions, taking into account viscous effects, using CFD.

This thesis is based on two approaches: potential flow and unsteady RANS methods. The focus will be on the CFD-based unsteady RANS simulations of ship motions and resistance. The later chapters will assess how well RANS simulation results compare with those obtained from experiments, in relation to ship hydrodynamic problems.

To the best of this author's knowledge, this thesis introduces novel research which builds on that found in the current literature.

Throughout this thesis, the commercial CFD software Star-CCM+ version 9.0.2, which was developed by CD-Adapco, is used wherever an unsteady RANS approach has been applied. Additionally, the supercomputer facilities at the University of Strathclyde have been utilised to allow much faster and more complex simulations to be performed.

1.2 Motivations behind this Work

Before detailing the specific objectives of this thesis, an overview of the general motivations behind the studies given in each chapter will be presented, along with a brief demonstration of how these studies address at a gap in the literature.

- The growing popularity of passenger cruise lines means continual challenges are faced concerning both a vessel's design and its operational ability. Vessel dimensions, service speeds and performance rates are rapidly increasing to keep pace with this expanding interest. It is essential that vessels demonstrate high performances, even in adverse sea and weather conditions, and ensure the comfort of passengers and the safety of cargo. It is therefore critical to calculate a vessel's operability index, which is defined as the percentage of time during which a vessel is capable of performing her tasks securely. As can be seen from Chapter 2, Section 4, similar studies have been published in the literature. However, no study has looked into the effects of employing different seakeeping theories on a ship's operability index (Chapter 3).
- The successful estimation of a ship's motions in regular waves requires an accurate calculation of its hydrodynamic properties and exciting forces. As stated previously, viscous effects are likely to be the most significant, particularly for lateral plane motions (sway, roll and yaw) and for some ship sections. An appropriate numerical model therefore has to be developed to determine the added mass and fluid damping coefficients of a ship-like two-dimensional section by incorporating the viscous effects. Unsteady RANS methods can therefore be employed to calculate the hydrodynamic coefficients of a 2-D section. Related studies have been published in the literature; however, to date there is no such work which has been applied to twin-sections (Chapter 4).

- It is critical to be able to estimate a ship's response to waves, since the resulting added resistance and loss of speed may cause delays or course alterations, with consequent financial repercussions. Slow steaming has recently become a popular approach for commercial vessels. It offers a means of reducing fuel consumption, and therefore operating costs, in the current economic and regulatory climate. For this reason, the potential advantages of slow steaming operational conditions in terms of fuel consumption and CO_2 emissions should be investigated. It may be interesting to perform a comparative study, to investigate the difference between the results obtained using CFD and potential flow theory as two different approaches (Chapter 5).
- The seakeeping behaviour of a vessel in shallow water differs significantly from its behaviour in deep water. In shallow water, a vessel's motion responses to incident waves will be affected by hydrodynamic effects caused by the presence of a finite depth. Given that a vessel will sail in shallow water at various times during its service life, such as when entering harbours, it is important to have an understanding of the influence of shallow water on ship motions. To the best of this author's knowledge, no such study exists in the published literature, using a CFD-based unsteady RANS method (Chapter 6).
- As a ship approaches shallow water, a number of changes arise owing to the hydrodynamic interaction between the bottom of the ship's hull and the sea floor. The flow velocity between the bottom of the hull and the sea floor increases, which leads to an increase in sinkage, trim and resistance. As the ship travels forward, squat of the ship may occur, stemming from this increase in sinkage and trim. Knowledge of a ship's squat is necessary when navigating vessels through shallow water regions, such as rivers, channels and harbours. Accurate prediction of a ship's squat is therefore essential, to minimise the risk of grounding for ships. Similarly, predicting a ship's resistance in shallow water is equally important, to be able to calculate its power requirements. Historically, various approaches have been proposed to predict squat and shallow water resistance. These methods comprise empirical or analytical investigations and experiments. The analytical methods mainly use the assumptions used in potential flow theory, presuming

the ship to be a slender body. The empirical formulae also have certain constraints and conditions which must be satisfied. In addition, as mentioned earlier, performing towing tank experiments may be costly and time-consuming. On the other hand, CFD techniques are easily capable of predicting the trim, sinkage and resistance of a vessel in shallow water, incorporating both viscous and nonlinear effects in the flow and free surface. Limited studies exist which include CFD simulations of ship squat, however they do not include any discussion about the resistance of such ships (Chapter 7).

1.3 Research Aims and Objectives

The main aims of this thesis are to perform hydrodynamic analyses of mono- and multi-hull ships, and to develop a CFD-based unsteady RANS numerical model to predict the hydrodynamic performance of these ships. This model will cover seakeeping and resistance calculations in both deep and shallow water regions.

The specific objectives of this thesis have been formulated to cover all of the issues mentioned in the previous section and stated as follows:

- To review the available literature on seakeeping of ships and to investigate the differences between various prediction techniques
- To describe an operability assessment procedure invoking seakeeping analyses in accordance with reliable seakeeping criteria
- To demonstrate the sensitivity of the adopted seakeeping theories to the vessel's expected operability
- To make a comparison between different methodologies for the calculation of motion induced sickness values for passengers on a catamaran ferry
- To obtain the hydrodynamic coefficients of heaving twin cylinders in a free surface by employing a CFD-based RANS solver
- To gain a better understanding of the effects of operating at a lower speed on the behaviour of a vessel in deep water

- ❖ To introduce a CFD-based unsteady RANS simulation model to predict the resistance and motions of a ship operating in head seas
- ❖ To test this proposed numerical model for a vessel in shallow water, in order to predict vertical motions of the vessel in different ship drafts at zero speed
- ❖ To predict the squat and resistance of a vessel advancing through a canal using this RANS solver

1.4 Thesis Structure

The structure of this thesis is summarised briefly below.

- Chapter 2 (CRITICAL REVIEW) presents a detailed literature survey on the current numerical techniques developed to solve seakeeping problems for vessels. It first outlines the historical development of modern seakeeping methods, and then provides a classification of these seakeeping theories. Finally, the chapter presents a literature survey on the specific areas that will be discussed in the main chapters of this thesis.
- Chapter 3 (OPERABILITY ASSESSMENT OF HIGH SPEED PASSENGER SHIPS BASED ON HUMAN COMFORT CRITERIA) presents a procedure to calculate the operability index of a ship using seakeeping analyses. A discussion of the sensitivity of the results relative to three different seakeeping methods is then given. In order to apply these theories in the operability assessments, VERES is utilised, which is a potential theory-based linear strip theory software package. The effect of seasonality on a ship's estimated operability is also investigated using wave scatter diagrams. Finally, a high speed catamaran ferry is explored as a case study and its operability is assessed with regards to human comfort criteria.
- Chapter 4 (PREDICTING THE HYDRODYNAMICS OF HEAVING TWIN CYLINDERS IN A FREE SURFACE) presents a CFD-based unsteady RANS approach to predict the hydrodynamic coefficients of any two-dimensional section. This work may be regarded as the first step towards an improved strip theory which uses the hydrodynamic coefficients of each section of a catamaran, obtained using this proposed RANS method, to predict its

responses to regular waves. In this chapter, the added mass and fluid damping coefficients of a two-dimensional circular section of a cylinder heaving at a free surface are calculated, covering a range of frequencies. The time variation of these coefficients in heave for various frequencies is then explored. Finally, the results obtained in the frequency domain are compared with the potential flow solutions and related experimental work.

- Chapter 5 (FULL-SCALE UNSTEADY RANS CFD SIMULATIONS OF SHIP BEHAVIOUR AND PERFORMANCE IN HEAD SEAS) presents fully nonlinear unsteady RANS simulations to predict the ship motions and added resistance of a full-scale KRISO Container Ship model, and estimates the increase in effective power and fuel consumption due to its operation in waves. The analyses are performed using CFD at design and slow steaming speeds, covering a range of regular head waves. The results are validated against available experimental data and are found to be in good agreement with the experiments. The results are also compared to those from potential flow theory-based two-dimensional linear strip theory (obtained using VERES).
- Chapter 6 (FULL-SCALE UNSTEADY RANS SIMULATIONS OF VERTICAL SHIP MOTIONS IN SHALLOW WATER) provides a numerical study of ship motions in shallow water, using a fully nonlinear unsteady RANS solver. Firstly, the characteristics of shallow water waves are investigated by conducting a series of simulations. Then, a full-scale large tanker model is used as a case study to predict its heave and pitch responses to head waves at various water depths, covering a range of wave frequencies at zero speed. The motion results obtained are then validated against related experimental studies available in the literature, and are also compared to those from 3-D potential theory. The results are found to be in good agreement with the experimental data. Finally, it is shown that vertical motions are significantly affected by shallow water.
- Chapter 7 (A NUMERICAL INVESTIGATION OF THE SQUAT AND RESISTANCE OF SHIPS ADVANCING THROUGH A CANAL USING CFD) provides details of a numerical study to perform fully nonlinear unsteady RANS simulations to predict the squat and resistance of a model scale Duisburg Test Case

Container Ship advancing in a canal. The analyses are carried out in different ship drafts at various speeds, utilising a commercial CFD software package. The squat results obtained by CFD are then compared with available experimental data.

- Chapter 8 (CONCLUSIONS AND FUTURE RESEARCH) provides a discussion of how this thesis has contributed to existing knowledge, and assesses how well the aims and objectives have been achieved. It also makes suggestions for future research.

2. CRITICAL REVIEW

The current numerical methods used to solve seakeeping problems for ships are introduced in this chapter. Firstly, the historical development of modern seakeeping methods will be briefly presented. Then, a classification of the seakeeping methods which are still in use will be made. Finally, the chapter will focus on a literature survey on the specific areas that will be examined in the later chapters of this thesis.

2.1 Introduction

Naval architects and marine engineers routinely use seakeeping computations in many aspects of their work. Such computations are invaluable as they can be used in simulators to predict vessel motions in real time. The literature offers a wealth of techniques with which to conduct seakeeping calculations. These techniques vary from the conventional strip theory to the state-of-the-art fully nonlinear unsteady RANS computations.

According to Beck and Reed (2001), ship seakeeping is one of the most demanding problems of marine hydrodynamics, owing to several reasons. To begin with, seakeeping problems involve the intricacy of wave resistance or manoeuvring problems, along with their contributions to unsteadiness, occurring due to the presence of incoming waves. The key objective of researchers is to develop a unified, elegant theory treating all resistance, manoeuvring and seakeeping problems. Historically, these areas have been investigated individually, rather than together, since seakeeping began.

Nonlinearities are known as the primary source of the difficulties in this field. These nonlinearities stem from the viscosity and the second-order velocity terms involved in the pressure equation. The free surface itself creates nonlinearities, due to the natural nonlinear behaviour of the incident waves. Also, the body geometry leads to nonlinear hydrostatic restoring forces. Lastly, shallow water waves, current effects and non-uniform sea bottom topography also contribute to the nonlinearities. These nonlinearities increase the complexity of the problem to be solved. Fortunately, some

approximations have been developed to diminish the computational power required for seakeeping calculations. For example, ships are commonly designed to be long and slender, with gradual variation along their length. This particular geometric property of the vessels forms the basis of slender-body approaches.

Throughout this thesis, the assumption is made that water is incompressible and has a constant density. The compressibility of water, which is a function of temperature and pressure, may be a critical parameter in the fields of underwater explosions and related problems. However, for seakeeping problems, the incompressible assumption is a reasonable approach. Similarly, although water has a varying density in real ocean or sea conditions, this can be imperceptible in the environ of the vessel depending on where the ship operates.

2.2 A Historical Overview of Seakeeping Methods

The history of prediction of ship motions starts with Froude's novel study on rolling (Froude, 1861). Sources such as Newman (1978) and Beck and Reed (2001) can be referred to for a very detailed historical approach to seakeeping.

Two developments in the 1950's pioneered modern seakeeping computations. The first development was the proposal of the random process theory to obtain short term responses to an irregular sea, and the second one was associated with the development of linear ship motion theories to obtain ship responses to regular waves (Beck and Reed, 2001).

St. Denis and Pierson (1953) pioneered a new method to estimate the statistics of ship motions in a seaway, which involved the application of spectral methods. This original theory was based on two fundamental assumptions:

- The sea surface has an ergodic Gaussian distribution,
- There is a linear relationship between wave elevation, wave loads and ship motions.

The first assumption allows the probability density function of the ship motions to be identified by its variance. The latter assumption allows calculation of the spectral

density of any response by simply multiplying the wave spectrum by the square of the response amplitude operator (RAO, or transfer function).

The transfer functions can be computed either experimentally or numerically. Experimental methods are generally used for the validation of numerical results since conducting experiments for each ship speed, wave frequency and heading would be very expensive and time-consuming. There is therefore a wide range of commercial software available which can calculate the RAOs of a desired vessel within a few minutes.

The development of numerical techniques started in the 1950's, based on the novel work of Michell (1898). His theory was based on the thin-ship approximation, which assumes the breadth of a ship is small relative to its length and draft. Peters and Stoker (1957) modified Michell's (1898) theory by using a systematic perturbation procedure with the ship's breadth. Their theory assumed the wave amplitudes to be small and that the unsteady ship motions were of the same small order with the wave amplitudes. By using linear theory and the thin-ship approximation, they developed a numerical method to predict the motions of a freely floating rigid body under an external force. Following this, Newman (1961) overcame the deficiencies in the theory of Peters and Stoker (1957), by employing a set of small parameters and by refining the body boundary conditions. However, his numerical results were not compatible with the experiments.

The majority of ship geometries are elongated, with their breadth and draft of the same order of magnitude relative to the length. This geometric feature is the basis of the slender-body assumptions. Slender-body theory found its earliest use in aerodynamics with Munk's (1924) study on the flow around airships. Long after his study, its application to ships started in the 1950's, first used in the steady-state wave resistance problem by Cummins (1956). Another noteworthy restriction from the theory is that the ship is slender compared to the characteristic incident wavelength. As a consequence of this, the beam and draft are thought to be small relative to both the wavelength scale U^2/g and the ship length L. Similarly, the Froude number ($Fn=U/(gL)^{0.5}$) is assumed to be of order one (g denotes gravitational acceleration).

The slender body theories are therefore termed long-wavelength theories (Newman, 1978).

As explained by Wang (2000), in the slender-body theories, the inner fluid is treated as two-dimensional, whereas the outer solution for the far-field is treated as three-dimensional. Many different slender body theories have been developed regarding the different treatments of the inner two-dimensional problem, such as the original slender body theory (Newman, 1964), the unified slender body theory (Newman, 1978), the high speed slender body theory (Chapman, 1975), and the new slender body theory (Yueng and Kim, 1985).

Around the same time as the studies into slender-body theories, Korvin-Kroukovsky (1955) and Korvin-Kroukovsky and Jacobs (1957) pioneered an alternative strip slender-body theory. They developed a mathematical theory to predict the heave and pitch responses of a ship to incident regular waves, by utilising the slender-body approach. Their first results produced larger damping coefficients compared to the experimental results. After applying an empirical correction to the theory, they obtained an improved agreement with the experimental data.

Beck and Reed (2001) point out that strip theory was regarded as the first ship motion theory giving results with adequate engineering accuracy. For example, a modified strip theory developed by Gerritsma and Beukelman (1967) demonstrated reasonably good comparison with the experiments in head seas. More extensive strip theories were probed in the late 1960's. Salvesen with his colleagues (1970) developed a form of strip theory by combining mathematics with careful assumptions. This form of strip theory is currently the most common method with which to perform seakeeping analyses of ships.

Ogilvie and Tuck's (1969) work reinvigorated strip theory. They applied three restrictions to maintain simplicity: i) the ship geometry is slender, ii) the motion response amplitudes are small compared to the ship's beam or draft, and iii) the incident wave frequency is high. These assumptions enabled the problem to be reduced to a singular perturbation problem, solved by using the matched asymptotic expansions. They then evolved formulations to predict the hydrodynamic heave force

and pitch moment of ships floating in regular waves. The forward-speed corrections were almost identical to those applied in Salvesen et al. (1970). Their theory was reduced to simple strip theory when the ship is stationary. Due to having a high frequency of incoming waves, the diffraction potential rapidly changes along the ship's length. This therefore poses a problem in strip theory when calculating the diffraction exciting forces.

As discussed by Wang (2000), despite the slender body theory being more rational than the conventional strip theory from a physical point of view, it is not extensively used due to its arduous and difficult numerical evaluation of the necessary coefficients. According to real case studies performed by Sclavounos (1984, 1985) at Fn=0.2 and 0.35, although the exciting force is calculated more accurately in the slender-body theories, the ship motion predictions are not significantly better than those from the linear strip theory. Also, it is revealed by ITTC (1987) that the slender body theory gives no advantage over strip theory for predicting a ship's vertical motions at forward speed, though it does demonstrate advantages for the prediction of sway and yaw motions.

Strip theory is commonly known as a theory of short wavelength, whereas slender-body theory is a theory of long wavelength. There therefore have been several approaches into developing a theory applicable to a wider range of wave frequencies. Maruo's (1970) interpolation theory and Newman's (1978) unified theory are examples of this. A brief summary of Newman's unified theory is that it was a mixture of strip theory and slender-body theory. The comparison of the results obtained using this unified theory with the experimental work of Sclavounos (1990) showed that refined results were obtained compared to classical strip theory. Later research conducted by Kashiwagi et al. (2001) investigated the robustness of the enhanced unified theory through comparisons of the results for a very large crude carrier (VLCC) and container ship models with conventional strip theory and experiments. Their study aimed to predict ship motions, wave loads and pressure distributions along the ship's length for a wide range of wave headings at several forward speeds. The results showed that unified and strip theories give almost identical results for ship motions, whereas the unified theory gives slightly better

results for vertical bending moments at some ship stations compared to those obtained from strip theory.

Beck and Reed (2001) estimate that in the early 2000s, 80% of all seakeeping computations at forward speeds were performed using strip theory, because its fast, reliable solutions have sufficient accuracy for engineering purposes. Another advantage of strip theory is that it is also applicable to most conventional hull forms. However, discrepancies between strip theory and experiments for higher speed vessels, or highly non-wall sided hull forms, have motivated research to develop more advanced theories. As discussed by Newman (1978), the conventional strip theory shows deficiencies both for low encounter frequencies and high speeds, due to assumptions used in the theory. When the theory is applied to low encounter frequencies, some fundamental problems occur, stemming from the evolution of forward speed effects and the complex nature of the diffraction problem in short incoming waves. The conventional strip theory is therefore questionable at low encounter frequencies and this is visible in the trend of a two-dimensional heave added mass curve plotted against the frequency of oscillation, as shown in Figure 2.1. As the frequency of encounter goes to zero ($\omega_e \rightarrow 0$), the added mass coefficients for vertical motions exponentially become infinite ($a \rightarrow \infty$). For this reason, strip theory is named a short-wavelength (high frequency) theory (Beck and Reed, 2001). The other problem strip theory suffers from is related to forward speed effects. In strip theory, the forward speed has a direct bearing on the hydrodynamic force due to the simple introduction of terms which are proportional to (U/ω_e) and $(U/\omega_e)^2$ (where *U* denotes forward speed). Faltinsen and Zhao (1991b) also point out that strip theory is the most robust theory when applied at a moderate forward speed of a vessel, though it is dubious for high speed applications because it models the interaction with the forward speed in a simplistic way. Furthermore, the effect of the local steady flow around the vessel is omitted.

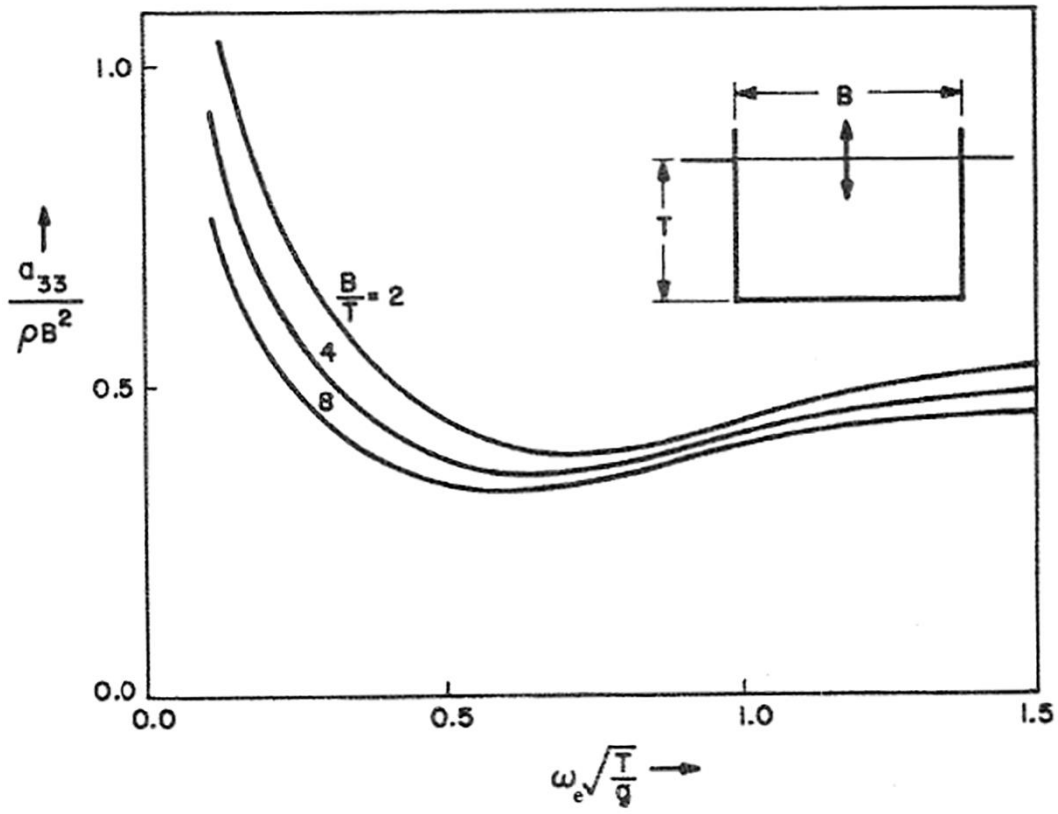

Figure 2.1 Added mass coefficients for a family of 2-D rectangular cylinders, based on the computations of Vugts (1968), taken from Newman (1978)
(a_{33}: heave added mass, ρ: fluid density, ω_e: frequency of encounter, T: draft of the cylinder and B: beam of the cylinder).

A compromise between 2-D and 3-D methods has been made and a new approach to treat the nonlinear problem in the down-stream direction has been developed. This theory is the so-called high-speed slender body theory, or 2.5-D theory. Faltinsen and Zhao (1991a, 1991b) treated the two-dimensional problem by using a hybrid boundary element method in their high-speed slender body theory. The simple source-dipole distribution is applied in the inner region, whereas the outer region benefits from analytical wave-free expressions. By using this method, the important diverging wave system around a high speed hull is accurately incorporated, whereas the transverse waves, which are very significant at lower speeds, cannot be included in the theory. Consequently, this method is only convenient to high speed ships. Numerically, only a side of the vessel is discretised to decrease computational effort. However, it is still possible to incorporate hydrodynamic interactions between demi-hulls within the theory. If the hull interaction is not accounted for, this means the

effect of the other demi-hull is neglected while calculating the velocity potential of one hull (Hermundstad et al., 1999).

Hess and Smith (1964) were the first researchers who implemented boundary element methods for flows without a free surface in the field of aerodynamics. In their theory, the body surface is divided into a finite number of flat quadrilaterals, and sources, in constant strength, are distributed over them. Then, the body boundary condition is satisfied at the centre of each quadrilateral (termed a node point); ultimately, unknown source strengths are determined from the same number of linear equations. The velocity and pressure values at each node point can then be easily predicted with the knowledge of source strengths. This technique is referred to as the so-called "panel method" in the literature. Higher-order panel methods suggest the use of non-flat panels over which the singularities have strengths which are not constant. In such a case, a Galerkin approach can be employed, in order to solve the integral equation over each individual panel (Okan and Umpleby, 1985a, Okan and Umpleby, 1985b, Maniar, 1995, Hsin et al., 1994).

As computers become more powerful, the use of 3-D techniques to investigate seakeeping problems is more common. Principally, there are two methods to solve three-dimensional features of seakeeping problems at a forward speed, namely, the Neumann-Kelvin theory (Brard, 1972, Guevel et al., 1974) and the Dawson (double-body) method (Dawson, 1977).

The Neumann-Kelvin approach began to be used after the late 1970's. In this approach, a linearised free-surface boundary condition is employed and the exact-body boundary condition is applied at the mean position of the body surface. The Neumann-Kelvin problem is often treated by the use of boundary integral methods in which the solution is defined by means of integrating the singularities over the surface encompassing the fluid domain. Typically, the integral equation had to be solved over all surfaces of the fluid domain. However, by employing Green functions, which meet all the boundary conditions on each surface of the domain except on the body surface, the governing integral equation must only be solved on the body surface. Hence, the major difficulty in solving the seakeeping problems turns into the evaluation of Green functions. The Green function is solved with

panels distributed over the wetted hull surface (Beck and Reed, 2001). Some numerical drawbacks may occur in the area where the intersection angles between the hull surface and the free surface are small. A highly oscillatory structure of the transient Green function in the vicinity of the free surface causes this numerical difficulty (Shin et al., 2003).

In the Dawson approach, the free surface linearisation is about the double-body flow, and Rankine source methods are treated with source distribution over the free surface and the body surface (Wang, 2000, Beck and Reed, 2001). Rankine sources are quite appropriate for wall-sided or non-wall-sided hull geometries. Rankine sources are distributed over both the hull surface and free surface to meet the free surface boundary condition (Shin et al., 2003).

Shin et al. (2003) developed a mixed numerical method blending both the transient Green functions and Rankine sources. This hybrid approach has been termed the "mixed source formulation". In this formulation, the fluid domain is separated into two regions as illustrated in Figure 2.2. In this formulation, the outer domain is treated with Green functions, whereas the inner domain is treated with Rankine sources.

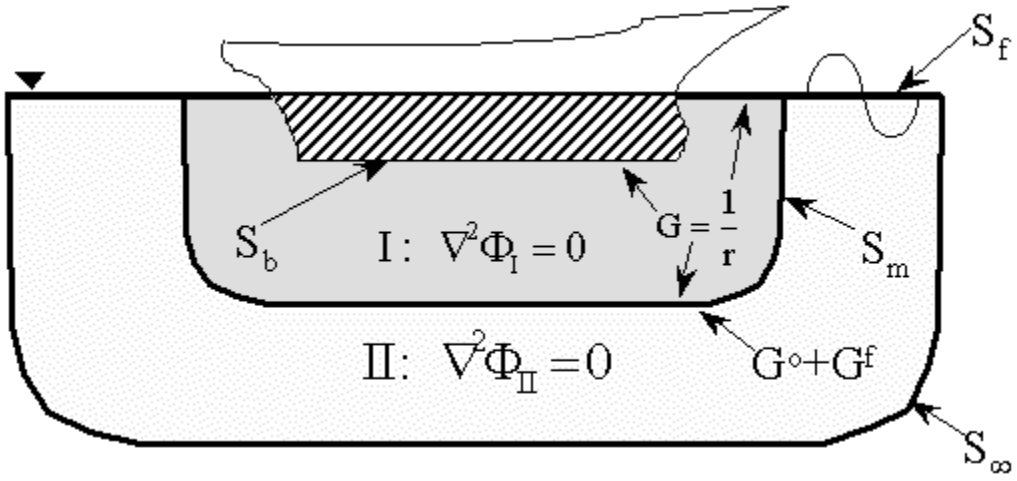

Figure 2.2 Mixed source formulation, taken from Shin et al. (2003).

Shin et al. (2003) state the advantage of using this method: "*Rankine sources behave much better than the transient Green function near the body and free surface juncture, and the matching surface can be selected to guarantee good numerical*

behaviour of the transient Green functions. The transient Green functions satisfy both the linearized free surface boundary condition and the radiation condition, allowing the matching surface to be placed fairly close to the body". It was concluded in their study that this new formulation gave successful motion and load results for the non-wall sided ship geometries. The only drawback of this method reported by Shin et al. (2003) is that it gives unstable solutions at relatively high Froude numbers (Fn>0.5).

Yasukawa (2003) claims that 3-D Rankine panel methods have been developed to overcome the deficiencies in the strip theory methods. He suggests that for a detailed review of Rankine singularity methods, Bertram and Yasukawa (1996) and Bertram (1998) may be consulted. In the theory developed by Bertram and Yasukawa (1996), fully 3-D effects of the flow and forward speed are taken into account, in contrast to strip theory where these effects are not properly accounted for. Yasukawa (2003) applied the theory of Bertram and Yasukawa (1996) in the time domain to several container ships with strong flare. As a result of his validation study, it was found that hydrodynamic forces, ship motions and local pressures are much better predicted than those obtained by strip theory when compared with experiments. However, the calculated lateral hydrodynamic forces are not satisfactory, owing to the viscous flow effect. The author suggests that this problem can be reduced by applying empirical corrections, similar to those employed in strip theory.

Rather than working with frequency-domain Green functions, time domain functions can be used instead. Finkelstein (1957) pioneered research into the use of time-domain Green functions. Working in the time domain requires the inclusion of memory functions (i.e. convolution integrals) over all previous time-steps, which therefore dramatically increases the required computational time. When solving linear problems at zero forward speed, the time-domain computations take longer than the classical frequency-domain calculations, owing to the convolution integrals involved in the time-domain expressions. Conversely, at forward speeds, the calculations of the Green function in the time domain tend to be faster than the calculations of the Green function in the frequency domain (Beck, 1994).

As the boundary element method is the most widely used method to approach the Neumann-Kelvin problem, finite element or finite difference methods can be alternatives to the boundary element method. In addition, there have been some attempts to combine finite element and boundary element methods. For example, Wu and Taylor (2003) developed a coupled method to study the nonlinear interaction between floating or submerged bodies and water waves. The novelty in their approach was to combine the advantages of finite element and boundary element methods in computational efficiency and in mesh generation, respectively. Since the boundary element method is included, their theory is only applicable to potential flows. The results showed that the approach can be effectively used in the calculations of force and displacements. However, it is still necessary to perform further investigations on the implementations of the theory for its applications to a ship model.

Due to the high computational time and the numerical problems raised by the use of fully nonlinear computations, the so-called blending methods, which are a mixture of linear and nonlinear theories, have been developed. These theories integrate the motion equations in the time-domain by obtaining the hydrostatic and Froude-Krylov forces over the instantaneously-changing wetted surface. The added mass and damping coefficients are determined by means of a linear theory, typically a linear strip theory. For a detailed review of the various theories developed in this sense, and for comparisons of them with towing tank experiments, reference can be made to Jensen (2000). As Beck and Reed (2001) highlight, the blending theories are preferred owing to their fast solutions given in the time-domain, with sufficient engineering efficiency.

Most flows experienced in ship hydrodynamics are turbulent, and hence require differing treatments. The methods used to solve turbulent flow fluid problems will be discussed in the next section.

Solving Reynolds-Averaged Navier-Stokes equations in the time domain is the latest approach to seakeeping. A more detailed literature survey on this particular area of ship hydrodynamics will be presented in the later sections.

2.3 Classification of Seakeeping Methods

At present, research in the field of calculating ship motions is focused on panel methods, fully nonlinear and double body methods, blending methods, and finally the implementation of unsteady RANS. Figure 2.3, which is adopted from Beck and Reed (2001), depicts the classification of the various methods which can be employed to approach the general 3-D, incompressible, constant-density ship hydrodynamics problems.

As can be seen from Figure 2.3, the methods to solve the general 3-D problem can be classified into two categories, namely; viscous and inviscid flow approximations. Viscous flow approaches take viscous effects into account by retaining the viscosity-related terms in Navier-Stokes equations.

Of all of the methods used for the solution of motions in a turbulent flow, Direct Numerical Simulation (DNS) is the most accurate method to solve the Navier-Stokes equations without averaging. This method directly incorporates turbulence. In its output, DNS presents very detailed results about the flow properties. However, it is computationally very expensive; its application is therefore limited to only simple geometric domains for flows at low Reynolds (Re) numbers. For this reason, DNS is used as a research tool, rather than a design tool (Ferziger and Peric, 2002).

High Reynolds number fluid flows are distinctive in that the viscous effects are only significantly observed around the structure and a viscous wake. Boundary layer approximations can, however, only work until the separation point, and so do not give solutions after that point. Currently, there are two approaches to treat average viscous flow problems at high Re numbers: Large Eddy Simulations (LES) and Reynolds-Averaged Navier-Stokes equations. Each method has its own advantages and disadvantages (Beck and Reed, 2001). Ferziger and Peric (2002) state that although LES is less accurate than DNS; it is mainly used for high Reynolds number flows or very complex geometries. On the other hand, as clearly highlighted in Beck and Reed (2001), LES simulations are likely to be more accurate than RANS simulations. RANS methods are often applied to interior flows in ducts and exterior flows around structures.

Ferziger and Peric (2002) state that, "*in Reynolds-averaged approaches to turbulence, all of the unsteadiness is averaged out i.e. all unsteadiness is regarded as part of the turbulence*". Beck and Reed (2001) distinguish between steady and unsteady RANS methods as, "*RANS codes are iterated until a steady state solution is obtained. In unsteady RANS, iteration is still used at each time step but the global solution is made time accurate by using a time-stepping method*".

The RANS equations are time-averaged equations for turbulent fluid flows, as mentioned in the above paragraph. For incompressible flows without body forces, the averaged continuity and momentum equations may be written in tensor form and Cartesian coordinates as follows (Ferziger and Peric, 2002):

$$\frac{\partial\left(\rho\bar{u}_i\right)}{\partial x_i}=0 \tag{2.1}$$

$$\frac{\partial\left(\rho\bar{u}_i\right)}{\partial t}+\frac{\partial}{\partial x_j}\left(\rho\bar{u}_i\bar{u}_j+\rho\overline{u_i'u_j'}\right)=-\frac{\partial\bar{p}}{\partial x_i}+\frac{\partial\bar{\tau}_{ij}}{\partial x_j} \tag{2.2}$$

in which $\bar{\tau}_{ij}$ are the mean viscous stress tensor components, as shown below in Equation (2.3):

$$\bar{\tau}_{ij}=\mu\left(\frac{\partial\bar{u}_i}{\partial x_j}+\frac{\partial\bar{u}_j}{\partial x_i}\right) \tag{2.3}$$

and p is the mean pressure, $\bar{u}_i$ is the averaged Cartesian components of the velocity vector, $\rho\overline{u_i'u_j'}$ is the Reynolds stresses, ρ is the fluid density and μ is the dynamic viscosity.

In order to complete the RANS equations, some approximations relating to the Reynolds stress tensor and turbulent scalar fluxes in terms of the mean quantities are required. In engineering, such approximations are known as turbulence models (Ferziger and Peric, 2002).

The inviscid flow models form the second primary division of Figure 2.3. Viscosity is neglected in the methods under this category, implying that the Navier-Stokes equations become Euler equations. This simplified problem is still very difficult to solve, hence some approximations are needed to approach the problem.

For rotational flows, the vorticity equations and vortex methods can be employed. However, the application of these methods is restricted to areas such as roll damping computations and separated flows around circular cylinders (Ferziger and Peric, 2002).

Potential flow theory is the most popular method for the calculation of inviscid (or ideal) fluid flows. It assumes that the fluid is irrotational and incompressible. However, some empirical viscous corrections are employed in the potential theory-based methods in an attempt to incorporate viscous effects into the formulation. It has been used extensively in many ship hydrodynamic problems by numerous researchers.

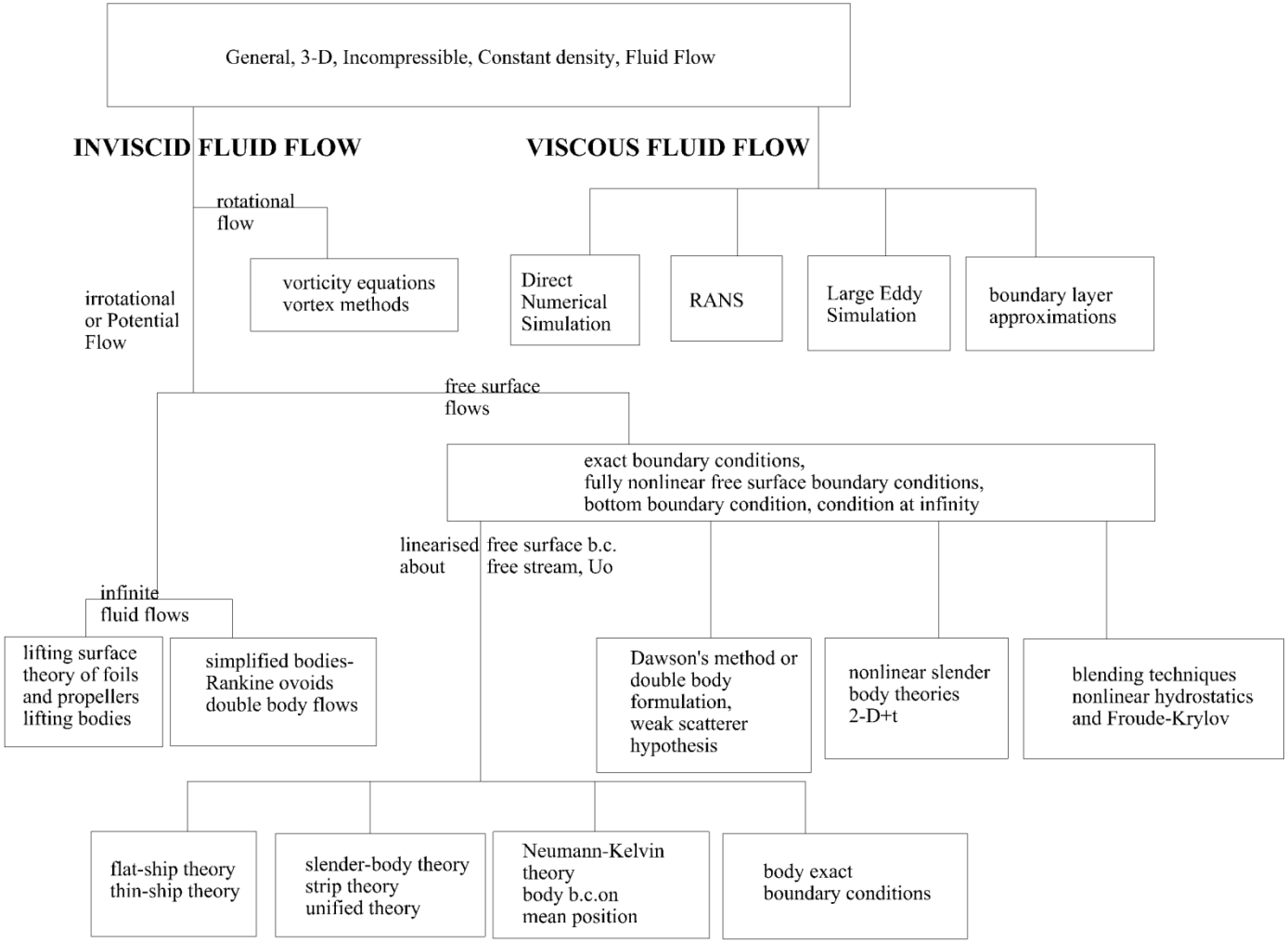

Figure 2.3 Classifications of hydrodynamic problems for seakeeping, adopted from Beck and Reed (2001).

2.4 Operability Analyses of Ships

Operability and habitability assessments have been conducted for a variety of ship types by many researchers. Some of their conclusions have had an impact on operability analyses of passenger ships, specifically with regards to human comfort. O'Hanlon and McCauley (1974) and McCauley et al. (1976) conducted simulation trials to investigate motion sickness caused by a ship's vertical sinusoidal motions. Their work was then combined with seakeeping analysis techniques (Salvesen et al., 1970, McTaggart, 1997), leading to the development of several suitable methods for the operability analysis of passenger ferries.

Ikeda et al. (1991) proposed a method to estimate the ratio of motion sick people on-board a ferry, by combining strip theory with O'Hanlon and McCauley's (1974) research. The operational performance of passenger ferries was evaluated by Dallinga et al. (2002) considering the influence of motion sickness on passengers and crew. In addition, Sarioz and Sarioz (2005) investigated the effect of limiting criteria on the seakeeping performance assessment for passenger vessels and concluded that the expected seakeeping performance of a passenger vessel is entirely related to the magnitude of the defined limiting criteria. They evaluated habitability of the passenger vessel based solely on vertical accelerations defined by the International Organization for Standardization (ISO) 2631/3 standard (1985). Tezdogan et al. (2014b) also presented operability analyses of two high speed car/passenger ferries. RAO databases of the ferries were generated using 2.5-D high speed theory. Their study explored the optimal hull distance configuration and loading condition with regards to operability.

Several researchers have carried out operability analyses on other ship types. Soares et al. (1995) offered a simple procedure for the seakeeping performance assessment of a fishing vessel. Then, Fonseca and Soares (2002) proposed a methodology to assess the seakeeping performance of vessels and argued the sensitivity of the results in relation to the use of various limiting criteria. They also revealed the influence of seasonality on the ship operability by comparing winter statistics to annual statistics. In their study, the calculation of operability indices and the sensitivity analyses were performed for both a container ship and a fishing vessel. Mortola et al. (2012)

proposed an operability evaluation methodology and developed a decision-making support tool to rapidly assess and compare the operability of the two candidate vessels, to provide an operational and maintenance support service to offshore wind farms.

2.5 Predicting the Hydrodynamic Coefficients of 2-D Sections using CFD

In 1994, a CFD workshop was organised in Tokyo to discuss the implementation of steady RANS methods to provide a solution for free-surface flows around surface ships. As explained by Wilson et al. (1998), from that point onwards, RANS methods have been widely used in many marine hydrodynamics applications.

Around this time, Gentaz et al. (1997) developed an original fully-coupled solver, in order to predict the added mass and damping coefficients of a two-dimensional section at a nonlinear free surface, accounting for viscous effects.

Utilising unsteady RANS-based solvers to predict 6-degrees-of freedom motions for a three-dimensional ship geometry at a free surface requires enormous computational power. Salui et al. (2000) therefore proposed an alternative approach to the 3-D problem. They used a commercial RANS solver (COMET) to predict the 2-D added mass and damping coefficients of rectangular, U-shaped and V-shaped sections of cylinders harmonically rolling in the presence of a free surface. The authors suggested that these coefficients be incorporated in a ship motion prediction code, based on strip theory. In their study, it was concluded that the RANS method improved roll damping predictions. Additionally, it was stated that the method gives better performance, even when viscous effects increase within the flow. Querard et al. (2008a, 2008b, 2009) also employed the unsteady RANS method in several studies to obtain 2-D hydrodynamic properties, incorporating viscous and rotational effects. They performed calculations for circular and rectangular sections of cylinders which were swaying, heaving and rolling with a nonlinear free surface boundary condition, covering a range of frequencies. They then compared their results with the numerical methods based on potential theory, and with the experimental results of Vugts (1968). Their results were found to be quite compatible with those of the experiments. Lastly, Field (2013) used Star-CCM+ as a RANS

solver, for comparison with potential flow methods, in the calculation of vertical plane radiation and diffraction problems. He determined the hydrodynamic coefficients for a cylinder oscillating in heave and sway about a calm free surface and concluded that the predicted values coincide with available experimental and linear potential flow results for most amplitudes and frequencies of oscillation.

2.6 CFD Applications to Seakeeping Problems

It was not until the late 1990s that RANS codes started to be used for steady resistance calculations and for unsteady ship motion predictions. According to Beck and Reed (2001), this is the state-of-the-art in the solution of seakeeping problems.

Wilson et al. (1998) performed verification and validation of a CFD code to simulate the unsteady flow of a fixed, steadily-advancing naval combatant in regular head waves. Around the same time, Gentaz et al. (1999) also studied three-dimensional free surface viscous flow problems around a ship in a forced motion. They used an unsteady RANS method with a nonlinear free surface boundary condition. In their work, the hydrodynamic loads and consequential hydrodynamic coefficients were compared to the results from the potential flow calculations and were validated against experiments conducted for a free surface piercing hemisphere and for a Series 60 model with a constant speed. Following this, Roddier et al. (2000) studied the effects of small bilge keels appended to the corners of a rectangular cylinder exposed to incident beam waves in water. They performed simulations of 3 degrees-of-freedom motions in the time domain across various wave frequencies by employing a Navier-Stokes solver. The results obtained from their study included sway, heave and roll transfer functions and the free surface elevations. They also compared the numerical results to their experimental results, concluding that the numerical results were fairly compatible with the experiments. In their study, it was revealed that the bilge keels can be used effectively as a way of reducing the resonant modes of motions.

As discussed by Simonsen et al. (2013), RANS-based CFD methods have been used extensively for seakeeping performance analyses with several ship types, by many scholars. Sato et al. (1999) conducted CFD simulations to predict motions of the

Wigley hull and Series 60 models in head seas. Hochbaum and Vogt (2002) then performed simulations of a C-Box container ship in 3 degrees-of-freedom motions (surge, heave and pitch) in head seas. Following this, Orihara and Miyata (2003) predicted the added resistance and pitch and heave responses of the S-175 container ship in regular head seas, using the Baldwin-Lomax turbulence model. In their work, they investigated the effect of two selected bulbous forms on the predicted added resistance.

CFD simulations have been also performed for more complex ship geometries. Weymouth et al. (2005), for example, simulated the pitch and heave motions of a Wigley hull in regular incoming waves. Carrica et al. (2007) studied the motions of a DTMB 5512 model in regular, small amplitude head waves. Hu and Kashiwagi (2007) also investigated the pitch and heave responses of a Wigley hull in head seas. Stern et al. (2008) studied the pitch and heave responses of BIW-SWATH in regular head waves. Wilson et al. (2008) and Paik et al. (2009) performed CFD simulations to predict the pitch and heave transfer functions of the S-175 ship in regular head waves. Carrica et al. (2008) demonstrated an application of an unsteady RANS CFD method to simulate a broaching event for an auto-piloted ONR Tumblehome in both regular and irregular seas. Then, Castiglione et al. (2011) investigated the motion responses of a high speed DELFT catamaran in regular head waves at three different speeds. Following this, Castiglione et al. (2013) carried out CFD simulations for seakeeping of the same catamaran model at two Froude numbers in both head and oblique regular waves.

In 2010, a workshop on numerical hydrodynamics was held in Gothenburg, which aimed to discuss the implementation of CFD in the field of ship hydrodynamics. Many institutions and organisations around the world contributed to the Gothenburg 2010 Workshop, with studies performed using three well-known ship hulls (the KVLCC2, the KCS, and the DTMB 5415) as benchmarks. The studies presented in the workshop gauged the numerical efficiency of CFD methods for the prediction of ship hydrodynamic quantities via comparison with the related experimental data (Larsson et al., 2011).

Bhushan et al. (2009) performed resistance and powering computations of the full-scale self-propelled Athena ship free to sink and trim using both smooth and rough wall functions. They also carried out seakeeping simulations at both full and model scale along with manoeuvring calculations for DTMB 5415 at full-scale. Mousaviraad et al. (2010) obtained heave and pitch response amplitudes and phases of the DTMB 5512 model in head seas using regular wave and transient wave group procedures. Following this, Simonsen and Stern (2010) performed CFD RANS simulations to obtain the heave and pitch motions and added resistance for the KCS model, presenting it at the Gothenburg 2010 CFD workshop. In addition, Enger et al. (2010) contributed to the same workshop with their study on the dynamic trim, sinkage and resistance analyses of the model KCS by using the Star-CCM+ software package. In their work, it was demonstrated that the CFD results agreed well with the experimental results.

Following this, Carrica et al. (2011) presented two computations of KCS in model scale, utilising CFDShip-Iowa, which is a general-purpose CFD simulation software developed at the University of Iowa. They performed self-propulsion free to sink and trim simulations in calm water, followed by pitch and heave simulations in regular head waves, covering three conditions at two different Froude numbers (Fn=0.26 and 0.33). Then, Kim (2011) carried out CFD analyses for a 6500 TEU container carrier, focusing on the global ship motions and structural loads by successfully validating the results against the model test measurements. After the validation study, Kim (2011) claimed that the current CFD technology would facilitate the decision making process in ship optimisation. Finally, Simonsen et al. (2013) investigated motions, flow field and resistance for an appended KCS model in calm water and regular head seas by means of Experimental Fluid Dynamics (EFD) and CFD. They focused mainly on large amplitude motions, and hence studied the near resonance and maximum excitation conditions. The results obtained using the CFD methods were compared to those from their experiments and the potential flow theory method.

2.7 Seakeeping Problems in Shallow Water

There have been many attempts to predict wave excited forces and moments on a vessel, and motion responses of a vessel, in shallow water. From a seakeeping

perspective, the use of two-dimensional strip theory methods to predict ship responses to waves, using a deep water assumption, can give satisfactory results at moderate speeds for conventional ship geometries. However, the use of strip theory is questionable when applied to shallow water conditions, since viscosity effects are amplified when the keel is very close to the seabed (Beukelman and Gerritsma, 1982). Because strip theory is a two-dimensional theory, it assumes that the water flow propagates entirely underneath the ship. However, Oortmerssen (1976a) claims that in shallow water, three-dimensional effects become considerably important because the water flow passes partly underneath the vessel and partly around the two ship ends. In some extreme cases, water can flow only around the ends of the vessel. This therefore causes a deviation from the two-dimensional flow features around the bow and stern ends.

Kim (1968) used strip theory in ship motion calculations for a finite water depth. His calculations assumed that the incident wavelength was comparable with the beam and draft of the ship. His approach provided reasonable results for vertical motions, whereas it did not give good results for lateral motions, specifically at lower frequencies.

Over the last five decades, potential flow theory-based three-dimensional methods have been used extensively to calculate the hydrodynamic responses of marine structures in both deep and shallow waters. There has therefore been a huge amount of research and opinion published in this specific area. A detailed discussion on the 3-D seakeeping methods was made in Section 2.2. In this sub-chapter of the thesis, the focus will be on their application to shallow water problems.

As clearly summarised by Yuan et al. (2014), the research devoted to this specific area can be classified into two categories depending on the Green function adopted in the boundary integral formulation. In the first category, the translating and pulsating sources are distributed over the mean wetted body surface. In this approach, a Green function is adapted to satisfy the free surface and the radiation conditions. This can be regarded as an effective method for the zero speed problems; however it has some restrictions when the forward speed effect is taken into account. The reason for this can be explained by the fact that it cannot take into account the near-field flow

condition, and the interaction between the steady and unsteady flow. A list of some of the studies in which this method was used is presented below.

Daubert (1970), Garisson and Chow (1972), Oortmerssen (1972), Boreel (1974), and Troesch and Beck (1974) are the pioneers who applied the 3-D techniques. They fall into the first category, for the calculation of wave loads on large offshore structures in a finite water depth. Following this, Oortmerssen (1976a, 1976b) successfully applied this numerical method to a tanker to calculate its wave excited forces, added mass and damping coefficients and motions when the vessel is stationary. He then compared his numerical results to the experimental data. In general, the level of agreement was found to be acceptable, except for the surge force and pitch and yaw moments in beam waves, which the author believed stemmed from asymmetry in the hull's shape. Later, Endo (1987) studied the motions of three-dimensional bodies floating freely in waves in shallow water. He calculated the hydrodynamic forces and wave loads of a rigid body using the surface source distribution method, with the same assumptions made as from linear wave potential flow theory. Li (2001) concluded that Endo's method provides more accurate seakeeping predictions in shallow water. Nonetheless, he suggested that some sections of Endo's code need to be altered. Then, Chan (1990) developed a three-dimensional numerical technique for predicting first and second order hydrodynamic forces on a vessel travelling in waves. He applied his code to a fully submerged ellipsoid, a half-submerged ellipsoid, a Series-60 ship and a 200 kDWT tanker, to predict their hydrodynamic properties. The obtained numerical results were found to be in good agreement with the available experimental data, except for roll and pitch damping coefficients and responses. The author hypothesises that the poor results in pitch and roll motions come from nonlinear effects in large roll amplitudes, and viscosity effects, which were ignored in his approach. By using this technique, he also provided a discussion about the effect of heading, forward speed and water depth on the hydrodynamic forces and ship motions in his study.

The second category is termed the Rankine source panel method, which utilises a very simple Green function in its boundary integral formulation. The distinct difference of this method is that the singularities are distributed not only over the hull

surface, but also over the free surface and control surface. In the Rankine source panel method, the body surface and the whole domain are described with an acceptable degree of fidelity and a large number of discrete panels. This method offers the advantage of being applicable to any ship geometry or floating body, and it can also model an arbitrary sea bed topology. In addition, this method enables the inclusion of nonlinearities in the free surface and the coupled behaviour between steady and unsteady wave potentials. As mentioned earlier, the Rankine source panel method was first proposed by Hess and Smith (1964). Then, Sclavounos and Nakos (1988) developed a numerical method to model the propagation of water waves on a panelised free surface. Their approach showed that the Rankine panel method can be used to predict wave patterns and excitation forces. Their study caused the development of the formulation of ship motions in the frequency-domain, which enables fast computations. For example, Yuan et al. (2014) developed a three-dimensional Rankine panel method in the frequency domain to predict the hydrodynamic properties of ships advancing at very low forward speeds. They adopted the radiation condition of Das and Cheung (2012) in their code. As a case study, they used a 'Wigley III' hull travelling at different forward speeds. By comparing their results with the available experimental data, they concluded that the new radiation condition gives good solutions of the scattered wave patterns, and the obtained wave exciting force and motion responses are compatible with the results from the related towing tank tests.

However, the linear methods cannot model any coupling with nonlinear external mechanisms. Therefore, Kring (1994) extended the use of the Rankine panel method to the time domain. This makes it possible to directly include any kind of external forces and nonlinear waves in the calculations. Kim and Kim (2013), for example, studied the motions of an LNG carrier in various bathymetries, using a Rankine panel method and by solving the nonlinear Boussinesq equations. They obtained the motion responses and the hydrodynamic coefficients of the vessel in shallow water in the time domain and compared their results to those in deep water conditions. Their findings showed that the hydrodynamic properties of the vessel are altered significantly as water depth decreases, particularly at lower frequencies. They also found that the nonlinear effects become more important as vessels enter shallow

water, especially when they are exposed to waves of longer wavelengths. The only shortcoming in their study was that they did not validate their theory with any experimental results, hence one cannot assess how close their results were to the experiments, and under which circumstances their theory gives successful results.

Recently, CFD-based RANS simulations have also been used to study shallow water problems, such as finite-bottom effects on ship resistance, free surface wave patterns, ship-to-ship interactions and ship manoeuvrability.

Sakamoto et al. (2007) presented RANS simulations and validation studies for a high-speed Wigley hull in deep and shallow water utilising CFDShip-Iowa, a general purpose ship hydrodynamics CFD code. Their results include resistance predictions and wave pattern analyses for a range of forward speeds in calm waters. Following this, Jachowski (2008) carried out a study on the assessment of ship squat in shallow water employing Fluent, a commercial RANS solver. He used a model scale KCS to calculate its squat for several water depths at different ship speeds. Then, Zou and Larsson (2013), using a steady-state RANS solver (SHIPFLOW), performed a numerical study on the ship-to-ship interaction during a lightening operation in shallow water. They used an Aframax tanker and the KVLCC2 in model scale, both appended with rudder and propeller. Also, Prakash and Chandra (2013) studied the effect of confined waters on ship resistance at various speeds, using Fluent as a RANS solver. They concluded that the CFD technique can successfully be used to predict ship resistance and the free surface wave pattern in shallow water. Finally, Castiglione et al. (2014) investigated the interference effects of wave systems on a catamaran in shallow water. They used CFDShip-Iowa as a RANS solver to calculate the resistance and the interference factor of the DELFT catamaran in two separation distances at various water depths. Their simulations were carried out in calm water conditions.

2.8 Squat and Resistance of Ships

Havelock (1908) performed shallow water investigations in which he showed that wave patterns were formed due to a single point source. His work led to the introduction of the depth Froude number (Fn_h), which takes vessel speed and water

depth into account when examining wave patterns in shallow water. The depth Froude number can be defined as follows:

$$Fn_h = \frac{U}{\sqrt{gh}} \quad \textbf{(2.4)}$$

where h is the water depth (m). In this equation, Fn_h is calculated to be the ratio of vessel speed to wave propagation speed in shallow water.

The well-known Kelvin wave pattern is generated at depth Froude numbers under 0.57. With increasing depth Froude number, the transverse wavelengths will increase (International Navigation Association, 2003). When the depth Froude number approaches 1.0, the ship's speed becomes equal to the maximum wave propagation speed for a given water depth. This speed is often termed the critical speed (International Navigation Association, 2003). If the depth Froude number exceeds 1.0, then a vessel is defined as operating at supercritical speeds, whereas if the depth Froude number is less than 1.0, then the vessel is defined as operating at subcritical speeds.

Many researchers have studied the squat and resistance of ships in shallow water. As indicated in Varyani (2006), the research in this particular area of ship hydrodynamics began with Kreitner (1934), who predicted sinkage by adopting the hydraulic theory in one dimension. Later, Constantine (1960) investigated the movement of floating objects along canals. The purpose of his investigation was to explain the relationships between three flow regimes (subcritical, critical and supercritical) and the incidence of squat, by developing a theoretical model. It is known from his work that if a channel has a restricted width, then this has a drastic influence on hydrodynamic forces in a limited range of Froude numbers. After this, Tuck (1966) developed a slender-body theory using matched asymptotic expansions to approach ship hydrodynamic problems in shallow water of constant depth and infinite horizontal extent. He derived formulae to predict the wave resistance and vertical forces at both sub- and supercritical speeds. He used the vertical forces to obtain the sinkage and trim of ships, finding that his numerical results were compatible with model ship experiments. The only drawback in his theory is that when the ship speed is close to the speed of the waves in shallow water, the theory

fails because the formulations become singular. From his study, it was concluded that sinkage is prominent for subcritical speed regimes, whereas trim is the major factor for supercritical speed regimes. Then, Tuck (1967) extended his previous theory to incorporate the effects of the canal having a restricted width. By extending Tuck's work (1966), Beck et al. (1975) studied the longitudinal motion of a vessel in a dredged channel. By solving boundary value problems, they computed the trim, sinkage and wave resistance of a ship in a dredged channel for a range of depth Froude numbers. The dredged channel geometry that was investigated in their study is surrounded by shallow regions, with a vertical step on either side of the channel. They revealed that the exterior shallow water regions have a considerable effect on the trim, sinkage and wave resistance of narrow channels. They also clearly declared that wave resistance increases with diminishing channel width. It should be noted that their numerical results were not validated against any experimental data.

More recently, Yasukawa (1993) developed a Rankine source panel method to calculate the steady wave-making resistance of a ship, incorporating the effects from trim and sinkage. He applied his theory to the Wigley hull model, and found that the results obtained agreed well with the available experimental results. Then, Jiang (1998) numerically investigated the waves generated due to the presence of a ship at three different speed regimes, by using the Boussinesq type shallow-water equations. He iteratively solved the finite-difference equation system by using the Crank-Nicholson time and space discretisation scheme. His theory assumes the ship to be a slender ship and approximates the flow field by using the matched asymptotic expansions technique. He carried out calculations for a Series 60 ship hull with block coefficient C_B=0.594 to predict its wave resistance, sinkage and trim. He then compared his numerical results with model tests, and a satisfactory agreement was found between the numerical and experimental data. Later, Gourlay (2008b) compiled a review on linear slender-body theories to calculate the squat of a ship in shallow water regions. He expressed a general Fourier method to predict the squat of a ship advancing through shallow open water, a rectangular canal, a dredged channel, a stepped canal or a channel of arbitrary cross-section. In his paper, Gourlay (2008b) only concentrated on cases in the subcritical flow regime, which he proposes is the most important regime for mariners. Following this, Gourlay (2008a) developed a

numerical method to predict the sinkage and trim of a fast displacement catamaran running in shallow open water, by utilising a linear slender-body theory. His theory is applicable for all three speed regimes. He also demonstrated the effect of centreline spacing between the demihulls of the catamaran on trim and sinkage. He claims that the theory he developed can be used to produce guidelines to predict the maximum squat of any fast displacement catamaran model. However, his study has not been validated against any experimental data. Then, Alderf et al. (2011) developed a method for the numerical modelling of dynamic squat, by using a finite element method. Their model is robust and can give results for the dynamic responses of a ship in highly restricted canals on any arbitrary-shaped sea floors. They also studied the influence of sea floor topology on a ship's critical velocity. Next, Yao and Zou (2010) performed a numerical study to predict the sinkage and trim of a vessel advancing in a shallow channel by using a first-order 3-D panel method. They discretised the hull surface, free surface and channel wall surfaces into panels and distributed Rankine sources of constant strength on them. In their theory, a nonlinear boundary condition is used on the free surface. They calculated the vertical force and pitch moments by integrating the hydrodynamic pressure over the wetted hull body, and obtained the sinkage and trim from the dynamic equilibrium. They carried out calculations for a Series 60 ship model (C_B=0.60) in a restricted channel. Their numerical results, covering sinkage, trim, wave-making resistance and wave patterns at subcritical and supercritical speeds, were found to be compatible with the experimental data. Lastly, Alidadi and Calisal (2011) performed a numerical study to predict the sinkage and trim of a Wigley hull. They developed a 2-D boundary element method using the slender body approach. To calculate the free surface flow, they used the Mixed Eulerian-Lagrangian (MEL) procedure. They also conducted a validation study by comparing the wave profile and resistance results of the ship in question with those from towing tank tests, and showed that the numerical results agreed well with those from the experiments at various ship speeds.

As opposed to potential flow-based theories, there have only been a few studies conducted using a CFD model to predict trim, sinkage and/or resistance of a ship entering into a shallow water area. Jachowski (2008) carried out a study assessing ship squat in shallow water employing Fluent, a commercial RANS solver. He used a

model scale KCS to calculate its squat for several water depths at different ship speeds. He then compared his CFD results with those calculated using the empirical formulae. His comparison found that the empirical methods show good agreement with the simulated results. Prakash and Chandra (2013) studied the effect of confined waters on ship resistance at various speeds, using Fluent as a RANS solver. They concluded that the CFD technique can be used successfully to predict ship resistance and the free surface wave pattern in shallow water. Then, Wortley (2013) studied the squat and resistance of the DTC container ship model using a CFD-based RANS solver, OpenFOAM. He also compared his CFD results to the experimental findings, reporting that OpenFOAM overestimates drag forces, especially the wave resistance, due to the generation of a coarse mesh in the domain. He noted that the squat and trim results of a ship model in a canal obtained using CFD are much larger than the experimental results. The author of this thesis believes that his numerical setup should be improved and reconsidered, in order to obtain results that are more compatible with experiments. Finally, He et al. (2014) investigated the interference effects of wave systems on a catamaran in shallow water. They used CFDShip-Iowa as a RANS solver to calculate the resistance and the interference factor of the DELFT catamaran in two separation distances at various water depths.

2.9 Concluding Remarks

Up until this point, a broad literature review has been made on existing seakeeping prediction methods and on other related topics which will be covered in the following chapters of this thesis. During this literature review, the following gaps in the literature have been detected:

i. No study has looked into the effects of employing seakeeping prediction methods on a ship's operability index.
ii. No study has been performed to compare the motion induced sickness values of a vessel, obtained using different seakeeping theories.
iii. No study has been performed to predict the added mass and damping coefficients of a two-dimensional twin section using CFD.
iv. There exist no CFD studies in the literature looking at the behaviour and performance of a vessel under slow steaming conditions.

v. The CFD studies performed to date have not predicted the increase in the effective power of a vessel due to its operation in waves.

vi. No studies have been performed on the calculation of ship motions in shallow water using a CFD-based unsteady RANS method.

vii. To date, studies performed on the squat and resistance of a vessel in a restricted canal or channel have not investigated the changing resistance and wave patterns of the vessel advancing through a canal under different loading conditions.

The following main chapters of this thesis aim to fill these gaps listed above, using either potential flow theory or the state-of-the-art CFD methods.

3. OPERABILITY ASSESSMENT OF HIGH SPEED PASSENGER SHIPS BASED ON HUMAN COMFORT CRITERIA

3.1 Introduction

Recently, a rapid increase has been seen in the number of passengers travelling worldwide by passenger vessels. Annually, throughout the world, it is estimated that roughly 10 million people travel on over 230 cruise vessels (Riola and Arboleya, 2006). A key responsibility of naval architects is to ensure the comfort and well-being of such passengers.

Due to the dynamic nature of a seaway, a vessel's performance and safety are often disrupted by enormous dynamic loads, motions and accelerations. Such factors may seriously affect both the well-being and safety of the passengers and crew, leading to motion sickness and similar motion-induced forms of discomfort.

For this reason, an operability analysis, considering human comfort criteria, plays a vital role in ship design, especially for the design of passenger ships - from small leisure craft, to extremely large cruisers. Considerable investment is made when building a passenger vessel. The comfort level of the passengers is of paramount importance, and must be maintained above a specific threshold. This threshold must therefore be continually considered during the design of a passenger vessel. This should be quantified by applying an operability assessment procedure invoking seakeeping analyses in accordance with reliable seakeeping criteria.

The major parameters which are required to perform such an operability analysis can be divided into the following three main categories:

i) vessel geometry and loading condition

ii) definition of the seaway and wave data

iii) limiting criteria

An overview of the operability assessment procedure is illustrated in Figure 3.1.

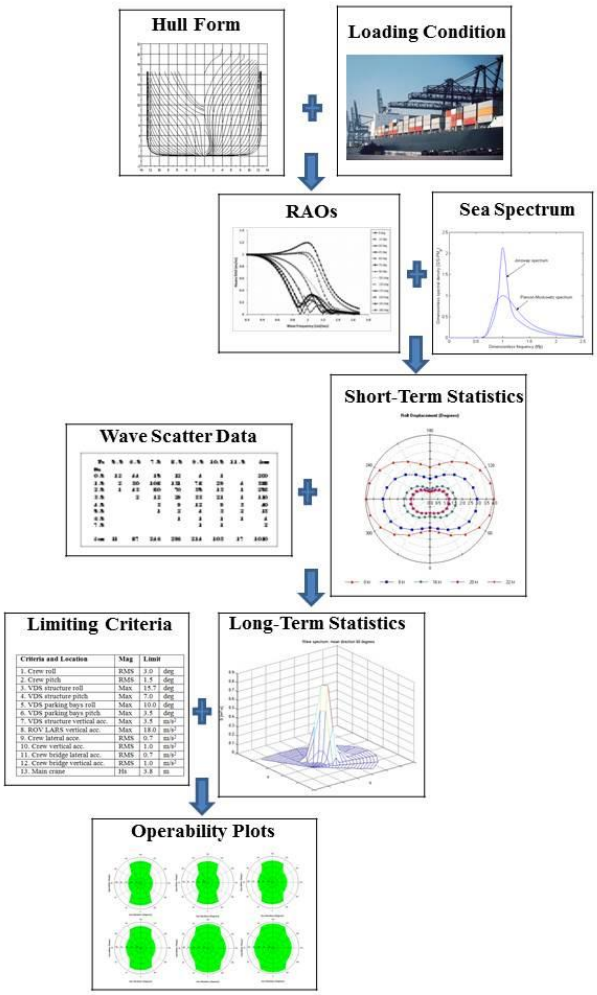

Figure 3.1 Overview of the operability analysis procedure.

Figure 3.1 demonstrates that knowledge of both a vessel's hull form, and its loading conditions (such as draft, trim, centre of gravity and radii of gyration), are necessary to predict a ship's responses to regular waves (such as RAOs). The literature offers a wealth of seakeeping techniques which can be employed at this stage, ranging from simple strip theory to complex, fully nonlinear Reynolds-Averaged Navier-Stokes computations. Since each method has a different theoretical background, with associated limitations, the selection and use of a particular method will greatly affect

the prediction of RAOs. The results of an operability analysis will therefore be dependent on the seakeeping technique employed. This chapter will demonstrate this effect.

The seaway where a ship operates may be represented by sea spectra dedicated to different specific sea areas. Short-term responses of the vessel are easily derived by combining the RAOs with the incident wave spectrum. However, it is of note that a ship encounters many different sea states on her voyage. It is therefore desirable to know the frequency of occurrence of wave height and wave period combinations in a specific geographic site. This data is generally found in wave scatter diagrams (WSD), which can be given yearly, monthly, or seasonally. Once wave scatter data is obtained, long term responses can be computed by means of statistical techniques. As seasons change, wave scatter data in a geographic area varies accordingly. As expected, this change can remarkably affect a vessel's operability. This chapter also assesses the effect of seasonality on ship's expected operability.

This chapter begins with a brief discussion on the methods that will be used to calculate a vessel's operability. Afterwards, an overview of the procedure for operability assessment is presented. Each stage of the methodology is introduced in detail in the subsequent sub-sections. A high speed catamaran car/passenger ferry operating in the west coast of Scotland is then explored as a case study, and the operability indices of the vessel are calculated. The results explicitly reveal the influence of seasonality on the predicted ship operability. This chapter also investigates the sensitivity of the operability index to the adopted seakeeping technique to generate an RAO database. Finally, a summary of the chapter will be provided in the last section.

3.2 Background

As mentioned in the Critical Review chapter, several methods are available with which to determine the response amplitude operators. Each technique features different assumptions and limitations, and therefore the output from a given technique will have a significant impact on the operability calculations. In order to

highlight this problem, three particular methods will be employed to estimate the RAOs of a catamaran ferry. These are:

- Theory 1: Conventional strip theory formulation (2-D)
- Theory 2: High-speed formulation in which hull interaction is *not* included (2½-D)
- Theory 3: High-speed formulation in which hull interaction *is* included (2½-D)

In order to apply these theories in the operability calculations, VERES, which is based on a linear, potential, strip theory software package, is used in this study (Fathi, 2004). The fluid is assumed to be homogeneous, non-viscous, irrotational and incompressible. However, viscous roll damping is taken into account in this seakeeping package, employing some empirical formulae. For more information, the theory manual of the software may be consulted (Fathi and Hoff, 2013).

Theory 1 is based on the strip theory formulation by Salvesen, Tuck and Faltinsen (1970), which is of most use for low ship speeds. The restrictions of this theory were explained in detail in Chapter 2.

Theory 2 is based on a strip theory approach of Faltinsen and Zhao (1991a) and Faltinsen et al. (1991, 1992), and is briefly explained by Fathi and Hoff (2013) as follows: "*The high-speed formulation is based on a strip theory approach, where the free-surface condition is used to step the solution in the downstream direction. The solution is started assuming that both the velocity potential and its x-derivative are zero at the first strip, counted from the bow*". Hoff (2014) describes the principal difference between the traditional strip theory and the high speed formulation as that both formulations solve a two dimensional problem for each strip, but only the high speed formulation accounts for the interaction between the solutions of each strip by stepping the solution in the downstream direction.

In Theory 3, the forces exerted on the ship are directly calculated from the velocity potentials, employing integral theorems, similar to Theory 1. In the high speed formulation without hull interaction (Theory 2), the forces are calculated by

integration of the pressure over the hull surface. Hermundstad et al. (1999) has found that these two methods (Theory 2 and 3) result in differences in the calculated heave and pitch motions; particularly around resonance.

Since a catamaran model is used in this chapter as a real case study, it will first be necessary to investigate the wave generation between demi-hulls of a catamaran.

Wave interference occurs between the waves generated by each single hull of a catamaran. Faltinsen (2005) defines this wave interference as follows "*the waves generated from each hull are superimposed without accounting for the fact that the waves generated by one hull will be modified because of the presence of another hull*". The waves generated by one hull may become incident to another demihull, causing wave diffraction to occur. In the theory, a first assessment to determine whether any wave interaction is expected between the two side hulls of a catamaran can be performed by assuming there is no hydrodynamic hull interaction. The wave angle (α_c), given by Equation (3.1), can then be calculated, to determine whether the waves inside the wave angle become incident to the other hull. It should also be highlighted that Theory 3 is capable of accounting for this diffraction effect occurring between the demihulls of a catamaran (Faltinsen, 2005).

$$\tan \alpha_c = \frac{g}{2U\omega_e} \tag{3.1}$$

$$\frac{L_1}{L} = 1 - \left(\frac{b_1 + 0.5b_2}{L} \right) 2\frac{\omega_e U}{g} \tag{3.2}$$

Here, b_2 is the beam of a single hull and b_1 is the distance between hull sides, as shown in Figure 3.2. L is the ship length and L_1 is the length of the aft part of the side which is affected by the other hull. Throughout this thesis, ω_e denotes the frequency of encounter and gravitational acceleration, g, is taken as 9.81 m/s^2.

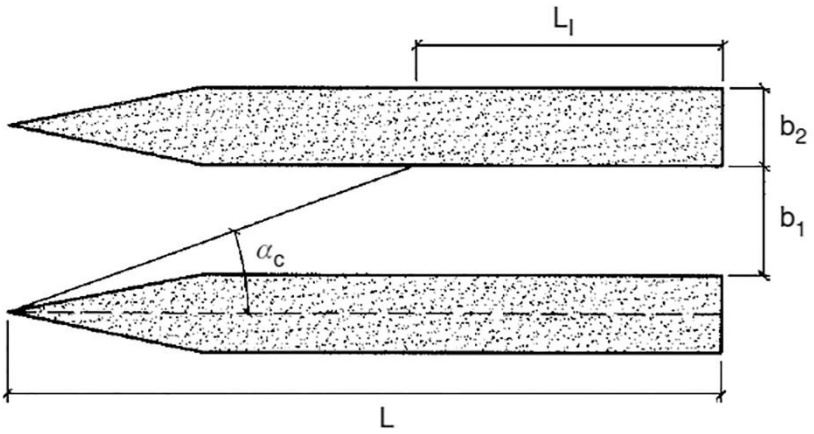

Figure 3.2 Hull interaction in a catamaran due to the wave effect, taken from Faltinsen (2005).

Each of the methods explained above will be used to independently calculate the motion responses of the ferry to regular waves, for a range of wave headings, to predict its operability. It should be stated that a 0° wave headings ($\beta=0^{\circ}$) corresponds to a head sea condition in this chapter.

3.3 Methodology

The methodology towards the prediction of the operability of ships is briefly presented in this sub-section.

The operability assessment technique typically begins with the calculation of motion characteristics of the given ship for all headings at the sea area which is particular to the vessel's course. Then, these responses (RAOs) are combined with the wave spectrum to predict the short-term responses to irregular seas. Next, limiting significant wave heights are calculated for each seakeeping criterion by utilising the short term responses. Finally, the calculation of the operability index, which is the percentage of the number of wave height and wave period combinations not violating the predetermined criteria, can be computed taking into account long term statistics of the wave data.

A high speed catamaran car/passenger ferry is used in this chapter as a case study to argue the effect of the various methods to predict RAOs. The main characteristics and geometry of the ferry are given in Table 3.1 and Figure 3.3, respectively.

Table 3.1 Main characteristics of the catamaran ferry (Tezdogan et al., 2014b).

Length between perpendiculars (L_{BP})	151.12 m
Overall beam of twin-hull (B_{OA})	36.72 m
Beam of demi-hull (B_{DH})	10.68 m
Design draught (T)	9.4 m
Displacement (Δ)	16,448 m^3
Hull centre line spacing	26.04 m
Longitudinal centre of gravity (LCG) aft of amidships	11.84 m
Vertical centre of gravity (VCG) from the base line	13.28 m
Pitch radius of gyration (r_{55})	39.24 m
Roll radius of gyration (r_{44})	13.36 m
Yaw radius of gyration (r_{66})	40.88 m
Design speed (U)	20 knots

The Marintek Catamaran is taken as a ship model and has been scaled to real ship dimensions. All details related to the catamaran model can be found in Hermundstad et al. (1999).

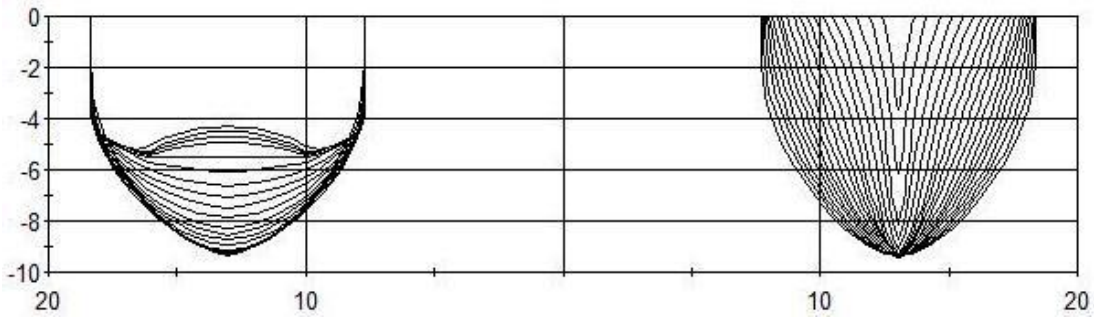

Figure 3.3 Sections of a demihull (left- and right-hand sides of the graph show aft and forward stations, respectively).

Although the demi-hulls of the catamaran geometry are connected to each other above the water line, only the sections under the free surface are illustrated in Figure 3.3.

Each of the necessary stages to predict the operability of the vessel are briefly explained in the following sub-sections.

3.3.1 Ship responses to regular waves

Typically, the first stage in the assessment of a ship's operability is to predict the ship response characteristics in regular waves for a range of headings and ship speeds in the frequency domain. The transfer functions are usually calculated due to either a unit wave amplitude elevation for translational motions, or a unit wave slope amplitude for angular motions.

The numerical RAOs of the ferry, obtained using each theory, are compared to the experimental data published by Hermundstad et al. (1999). Four different combinations of ship speed and wave heading are presented below, each identified by their case numbers.

- Case 1: Froude number 0.47 (corresponds to a forward speed of 35.18 knots). Head seas.
- Case 2: Froude number 0.63 (corresponds to a forward speed of 47.16 knots). Head seas.
- Case 3: Froude number 0.63. Bow seas ($\beta=30^{\circ}$).
- Case 4: Froude number 0.47. Beam seas ($\beta=90^{\circ}$).

The comparisons are shown between Figure 3.4 and Figure 3.7, with the experimental results represented using triangles. The heave responses are non-dimensionalised by wave amplitude (*A*), whereas the pitch and roll responses are non-dimensionalised by wave amplitude over ship length (A/L_{BP}). It is worth noting that the angular responses are given in radians. The graphs, demonstrated between Figure 3.4 and Figure 3.7, are all plotted against non-dimensional wave frequency, $\omega'=\omega(L_{BP}/g)^{1/2}$.

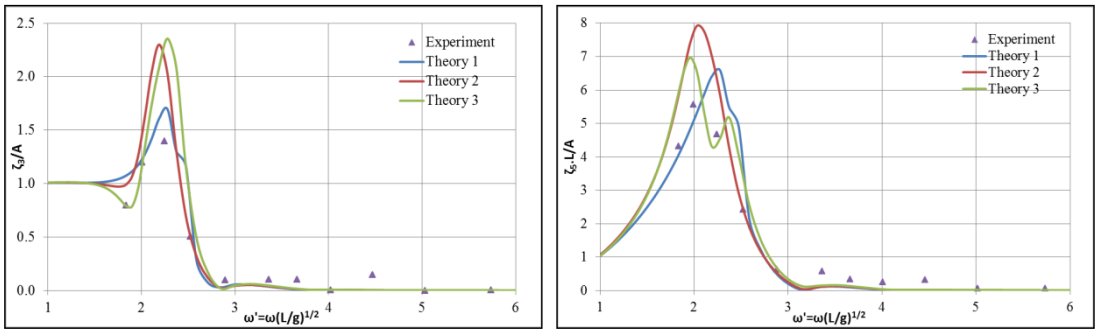

Figure 3.4 Experimental and numerical RAOs for Case 1. The left- and right-hand sides of the graph show heave and pitch RAOs, respectively.

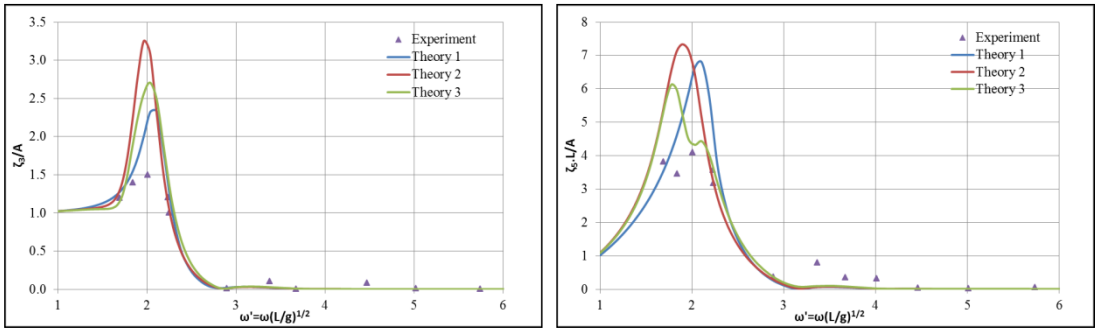

Figure 3.5 Experimental and numerical RAOs for Case 2. The left- and right-hand sides of the graph show heave and pitch RAOs, respectively.

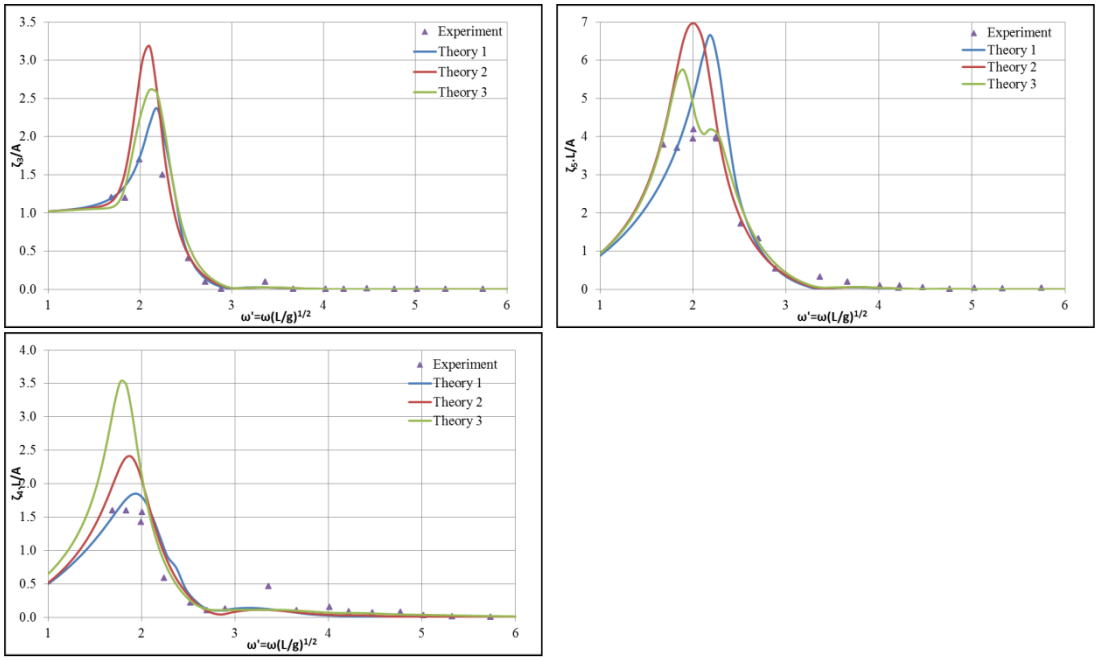

Figure 3.6 Experimental and numerical RAOs for Case 3. The upper left- and right-hand sides of the graph show heave and pitch RAOs, respectively. The lower part shows roll RAOs.

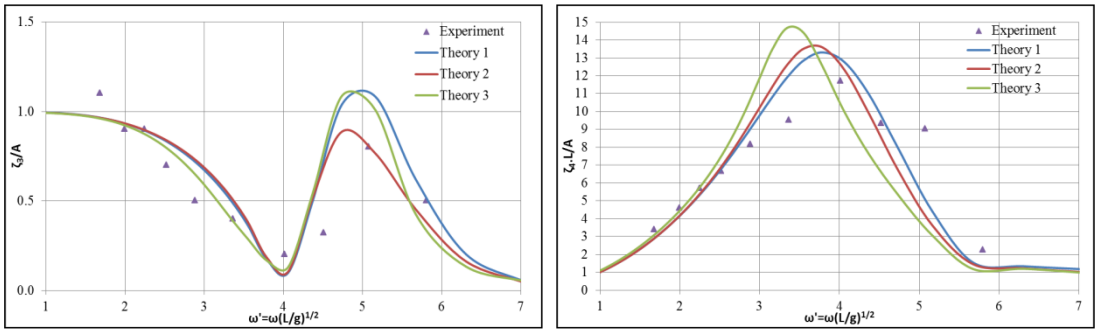

Figure 3.7 Experimental and numerical RAOs for Case 4. The left- and right-hand sides of the graph show heave and roll RAOs, respectively.

The figures between Figure 3.4 and Figure 3.7 appear to demonstrate the discrepancies between each numerical technique and the experimental results. If

Theory 2 is compared to Theory 3, it is evident from Figure 3.5 and Figure 3.6 that the numerical calculation of the resonant heave motion is improved when hull interactions are taken into account. In most cases, Theory 3 shows better agreement with the experimental data relative to Theory 2. This applies to both head and bow seas. It is worth noting that hull interactions are more dominant in heave motion, compared to pitch motion, at two high speeds. Conversely, for the roll motions, the discrepancies are much larger when hull interactions are taken into consideration. In most cases, of the three theories, conventional strip theory (Theory 1) is still the most compatible with the experiments, as this shows consistency with the ITTC's (1987) conclusion, explained in Chapter 2, Section 2.2.

Given that wave frequency equals the encounter frequency in beam seas, it is more convenient to compare the natural roll frequency of the vessel with the peak frequencies obtained by each numerical method in Figure 3.7. The natural roll frequency of the vessel (ω_{roll}=0.96 rad/sec), which coincides with ω'_{roll}=3.77, is very close to the peak frequency estimated by both Theory 1 and 2 (ω'_p=3.79), followed by Theory 3 (ω'_p=3.34), in beam seas.

Furthermore, the effects of three-dimensional flow, viscosity and nonlinearities are neglected in all three methods. This therefore causes an increase in the discrepancies between the numerical analyses and experiments (Hermundstad et al., 1999).

Additionally, a comparison of the vertical accelerations at the centre of gravity (CoG) using the different theories in head seas at 20 knots ship speed (Fn= 0.267) is given in Figure 3.8. The abscissa of the figure is the encounter frequency, whereas the ordinate is the vertical acceleration, non-dimensionalised by gA/L_{BP}, conforming with the ITTC guideline (2011a).

Figure 3.8 clearly demonstrates discrepancies between the vertical accelerations calculated using the different theories, particularly when applied to the resonance heave frequency (the natural heave frequency of the vessel, ω_{heave}=1.184 rad/sec). The RAO vertical acceleration calculated using Theory 3 is 4.18 and 2.18 times higher than that obtained by Theory 1 and 2 in the resonance frequency, respectively. The vertical acceleration obtained using Theory 3 gives higher results because of the

effect of wave interactions between each demihull. This will be discussed in detail in the following paragraphs. If Theory 1 is compared to Theory 2, the differences in the vertical acceleration around the resonance frequency arise from the evaluation of forward speed in the free surface condition.

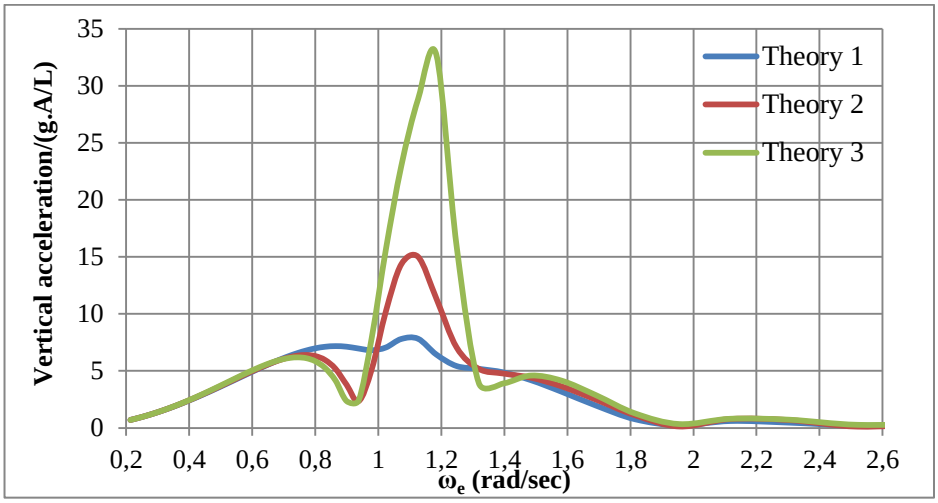

Figure 3.8 Vertical acceleration RAOs at the centre of gravity against encounter frequency in head seas at 20 knots speed.

Typical vertical acceleration RAOs in head seas as a function of wave frequency and ship service speed, calculated using Theories 1, 2 and 3, are shown between Figure 3.9 and Figure 3.11, respectively.

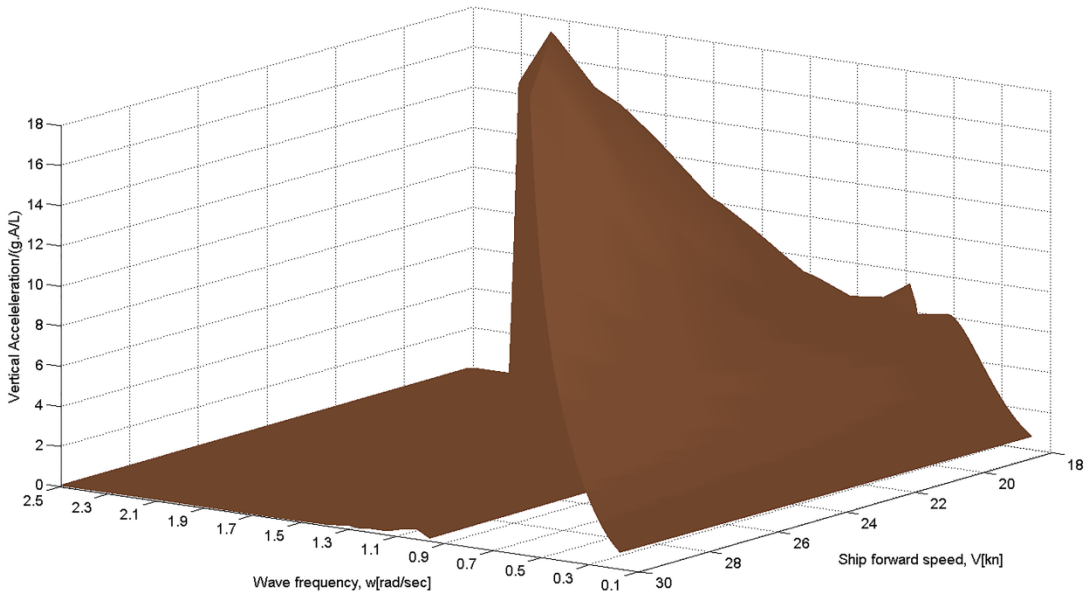

Figure 3.9 Vertical acceleration RAOs at the centre of gravity in head seas, calculated using Theory 1 at a range of forward speeds.

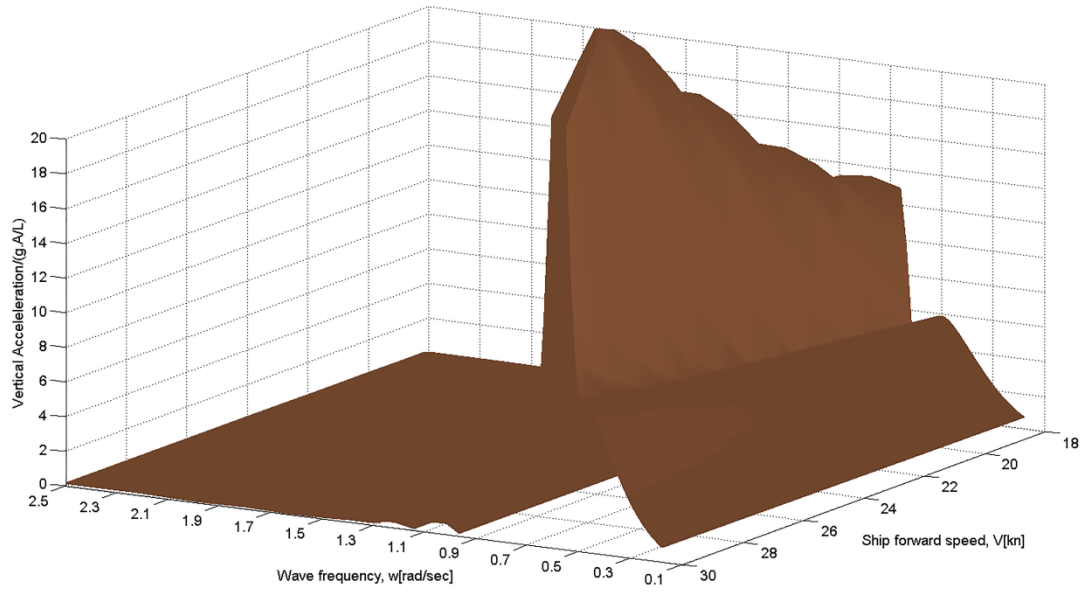

Figure 3.10 Vertical acceleration RAOs at the centre of gravity in head seas, calculated using Theory 2 at a range of forward speeds.

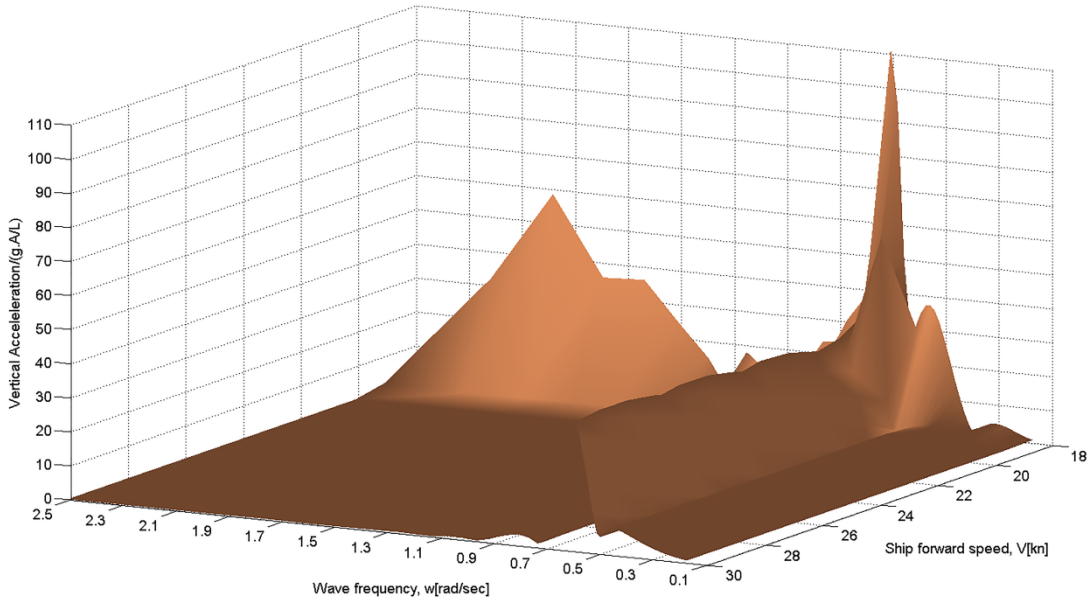

Figure 3.11 Vertical acceleration RAOs at the centre of gravity in head seas, calculated using Theory 3 at a range of forward speeds.

The figures between Figure 3.9 and Figure 3.11 demonstrate that vertical acceleration RAOs obtained using Theory 1 and 2 are very similar to each other, showing a gradual increase with increasing speed. Conversely, vertical accelerations generated using Theory 3 (Figure 3.11) show a different trend. They decrease with increasing speed between a speed range of 18-21 knots, and after this range they gradually increase with increasing speed, showing an expected trend. This is due to

the fact that hydrodynamic hull interactions are most significant within a speed range of 18-21 knots for the ferry in question, and the waves generated by each demihull affect the vertical accelerations. According to Equation (3.2), for a given frequency of encounter, the wave interaction between demihulls decreases as ship speed increases. This clearly explains why the vertical accelerations obtained using Theory 3 show a reversed trend within this particular speed range.

Table 3.2 presents L_1/L ratios (based on Equation (3.2)) against a range of wave frequencies, for varying forward speeds of the ferry.

Table 3.2 L_1/L ratios of the ferry, calculated based on Eq. (3.2), for a range of ω at different speeds.

ω (rad/s)	Ship forward speed, U (knots)												
	18	**19**	**20**	**21**	**22**	**23**	**24**	**25**	**26**	**27**	**28**	**29**	**30**
0.1	0.97	0.97	0.97	0.97	0.97	0.96	0.96	0.96	0.96	0.96	0.95	0.95	0.95
0.2	0.94	0.93	0.93	0.93	0.92	0.92	0.91	0.91	0.91	0.90	0.90	0.89	0.89
0.4	0.86	0.85	0.84	0.83	0.82	0.80	0.79	0.78	0.77	0.76	0.75	0.73	0.72
0.6	0.76	0.74	0.72	0.70	0.68	0.66	0.64	0.62	0.59	0.57	0.55	0.52	0.50
0.8	0.64	0.61	0.58	0.55	0.51	0.48	0.45	0.41	0.38	0.34	0.30	0.26	0.22
1.0	0.50	0.46	0.41	0.37	0.32	0.27	0.22	0.17	0.12	0.06	0.01	[ ]	[ ]
1.2	0.34	0.28	0.22	0.16	0.10	0.03	[ ]	[ ]	[ ]	[ ]	[ ]	[ ]	[ ]
1.4	0.16	0.08	0.01	[ ]	[ ]	[ ]	[ ]	[ ]	[ ]	[ ]	[ ]	[ ]	[ ]

Empty brackets [ ] indicate that there is no applicable hull interaction. Table 3.2 shows that the length L_1 decreases as the wave frequency increases, in other words the L_1/L ratio decreases with decreasing wavelength. It is evident that the hull interaction is most significant in low encounter frequencies at relatively lower ship speeds.

3.3.2 Ship responses to irregular waves

The real seaways can only be modelled by virtue of a statistical model. Ship responses to natural irregular seas (S_z) are calculated by the linear superposition principle, using the seaway spectrum (S_ζ) and the transfer functions in the frequency domain as given below.

$$S_z(\omega) = S_\zeta(\omega)\left|RAO(\omega)\right|^2 \quad \textbf{(3.3)}$$

Several spectral formulations are available in the literature. One of the most frequently used spectrums is the JONSWAP spectrum, which was developed in 1973

by the Joint North Sea Wave Project and described by Hasselmann et al. (1973). The JONSWAP formulation has been adopted for the fetch limited North Sea and can be expressed as follows:

$$S_\zeta(\omega) = \left[\frac{\alpha g^2}{\omega^5}.\exp\left\{-\frac{5}{4}\left(\frac{\omega_p}{\omega}\right)^4\right\}\right].\gamma^{\exp\left\{-\frac{(\omega-\omega_p)^2}{2\sigma^2\omega_p^2}\right\}} \quad \textbf{(3.4)}$$

where ω and ω_p are the incident wave and modal wave periods, respectively. σ represents the spectral width parameter and is calculated according to the following expression:

$$\sigma = \begin{cases} 0.07 & \omega \le \omega_p \\ 0.09 & \omega > \omega_p \end{cases} \quad \textbf{(3.5)}$$

γ refers to the peak-enhancement factor and is generally taken to be 3.30. α is the normalisation factor, given by

$$\alpha = 5.061(2\pi)^{-4} H_s^2 \omega_p^4 \left[1 - 0.287\ln(\gamma)\right] \quad \textbf{(3.6)}$$

The JONSWAP parametric spectrum is chosen for this study. The spectral density distribution of the spectrum for H_s=3.5m is illustrated in Figure 3.12.

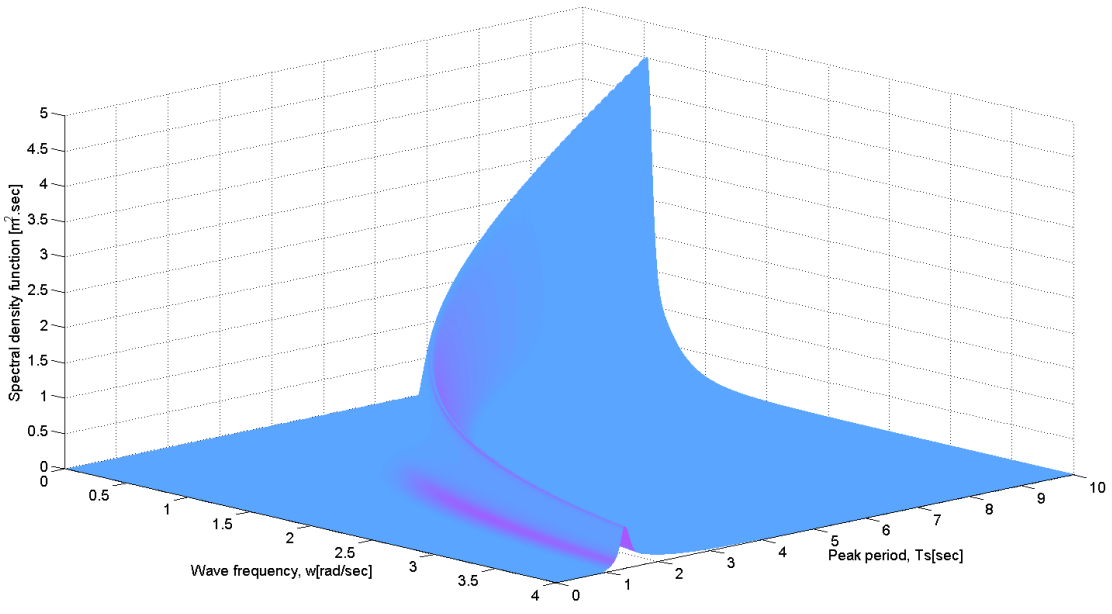

Figure 3.12 Spectral density distribution of the JONSWAP spectrum for H_s=3.5m.

The response spectrum $S_z(\omega)$ is the product of the defined sea spectrum $S_\zeta(\omega)$ and square of the transfer function $RAO^2(\omega)$ as given in Equation (3.3). Once the response spectrum is obtained, all statistical values of the response are derived by using the spectral technique.

The variance of the response spectrum is the area under the spectrum curve with respect to incident wave frequency and can be shown by:

$$m_0 = \int_0^\infty S_z(\omega) d\omega \tag{3.7}$$

The square root of Equation (3.7) gives the root mean square (RMS) of the response, which describes the most frequently observed amplitude of the waves or responses.

$$x_{RMS} = \sqrt{m_0} \tag{3.8}$$

in which m_0 is the zeroth spectral moment. Principally, the n^{th} order spectral moment can be presented by

$$m_n = \int_0^\infty \omega^n S_z(\omega) d\omega \tag{3.9}$$

The square roots of the m_2 and m_4 spectral moments correspond to RMS velocity and acceleration responses, respectively.

3.3.3 Determination of the limiting significant wave heights

Soares et al. (1995) suggest that the wave spectrum can be represented as the product of the normalised wave spectrum in terms of the significant wave height $S_{\zeta 1}(\omega)$ and square of the significant wave height H_s due to the linearity assumption.

$$S_\zeta(\omega, H_s, T_s) = H_s^2 S_\zeta(\omega, 1, T_s) = H_s^2 S_{\zeta 1}(\omega, T_s) \tag{3.10}$$

By analogy to Equation (3.10), the response spectrum may also be formulated as:

$$S_z(\omega) = H_s^2 S_{z1}(\omega) = H_s^2 S_{\zeta 1}(\omega, T_s) RAO^2(\omega) \tag{3.11}$$

and the variance of the response can be given by:

$$m_0 = \int_0^\infty S_z(\omega) d\omega = H_s^2 \int_0^\infty S_{\zeta 1}(\omega, T_s) RAO^2(\omega) d\omega \tag{3.12}$$

which can briefly be symbolised as follows:

$$m_0 = H_s^2 m_{01} \tag{3.13}$$

For cases in which a seakeeping criterion is defined as a root mean square of a response x_{RMS}, the limiting significant wave height for a specific modal wave period T_s, and ship heading β is determined by using the following equation:

$$H_s^{\lim}(T_s, \beta) = \frac{x_{RMS}^{\lim}}{x_{RMS,1}} \tag{3.14}$$

3.3.4 Calculation of the operability index

Fonseca and Soares (2002) define the operability index as "*the percentage of time during which the ship is operational*". The operability index is calculated according to the following common expression, which was also used in Khalid et al. (2009):

$$\text{Op.}(\%) = \frac{\sum_{H_s,T_s} n_{ss,\beta}(H_s < H_s^{\lim})}{N} x100 \tag{3.15}$$

With regards to Equation (3.15), the operability index is the ratio of the number of waves (for all available zero crossing periods) with significant wave heights not exceeding the maximum significant wave height ($n_{ss,\beta}$) relative to the total number of waves (N) in the wave scatter diagram of interest.

3.4 Operability Analysis

The procedure presented in the previous sections can be used to evaluate ship motions and motion-related responses to both regular waves and irregular seaways. Short term and long term statistics are obtained in irregular seas to predict the most probable maximum values of the ship responses. On the other hand, if these results are evaluated alone, they cannot properly express the performance of a ship from a seakeeping point of view. An operability index which measures a ship's capability to accomplish her tasks should be computed to quantify the seakeeping ability of the vessel (Fonseca and Soares, 2002).

3.4.1 Selection of the limiting criteria

In order to calculate the operability index of the ferry, the limiting criteria should be defined concerning passenger comfort and safety. A passenger ship's seakeeping performance depends partly on lateral accelerations, but mostly on vertical accelerations (Riola and Arboleya, 2006).

The influence of vertical accelerations on human metabolism is the major reason for sea-sickness. Discomfort regions are determined by the International Standard as a function of acceleration levels, frequencies, and exposure times. Parameters exist to quantify the effects of accelerations on human performance on-board. These may be regarded as a good reference with which to compare human performance between ship designs (Giron et al., 2001).

The International Standard (ISO) 2631/1 (1997) presents an approach to measure whole-body vibration in connection with human health and comfort, relating this to the probability of vibration and motion sickness incidence.

Motion Sickness Incidence (MSI) and Motion Induced Interruptions (MII) are the two most highly referenced parameters to quantify ship motion effects on human performance and comfort. MSI indicates the percentage of people experiencing vomiting when exposed to motion for a certain length of time. It was proposed as a function of wave frequency and vertical acceleration by O'Hanlon and McCauley (1974), following which a mathematical expression was developed by McCauley et al. (1976).

Graham (1990) developed the motion induced interruption concept, which is defined as the number of loss-of-balance events that occur during an arbitrary operation on-board. The theory, which is explained in detail in his study, is based on the calculation of the lateral force estimator (LFE) which causes objects to topple or slide, and people to lose their balance, in the frequency domain. Graham concluded that a limit on the number of MIIs can be applied as the most appropriate criterion for deck operations. Table 3.3 presents the proposed values in terms of different risk levels.

Table 3.3 MII risk levels (Graham, 1990).

Risk level	MIIs per minute
1. Possible	0.1
2. Probable	0.5
3. Serious	1.5
4. Severe	3.0
5. Extreme	5.0

The derived transfer functions are normally calculated with respect to specific positions on the ship which are closely associated with the limiting criteria to be used. Table 3.4 lists these locations on the ship and the seakeeping criteria that are selected for the operability assessment of the ferry. The locations in Table 3.4 are given according to *x, y,* and *z* coordinates, where *x* denotes the point forward after aft peak, *y* denotes the position off centre (positive starboard), and *z* denotes the location above the base line.

Table 3.4 Seakeeping criteria for the high speed passenger ferry.

Description	Criterion	Location	Coordinates (m)	Reference
Vertical acceleration	2 hours exposure 0.05g	Passenger deck	80, 0, 10	ISO 2631/3, (1985)
MII	0.5 MII per minute	Car deck	150, 0, 11	Graham, (1990)
MSI	35% MSI in 2 hours	Crew accommodation	25, -4, 9.5	ISO 2631/1, (1997)
Lateral acceleration	0.025g (RMS)	Centre of gravity	63.72, 0, 13.28	ISO 2631/1, (1997)

3.4.2 Definition of the sea spectrum and wave scatter data

It is assumed that the car/passenger ferry provides a fast transportation service across the west coast of Scotland (Figure 3.13, Global Wave Area 10).

As outlined earlier on, the JONSWAP spectrum has been selected to represent the area of operation. In order to determine the long-term responses of the vessel, the probability of occurrence of the sea states at the operation area is necessary. WSD provides such information as it gives a joint probability table of significant wave heights, characteristic wave periods, and the number of occurrences for a specific sea site. The statistics of ocean wave climates for the entire globe is available in Global Wave Statistics for a specific area based on instrumental, hindcasting, and visual observation methods (Hogben et al., 1986).

The operability calculations are performed using annual and seasonal WSD. Figure 3.14 depicts the wave scatter data of Area 10 using annual and seasonal statistics for the wave climate. The bars in the graphs demonstrate the number of waves observed in that combination of significant wave height and wave period.

According to Lloyd (1989), for ship design purposes the most common practice is to use short crested sea with a 90° spreading angle, hence the problem is treated in this fashion.

Figure 3.15 shows the percentage of time variances of significant wave heights observed in Area 10 with regards to annual and seasonal wave statistics.

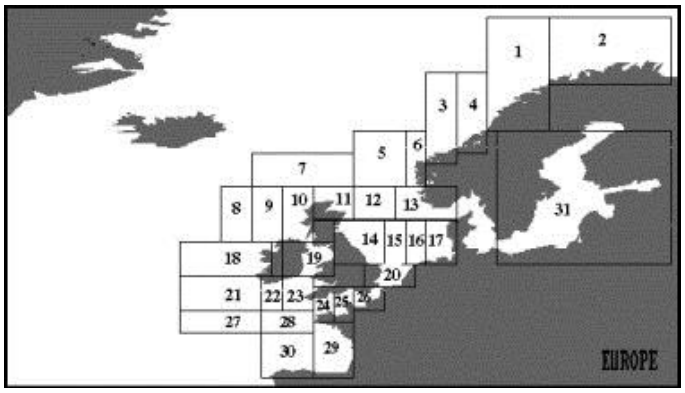

Figure 3.13 Global wave statistics of coastal areas (Luis et al., 2009).

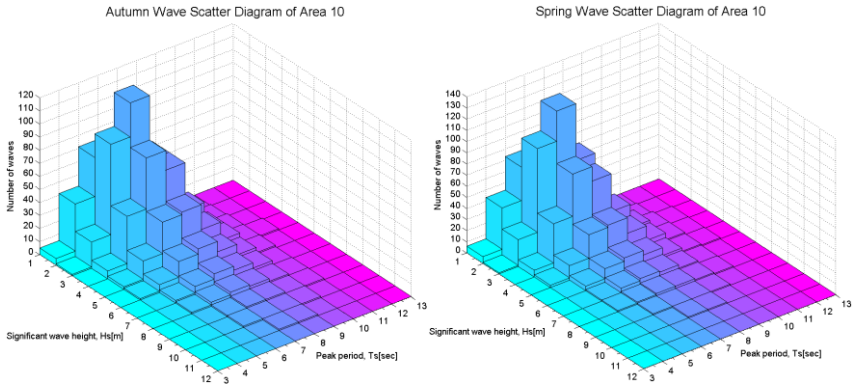

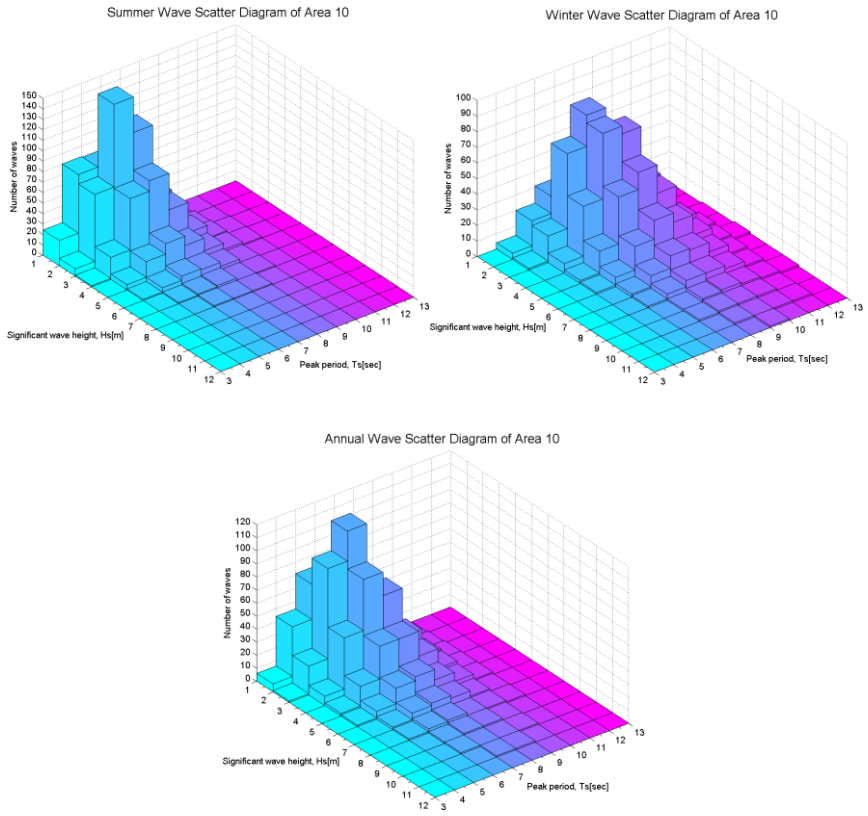

Figure 3.14 Wave scatter data of Area 10 regarding seasonal and annual statistics (Hogben et al., 1986).

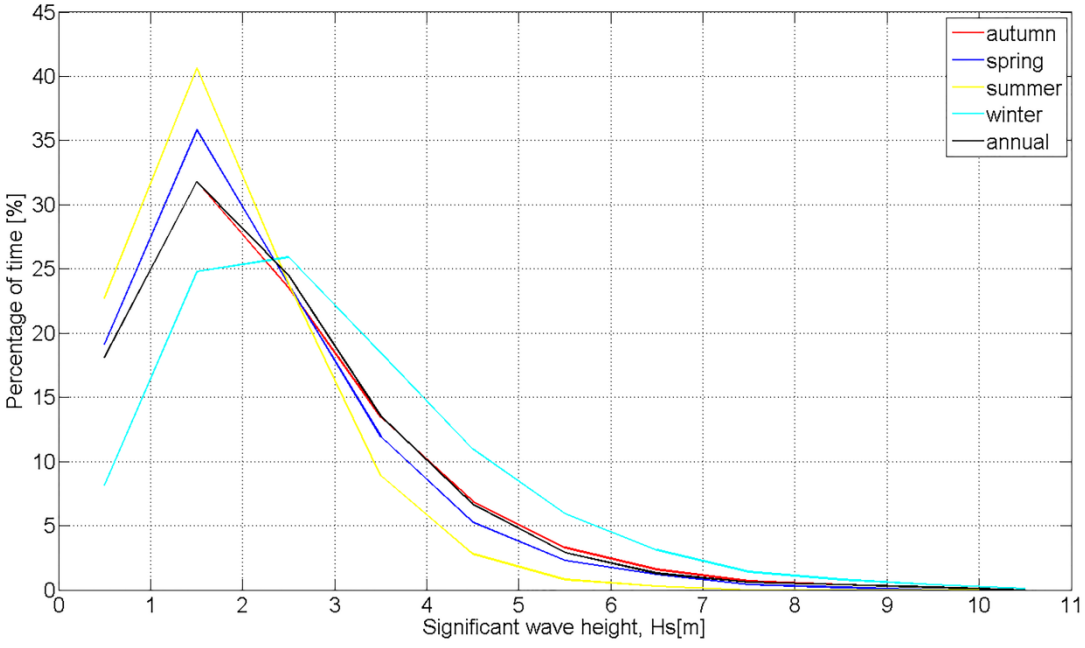

Figure 3.15 Percentage of time variances of significant wave heights observed in Area 10 over various durations.

3.5 Results

3.5.1 Motion sickness incidence

The operability indices will be calculated in this work based on human comfort-oriented criteria. Beyond any doubt, motion sickness incidence is one of the most important criteria used to quantify human comfort due to motion in any vessel (such as a car, train or ship). Special attention will therefore be paid to investigate possible MSI features of the vessel.

In this sub-section, MSI values of the ferry at the crew accommodation location will be calculated using the three different theories. MSI values are determined according to ISO 2631/1 (1997) using the following formulae:

$$MSDV_z = \left[\int_0^T a_{wf}^2(t)dt \right]^{0.5} \quad \left[m/s^{1.5} \right] \tag{3.16}$$

$$MSI = K_m.MSDV_z \quad [\%] \tag{3.17}$$

where $MSDV_z$ stands for Motion Sickness Dose Value in the vertical direction. a_{wf} is the frequency-weighted acceleration. The integration time T varies between 20 min and 6 hours and is taken as 2 hours in this work. K_m is a constant in the formula and is taken as 1/3, which indicates a mixed population of unadapted male and female adults. For more information about how to predict MSI values, reference can be made to ISO 2631/1 (1997).

In order to be able to predict the MSI values of the vessel in any sea state, the statistical parameters based on the annual sea state occurrences in the open ocean Northern Hemisphere, given in Table 3.5, will be used.

According to the data presented in Table 3.5, sea state 4 is the most frequently seen sea state, with a probability of 28.3%. On the other hand, sea states 2 and 7 are the least frequently observed sea states in this geographic area of interest, with probabilities of 5.7% and 7.6%, respectively.

Table 3.5 Annual sea state occurrences in the open ocean Northern Hemisphere (Bales, 1983).

Sea State No.	Significant wave heights (metre)	Sustained wind speed (knot)	Modal wave period (second)	Percentage probability of sea state (%)
2	0.30	8.5	7	5.7
3	0.88	13.5	8	19.7
4	1.88	19.0	9	28.3
5	3.25	24.5	10	19.5
6	5.00	37.5	12	17.5
7	7.50	51.5	14	7.6

The MSI values of the ferry are predicted for various sea states at a ship speed of 20 knots. The significant wave height and modal wave period data, used in the JONSWAP spectrum, are shown in Table 3.5. The calculated MSI values using each theory are compared in Figure 3.16.

Figure 3.16 demonstrates the differences in MSI values using each theory. Higher sea states cause higher MSI values, as clearly seen in the figure. Also, it is evident that in the low sea states (sea states 2-4), the MSI results from each theory appear similar to each other. However, in the high sea states, the discrepancies become significant. Theory 3 gives the highest results, whereas Theory 1 gives the lowest result in the high sea states. This is as expected since the vertical accelerations at 20 knots ship speed demonstrate the same trend, as shown in Figure 3.8.

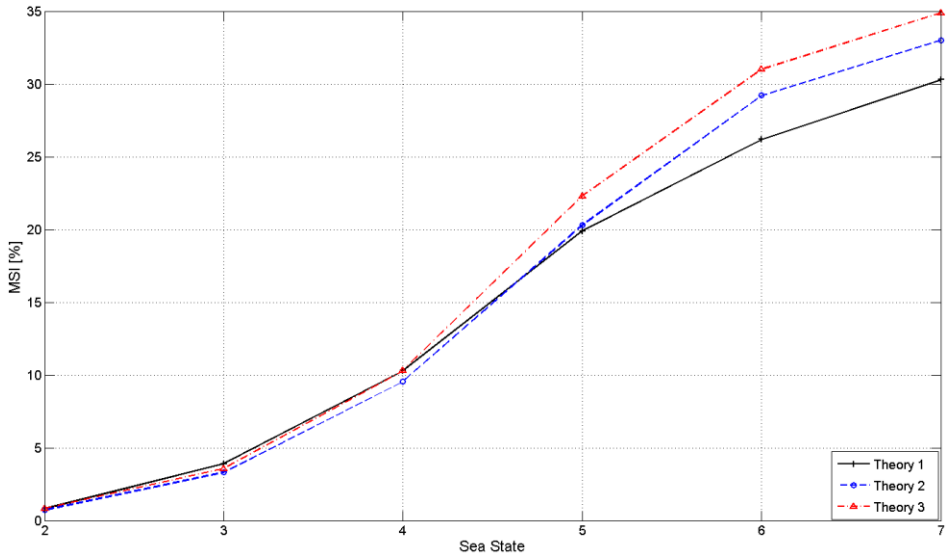

Figure 3.16 Motion sickness incidences calculated using each theory for varying sea states.

3.5.2 Limiting significant wave heights

The methodology presented in the third section of this chapter is applied to the ferry to measure the seakeeping performance of the vessel in terms of its operability index. All calculations have been carried out at a forward speed of 20 knots.

The limiting significant wave heights are calculated based on each criterion as a function of peak wave periods for a range of wave headings, using Theories 1, 2, and 3 independently. The results are displayed in Figure 3.17, Figure 3.18, and Figure 3.19, respectively.

A comparison of the limiting significant wave heights in head seas for each criterion is displayed in Figure 3.20. This clearly illustrates the influence of the employed theories on the maximum allowed significant wave heights. It is seen from the figure that the differences in the limiting significant wave heights obtained using each theory are most pronounced in the vertical acceleration criterion. This will lead to noticeable discrepancies in the resultant operability indices due to vertical acceleration.

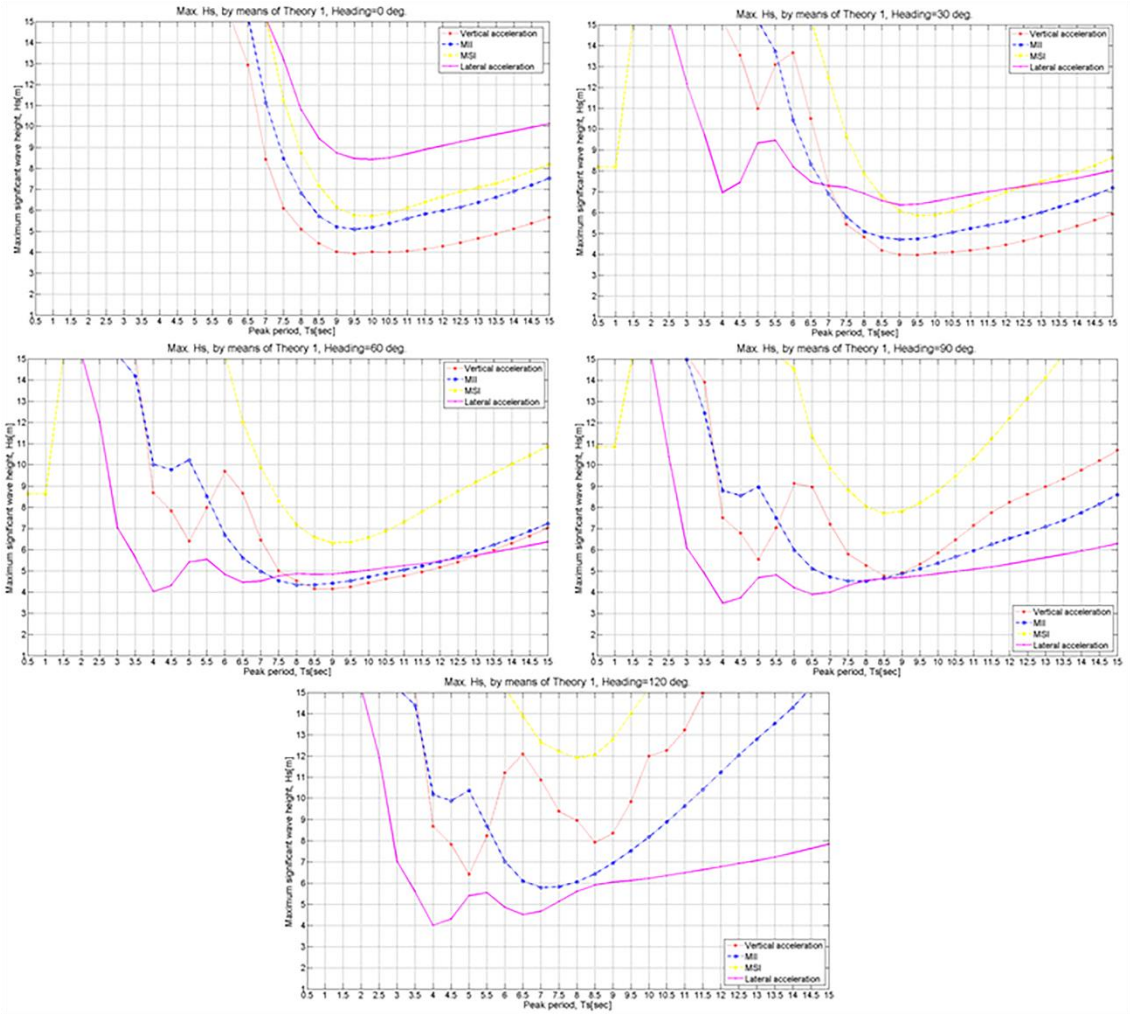

Figure 3.17 Limiting significant wave heights calculated using Theory 1 for various wave headings.

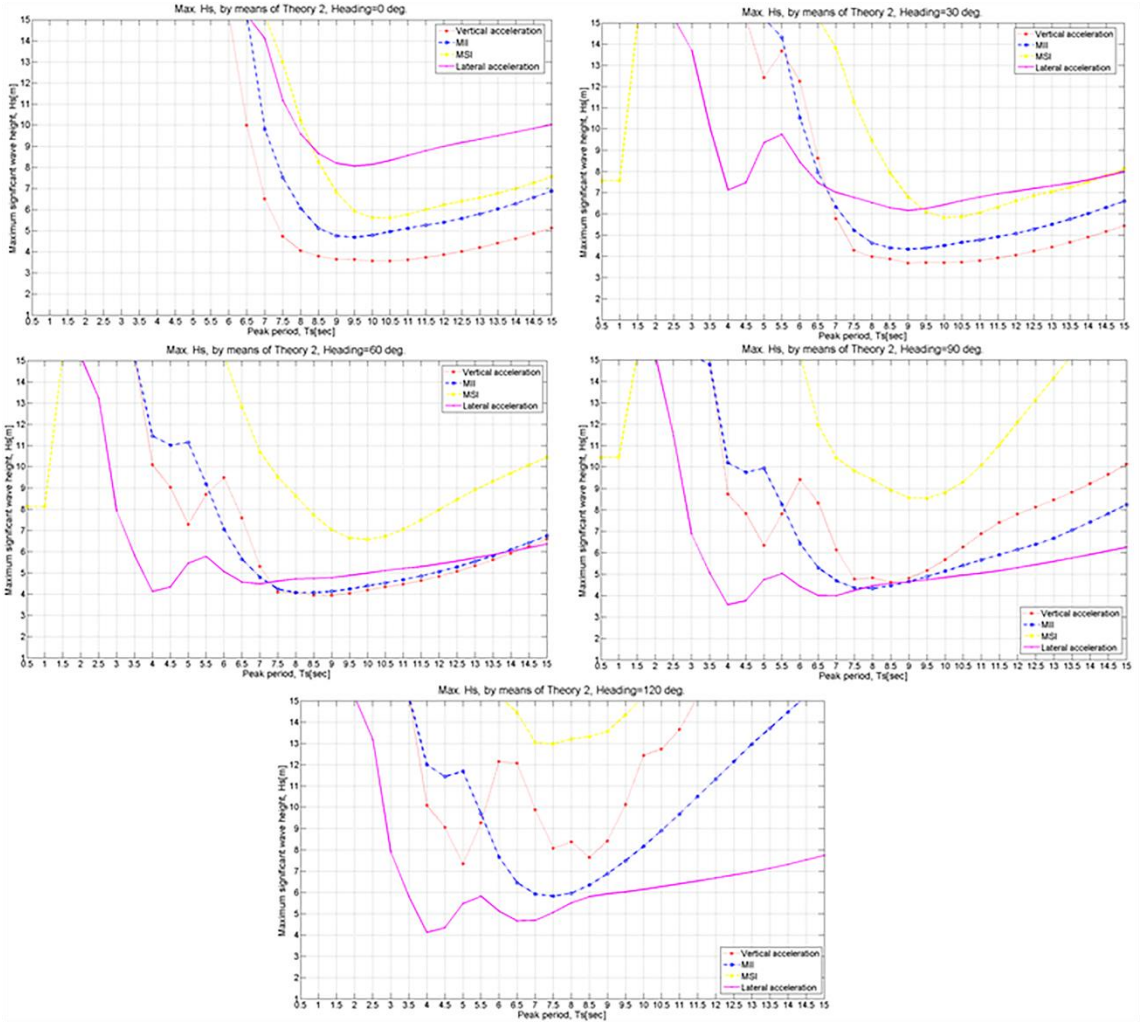

Figure 3.18 Limiting significant wave heights calculated using Theory 2 for various wave headings.

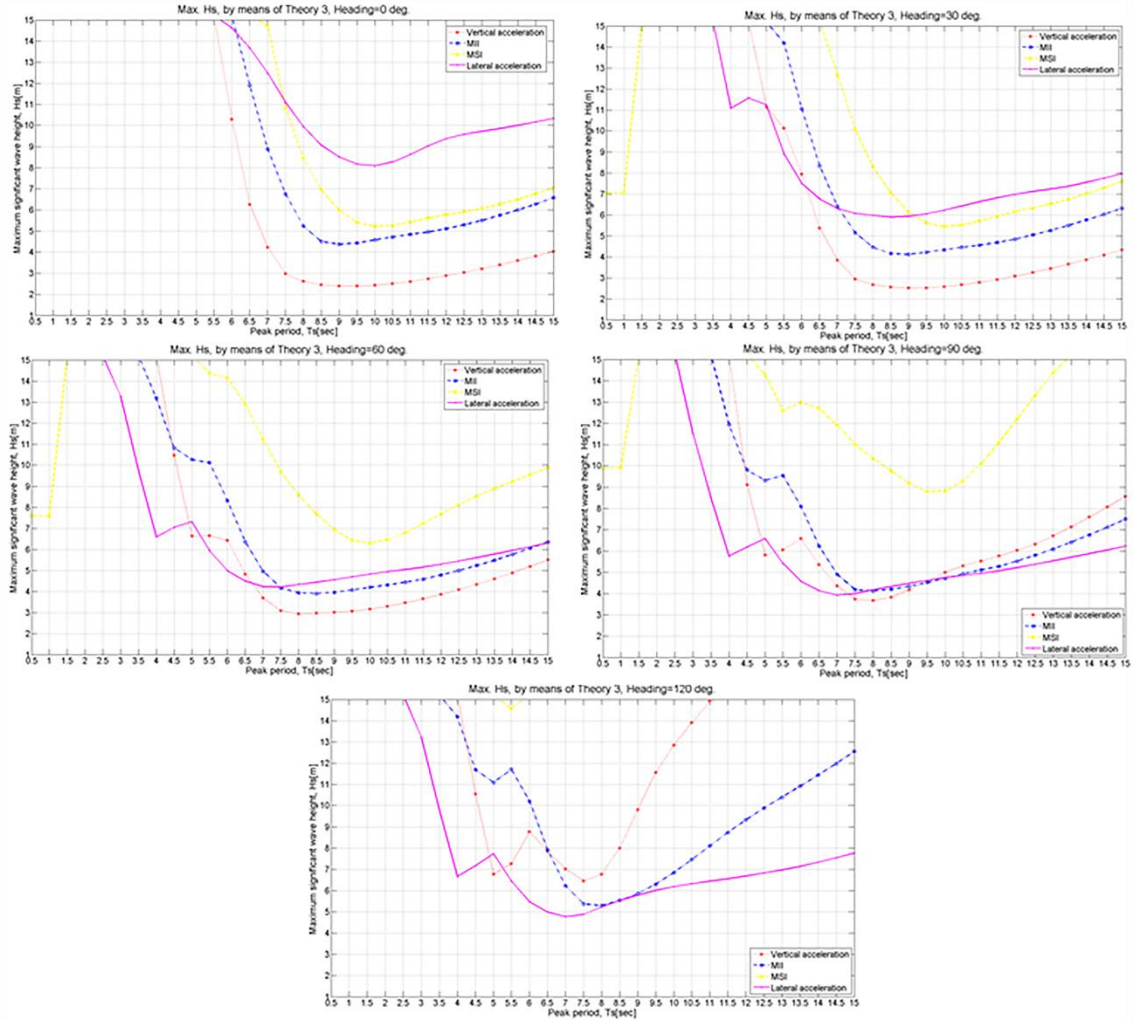

Figure 3.19 Limiting significant wave heights calculated using Theory 3 for various wave headings.

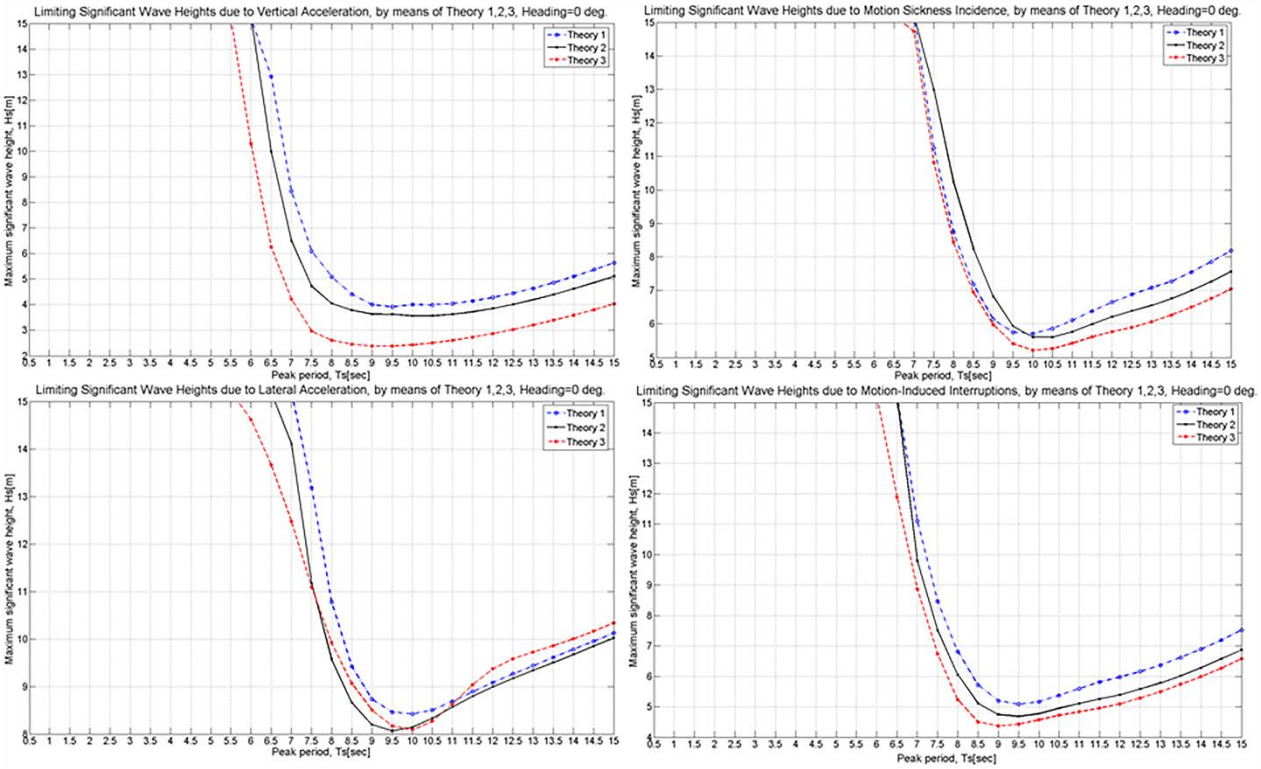

Figure 3.20 Effect of the employed theories on the limiting significant wave heights.

3.5.3 Operability indices

Operability calculations have been performed, individually, using each theory. The indices for the car/passenger ferry, resulting from these calculations, are summarised in Table 3.6, which includes both annual and seasonal wave statistics for Area 10, across several headings. In the main columns of the table, the operability indices satisfying each limiting criterion are shown, independently. The overall indices, which decide whether a vessel satisfies all the limiting criteria of interest, are calculated by taking the minimum values of each operability index, and are given in the right-hand block of columns. The average values, which are presented in the bottom row of each theory, are calculated by taking the average of the operability indices in each wave heading. It is based on the assumption that each wave heading has an equal probability of occurrence. Using this set of average outputs, the operability results can be compared with each other more efficiently, regardless of the wave heading.

The average annual, spring, summer, autumn and winter operability indices for the ferry are 86.15%, 88.67%, 91.61%, 85.80% and 83.43%, respectively, when calculated using Theory 3. The results show that, on average, the ship is operational, satisfying all necessary criteria, during 86.15% of a year. A more detailed breakdown for each season is also provided, for example the ship is, on average, operational 83.43% of the time during winter. When Theory 1 is used to generate RAOs, these indices increase to 95.21%, 96.46%, 98.60%, 94.73%, and 93.39%. Using Theory 2, the values are 93.80%, 95.28%, 97.92%, 93.31%, and 91.42%, respectively.

As Table 3.6 shows, the operability is generally small in head and bow seas due to the vertical acceleration at the fore perpendicular. The vessel’s operability is highest in following or quarter seas. Also, it can be concluded from the table that the vessel's operability is highest in the summer, closely followed by spring and autumn. Conversely, the vessel has the worst seakeeping performance during winter, as expected.

Table 3.6 Operability indices for the car/passenger ferry operating in Area 10.

Heading (deg)	Vertical acceleration					MII					MSI					Lateral acceleration					All criteria				
	Year	Spring	Summer	Autumn	Winter	Year	Spring	Summer	Autumn	Winter	Year	Spring	Summer	Autumn	Winter	Year	Spring	Summer	Autumn	Winter	Year	Spring	Summer	Autumn	Winter
Theory 1																									
0	90.42	92.62	97.15	89.45	84.40	97.30	98.12	99.52	96.83	95.73	98.22	98.92	99.78	97.97	97.28	99.72	99.92	100	99.72	99.66	90.42	92.62	97.15	89.45	84.40
30	90.81	92.98	97.23	89.88	86.06	95.67	96.88	99.03	95.06	94.04	98.37	99.07	99.84	98.20	97.89	98.68	99.32	99.92	98.62	98.57	90.81	92.98	97.23	89.88	86.06
60	93.19	94.98	98.05	92.46	91.61	94.14	95.76	98.39	93.50	93.23	98.86	99.37	99.93	98.80	98.96	95.34	96.68	98.79	94.76	94.29	93.19	94.98	98.05	92.46	91.61
90	97.22	98.20	99.37	97.09	98.20	95.91	97.25	98.90	95.60	96.59	99.70	99.91	100	99.70	99.91	94.39	96.02	98.25	93.76	93.64	94.39	96.02	98.25	93.76	93.64
120	99.91	100	100	99.91	100	99.08	99.49	99.91	99.07	99.71	100	100	100	100	100	97.65	98.61	99.52	97.54	98.03	97.65	98.61	99.52	97.54	98.03
150	100	100	100	100	100	100	100	100	100	100	100	100	100	100	100	100	100	100	100	100	100	100	100	100	100
180	100	100	100	100	100	100	100	100	100	100	100	100	100	100	100	100	100	100	100	100	100	100	100	100	100
Average	95.94	96.97	98.83	95.54	94.32	97.44	98.21	99.39	97.15	97.04	99.31	99.61	99.94	99.24	99.15	97.97	98.65	99.50	97.77	97.74	95.21	96.46	98.60	94.73	93.39
Theory 2																									
0	86.01	88.90	94.86	85.07	78.28	96.00	97.08	99.20	95.34	93.46	98.06	98.66	99.70	97.69	96.36	99.67	99.87	100	99.67	99.60	86.01	88.90	94.86	85.07	78.28
30	87.32	90.04	95.48	86.38	81.15	93.52	95.19	98.26	92.78	91.17	98.37	98.98	99.80	98.13	97.28	98.51	99.21	99.88	98.44	98.45	87.32	90.04	95.48	86.38	81.15
60	91.57	93.69	97.40	90.76	89.27	92.51	94.49	97.77	91.75	90.89	99.04	99.53	99.96	99.00	98.95	95.03	96.46	98.64	94.44	94.07	91.57	93.69	97.40	90.76	89.27
90	96.68	97.82	99.19	96.53	97.84	95.30	96.74	98.64	94.88	95.78	99.83	99.96	100	99.82	99.92	94.20	95.85	98.19	93.55	93.41	94.20	95.85	98.19	93.55	93.41
120	99.88	99.98	100	99.88	100	99.07	99.48	99.91	99.07	99.69	100	100	100	100	100	97.52	98.49	99.49	97.38	97.83	97.52	98.49	99.49	97.38	97.83
150	100	100	100	100	100	100	100	100	100	100	100	100	100	100	100	100	100	100	100	100	100	100	100	100	100
180	100	100	100	100	100	100	100	100	100	100	100	100	100	100	100	100	100	100	100	100	100	100	100	100	100
Average	94.49	95.78	98.13	94.09	92.36	96.63	97.57	99.11	96.26	95.86	99.33	99.59	99.92	99.23	98.93	97.85	98.55	99.46	97.64	97.62	93.80	95.28	97.92	93.31	91.42
Theory 3																									
0	66.39	71.36	80.26	65.93	56.92	93.87	95.45	98.39	93.12	91.23	97.39	98.15	99.56	96.84	95.05	99.60	99.82	100	99.60	99.55	66.39	71.36	80.26	65.93	56.92
30	68.86	73.84	81.62	68.40	61.58	92.32	94.23	97.81	91.50	89.34	97.79	98.51	99.65	97.38	96.18	98.29	99.03	99.84	98.20	98.29	68.86	73.84	81.62	68.40	61.58
60	78.88	83.21	88.72	78.21	76.26	90.42	92.82	96.73	89.57	87.96	98.83	99.41	99.93	98.76	98.69	93.80	95.55	97.95	93.15	93.08	78.88	83.21	88.72	78.21	76.26
90	93.34	95.28	97.62	92.80	94.39	92.79	94.79	91.62	92.12	92.38	99.83	99.97	100	99.83	99.93	92.27	94.42	96.82	91.61	92.05	92.27	94.42	91.62	91.61	92.05
120	99.60	99.75	99.95	99.60	99.95	97.58	98.47	99.52	97.52	98.68	100	100	100	100	100	96.69	97.88	99.05	96.48	97.21	96.69	97.88	99.05	96.48	97.21
150	100	100	100	100	100	100	100	100	100	100	100	100	100	100	100	100	100	100	100	100	100	100	100	100	100
180	100	100	100	100	100	100	100	100	100	100	100	100	100	100	100	100	100	100	100	100	100	100	100	100	100
Average	86.72	89.06	92.59	86.42	84.16	95.28	96.54	97.72	94.83	94.23	99.12	99.43	99.88	98.97	98.55	97.24	98.10	99.10	97.01	97.17	86.15	88.67	91.61	85.80	83.43

It is interesting to note that the overall performance of the vessel is mainly determined by the vertical acceleration. Also, the operability indices calculated solely with regards to the vertical acceleration criterion show a remarkably strong dependence on the chosen theory. It should be kept in mind that operability, as a function of limiting criteria, is dependent on predetermined criteria. If the selected threshold values given in Table 3.4 were lowered, it is obvious that the resultant operability indices would undergo far greater changes when using the employed theories.

The data generated using Theory 3, listed in Table 3.6, is illustrated graphically in Figure 3.21. This gives a clearer depiction of the overall operability indices of the vessel, enabling a more facile comparison between seasons.

It should be mentioned that in the figures given between Figure 3.21 and Figure 3.23, the polar axis shows wave headings, whereas the vertical axis shows operability indices.

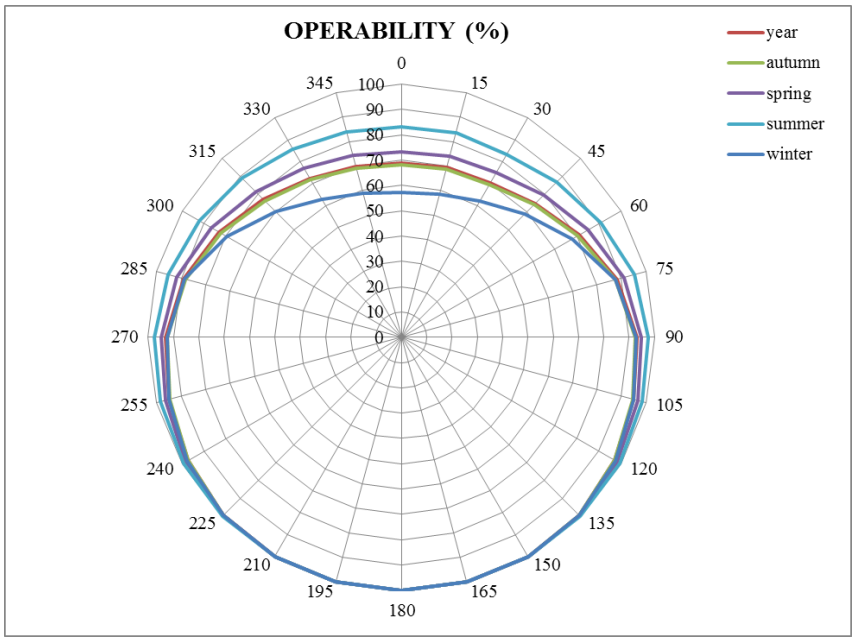

Figure 3.21 Influence of seasonality on the ship operability (generated using Theory 3, considering all criteria).

Figure 3.22 displays the operability polar diagrams of the ferry using the "all criteria" data from Table 3.6. The figure includes the operability results from all three theories and includes both annual and seasonal results. Shaded areas indicate the area where the ship is operational. The data contained in Table 3.6 and Figure

3.22 both express how much the vessel's operability appears to change when using the different theories and the seasonal statistical wave data in the area of interest.

	THEORY 1	THEORY 2	THEORY 3
YEAR			
AUTUMN			
SPRING			
SUMMER			
WINTER			

Figure 3.22 Operability polar diagrams of the ferry operating in Area 10.

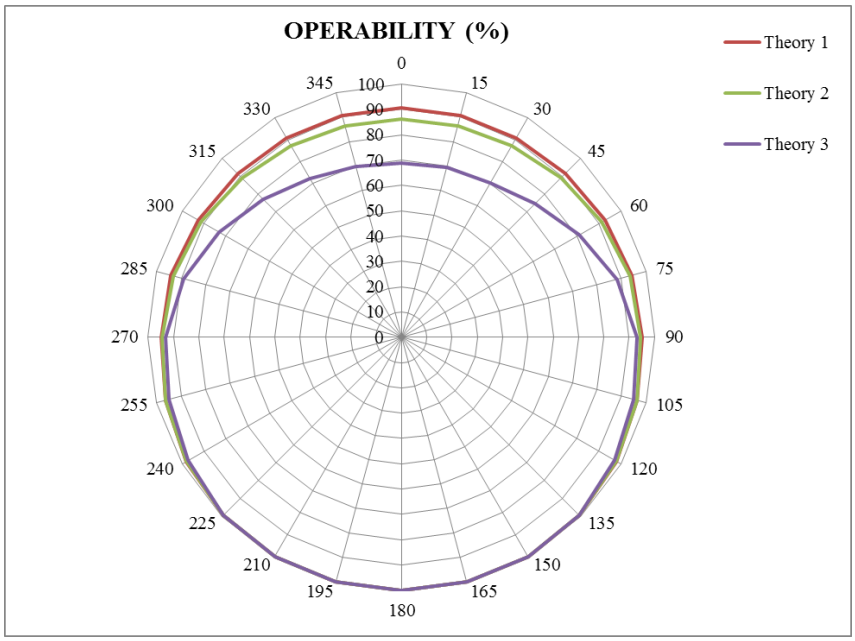

Figure 3.23 Influence of the different seakeeping techniques on the ship operability.

Figure 3.23 examines how a chosen seakeeping method affects subsequent operability analyses, specifically for head seas, taking into account all selected criteria. According to Figure 3.23, changing the method from 2-D classic strip theory to 2.5-D theory, which includes hull interactions, results in a decrease from 84.40% to 56.92% in the operability index, taking into account the winter statistics of Area 10.

3.5.4 Sensitivity analysis

Sensitivity analyses show how the operability index of the car/passenger ferry varies with seasonality and the employed theories, in accordance with the results given in this chapter, Section 3.5.3. The sensitivity analyses in this sub-section have been conducted in terms of satisfying all limiting criteria.

Figure 3.24 depicts the sensitivity of the operability index to the selected seakeeping theories. The results obtained using Theory 1 are retained as original values. The vertical axis represents the percentage difference between two theories to the original data, whereas the horizontal axis corresponds to the wave headings. The graph shows the results using annual statistics for the wave climate. It can be concluded from Figure 3.24 that there is a significant difference in the indices obtained using Theories 2 and 3, compared to those of Theory 1.

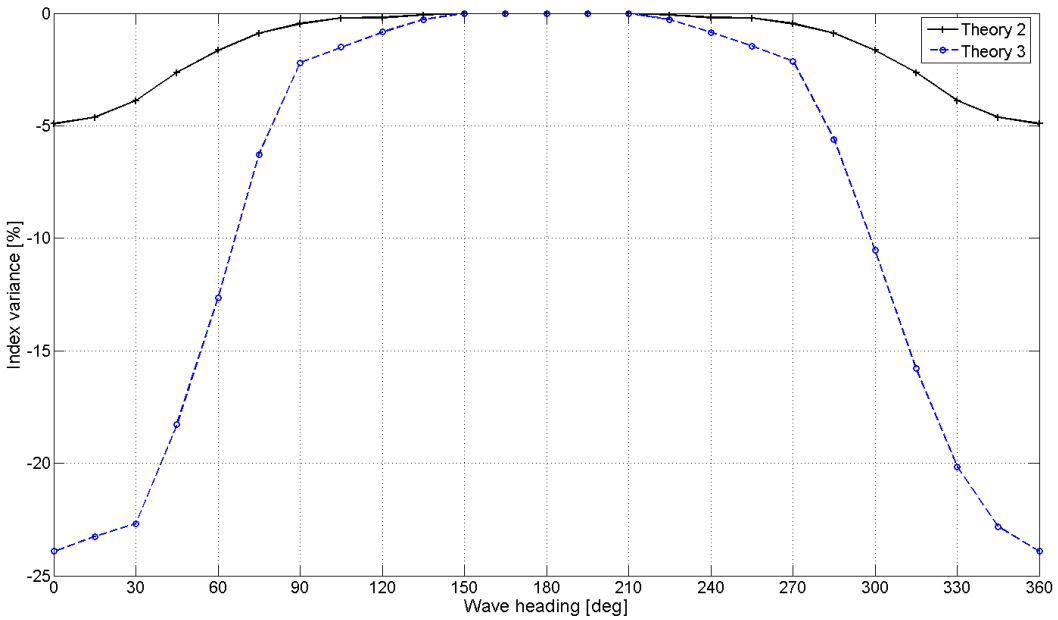

Figure 3.24 Sensitivity of the operability index to the employed seakeeping theories.

Figure 3.25 illustrates how seasonality affects the indices, with the indices obtained using annual wave statistics used as reference data. The sensitivity results are given as a percentage difference relative to the reference values, as a function of heading. The calculations are performed by employing Theory 3. Figure 3.25 clearly shows that the indices calculated using the autumn wave scatter data are the closest to those calculated using the annual wave climate data.

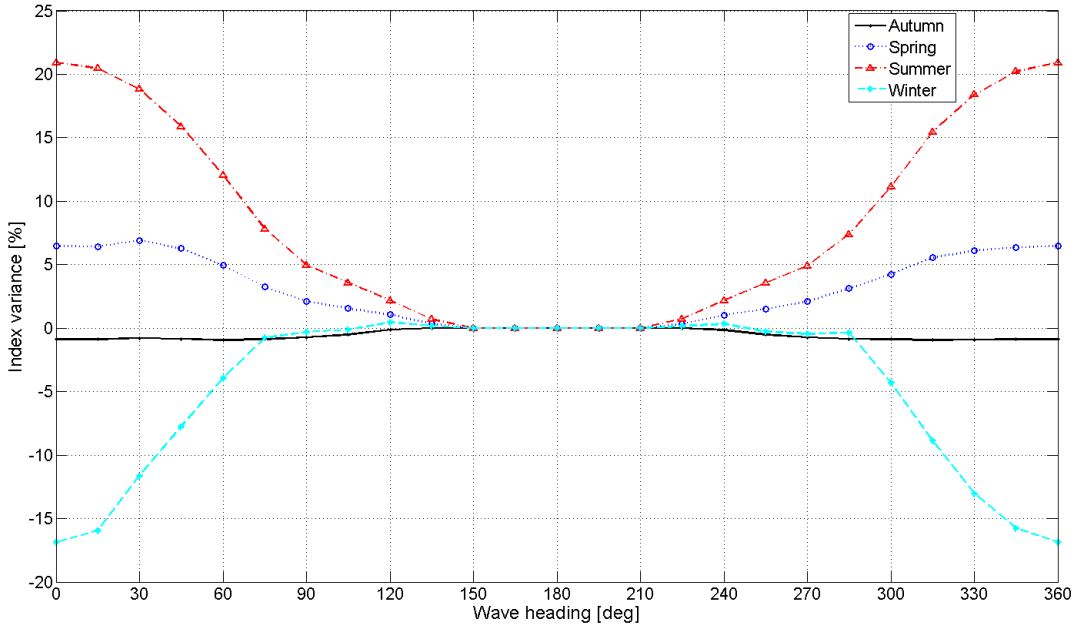

Figure 3.25 Sensitivity of the operability index to seasonality.

3.6 Concluding Remarks

A methodology to calculate the seakeeping performance of ships in a specified sea area was presented in this chapter. Three different methods to generate RAOs of the vessel, to be used in the operability analyses, were chosen and discussed.

The numerical transfer functions of the ferry, calculated using each theory, were compared to the experimental data at four different combinations of forward speed and wave heading. The outputs from the comparison showed the discrepancies between each applied theory and the experiments. When Theory 2 (high speed formulation *without* hull interaction) was compared with Theory 3 (high speed formulation *with* hull interaction), some differences were seen in the calculated heave and pitch motions at the resonance frequency. Numerical prediction of the

resonant heave motion was improved when hull interactions were accounted for. Theory 3 therefore showed better agreement with the experimental data compared to Theory 2. It could also be drawn from comparison of the RAOs that hull interactions are more dominant in heave motion than pitch motion. On the other hand, the discrepancies are larger when hull interactions are taken into account for the roll motions. More interestingly, in most cases, Theory 1 (conventional strip theory) still gave the best numerical results when compared to the experimental results.

In addition to this, vertical acceleration RAOs in head seas at a range of forward speeds were calculated, using Theories 1, 2 and 3. The vertical acceleration RAOs obtained using Theory 1 and 2 appeared similar to each other, showing a gradual increase with increasing speed. Conversely, the vertical accelerations generated using Theory 3 showed a different trend. They decreased with increasing speed between a relatively low speed range, and after this range they gradually increased with increasing speed. This is due to the fact that hydrodynamic hull interactions are most significant within this speed range for the ferry, and the waves generated by each demihull affect the vertical accelerations. It was also shown that for a given frequency of encounter, the wave interaction between demihulls decreases as a ship's speed increases.

Afterwards, in the results section, the motion sickness incidence values of the vessel were calculated using each theory. It was demonstrated that in the low sea states, the MSI results from the different theories appeared similar to each other, though in the high sea states, the discrepancies became significant. Theory 3 gave the highest results, whereas Theory 1 gave the lowest result in the high sea states, similar to the vertical accelerations at 20 knots ship speed.

Following this, the limiting significant wave heights due to each criterion were investigated. It was seen that the differences in the limiting significant wave height using each theory were most pronounced in the vertical acceleration criterion, which also led to noticeable discrepancies in the resultant operability indices due to vertical acceleration.

Then, operability results, based on human comfort-oriented criteria, were extensively demonstrated and discussed. The results of the operability assessment were given as an operability index which indicates the percentage of time when a vessel is operational. The procedure was applied to a car/passenger ferry operating near the west coast of Scotland. This work showed that the overall performance of the vessel, in terms of its operability, was mainly dominated by the vertical acceleration criterion. It appeared that the vessel had no problems in meeting the other criteria. Given that a vessel's operability is a function of selected limiting values, defining a lower limiting value will result in a different operability being obtained. It should therefore be kept in mind that the findings presented in this work are only valid for the predetermined criteria given in Table 3.4. Additionally, the operability analyses were performed at a forward speed of 20 knots, which coincides with the ship's service speed. It should be highlighted that, for instance, if the vessel travels at a reduced speed in a higher sea state, then its related vertical accelerations may reduce. This means that in this situation, the vessel may completely satisfy the MSI limiting values in accordance with the ISO criterion.

Finally, in the sensitivity analysis section, the effect of using annual and seasonal wave statistics for the operation site was demonstrated numerically. Additionally, the sensitivity of the adopted seakeeping theories to the expected vessel's operability was shown graphically, in a comparative manner.

The following chapters will provide individual studies on unsteady RANS CFD applications in typical ship hydrodynamic areas.

4. PREDICTING THE HYDRODYNAMICS OF HEAVING TWIN CYLINDERS IN A FREE SURFACE

4.1 Introduction

The successful estimation of a ship's motions in regular waves depends on the accurate calculation of its hydrodynamic properties and exciting forces. Estimation of the hydrodynamic coefficients and the excitation force/moment of a ship's sections is the most time-consuming aspect of the strip theory approach. The vast majority of the available techniques rely on assumptions from potential flow theory, including free surface effects. The key objective of this work is to perform a fully nonlinear unsteady RANS simulation to predict the hydrodynamic coefficients of a two-dimensional twin section heaving at a free surface, covering a range of oscillation frequencies. The outputs are then compared with the potential flow results of Lee et al. (1971) and the experimental results of Wang and Wahab (1971).

The study presented in this chapter forms part of a larger body of a piece of work, as first proposed by Salui et al. (2000), aiming to develop an improved strip theory which uses the hydrodynamic coefficients of each section of a catamaran, obtained using the unsteady RANS method, to predict its responses to regular incident waves. The resulting model is expected to be robust, reliable and provide more accurate results than the conventional strip theories. Figure 4.1 illustrates an overview of the stages of this proposed model to predict ship motion characteristics.

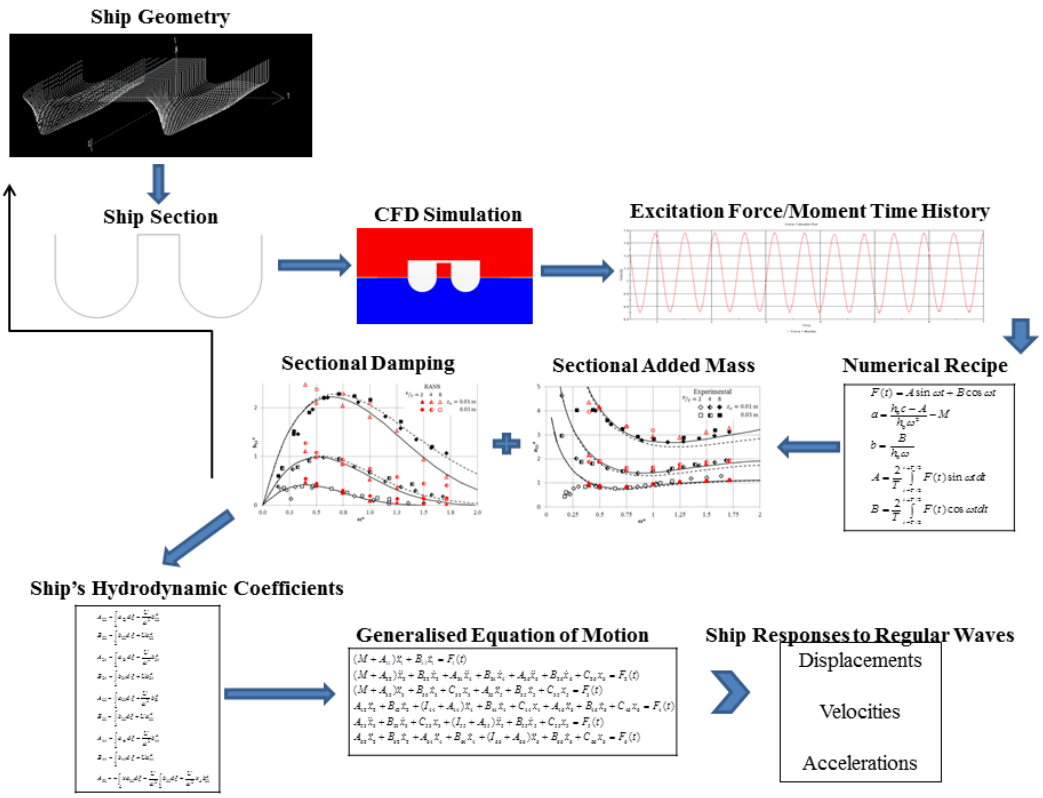

Figure 4.1 Overview of the proposed strip theory model, using a CFD-based unsteady RANS method.

As illustrated in Figure 4.1, a fully nonlinear unsteady RANS solver is employed to obtain the excitation force/moment time history of different ship sections. In this stage, both viscous and rotational effects in the flow and generated free surface wave are taken into account. Fourier analysis is then applied to the hydrodynamic force/moment time histories to determine the sectional hydrodynamic coefficients of the ship. The proposed method will be applied to a circular cylinder harmonically heaving about a calm free surface. This study will explain this numerical procedure and the results will be discussed in detail in the following sections.

As discussed in Chapter 2, Section 2.5, the majority of the research in this area has been devoted to the problem of the hydrodynamics of oscillating single cylinders in a free surface using a RANS method. No study has been performed to provide a solution to the two-dimensional viscous fluid flow problem associated with harmonic oscillations of a twin-hull body in a free surface, employing a RANS solver. In order to estimate the hydrodynamic characteristics of catamarans, their hydrodynamic coefficients should be determined. This process should take into account nonlinear

viscous effects and the interactions between the demi-hulls, since interactions between each hull of a catamaran causes them to undergo significant viscous effects. The aim of the present study is therefore to fill this gap by utilising a CFD-based unsteady RANS method.

The chapter is organised as follows: The theory behind this chapter's study is introduced in detail in Section 4.2. Next, in Section 4.3, the numerical setup of the CFD model is explained, with details provided in the sub-sections. Following this, the results obtained from this study are demonstrated and discussed in Section 4.4. Finally, in Section 4.5, a brief summary of the chapter is provided.

4.2 Theory

Hydrodynamic coefficients of a section are obtained by oscillating the section with regards to a harmonic function and then measuring the total force exerted on the model in the direction of motion. For the case of heave displacement, a harmonic function of the form $z_3=z_a\sin(\omega t)$ is imposed for an amplitude of z_a and a circular frequency of ω. The resulting total heave force (F_z) can then be written as time histories in the following form:

$$F_z(t) = -\left[a_{33}(\omega)\ddot{z}_3 + b_{33}(\omega)\dot{z}_3 + c_{33}z_3\right] \quad \textbf{(4.1)}$$

where a_{33} and b_{33} are the heave added mass and damping coefficients as functions of frequency, respectively. The force on the left-hand side of Equation (4.1) is provided by the RANS solver. The restoring force ($F_{restoring,3}=-c_{33}z_3$) can be calculated according to the instantaneously-changed body cross-sectional geometry, defined with the calm free surface over time. This force, as a per unit length, can be estimated using

$$F_{restoring,3} = \Lambda\rho g \quad \textbf{(4.2)}$$

where Λ is the submerged sectional area, corresponding to the instantaneously-changed underwater part of the body, and ρ is the water density. The restoring force given in Equation (4.2) is subtracted from the total heave force $F_z(t)$, and the purely hydrodynamic force in Equation (4.3) (F_{H3}) will then be formulated as follows:

$$F_{H_3}(t) = -a_{33}(\omega)\ddot{z}_3 - b_{33}(\omega)\dot{z}_3 \quad \textbf{(4.3)}$$

As the added mass term is in phase with the displacement motion, and damping is in quadrature, these two terms can be obtained by applying Fourier analysis to the force on the left-hand side of Equation (4.3). Instantaneous values of each coefficient can be determined from the force time history by analysing discrete windows equal to a single period of oscillation (Yeung et al., 1998):

$$a_{33} = \frac{1}{\pi z_a \omega} \int_{t-T/2}^{t+T/2} F_{H_3}(t)\sin(\omega t)dt \quad \textbf{(4.4)}$$

$$b_{33} = \frac{1}{\pi z_a} \int_{t-T/2}^{t+T/2} F_{H_3}(t)\cos(\omega t)dt \quad \textbf{(4.5)}$$

Once obtained, the instantaneous hydrodynamic coefficients are non-dimensionalised for the purpose of comparison. The non-dimensional parameters are given by:

$$\bar{a}_{33} = \frac{a_{33}}{A_x \rho} : \text{ added mass coefficient} \quad \textbf{(4.6)}$$

$$\bar{b}_{33} = \frac{b_{33}}{A_x \rho \omega} : \text{ damping coefficient} \quad \textbf{(4.7)}$$

$$\delta = \frac{\omega^2 b}{2g} : \text{ frequency number} \quad \textbf{(4.8)}$$

where b is the beam of a single cylinder and A_x is the submerged cross-sectional area of the body in the undisturbed free surface.

The total excitation force acting on the body can be decomposed to identify which contributions are attributed to hydrostatics, added mass and damping. The damping is only a small proportion of the total force acting on the body and it may therefore be more difficult to obtain accurate results for the damping, compared to the added mass. For this reason, in order to obtain the damping coefficient, the alternative approach, which is given below, can be employed as detailed in Faltinsen (1990).

The expression given by Equation (4.9), below, relates b_{33} to the wave amplitude A generated by the force oscillations, and is valid for any frequency of oscillation

(Faltinsen, 1990). Figure 4.2 depicts the correction between the heave damping coefficient and the generated far-field wave amplitude *A*.

$$b_{33} = \rho \left(\frac{A}{z_a} \right)^2 \frac{g^2}{\omega^3} \tag{4.9}$$

Equation (4.9) clearly shows that the damping coefficient is always positive. This cannot be said for the added mass coefficient, which can be negative for some specific sections and certain frequencies. Some negative added mass coefficients have been encountered for catamarans, bulb sections and totally submerged sections close to the free-surface (Faltinsen, 1990).

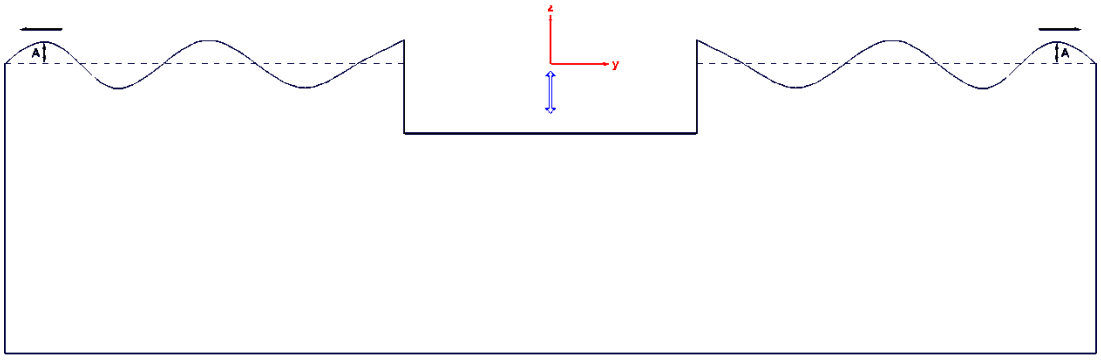

Figure 4.2 The waves generated by the forced oscillations in the far-field, adopted from Faltinsen (1990).

Once the hydrodynamic coefficients have converged (usually after 4 to 7 oscillation cycles for this study), they are averaged over the last three oscillation cycles, to yield the equivalent steady-state coefficients.

4.3 Numerical Modelling

4.3.1 Domain size

In order to approach a 2-D problem, using Star-CCM+ with a Volume of Fluid (VOF) formulation, a one-cell-thick meshed domain was created, with a periodic boundary condition on the two planes encompassing the domain, as suggested by Field (2013). With a VOF application, the physics section of the software package suggests that it is most suitable for tackling 3-D problems, but using this thin domain with periodic boundaries, the problem is essentially 2-D. A piece of detailed

information about this VOF model and the physics modelling will be given in the following chapter (Chapter 5).

As heaving twin cylinders establish a symmetric flow about a vertical plane, symmetry about the centreline is applicable in this work. Hence, only a half part of the twin-sections was modelled in CFD, as seen in Figure 4.3. This gives the advantage of reduced mesh generation, and hence a reduction in computational power and time.

Querard et al. (2008a) recommend, using the dispersion equation,

$$\lambda = \frac{2\pi g}{\omega^2} \tag{4.10}$$

that the sides of the domain should be positioned 7 wavelengths (λ) away from the section to prevent wave reflection. For this reason, the far-field wall of the domain was positioned 45 metres away from the symmetry plane to satisfy this suggestion over all frequencies.

Additionally, the VOF wave damping capability of the software package was applied with a damping length equal to 11.825 m for all cases given in this chapter. A detailed explanation about the numerical wave damping can be found in Chapter 6. The dimensions of the enclosing rectangular domain are sketched in Figure 4.3.

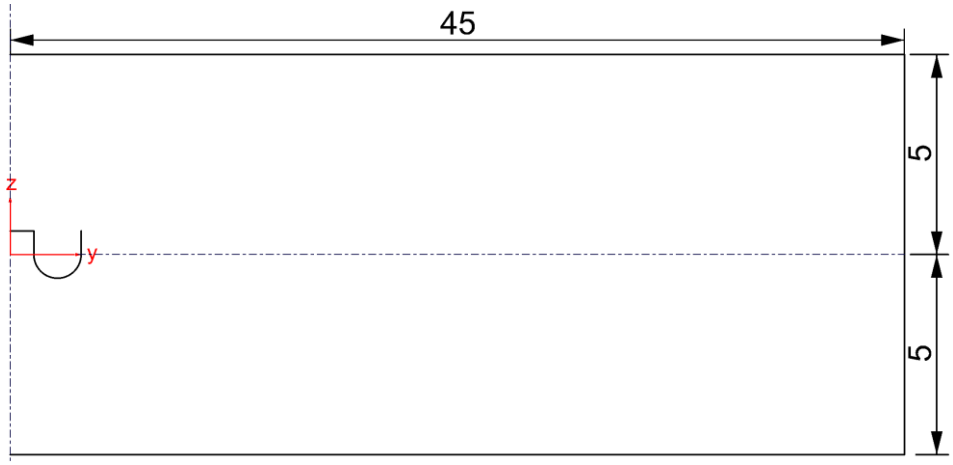

Figure 4.3 The dimensions of the enclosing domain (measured in metres).

4.3.2 Mesh generation

Mesh generation was carried out using the automatic meshing facility in Star-CCM+, resulting in a computation mesh of 645,320 cells in total. The simulation mesh had progressively local refined areas about the body and a body-fitted prism layer, as well as in the free surface region, to ensure that complex features of the resulting flow were properly captured. The mesh was unstructured, rigid and body-fixed. Figure 4.4 displays the general overview of the simulation mesh. Much more detail about the mesh generation of the RANS solver will be given in the next chapter, Section 5.3.4.

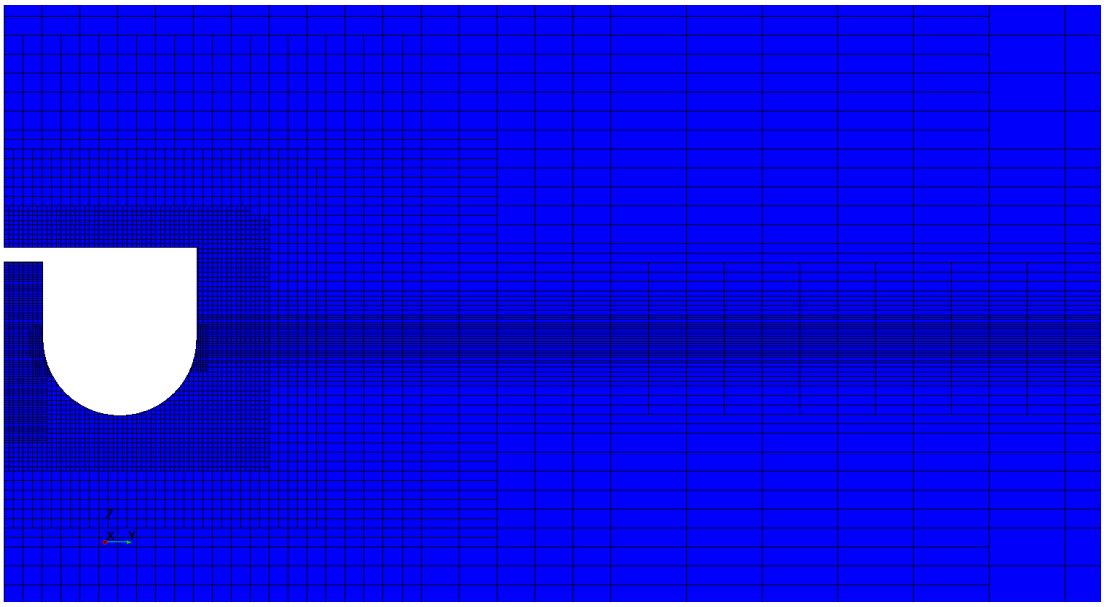

Figure 4.4 An overview of the generated volume mesh.

Figure 4.5, below, provides a closer view of the mesh refinement around the body and the free surface.

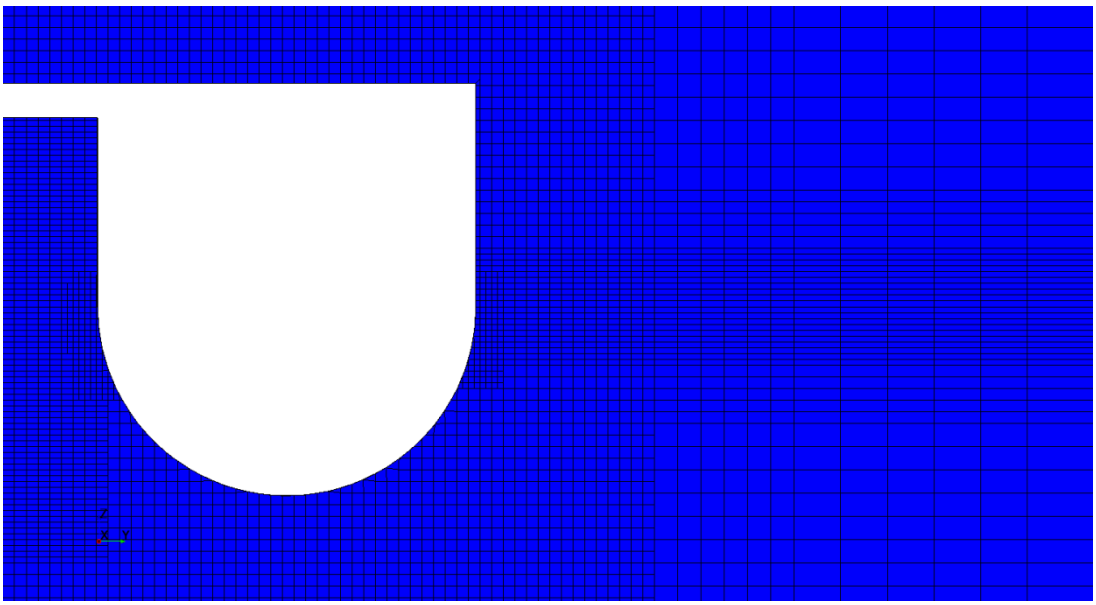

Figure 4.5 A closer look at the mesh refinement around the body and surrounding free surface.

A non-dimensional wall distance (y^+) for a wall-bounded flow is defined as follows:

$$y^+ = \frac{y_0 u^*}{\upsilon} \tag{4.11}$$

where u^* is the reference velocity, y_0 is the normal distance from the centroid to the wall in wall-adjacent cells and υ is the kinematic viscosity (CD-Adapco, 2014). The cell size was carefully chosen to ensure that all y^+ values remained below 5. Querard et al. (2008a) suggest that this value should be kept below 10. Much more information about y^+ will be provided in Chapter 6, Section 6.3.4.

4.3.3 Boundary conditions

The boundary conditions used in this specific problem were based on suggestions by Querard et al. (2008a, 2008b, 2009). Since viscous fluid flows over a solid surface, the no-slip boundary condition applied at the surface of the twin-cylinders. The two planes encompassing the domain were set as symmetric with a periodic boundary condition. The far-field wall of the domain was set as a slip wall boundary condition, and the top of the domain was set to be a Neumann boundary condition with static pressure which coincides with the reference pressure (0 Pa). The centre plane of the section was defined as having a symmetric boundary condition, and the bottom of the domain was set as a slip wall boundary condition to mimic a deep-water condition.

The boundary conditions applied to each surface of the domain are illustrated in Figure 4.6. A discussion about these boundary conditions will be provided in Chapters 5 and 7.

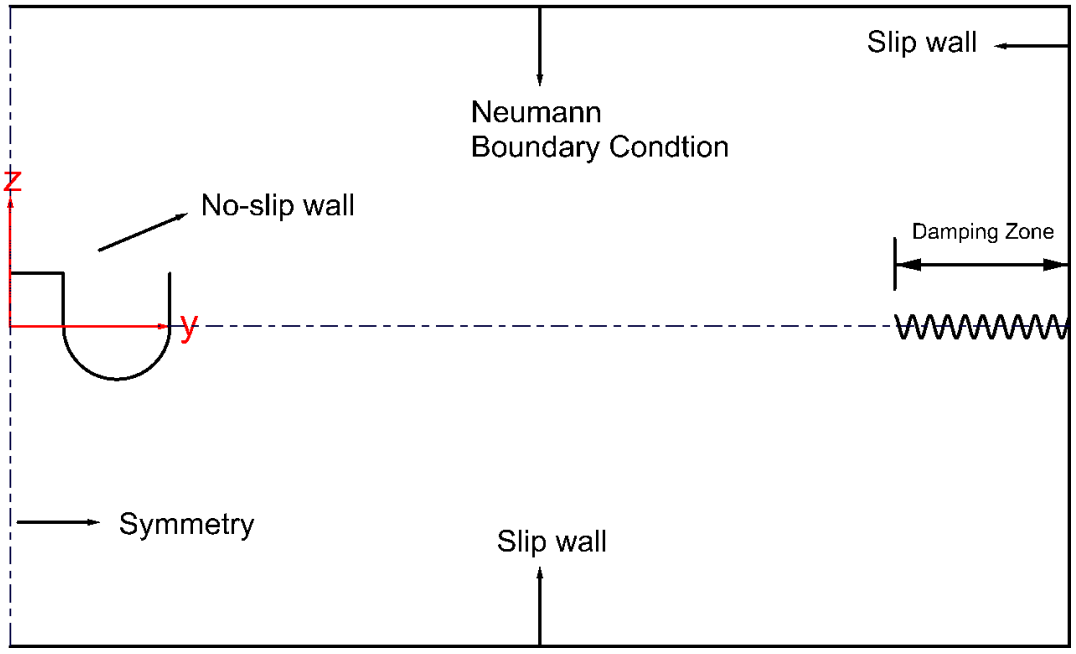

Figure 4.6 Illustration of the boundary conditions.

4.3.4 Time-step selection

The Courant number, which is the ratio of the physical time-step to the mesh convection time scale, relates the mesh cell dimension Δx to the mesh flow speed U as given below:

$$C = \frac{U\Delta t}{\Delta x} \tag{4.12}$$

where Δt is the time step size. The Courant number is typically calculated for each cell and should be less than or equal to 1 for numerical stability. Also, a second-order temporal scheme is applied to discretise the unsteady term in the Navier-Stokes equations.

In this chapter, two different constant time-step sizes were used throughout the simulations, depending on the values of the frequency number δ. For frequency numbers (δ) smaller than 0.60, a time-step of 0.002 seconds was chosen, and for all other cases, a value of 0.001 seconds was used.

The time-step size was selected such that the Courant number criterion was met throughout the domain, without compromising solution stability. Throughout all simulations presented in this chapter, the Courant number was retained below 0.5.

The simulations were run for a maximum run-time of eleven periods in each case, and a minimum of ten inner iterations were applied on each time step.

4.3.5 Turbulence model

The turbulence model selected throughout all CFD work presented in this thesis was a standard k-ε model, which has been extensively used for industrial applications (CD-Adapco, 2014). Also, Querard et al. (2008a) note that the k-ε model is quite economical in terms of CPU time, compared to, for example, the SST turbulence model, which increases the required CPU time by nearly 25%. The k-ε turbulence model has also been used in many other studies performed in the same area, such as Kim and Lee (2011) and Enger et al. (2010). In addition to this, as reported in Larsson et al. (2011), the majority of the numerical methods presented in the 2010 Gothenburg Workshop used either the k-ε or the k-ω turbulence model. At the workshop, most of the studies performed using Star-CCM+ as a RANS solver employed the standard k-ε model, as is used in this work.

4.4 Results and Discussion

The current method, explained in the previous sections, was applied to a circular cylinder at a calm free surface so as to predict its hydrodynamic features. The section, illustrated in Figure 4.7, performs harmonic oscillations in the z-direction (heave direction) with the velocity $z' = z_a \omega \cos(\omega t)$. The heave amplitude z_a is chosen as 0.0127 m (0.50 inch), in a similar manner to the experiments of Wang and Wahab (1971).

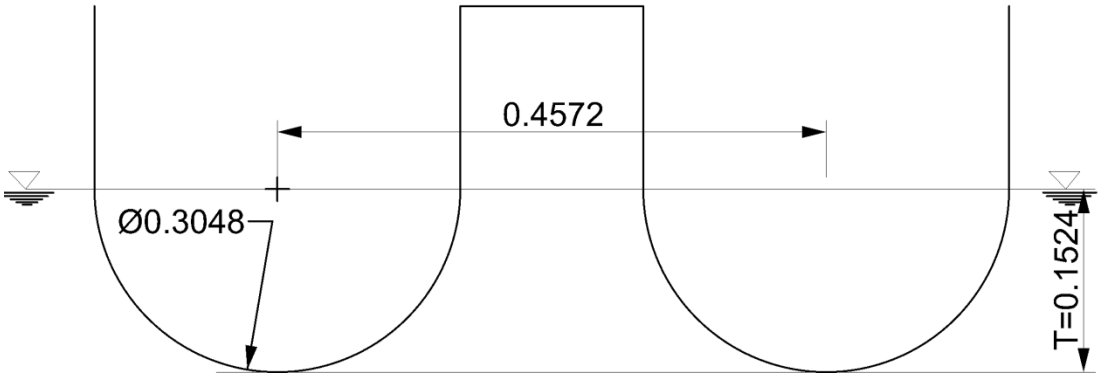

Figure 4.7 The main dimensions of the circular twin section (dimensions are given in metres).

As seen in Figure 4.7, the demi-hulls of the section are connected to each other above the water line. It should also be mentioned that the section has a separation distance of 0.4572 m, measured from each hull's centreline.

The hydrodynamic coefficients of the section were calculated at fifteen different frequencies of oscillation. Table 4.1, below, provides these particular frequencies, each identified by their case numbers, along with the wave-lengths of generated waves according to Equation (4.10).

The non-dimensional added mass and damping coefficients for the section, obtained using the proposed CFD model, are demonstrated in Figure 4.8 and Figure 4.9, respectively. The results were then compared to the experimental results, as well as the potential theory results, obtained using the source distribution method of Lee et al. (1971).

Table 4.1 The cases to which the CFD model is applied.

Case Number	ω (rad/s)	δ	Period, T (s)	λ (m)
1	3.5880	0.20	1.751	4.788
2	4.0115	0.25	1.566	3.830
3	4.8139	0.36	1.305	2.660
4	5.2611	0.43	1.194	2.227
5	5.7296	0.51	1.097	1.878
6	6.2662	0.61	1.003	1.570
7	6.7126	0.70	0.936	1.368
8	6.9482	0.75	0.904	1.277
9	7.1761	0.80	0.876	1.197
10	7.8199	0.95	0.803	1.008
11	8.3764	1.09	0.750	0.878
12	8.9701	1.25	0.700	0.766
13	10.1485	1.60	0.619	0.598
14	11.4312	2.03	0.550	0.472
15	12.6856	2.50	0.495	0.383

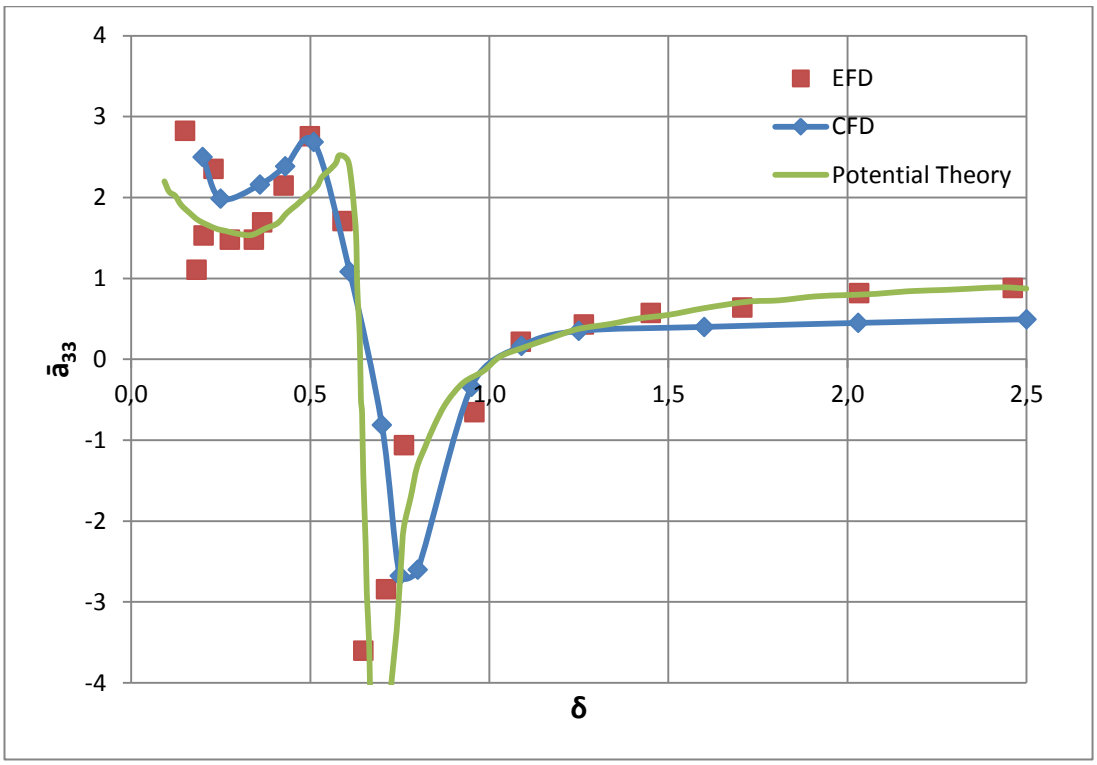

Figure 4.8 Non-dimensional added mass coefficients in heave as a function of non-dimensional frequency.

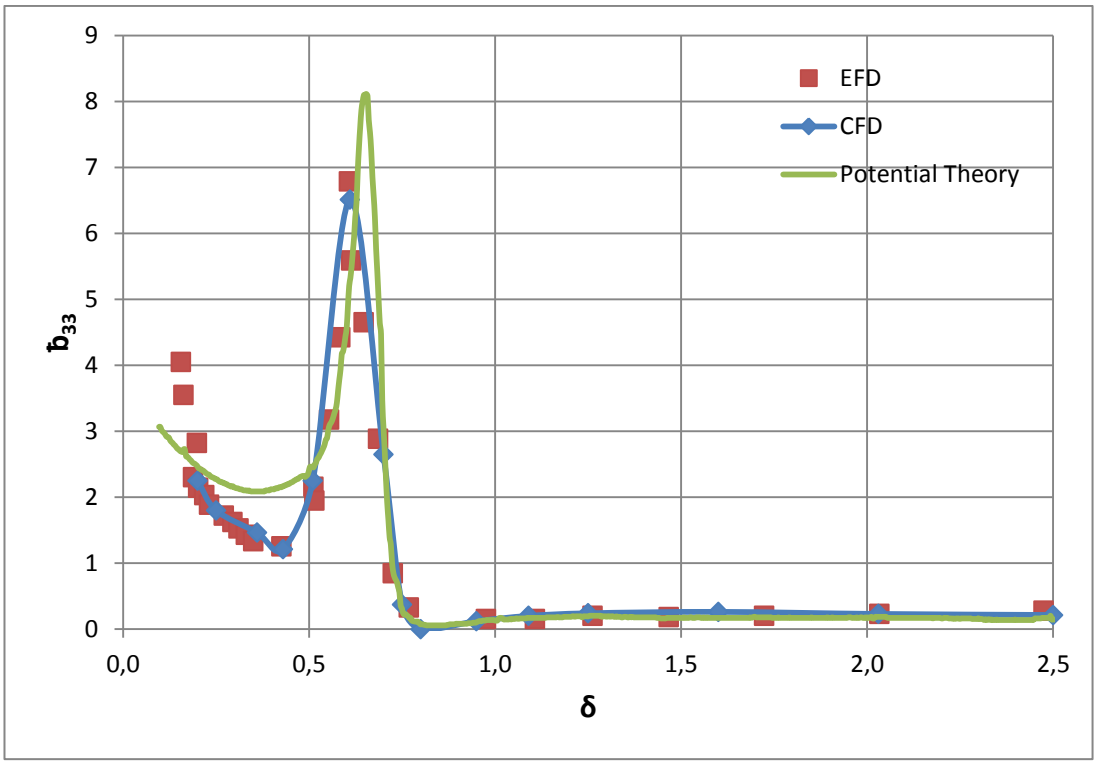

Figure 4.9 Non-dimensional damping coefficients in heave as a function of non-dimensional frequency.

As can be seen from Figure 4.8, the non-dimensional added mass coefficients obtained by the CFD method show relatively good agreement with the experimental data, particularly for low frequency numbers. For frequency numbers above 1.25, the added mass coefficients obtained using the current method are underestimated, compared to the experimental data. This may be due to the fact that high frequencies exhibit highly nonlinear features. As Field (2013) points out, in cases of high amplitudes and frequencies of oscillation, the hydrodynamic force shows a remarkable deviation from sinusoidal form and that consequently leads to a breakdown in the Fourier analysis.

On the other hand, Figure 4.9 demonstrates that the non-dimensional damping coefficients, calculated using the unsteady-RANS method, are fairly compatible with the experimental results. At low frequencies of oscillation, the damping coefficients are calculated using the wave amplitude information, generated by the force oscillation, using the expression given by Equation (4.9).

Wang and Wahab (1971) conclude from their experimental work that at a particular frequency, the surface between each demi-hull moves about 90 deg relative to the oscillation and consequently the hydrodynamic quantities peak. The added mass and fluid damping vary dramatically in the vicinity of this frequency, as is clearly visible in Figure 4.8 and Figure 4.9 around the frequency number of 0.61. According to Wang and Wahab (1971), this peak exists in all twin-hull vessels. The proposed CFD method is reasonably successful in capturing this feature of the twin-section in question.

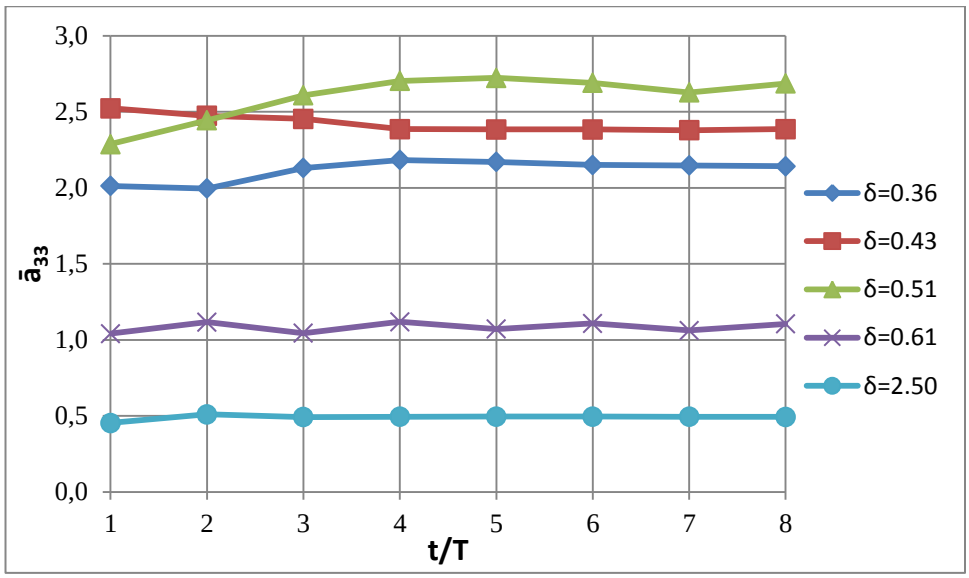

Figure 4.10 Time history of the non-dimensional added mass coefficients at various frequencies.

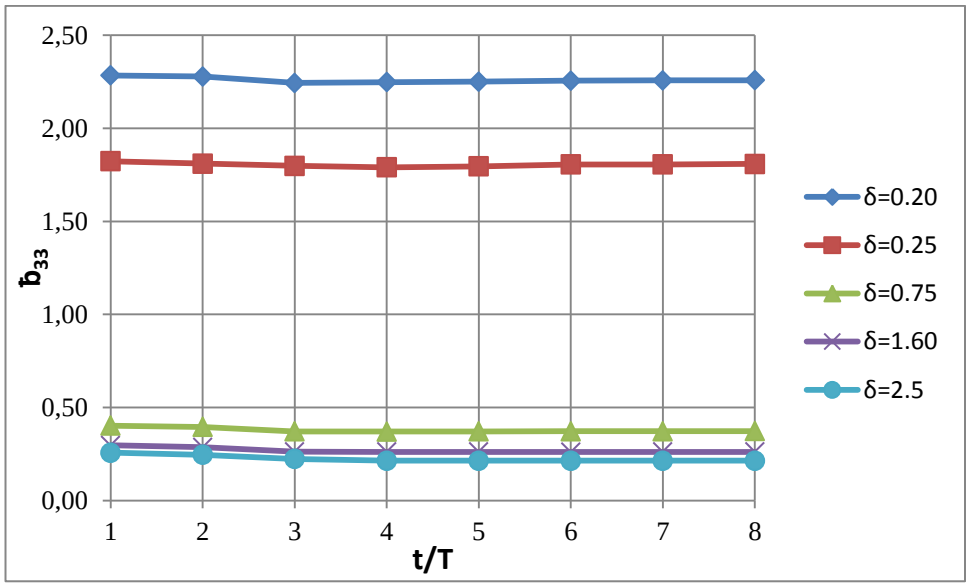

Figure 4.11 Time history of the non-dimensional damping coefficients at various frequencies.

Figure 4.10 and Figure 4.11 show the time variations of the added mass and fluid damping coefficients in heave at five different frequencies, respectively. The time-dependent damping coefficients converge very rapidly, whereas the added mass coefficients reach a steady state after the third cycle of harmonic oscillation. Querard et al. (2008a) claims that this may be due to the small amplitude of oscillation, because a finer mesh generation is needed in the direction normal to the free-surface to capture the harmonic motion more precisely. However, this will cause a significant increase in the total number of cells required.

The waves generated by oscillation of the section at the far-field are observed with the aid of a point probe located just before the damping zone. The results of the generated far-field wave amplitude ratio over the amplitude of oscillation by the RANS method are given in Figure 4.12 at low frequencies, along with a comparison with those using the potential theory of Wang and Wahab (1971). Since the amplitudes of waves generated by the oscillation at high frequencies are relatively low, a much finer mesh around the free surface is needed to capture it properly. This would ultimately increase the Central Processing Unit (CPU) time considerably. Utilising the RANS method, the wave amplitude ratios at high frequencies are therefore not calculated. This also well explains the discrepancies between CFD and the experiments in the calculation of added mass coefficients at high frequencies.

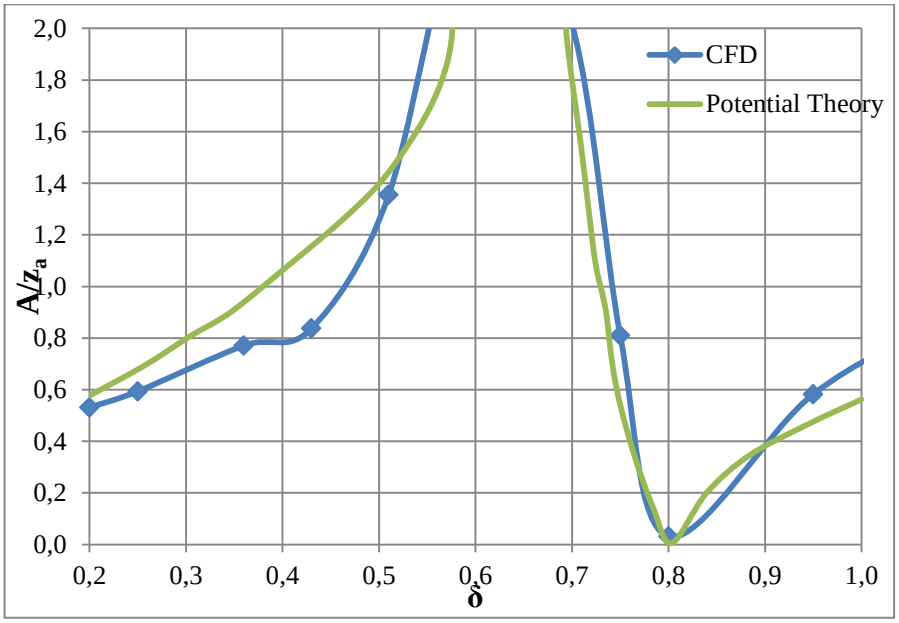

Figure 4.12 Wave amplitude ratios at low frequency numbers.

4.4.1 Systematic studies

Several systematic studies to reveal the effect of near-wall distance (y_0), time step (Δt) and total cell number (N) on the hydrodynamic coefficients are performed in this sub-section.

Firstly, a near-wall grid independence study was conducted for Case 6 (δ=0.61). To generate each mesh, the distance of the first grid from the section wall was gradually changed, whilst keeping all of the other properties the same. The results, presented in

Table 4.2, demonstrate that the solution with a near-wall thickness of $2x10^{-5}$ m converged fairly well. This resolution was therefore used throughout all of the cases in this study.

Table 4.2 Influence of near-wall distance on hydrodynamic coefficients, for Case 6 (Δt=0.001s).

y_0 (m)	y^+ max	y^+ avg	$\bar{\alpha}_{33}$	$\bar{b}_{33}$
$5x10^{-4}$	31.76	1.09	1.0841	6.8346
$1x10^{-4}$	12.87	0.25	1.0826	6.7770
$2x10^{-5}$	3.35	0.31	1.0834	6.5113

Following this, a time step convergence study was performed by taking the same case into account. The time steps were systematically refined by a factor of 2, starting from 0.001. The hydrodynamic coefficients obtained using each time step are presented in Table 4.3. The simulation for the time step of 0.008 s did not converge, owing to an error from an excessively-high Courant number.

Table 4.3 Influence of time step on hydrodynamic coefficients, for Case 6 ($y_0=2x10^{-5}$ m).

Δt (sec)	$\bar{\alpha}_{33}$	$\bar{b}_{33}$
0.001	1.0834	6.5113
0.002	1.0791	6.9426
0.004	1.0815	17.1808
0.008	[ ]	[ ]

Next, a mesh dependence study was conducted for Case 6. Four different mesh configurations (coarse, medium, fine, and finer mesh) were created, by solely changing the base size in the "mesh continua" menu in the software package. The added mass and fluid damping coefficients for each mesh configuration are shown in Table 4.4. It was seen that the relative difference between the fine and finer mesh is minimal; hence the fine mesh configuration was used throughout the study presented in this chapter.

Table 4.4 Influence of total cell number on hydrodynamic coefficients, for Case 6 ($y_0=2x10^{-5}$ m, Δt=0.001s).

Mesh configuration	Total cell number	$\bar{\alpha}_{33}$	$\bar{b}_{33}$
Coarse	243,303	1.0796	6.0659
Medium	412,206	1.0831	6.3415
Fine	645,320	1.0834	6.5113
Finer	1,137,889	1.0835	6.5203

4.5 Concluding Remarks

A method to obtain the hydrodynamic features of a circular section of a 2-D twin cylinder heaving about a calm free surface, utilising a commercial RANS solver, was presented in this chapter and was successfully validated against the experimental data available in the literature.

The added mass and fluid damping coefficients of the section in question were obtained at fifteen frequencies of oscillation, using the same amplitude of oscillation in each case. The results were found to be in reasonably good agreement with the experimental results. At high frequencies, the added mass coefficients were underestimated in the CFD method. These discrepancies may be attributed to the highly nonlinear feature of the flow at high frequencies, and to the need for finer mesh generation at such frequencies. The current CFD simulation can be developed further in order to capture this phenomenon more precisely.

The damping coefficients were calculated using an expression which relates the generated wave amplitude in the far-field to the fluid damping. The results obtained using CFD were very compatible with the experimental results.

In addition, time-dependent added mass and damping coefficients were presented for eight periods of oscillation. It was clearly demonstrated that the added mass is more time-dependent than damping is.

Following this, the ratio of far-field wave amplitudes, generated by the oscillation of the section over the amplitude of oscillation, were determined at low frequencies and compared to those from potential theory. The oscillations in heave closely matched the potential flow solutions as the oscillation amplitude and frequency decreased. The wave amplitude ratios by CFD were therefore seen to be fairly close to those from potential flow theory at low frequencies. With the knowledge that low amplitude waves are generated by high amplitude oscillations, very fine mesh generation is required to capture the waves at these frequencies. Therefore, wave amplitudes at high frequencies were not calculated by the CFD method in this study.

During this particular study, it was seen that the improved strip theory, as outlined in Figure 4.1, was not practical from an engineering point of view. Beyond any doubt, the implementation of this CFD model for each of the ship sections would be a time-consuming and demanding process. Instead, the time and effort spent on accomplishing the proposed strip theory could be dedicated towards 3-D CFD simulations of ship motions, which would likely be achieved with more accuracy.

The implementation of CFD in ship hydrodynamic problems will be introduced in the following three chapters. Chapter 5 will demonstrate full-scale unsteady RANS CFD simulations of ship motions and resistance in deep water. Chapter 6 will test this CFD modelling in shallow water with an application to a full-scale tanker model. Following this, Chapter 7 will provide a CFD investigation of the squat and resistance of a ship passing through a canal in calm water.

5. FULL-SCALE UNSTEADY RANS CFD SIMULATIONS OF SHIP BEHAVIOUR AND PERFORMANCE IN HEAD SEAS

5.1 Introduction

Understanding the behaviour of a vessel in a real seaway is critical for determining its performance. Rough sea conditions induce significant ship motions, which affect a ship's resistance. The resulting increase in resistance will compromise propulsive efficiency and will increase fuel consumption. Ship motions and seakeeping behaviour are also very important with regards to crew, vessel and cargo safety. An awareness of the impacts of ship motions on resistance is particularly important in the current economic climate, which has seen a significant increase in fuel costs in comparison to charter rates. For example, for a typical commercial vessel, the fuel costs will now account for well over half of its operating costs, whereas for a container ship, the figure may be as high as 75% (Ronen, 2011).

The current economic climate is very different from the "boom years" in which modern vessels were designed. In response to recent fuel price increases, ship operators have begun to apply the slow steaming approach, which was initially proposed by Maersk technical experts post-2007 (Maersk, n.d.). In this approach, a vessel is operated at a speed significantly below its original design speed in order to reduce the amount of fuel that is required. Slow steaming is typically defined as being down to around 18 knots for container vessels, with operational speeds below this being termed 'super slow steaming'. Figure 5.1 below, taken from Banks et al. (2013), shows how the operating speeds for container vessels have decreased over recent years, comparing the period from 2006-2008 with 2009-2012. It can be seen that a typical operating speed is now significantly below the original design speeds

which would have been specified for these vessels. In particular, it can be observed that for this collection of data, the most typical slow steaming speed is around 19 knots. This speed will therefore be used as a representative slow steaming speed in this study.

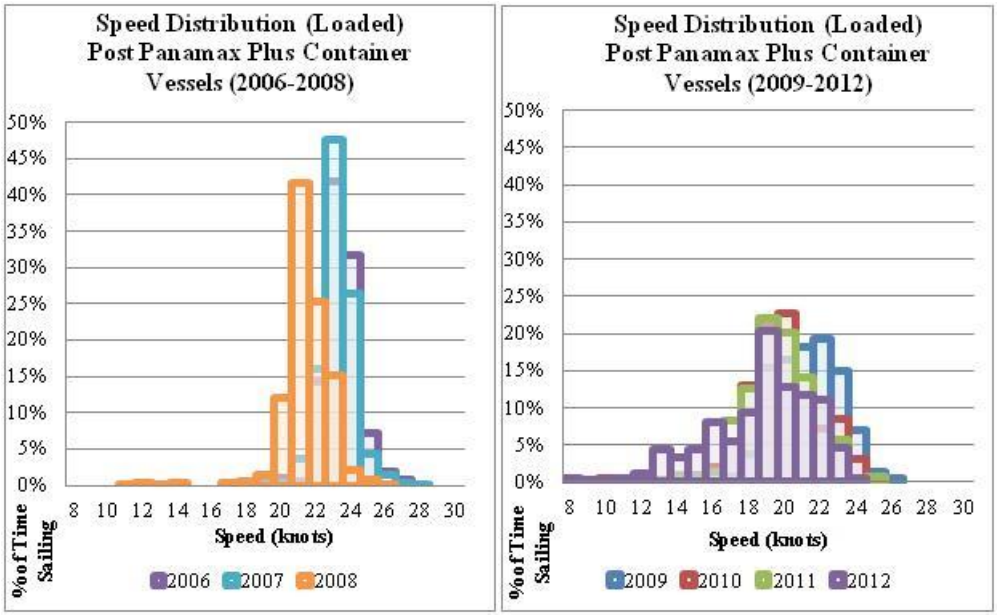

Figure 5.1 Comparison of the speed distributions for container vessels, taken from Banks et al. (2013).

Other concepts such as "just-in-time" operation and "virtual arrival" are also applied as a means of reducing speed without compromising the agreed dates for charter cargo delivery into port. In some cases, vessels are even retro-fitted with lower power propulsion systems to reduce weight and improve efficiency, as well as reduce the problems which may arise from the long-term operation of machinery in off-design conditions. However, little research has been carried out into the effect that these lower speeds may have on the behaviour of the vessel, and whether further fuel savings may be an additional benefit. This chapter addresses the gap in current knowledge by comparing pitch and heave motions, as well as added resistance, at both design and slow steaming speeds. More importantly, although extensive research has been performed to investigate increases in effective power, ship fuel consumption and CO_2 emissions, no specific study exists which aims to predict the increase in the above-mentioned parameters due to the operation in waves, using a CFD-based RANS approach. Therefore, the main aim of this study is to directly predict the increase in the required effective power of a vessel operating in regular

head seas. This leads to a rough estimation of the fuel penalty to counter the additional CO_2 emissions from the vessel. The potential benefits of slow steaming will be probed by invoking added resistance predictions.

The Energy Efficiency Operational Indicator (EEOI) was introduced by the International Maritime Organization (IMO) in 2009 as a voluntary method for monitoring the operational performance of a ship. The EEOI enables an assessment to be made of the operational energy efficiency of a ship, which is expressed in terms of the CO_2 emitted per unit of transport work . Alongside this, regulations relating to the control of SO_x emissions from shipping were introduced, with specific limits stipulated. This will be followed by limits for NO_x emissions in 2016, with limits for CO_2 and particulate matter (PM) emissions also likely to be introduced in the future. Reducing the fuel consumption through slow steaming, and improving or at least maintaining propulsive efficiency, will take steps towards addressing these requirements.

The resistance of a ship operating in a seaway is greater than its resistance in calm water. The difference between these two resistances arises from ship motions and wave forces in waves and has been termed the added resistance due to waves. Added resistance can account for up to 15-30% of the total resistance in calm water (Arribas, 2007). It is therefore critical to be able to accurately predict the added resistance of a ship in waves, and this should be included in ship performance assessments. One purpose of this study is to predict the added resistance due to waves with higher accuracy than potential theory-based methods.

The KRISO Container Ship (KCS), developed by the Korean Maritime and Ocean Engineering Research Institute (now MOERI), has been used in a wide range of research studies. There is consequently a wide range of experimental and simulation data available for comparison, and for verification and validation purposes. The KCS has therefore been investigated in this study due to the ready availability of this data and research in the public domain. Moreover, container ships are particularly affected by slow steaming, as they were designed to operate with very high design speeds, in the region of up to 25 knots. The service speed for the KCS is 24 knots. This makes the KCS model particularly relevant for this study.

To the best of this author's knowledge, the majority of RANS seakeeping simulations have been performed at model scale. However, as Hochkirch and Mallol (2013) claim, model-scale flows and full-scale flows can show significant differences due to scale effects. They explain that the discrepancies between model and full scale mainly stem from relatively different boundary layers, flow separation and wave breaking, particularly behind transom sterns. Visonneau et al. (2006) draw a conclusion in their paper that, "*complete analysis of the scale effects on free-surface and of the structure of the viscous stern flow reveals that these scale effects are not negligible and depend strongly on the stern geometries*". As discussed in detail with several examples by Hochkirch and Mallol (2013), performing analyses at a full scale is of the greatest importance, especially for hulls appended with propulsion improving devices (PIDs). A decision was therefore made to use the full-scale KCS model in the CFD simulations presented in this chapter.

In addition, during this literature review, it was seen that when using the KCS model, although resistance predictions have been conducted for a range of Froude numbers (for example Banks et al. (2010) and Enger at al. (2010)), seakeeping analyses have only been performed at forward speeds corresponding to a Froude number of 0.26 or higher (for example Simonsen et al. (2013) and Carrica et al. (2011)). This study therefore may be useful to understand the seakeeping behaviour and performance of the KCS model at a slow steaming speed.

As explained above, a full-scale KCS hull model appended with a rudder was used for all simulations, to avoid scaling effects. The model was first run in calm water conditions free to trim and sink so that the basic resistance could be obtained, for both the design and the slow steaming speeds. The model was then run in a seaway, to allow the ship motions to be observed and to allow the added resistance due to waves to be calculated. This was again carried out for both speeds in question. The resistance was monitored as a drag force on the hull, and the pitch and heave time histories were recorded.

Within the above framework this chapter is organised as follows. Section 5.2 gives the main ship properties, and a list of the simulation cases applied to the current CFD model. Next, in Section 5.3, the numerical setup of the CFD model is explained, with

details provided in the contained sub-sections. Following this, all of the results from this work, including validation and verification studies, are demonstrated and discussed in Section 5.4. Finally, in Section 5.5, a summary of the chapter is made.

5.2 Ship Geometry and Conditions

A full-scale model of the KCS appended with a rudder was used within this study. The main properties of the KCS model are presented in Table 5.1 (Kim et al., 2001):

Table 5.1 KCS general properties.

Length between the perpendiculars (L_{BP})	230.0 m
Length of waterline (L_{WL})	232.5 m
Beam at waterline (B_{WL})	32.2 m
Depth (D)	19.0 m
Design draft (T)	10.8 m
Displacement (Δ)	52,030 m^3
Block coefficient (C_B)	0.6505
Ship wetted area with rudder (S)	9,539 m^2
Longitudinal centre of buoyancy (LCB) (%L_{BP}), fwd+	-1.48
Longitudinal centre of gravity (LCG) from the aft peak	111.603 m
Vertical centre of gravity (KG) from keel	7.28 m
Metacentric height (GM_t)	0.60 m
Moment of inertia (K_{xx}/B)	0.40
Moment of inertia (K_{yy}/L_{BP}, K_{zz}/L_{BP})	0.25

As stated previously, the service speed for this vessel is 24 knots (12.345 m/s). A slow steaming speed of 19 knots (9.773 m/s) was selected as a representative value for current container ship operations.

The CFD simulations were performed at twelve different conditions, as listed in Table 5.2, each identified by their case numbers. The frequency of encounter of the waves f_e is calculated by $f_e = \sqrt{g/(2\pi\lambda)} + U/\lambda$ for head seas. The waves were selected such that the ratio of wave over ship length varied between 1.0 and 2.0. Also, the wave steepness in all cases was chosen to be 1/60, in a similar manner to the experiments of Simonsen et al. (2013). It is also of note that the analyses were performed using deep water conditions.

Table 5.2 The cases to which the CFD model is applied.

Case no.	Ship speed (kn)	Froude number	Wave height (m)	Wave length (m)	Encounter period (s)	Encounter freq. (Hz)	Wave steepness	Wave/ship length
C	*U*	*Fn*	*H*	λ	T_e	f_e	H/λ	λ/L_{BP}
1	24	0.260	**Calm water**					
2			3.833	230.000	7.349	0.136	1/60	1.00
3			**4.424**	**264.494**	**8.097**	**0.124**	**1/60**	**1.15**
4			**5.108**	**306.480**	**8.956**	**0.112**	**1/60**	**1.33**
5			5.750	345.000	9.704	0.103	1/60	1.50
6			**7.689**	**460.000**	**11.751**	**0.085**	**1/60**	**2.00**
7	19	0.206	Calm water					
8			3.833	230.000	8.008	0.125	1/60	1.00
9			4.424	264.494	8.789	0.114	1/60	1.15
10			5.108	306.480	9.684	0.103	1/60	1.33
11			5.750	345.000	10.460	0.096	1/60	1.50
12			7.689	460.000	12.578	0.080	1/60	2.00

The bold rows in Table 5.2 indicate the conditions which were used for the validation of the CFD results against the available experimental results. Each case highlighted in bold has significantly different features, and was purposely selected to be used during the later validation stage. The validation and verification can be found in Section 5.4.1.

Resonance occurs when the frequency of encounter of waves f_e equals, or, is close to, the natural frequency of the ship f_n. For the present full-scale model, the natural heave and pitch frequencies were computed to be close to f_n=0.124 Hz based on the calculations given by Simonsen et al. (2013). Case 3 was therefore chosen to be investigated more closely in the verification study.

The excitation forces and moments are dependent on the ratio of wavelength over ship length. Simonsen et al. (2013) state that the maximum excitation force for the KCS occurs for wavelengths close to λ/L_{BP}=1.33. Case 4 is the condition in which the maximum excitation force is expected to occur.

Case 6, according to the work by Carrica et al. (2011), exhibits a very linear behaviour since the wavelength is very large. It can hence be regarded as the most linear condition amongst all of the cases.

5.3 Numerical Modelling

Up to this point, this chapter has given an introduction to the work. The following section will provide details of the numerical simulation approaches used in this study and will discuss the numerical methods applied to the current CFD model.

5.3.1 Physics modelling

To model fluid flow, the solver employed uses a finite volume method, which uses the integral form of the conservation equations and divides the computational domain into a finite number of adjoining control volumes.

In the CFD part of this thesis work, the 'Volume of Fluid' method was used to model and position the free surface, either with a flat or regular wave. CD-Adapco (2014) defines the VOF method as, "*a simple multiphase model that is well suited to simulating flows of several immiscible fluids on numerical grids capable of resolving the interface between the mixture's phases*". Because it demonstrates high numerical efficiency, this model is suitable for simulating flows in which each phase forms a large structure, with a low overall contact area between the different phases. One example of such flow is the sloshing of water in a tank, during which the free surface remains perpetually smooth. If the movement of the tank becomes stronger, then breaking waves, air bubbles in the water and airborne water droplets will form as a result. The VOF model uses the assumption that the same basic governing equations as those used for a single phase problem can be solved for all the fluid phases present within the domain, as it is assumed that they will have the same velocity, pressure and temperature. This means that the equations are solved for an equivalent fluid whose properties represent the different phases and their respective volume fractions (CD-Adapco, 2014). The inlet velocity and the volume fraction of both phases in each cell, as well as the outlet pressure, are all functions of the flat wave or regular wave used to simulate the free surface. The free surface is not fixed; it is dependent on the specifications of this flat or regular wave, with the VOF model making calculations for both the water and air phases. The grid is simply refined in order to enable the variations in volume fraction to be more accurately captured. In this work,

a second-order convection scheme was used throughout all simulations in order to accurately capture sharp interfaces between the phases.

Figure 5.2 demonstrates how the free surface was represented in this CFD model by displaying the water volume fraction profile on the hull. In the figure, for instance, a value of 0.5 for the volume fraction of water implies that a computational cell is filled with 50% water and 50% air. This value therefore indicates the position of the water-air interface, which corresponds to the free surface.

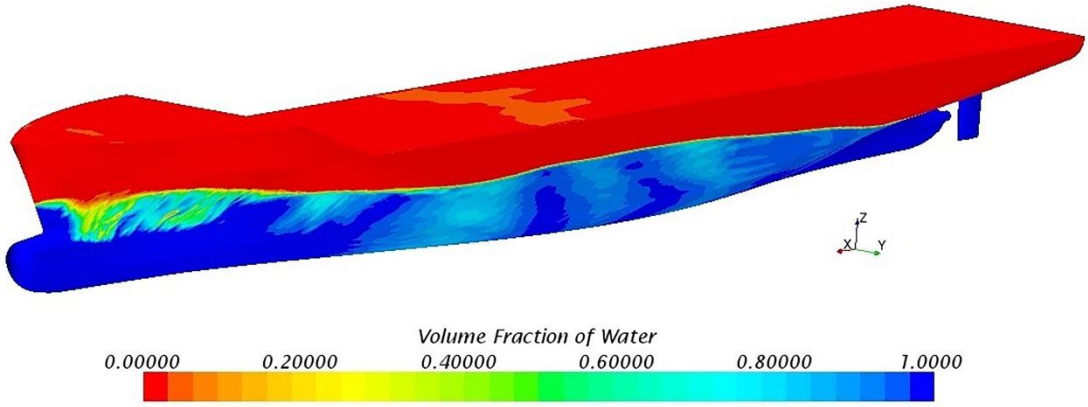

Figure 5.2 Free surface representation on the ship hull.

It should also be mentioned that throughout all simulations in this work, the segregated flow model, which solves the flow equation in an uncoupled manner, was applied in the RANS solver. Convection terms in the RANS formulae were discretised by applying a second-order upwind scheme. The overall solution procedure was obtained according to a SIMPLE-type algorithm.

In order to simulate realistic ship behaviour, a Dynamic Fluid Body Interaction (DFBI) model was used with the vessel free to move in the pitch and heave directions. The DFBI model enabled the RANS solver to calculate the exciting force and moments acting on the ship hull due to waves, and to solve the governing equations of rigid body motion in order to re-position the rigid body (CD-Adapco, 2014).

5.3.1.1 Choice of the time step

An implicit-unsteady approach was adopted throughout all the CFD simulations run in this thesis. Often, in implicit unsteady simulations, the time step is determined by

the flow properties, rather than the Courant number (see Equation (4.12)). In order to gain a suitable level of accuracy within a reasonable running time, two different time step resolutions were used based on the features of each simulation.

For resistance computations in calm water, the time step size is determined by $\Delta t=0.005\sim0.01L/U$ (where L is the length between perpendiculars) in accordance with the related procedures and guidelines of ITTC (2011b).

For the prediction of ship responses to incident regular waves, at least 100 time steps per encounter period should be used, as recommended by ITTC (2011b). In this particular study, a very small time step (1/256 of the wave period) was used over an encounter period.

It is also worth noting that a first-order temporal scheme was applied to discretise the unsteady term in the Navier-Stokes equations, throughout all the CFD simulations in this work after this point.

5.3.2 Computational domain and boundary conditions

Two different computational domains were created for each main simulation: a seakeeping analysis in waves and a resistance calculation in calm water.

In both domains, an overset mesh was used to facilitate the motions of the full-scale ship model. Rigid and deforming mesh motion options are available in the software package, but these methods have distinct disadvantages compared to the overset mesh approach when simulating bodies with large amplitude motions. The rigid mesh approach causes difficulties for free surface refinement, especially in pitch, and deforming meshes may lead to cell quality problems. On the other hand, the overset region, which encompasses the hull body, moves with the hull over a static background mesh of the whole domain (Field, 2013). For this reason, using the overset mesh feature of the software package saves computational costs, and allows the generation of a sufficiently refined mesh configuration around the free surface and the body, without compromising the solution's accuracy. Without the use of the overset mesh feature, simulating a full-scale ship model in waves would require a very high cell number, requiring much more computational power.

In all CFD problems, the initial conditions and boundary conditions must be defined depending on the features of the problem to be solved. The determination of these boundary conditions is of critical importance in order to be able to obtain accurate solutions. There are a vast number of boundary condition combinations that can be used to approach a problem. However, the selection of the most appropriate boundary conditions can prevent unnecessary computational costs when solving the problem (Date and Turnock, 1999).

When using the overset mesh feature, two different regions were created to simulate ship responses in waves, namely background and overset regions. A general view of the computation domain with the KCS hull model and the notations of selected boundary conditions are depicted in Figure 5.3.

In order to reduce computational complexity and demand, only half of the hull (the starboard side) is represented. A symmetry plane forms the centreline domain face in order to accurately simulate the other half of the model. It should be noted that in some figures given hereafter, the mirror image of the ship and domain is reflected on the port side for visual convenience.

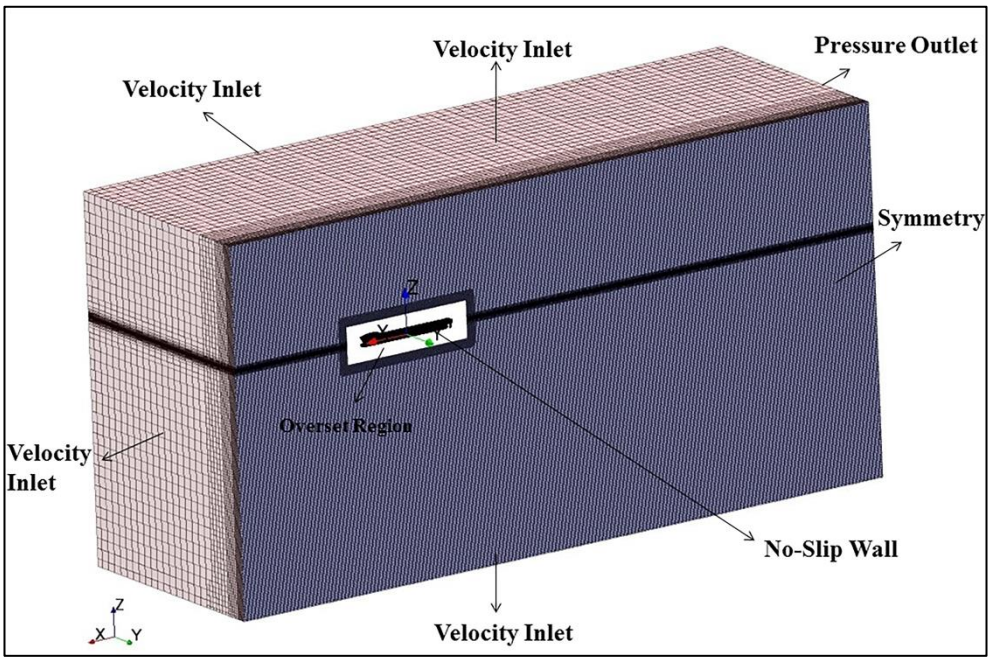

Figure 5.3 A general view of the background and overset regions and the applied boundary conditions.

Figure 5.3 illustrates that a velocity inlet boundary condition was set in the positive x-direction, where incident regular waves were generated. The negative x-direction was modelled as a pressure outlet since it prevents backflow from occurring and fixes static pressure at the outlet. The top and bottom boundaries were both selected as velocity inlets. The symmetry plane, as the name suggests, has a symmetry condition, and the side of the domain (the negative y-direction) has a velocity inlet boundary condition as well. These boundary conditions were used as they were reported to give the quickest flow solutions for similar simulations carried out utilising Star-CCM+ (CD-Adapco, 2014). The use of the velocity inlet boundary condition at the top and the side of the background prevents the fluid from sticking to the walls. In other words, it avoids a velocity gradient from occurring between the fluid and the wall, as in the use of a slip-wall boundary condition. It is of note that the initial flow velocity at all inlet conditions was set to the corresponding velocity of the head waves. Hence, the flow at the very top and very side of the background is also directed parallel to the outlet boundary. This enables fluid reflections from the top and side of the domain to be prevented. In addition to this, the selection of the velocity inlet boundary condition for the top and bottom facilitate the representation of the deep water and infinite air condition, which is also the case in open seas. The top, bottom and side boundaries could have been set as a slip-wall or symmetry plane. The selection of boundary conditions from any appropriate combination would not affect the flow results significantly, provided that they are placed far enough away from the ship hull, such that the flow is not disturbed by the presence of the body.

Throughout this thesis, a velocity inlet boundary condition is used to define the velocity at this boundary as equal to the stream flow velocity. This velocity, in fact, equals the velocity of a particular VOF wave model generated inside the computational domain. Similarly, a pressure outlet boundary condition sets the pressure at the boundary to the hydrostatic pressure of a particular VOF wave. A no-slip wall condition implies that the tangential velocity is set to zero. At a symmetry boundary, the convective fluxes of all quantities and the shear stresses are zero. Finally, the normal velocity component is zero, but its normal gradient is not; hence the normal stress is not zero (Ferziger and Peric, 2002, CD-Adapco, 2014).

Date and Turnock (1999) point out that, just as the selection of the boundaries is of great importance, their positioning is equally important.

ITTC (2011b) recommends that for simulations in the presence of incident waves, the inlet boundary should be located 1-2L_{BP} away from the hull, whereas the outlet should be positioned 3-5L_{BP} downstream to avoid any wave reflection from the boundary walls. Three other pieces of previous work similar to this study have been consulted to decide the locations of the boundaries. The findings are summarised in Table 5.3.

Table 5.3 The locations of the boundaries in similar previous studies.

	Directions				
Reference	Upstream	Downstream	Up	Bottom	Transverse
Shen and Wan (2013)	$1L_{BP}$	$4L_{BP}$	$1L_{BP}$	$1L_{BP}$	$1.5L_{BP}$
Ozdemir et al. (2014)	$2L_{BP}$	$3L_{BP}$	$2L_{BP}$	$2L_{BP}$	$2L_{BP}$
Simonsen et al. (2013)	$0.6L_{BP}$	$2L_{BP}$	N/A	N/A	$1.5L_{BP}$

The locations of the boundaries are illustrated in Figure 5.4, which gives front and side views of the domain. It is worth mentioning that throughout all the cases, in order to prevent wave reflection from the walls, the VOF wave damping capability of the software package was applied to the background region with a damping length equal to 1.24L_{BP} (~285 m.). This numerical beach model was used in downstream, bottom and transverse directions.

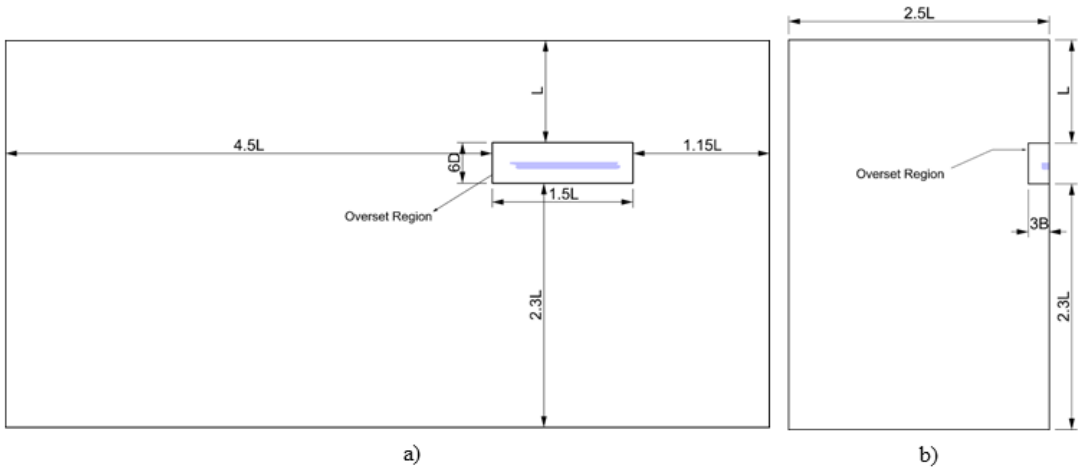

Figure 5.4 The dimensions of the computational domain for the seakeeping simulations: a) Front view, b) Side view (B: half beam of the ship, D: depth of the ship, L: length of the ship between the perpendiculars).

It should be noted that in CFD applications with ship models, there are no definite recommendations regarding how to define the dimensions of an overset region. In

this study, the dimensions of the overset region were defined such that the most significant flow features, for example flow separation, slamming, wave breaking and high vortices around the hull, remained within the overset domain.

As outlined previously, for the resistance simulations in calm water, another computational domain was created. The only difference from the domain created to simulate ship motions in waves is that the outlet boundary was located $2.5L_{BP}$ away from the ship body, as wave reflection from the walls was less prominent. Irrespective of this, the waves generated by the presence of the vessel were treated by applying a numerical damping beach in each boundary. It should be stated that the boundary conditions in the domain for the simulations in calm water were identical to the ones depicted in Figure 5.3.

5.3.3 Coordinate systems

Since the DFBI model was employed in the CFD modelling, throughout all CFD work given hereafter, two different coordinate systems were adopted to predict ship performance in either a regular or a flat wave. Firstly, the flow field was solved, and the excitation force and moments acting on the ship hull were calculated in the earth-fixed coordinate system. Following this, the forces and moments were converted to a body local coordinate system which was located at the centre of mass of the body, following the motions of the body whilst the simulation progressed. The equations of motions were solved to calculate the vessel's velocities. These velocities were then converted back to the earth-fixed coordinate system. These sets of information were then used to find the new location of the ship and grid system. The overset grid system was re-positioned after each time step (Simonsen et al., 2013). Information about the ship geometry and the position of the centre of gravity was provided in Section 5.2.

5.3.4 Mesh generation

Mesh generation was performed using the automatic meshing facility in Star-CCM+, which uses the Cartesian cut-cell method. Two different mesh generations were applied for each resistance and seakeeping simulation, resulting in a computation mesh of circa 4 and 10 million cells in total, respectively. A trimmed cell mesher was

employed to produce a high-quality grid for complex mesh generating problems. The ensuing mesh was formed primarily of unstructured hexahedral cells, with trimmed cells adjacent to the surface. The breakdown of the mesh number for each resistance and seakeeping simulation is shown in Table 5.4. It should be noted that the data contained in Table 5.4 for the 'seakeeping in waves' simulation reflects the exact number of grids generated for Case 3. The cell number of the other cases differs slightly from those listed in the table, due to variation in the wave conditions.

Table 5.4 The cell numbers for resistance and seakeeping simulations.

	Cell Number		Total
Simulation	Background	Overset	
Resistance in calm water	2,907,565	2,473,121	5,380,686
Seakeeping in waves	3,572,074	6,357,286	9,929,360

The computation mesh had areas of progressively refined mesh size in the area immediately around the hull and rudder, as well as the expected free surface and in the wake that was produced by the ship, to ensure that the complex flow features were appropriately captured. The refined mesh density in these zones was achieved using volumetric controls applied to these areas. The mesh was unstructured, rigid and body-fixed, so that motions of the body corresponded to the movement of grid points. The most refined mesh areas around the hull remained within the boundaries of the overset domain. When generating the volume mesh, extra care was given to the overlapping zone between the background and overset regions. In addition, it was ensured that the overlapping region consisted of at least 4 or 5 cell layers in both overset and background meshes. Also, it was verified that the cells in both meshes were of similar size on the overlapping region. CD-Adapco (2014) can be consulted for any further information as to how to generate suitable meshes when working with the overset mesh feature.

To simulate ship motions in waves, the mesh was generated based on the guidelines for ship CFD applications from ITTC (2011b). According to these recommendations, a minimum of 80 cells per wavelength should be used on the free surface. As suggested by Kim and Lee (2011), in order to capture the severe free surface flows such as slamming and green water incidents, a minimum of 150 grid points per wavelength was used near the hull free surface in both downstream and upstream

directions. Additionally, a minimum of 20 cells was used in the vertical direction where the free surface was expected.

When generating the mesh for the simulations in calm water, the refined mesh area for the free surface was kept relatively small, compared to that used in the seakeeping simulations. In this case, based on prior experience, a minimum cell size of 0.1% of L_{BP} in the vertical direction was used to capture the flow features in the free surface.

Figure 5.5, below, shows a cross-section of the computation mesh where the refinement to capture the Kelvin wake is clearly visible. Figure 5.6 shows the surface mesh on the KCS hull and rudder. The overset mesh region around the hull is also noticeable in Figure 5.5.

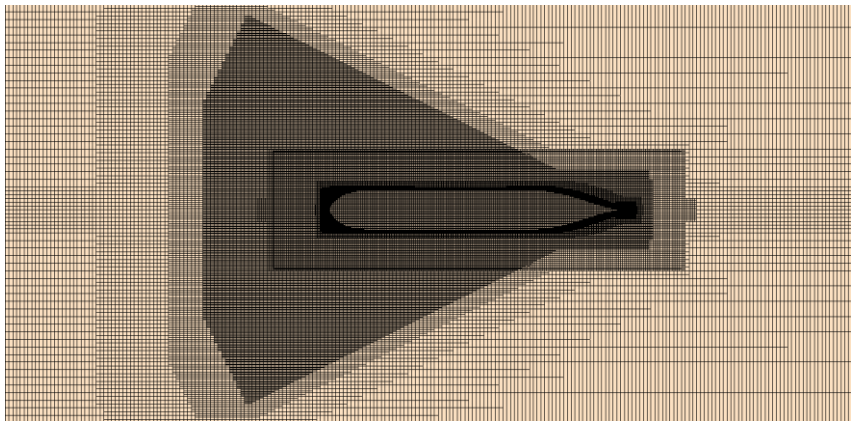

Figure 5.5 A cross-section of the computation mesh showing the refined mesh to capture the Kelvin wake.

Figure 5.6 Surface mesh on the hull and rudder.

5.3.5 Post-processing formulations

Before moving on to the results and discussion, it is first necessary to explain the formulations used during the processing of the results.

To begin with, Fourier Series (FS) were used to analyse the unsteady time histories of the force and motions due to waves. Each unsteady history φ(t) can be represented by a Fourier Series in time, as given by:

$$\varphi(t) = \varphi_0 + \sum_{n=1}^{N} \varphi_n . \cos(2\pi f_e nt + \gamma_n), \text{ n=1,2,3,...} \quad \textbf{(5.1)}$$

where φ_n is the n^{th} harmonic amplitude and γ_n is the corresponding phase. These values can be calculated using the following expressions:

$$\varphi_n = \sqrt{a_n^2 + b_n^2} \quad \textbf{(5.2)}$$

$$\gamma_n = arc\tan\left(\frac{b_n}{a_n}\right) \quad \textbf{(5.3)}$$

in which,

$$a_n = \frac{2}{T}\int_0^T \varphi(t)\cos(2\pi f_e nt)dt \quad \textbf{(5.4)}$$

$$b_n = -\frac{2}{T}\int_0^T \varphi(t)\sin(2\pi f_e nt)dt \quad \textbf{(5.5)}$$

In these equations T designates the encounter period of waves.

The 0^{th} harmonic amplitude φ_0 in FS is defined as the average value of the time history of φ(t), which can be obtained as follows:

$$\varphi_0 = \frac{1}{T}\int_0^T \varphi(t)dt \quad \textbf{(5.6)}$$

The first FS harmonic φ_1 refers to the linear term from the unsteady histories. Hence, the zeroth and first FS harmonics have been named as the fundamental components in the linear system. In particular, taking precedence from previous studies, this work

focused on the 0^{th} and 1^{st} order terms for the force and motions, as they are used for the calculation of resistance and transfer functions (TF), respectively (Shen and Wan, 2013). During the post-processing of the quantities, it was observed that for the resistance in waves, higher order terms have significant effects. This observation has also been reported in the literature. For example, Simonsen et al. (2013) claim that for the resistance in waves, second and third order FS terms may make up to 50 and 15% of the first order FS amplitude, respectively. For any further details regarding the higher order terms, reference can be made to Otzen and Simonsen (2010).

The ship motions in waves were quantitatively analysed with transfer functions. The definition of heave and pitch transfer functions, respectively, can be given by:

$$TF_3 = \frac{x_{31}}{\zeta_{I1}} \tag{5.7}$$

$$TF_5 = \frac{x_{51}}{k\zeta_{I1}} \tag{5.8}$$

where x_{31}, x_{51} and ζ_{I1} are the first FS harmonic amplitudes of heave, pitch, and incident wave time histories, respectively, and $k=2\pi/\lambda$ is the wave number. It must be highlighted that in this work, the heave and pitch motions were evaluated at the ship's centre of gravity.

For calm water and for wave conditions, the dimensionless total resistance coefficient C_T was used to analyse the total resistance of a ship. C_T is calculated by:

$$C_T = \frac{F_X}{\frac{1}{2}\rho U^2 S} \tag{5.9}$$

where F_X is the X-force measured in the global coordinate system (the total resistance) and S is the wetted area of the vessel in calm water.

The added resistance due to waves was calculated by first subtracting the calm water resistance $F_{X,calm}$ from the 0^{th} FS harmonic amplitude of the X-force in waves ($F_{X,wave}$) at the same ship speed. It was then non-dimensionalised, as follows:

$$\sigma_{aw} = \frac{(F_{X,wave} - F_{X,calm})}{\rho g \zeta_{I1}^2 B_{WL}^2 / L_{BP}} \quad \textbf{(5.10)}$$

σ_{aw}, given in the above equation, has been termed the added resistance coefficient. The added resistance of the vessel due to waves will be presented by giving the added resistance coefficients over the wave/ship length ratios at both speeds.

5.4 Results and Discussion

The following section will outline the simulation results achieved during this study, and will also provide some comparison with experimental results and the results from potential flow theory. It will then present a discussion on the observation of the results. This section is divided into five main sub-sections, each of which presents different aspects of this work's findings. Before proceeding to examine the results obtained, it is first necessary to validate the current CFD approach against the experimental results.

5.4.1 Validation and verification

Due to the large body of data available for the KCS, it is possible to use experimental data for comparison with the simulated results. This can then be used to validate the approach and results.

5.4.1.1 Ship resistance in calm water

The total resistance (drag) of a ship R_T is mainly composed of two components; the residuary resistance R_R and the frictional resistance R_F as given by Equation (5.11) (Gillmer and Johnson, 1982).

$$R_T = R_R + R_F \quad \textbf{(5.11)}$$

Equation (5.11) can also be expressed in its more common non-dimensional form. This is achieved by dividing each term by the denominator of Equation (5.9). Hence, the total resistance coefficient C_T is made up of the residuary resistance coefficient C_R and the frictional resistance coefficient C_F. Given that the residuary resistance coefficient is a function of the Froude number, and the frictional resistance

coefficient is a function of the Reynolds number, the total resistance coefficient can, therefore, be written in the following form (Schultz, 2007):

$$C_T = C_R(Fn) + C_F(Re) \quad \textbf{(5.12)}$$

The frictional resistance coefficient C_F, for both model and full-scale ships, can be found by using the following ITTC-1957 formula:

$$C_F = \frac{0.075}{(\log_{10} \mathrm{Re} - 2)^2} \quad \textbf{(5.13)}$$

The Reynolds number at a ship speed of 24 knots for the full-scale KCS model is calculated to be 2.839×10^9.

Ship resistance can be predicted through towing tank tests conducted with a ship model which is geometrically similar to the full-scale ship. To predict the resistance of the full-scale ship using the model test results, a dynamic similarity has to be achieved between the model and the full-scale ship.

In this work's CFD simulations, the full-scale model was initially towed in calm water conditions free to trim and sink at a speed of 24 knots (Case 1). After the solution had converged adequately, the last twenty seconds of F_x time history were used for the Fourier analysis. The 0^{th} FS harmonic of the total resistance coefficient was calculated to be 2.2945×10^{-3} by the CFD model used in this work. During the towing tank tests conducted by Simonsen et al. (2013) at a model speed of 1.701 m/s, which corresponds to 24 knots in full scale, the coefficients of total resistance and residuary resistance for a 1/52.667 scale model of the KCS ($\mathrm{Re}_{\mathrm{model}} = 6.517 \times 10^6$) were found to be 4.310×10^{-3} and 1.064×10^{-3}, respectively. In order to make a comparison to our case, the full scale C_{Ts} value was predicted to be 2.414×10^{-3} from the model tests. It should be highlighted that the towing tank experiments were also conducted in trim and sinkage free conditions.

As can clearly be seen from the above calculations, the C_T value of the vessel in calm water at 24 knots is quite compatible with the experiments, and is only under-predicted by 4.95% compared to the towing tank results.

5.4.1.2 Wave generation

5th-order Stokes waves were used inside the computational domain throughout all simulations. The theory of the 5th-order wave is based on the work by Fenton (1985). The reason for selecting this wave is that, according to CD-Adapco (2014), "*this wave more closely resembles a real wave than one generated by the first order method*". The first order wave mentioned here is the wave that generates a regular periodic sinusoidal profile.

To monitor the waves generated at the inlet, a wave probe was used to record the wave elevation in each case. Figure 5.7 illustrates the position of the wave probe between the inlet and vessel. Figure 5.8, as an example, displays the recorded time history of the wave elevation at the probe in Case 3.

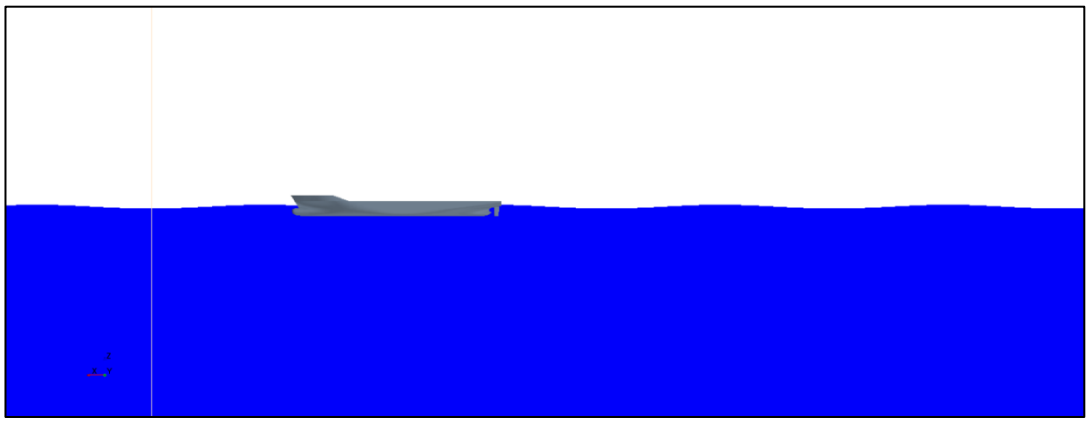

Figure 5.7 Numerical wave probe (the white line) to record the wave elevation.

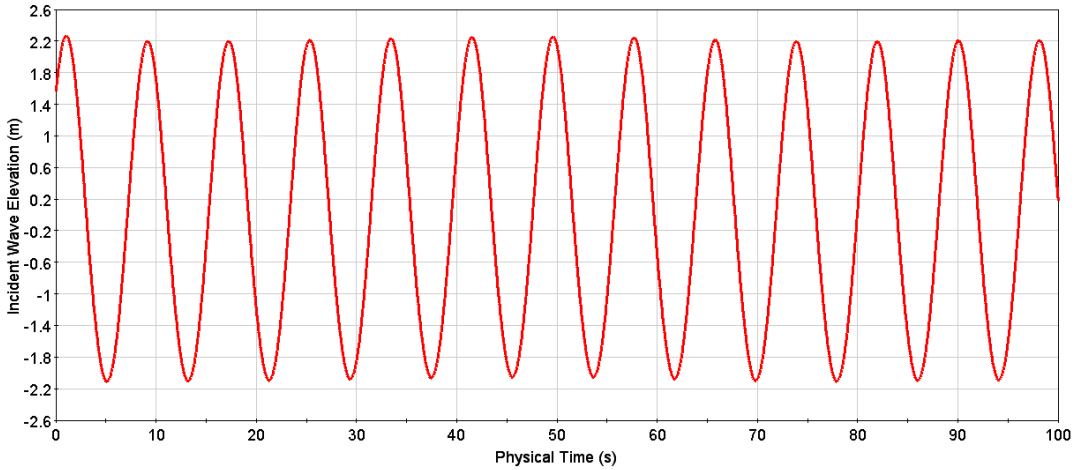

Figure 5.8 Time history of wave elevation at the numerical wave probe (Case 3).

By applying FS on a window of the time series of the wave elevation shown in Figure 5.8, the mean of the 1st harmonic wave amplitudes covering the last ten periods of encounter was calculated to be 2.140 m, which under-predicts the actual wave amplitude (2.212 m) by 3.23%. This slight reduction of the wave amplitude was found to be acceptable for the current cell size and time step, and was sufficiently reasonable for the validation of wave generation by the current CFD model.

5.4.1.3 Wave pattern

Case 3 was selected as a representative case to show both the wave contours and the motions of the vessel. Figure 5.9 shows the global wave pattern around the KCS when the solution was initialised, and Figure 5.10 shows the same plot after the simulation had completed its run. The Kelvin wake generated by the ship is clearly visible in Figure 5.10.

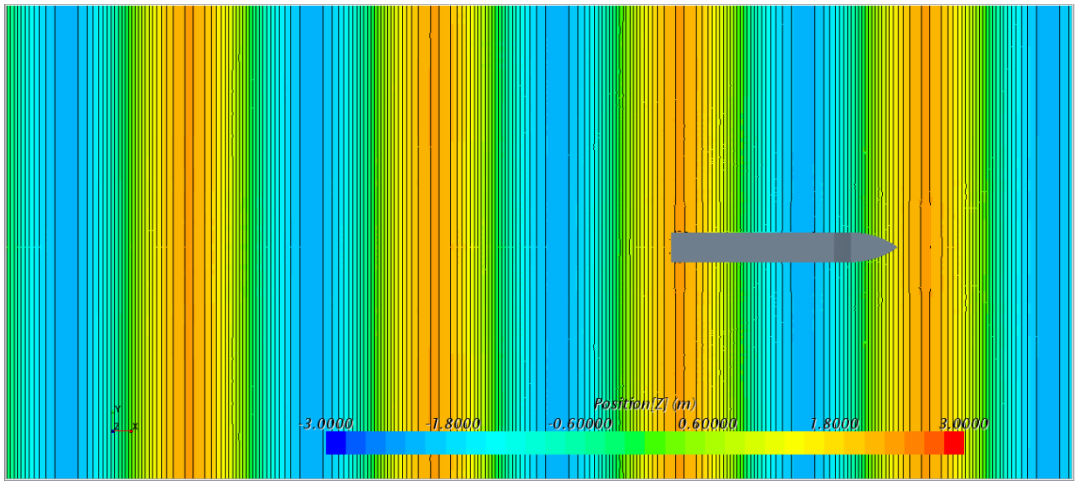

Figure 5.9 Measured wave pattern around the KCS hull when the simulation is initialised.

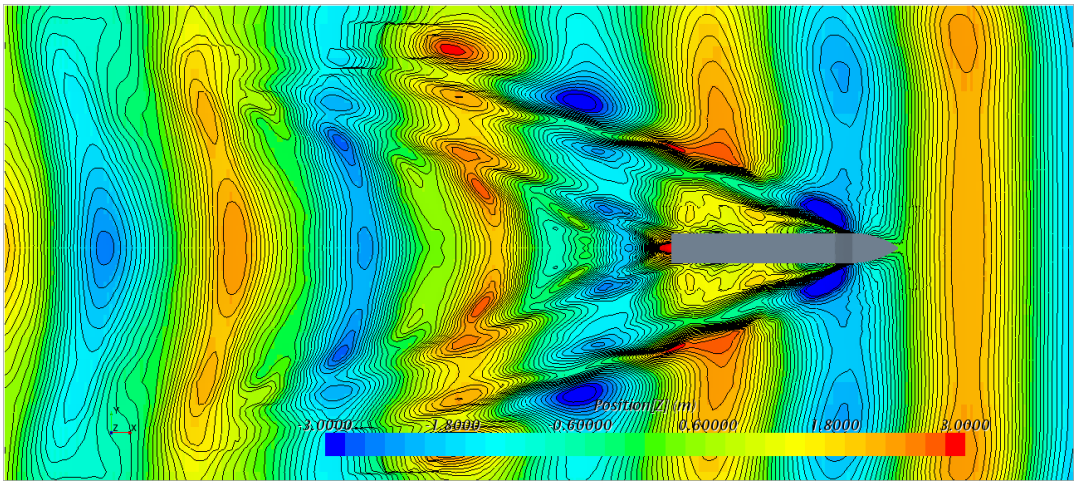

Figure 5.10 Measured wave pattern around the KCS hull after the simulation had completed its run.

In order to visualise bow motions of the vessel in waves, four snapshots of the waves and the bow movement of the vessel were taken in a period of encounter and are displayed in Figure 5.11. The figure expressly shows that breaking bow waves and the slamming incident have been successfully captured by the current CFD model. It is noteworthy to mention that the snapshots in the figure were recorded after the motions reached steady-state.

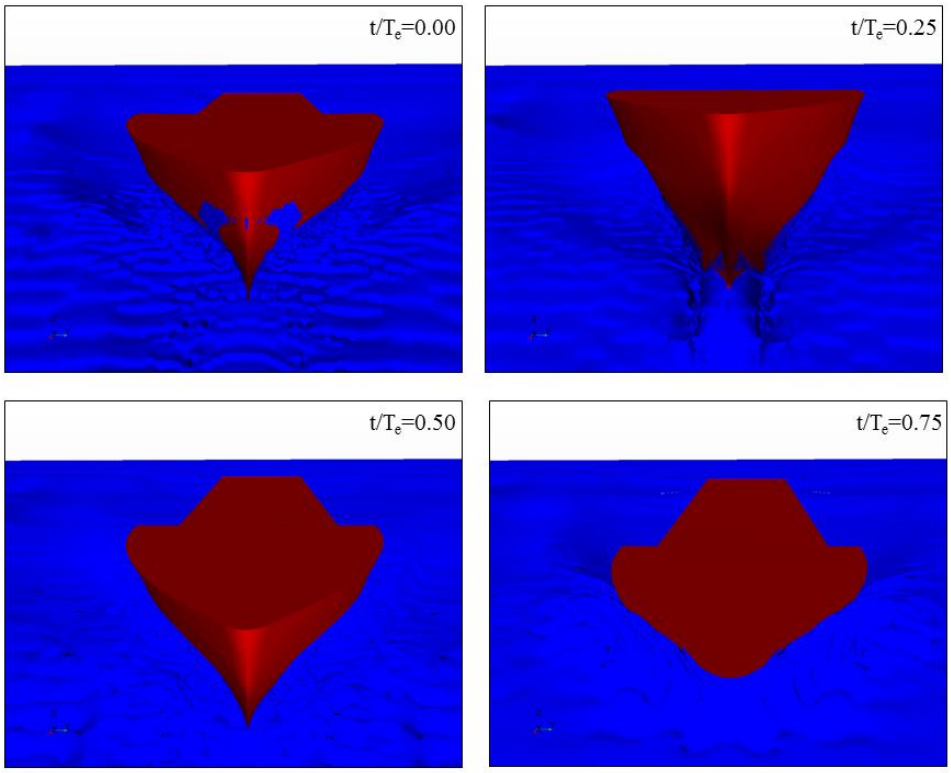

Figure 5.11 Four snapshots of wave patterns and bow movements of the vessel in a given period of encounter.

5.4.1.4 Ship motions and added resistance

As was mentioned in Section 5.2, three pre-selected different cases in waves were used for the validation of the CFD model against experiments. In this sub-section, heave and pitch as well as C_T histories of the vessel in each simulation will be given in detail and the results will then be compared to the available experimental and CFD data obtained by previous studies.

Simonsen et al. (2013), as mentioned in Chapter 2, Section 2.6, also investigated the KCS by means of EFD and CFD. They used CFDShip-Iowa as the RANS solver in all of their simulations, and Star-CCM+ for several specific simulations. Ultimately, they compared all of their CFD results to experimental findings. For this reason, this work's results for Cases 3 and 4 were compared to their CFD and EFD results. Also, for Case 6, this work benefited from the CFD work of Carrica et al. (2011), who performed computations with CFD Ship-Iowa. They compared their results with the experimental study of Otzen and Simonsen (2010), as well as with the CFD results of several researchers, who used different numerical approaches.

Table 5.5 presents a comparison of the heave and pitch transfer functions between the current CFD model and the other CFD simulations performed by other researchers, as well as the related experimental data. The comparison error (E), which is defined as the difference between the experimental data and the calculated data, is also included in the table. It should also be mentioned that in Table 5.5, the pitch responses are given in radians.

The total resistance coefficients obtained are given in Table 5.6 and are compared only to the EFD data, since all the other available CFD simulations were performed with a model scale KCS. However, the full-scale C_{Ts} values by EFD were predicted from the model tests in order to make a precise comparison with the experiments, for reasons discussed in the previous sub-section.

Table 5.5 The transfer functions in the validation study.

Case No.		TF_3	TF_5
3	EFD (Simonsen et al., 2013)	0.950	0.693
	CFDShip-Iowa (Simonsen et al., 2013)	0.995	0.769
	Error (% of EFD)	4.74	10.97
	Star-CCM+ (Simonsen et al., 2013)	0.861	0.731
	Error (% of EFD)	-9.37	5.48
	The Current CFD	0.946	0.664
	Error (% of EFD)	-0.42	-4.18
4	EFD (Simonsen et al., 2013)	1.107	0.971
	CFDShip-Iowa (Simonsen et al., 2013)	0.950	0.959
	Error (% of EFD)	-14.18	-1.24
	The Current CFD	1.003	0.895
	Error (% of EFD)	-9.39	-7.83
6	EFD (Otzen and Simonsen, 2010)	0.901	1.037
	CFDShip-Iowa (Carrica et al., 2011)	0.854	0.993
	Error (% of EFD)	-5.2	-4.2
	CFD (El Moctar et al., 2010)	0.891	1.044
	Error (% of EFD)	-1.1	0.6
	CFD (Manzke and Rung, 2010)	0.958	1.184
	Error (% of EFD)	6.3	-14.1
	CFD (Akimoto et al., 2010)	1.255	1.037
	Error (% of EFD)	39.2	0
	The Current CFD	0.847	1.085
	Error (% of EFD)	-5.99	4.63

Table 5.6 The total resistance and added resistance coefficients in the validation study.

Case No.		C_{Ts}	σ_{aw}
3	EFD (Simonsen et al., 2013)	5.133×10^{-3}	9.106
	The Current CFD	4.644×10^{-3}	8.128
	Error (% of EFD)	-9.52	-10.74
4	EFD (Simonsen et al., 2013)	5.843×10^{-3}	8.617
	The Current CFD	5.481×10^{-3}	8.269
	Error (% of EFD)	-6.19	-4.04
6	EFD (Otzen and Simonsen, 2010)	4.146×10^{-3}	1.916
	The Current CFD	3.794×10^{-3}	1.717
	Error (% of EFD)	-8.49	-10.37

The total resistance coefficients presented in Table 5.6 were calculated based on evaluating the 0^{th} FS harmonics of the drag force. As can be seen from Table 5.6, for the total resistance coefficients, the deviations between EFD and the current CFD model are in the range of 6.19 to 9.52%, whereas the current CFD model under-predicts the added resistance coefficients within approximately 10% of the experimental data.

For the purpose of visualisation, Figure 5.12 displays how the vessel responds to incident head seas in a period of encounter. The pictures are snapshots from the simulation of Case 3 after the solution had stabilised.

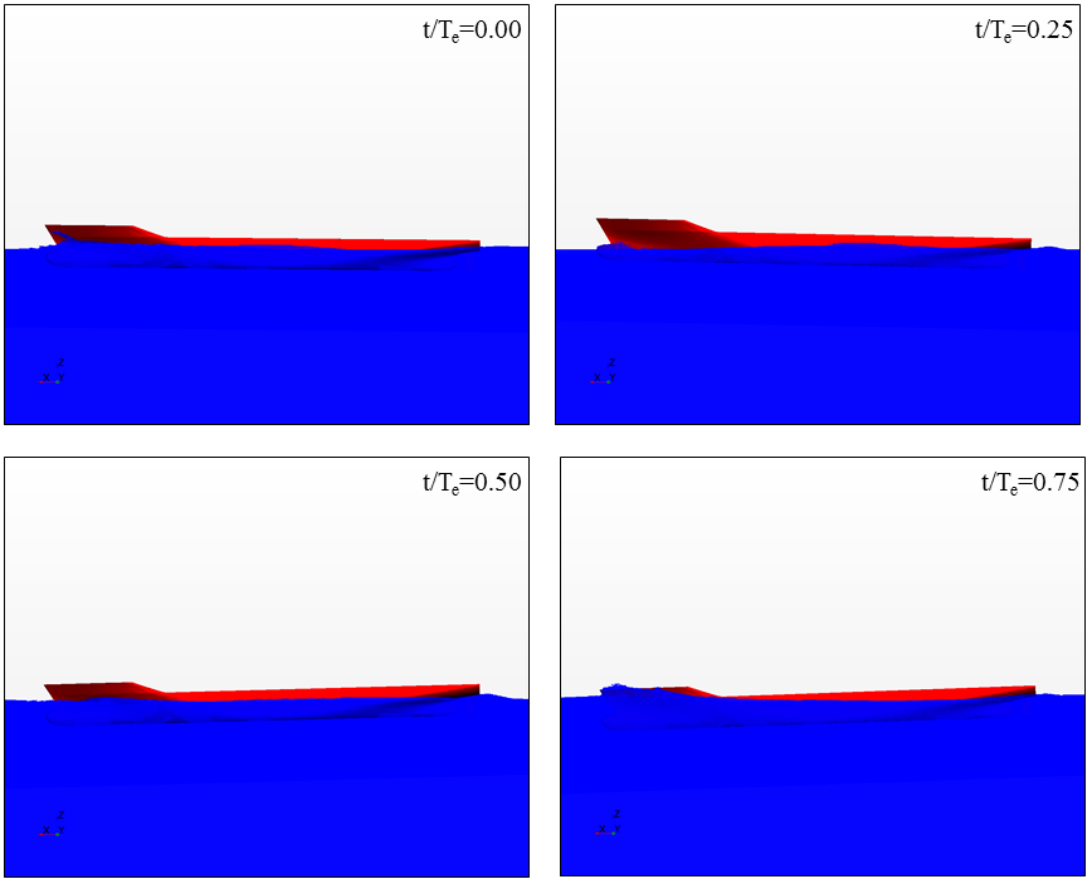

Figure 5.12 Four snapshots of motions of the vessel and the free surface in a given period of encounter.

The time histories of heave, pitch and C_T that belong to all the validation cases (as shown in Figure 5.13, Figure 5.14 and Figure 5.15) were recorded over the last ten periods of encounter.

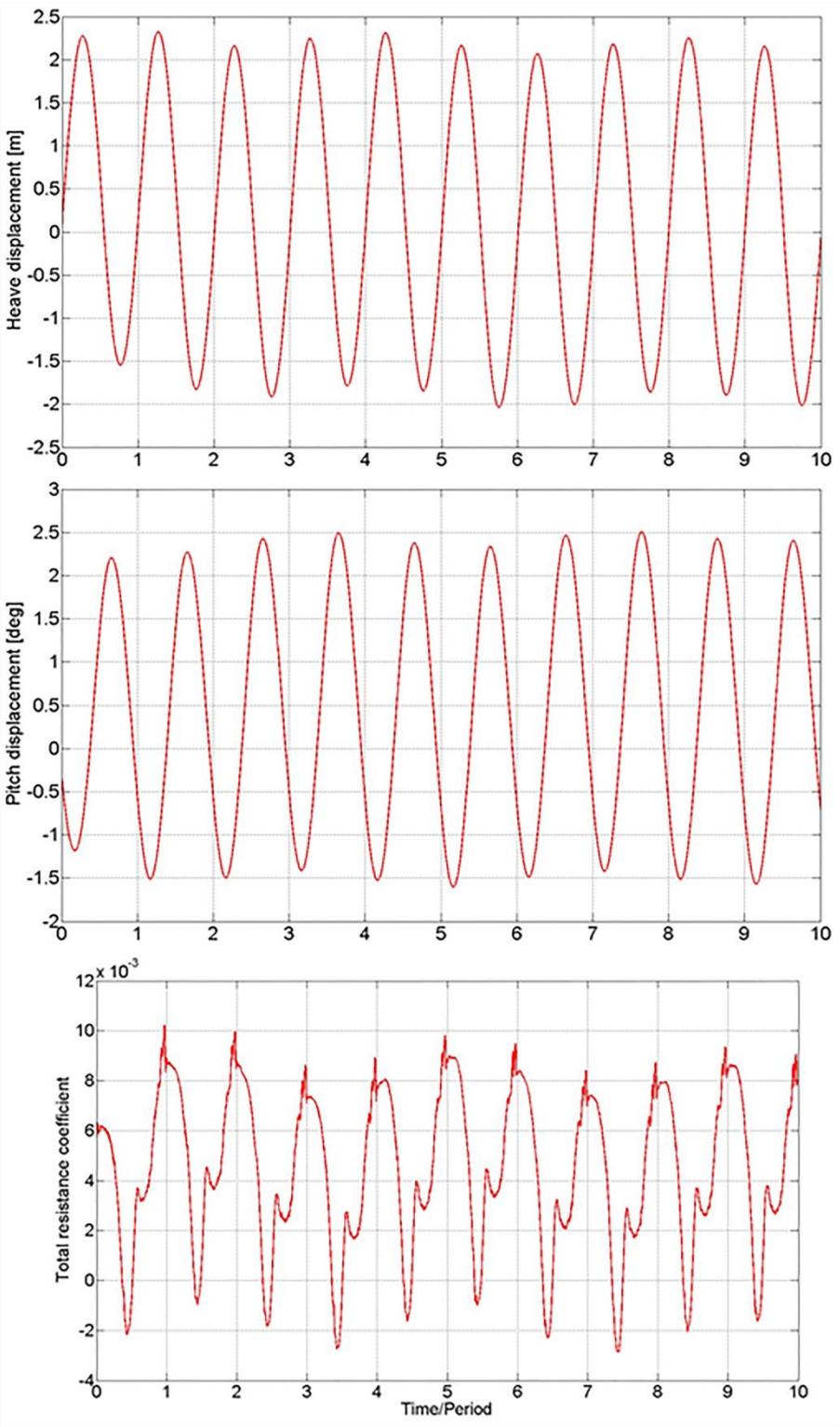

Figure 5.13 Time histories of heave, pitch, and C_T, Case 3.

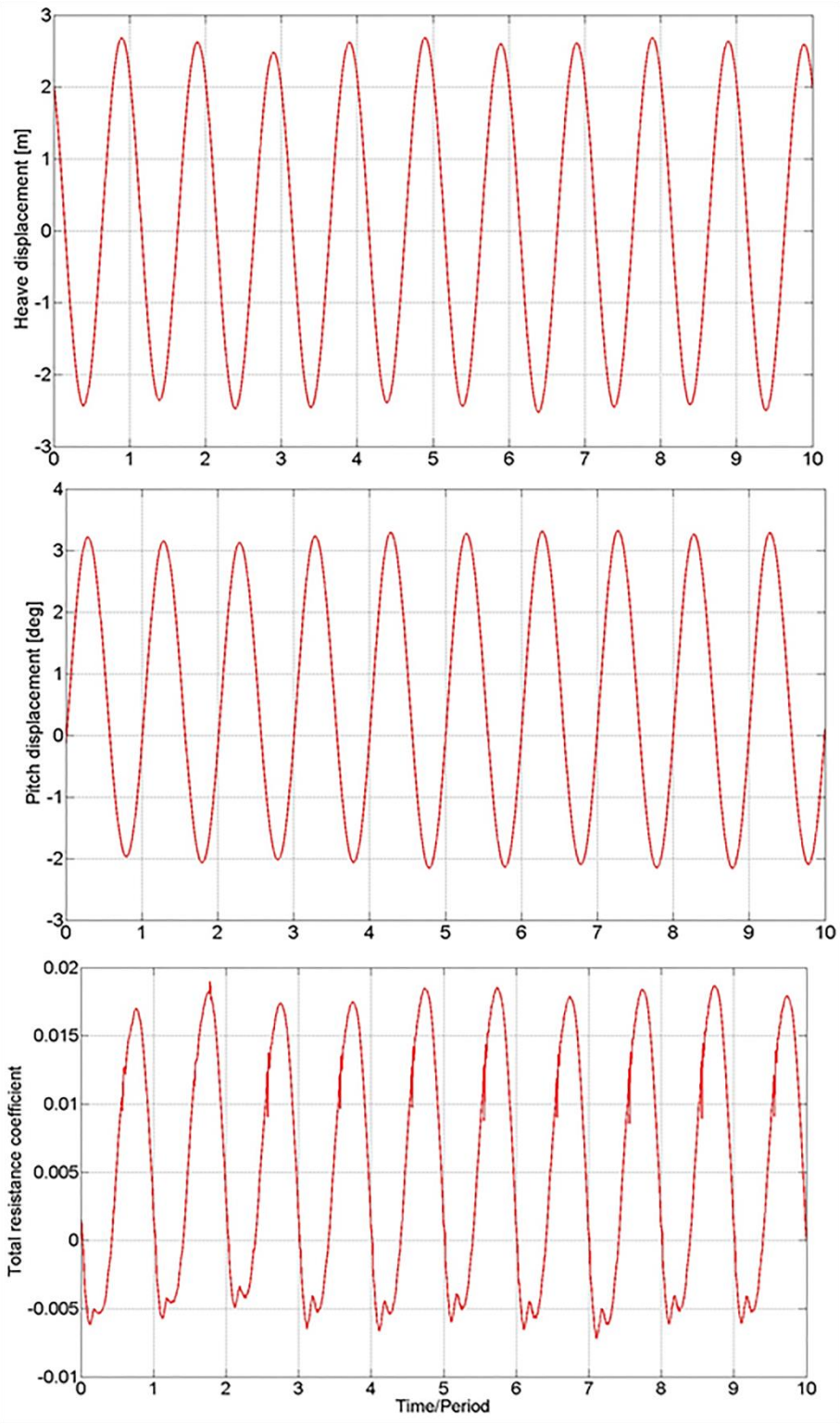

Figure 5.14 Time histories of heave, pitch, and C_T, Case 4.

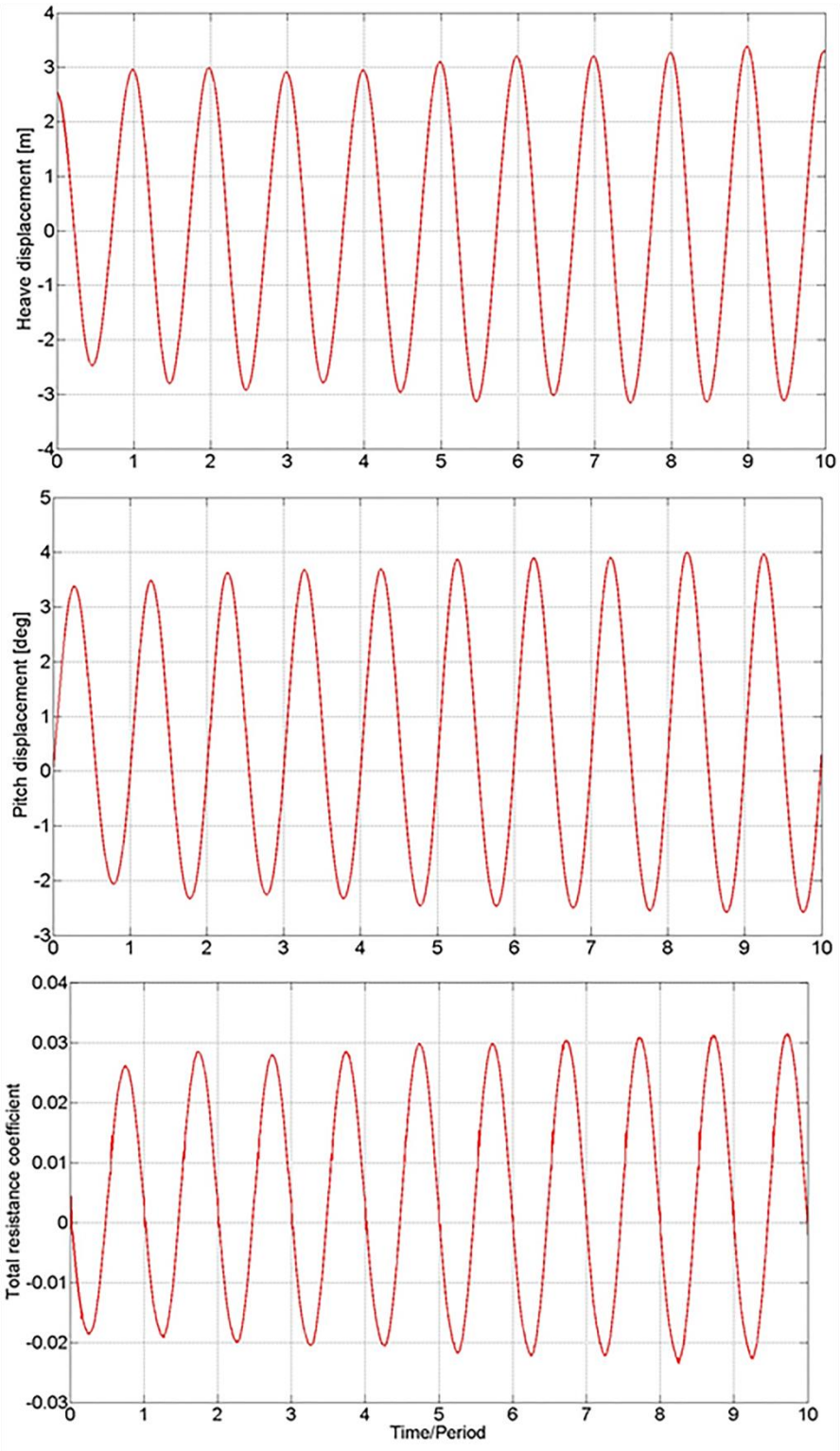

Figure 5.15 Time histories of heave, pitch, and C_T, Case 6.

As explained in the previous section, heave, pitch and the drag histories were evaluated by using the Fourier Series expansion. As an example, the FS approximations of the heave, pitch and C_T time histories in Case 3 covering the last

three periods of encounter are shown in Figure 5.16. In the figure, the heave and pitch time histories were evaluated by approximating a second order FS expansion to the raw record, however, for the C_T records, a FS expansion of a much higher order (thirty) was approximated to the raw data.

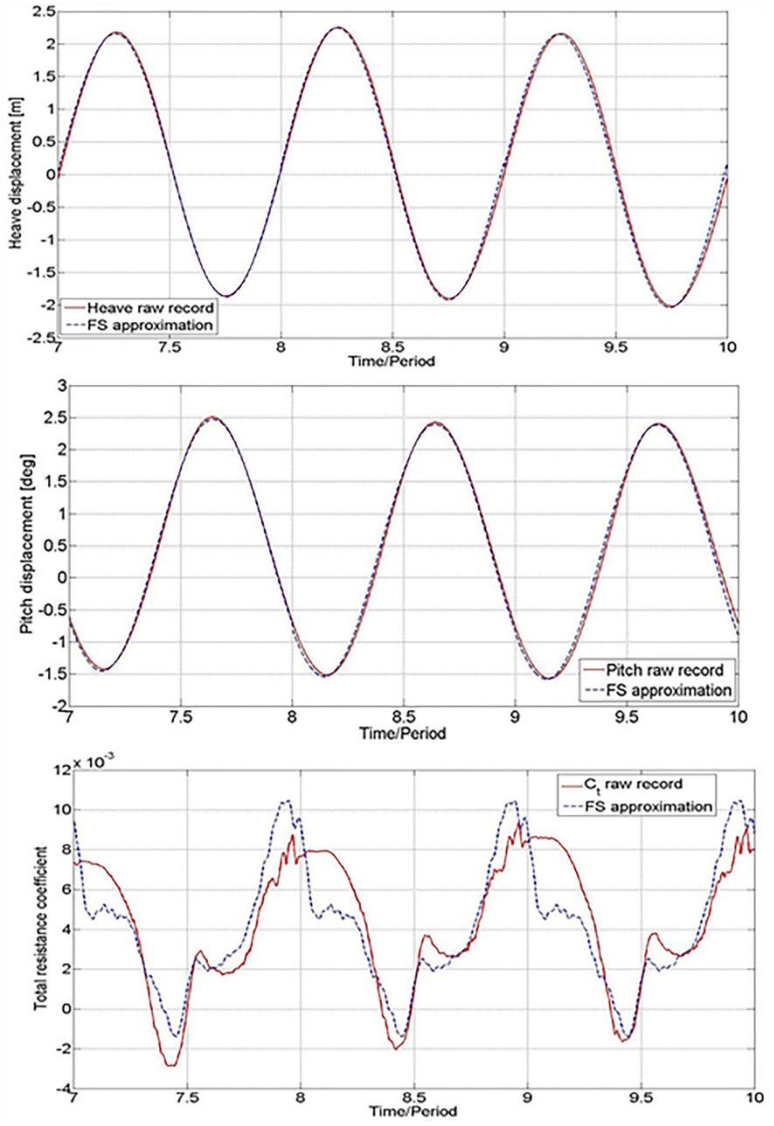

Figure 5.16 FS approximation of the heave, pitch and total resistance time histories for the last 3 periods of encounter, Case 3.

From the comparison in Figure 5.16, it is apparent that the heave and pitch responses of the vessel are well presented by the FS expansion, whereas the FS approximation does not match well with the raw C_T records. This is because in Case 3, the total resistance exhibits highly nonlinear behaviour, due to resonance. However, this should not pose a problem since the zeroth FS harmonics are used in C_T calculations.

The same approach is also used when evaluating experimental time records. Also, it should be borne in mind that in Cases 4 and 6, the total resistance time histories are much closer to linearity (see Figure 5.14 and Figure 5.15).

5.4.1.5 Verification study

A verification study was undertaken to assess the simulation numerical uncertainty, U_{SN}, and numerical errors, δ_{SN}. In the present work, it was assumed that the numerical error is composed of iterative convergence error (δ_I), grid-spacing convergence error (δ_G) and time-step convergence error (δ_T), which gives the following expressions for the simulation numerical error and uncertainty (Stern et al., 2001):

$$\delta_{SN} = \delta_I + \delta_G + \delta_T \quad \textbf{(5.14)}$$

$$U_{SN}^2 = U_I^2 + U_G^2 + U_T^2 \quad \textbf{(5.15)}$$

where U_I, U_G and U_T are the uncertainties arising from the iterative, grid-spacing convergence, and time-step convergence errors, respectively.

The verification study was carried out for the resonant case (Case 3) because, according to Weymouth et al. (2005), large motions and accelerations tend to cause the highest numerical errors. This therefore can be regarded as a 'worst-case test'.

Xing and Stern (2010) state that the Richardson extrapolation method (Richardson, 1911) is the basis for existing quantitative numerical error/uncertainty estimates for time-step convergence and grid-spacing. With this method, the error is expanded in a power series, with integer powers of grid-spacing or time-step taken as a finite sum. Commonly, only the first term of the series will be retained, assuming that the solutions lie in the asymptotic range. This practice generates a so-called grid-triplet study. Roache's (1998) grid convergence index (GCI) is useful for estimating uncertainties arising from grid-spacing and time-step errors. Roache's GCI is recommended for use by both the American Society of Mechanical Engineers (ASME) (Celik et al., 2008) and the American Institute of Aeronautics and Astronautics (AIAA) (Cosner et al., 2006).

For estimating iterative errors, the procedure derived by Roy and Blottner (2001) was used. The results obtained from these calculations suggest that the iterative errors for TF_3, TF_5, and C_T are 0.181, 0.164, and 0.312% of the solution for the finest grid and smallest time-step.

Grid-spacing and time-step convergence studies were carried out following the correlation factor (CF) and GCI methods of Stern et al. (2006). The convergence studies were performed with triple solutions using systematically refined grid-spacing or time-steps. For example, the grid convergence study was conducted using three calculations in which the grid size was systematically coarsened in all directions whilst keeping all other input parameters (such as time-step) constant. The mesh convergence analysis was carried out with the smallest time-step, whereas the time-step convergence analysis was carried out with the finest grid size.

To assess the convergence condition, the convergence ratio is used as given in Equation (5.16):

$$R_k = \frac{\varepsilon_{k21}}{\varepsilon_{k32}} \tag{5.16}$$

In Equation (5.16) $\varepsilon_{k21}=S_{k2}-S_{k1}$ and $\varepsilon_{k32}=S_{k3}-S_{k2}$ are the differences between medium-fine and coarse-medium solutions, where S_{k1}, S_{k2}, S_{k3} correspond to the solutions with fine, medium, and coarse input parameters, respectively. The subscript k refers to the k^{th} input parameter (i.e. grid-size or time-step) (Stern et al., 2006).

Four typical convergence conditions may be seen: (i) monotonic convergence ($0<R_k<1$), (ii) oscillatory convergence ($R_k<0$; $|R_k|<1$), (iii) monotonic divergence ($R_k>1$), and (iv) oscillatory divergence ($R_k<0$; $|R_k|>1$) (Stern et al., 2006).

For condition (i), the generalised Richardson extrapolation method is used to predict the numerical error and uncertainties. For condition (ii), the uncertainty is predicted by:

$$U_k = \frac{1}{2}(S_U - S_L) \tag{5.17}$$

where S_U and S_L are the maximum and minimum of the solutions from the corresponding convergence study. For diverging conditions (iii) and (iv), neither error nor uncertainty can be assessed (Stern et al., 2006).

For the mesh convergence study, a uniform refinement ratio (r_G) was chosen to be $\sqrt{2}$ which was applied only to the overset region, meaning that the background mesh configuration was not altered. This enabled the incident waves to be modelled efficiently through the computational domain. Without this adjustment, the wave would not have been captured well with a coarser grid configuration, leading to misleading results. Based on the mesh refinement ratio, the final mesh numbers for each mesh configuration are listed in Table 5.7.

Table 5.7 The final cell numbers for each mesh configuration as a result of the mesh convergence study.

Mesh Configuration	Cell Number (N)		
	Background	Overset	Total
Fine	3,572,074	6,357,286	9,929,360
Medium	3,572,074	3,143,679	6,715,753
Coarse	3,572,074	1,594,571	5,166,645

The time-step convergence study was conducted with triple solutions using systematically lessened time-steps based on a uniform refinement ratio (r_T) of 2, starting from $\Delta t=T_e/2^9$.

The verification parameters of the heave and pitch transfer functions and the total resistance coefficients for the grid spacing and time-step convergence studies are demonstrated in Table 5.8 and Table 5.9, respectively.

Table 5.8 Grid convergence study for TF_3, TF_5, and C_T.

Para-meter	r_G	Solutions			R_G	δ^*_G (%S_1)	U_G (%S_1)		U_{Gc} (%S_1)		S_c	EFD
		S_1	S_2	S_3			CF	GCI	CF	GCI		
TF_3	√2	0.946	0.918	0.814	0.270	-2.964	4.83	1.37	1.87	0.27	0.974	0.950
TF_5	√2	0.664	0.678	0.708	0.489	2.154	2.31	2.58	0.22	0.52	0.650	0.693
C_T	√2	$4.644x10^{-3}$	$4.485x10^{-3}$	$4.255x10^{-3}$	0.695	-3.430	16.53	9.75	4.37	1.95	$4.803\ x10^{-3}$	$5.133x10^{-3}$

Table 5.9 Time step convergence study for TF_3, TF_5, and C_T.

Para-meter	r_T	Solutions			R_T	δ^*_T (%S_1)	U_T (%S_1)		U_{Tc} (%S_1)		S_c	EFD
		S_1	S_2	S_3			CF	GCI	CF	GCI		
TF_3	2	0.946	0.925	0.846	0.259	-0.724	0.85	0.95	0.09	0.20	0.953	0.950
TF_5	2	0.664	0.646	0.578	0.274	-0.927	1.28	1.31	0.14	0.26	0.670	0.693
C_T	2	$4.644x10^{-3}$	$4.382x10^{-3}$	$3.504x10^{-3}$	0.298	-1.880	3.44	3.00	0.51	0.60	$4.731\ x10^{-3}$	$5.133x10^{-3}$

Table 5.10 Validation of heave and pitch transfer functions and total resistance coefficient.

Para-meter	U_{SN} (%EFD)		U_D	U_V (%EFD)		E (%)
	CF	GCI		CF	GCI	
TF_3	4.89	1.70	5.83	**7.61**	**6.07**	-0.42
TF_{3c}	1.87	0.38	5.83	**6.12**	**5.84**	3.07
TF_5	2.52	2.51	5.83	**6.35**	**6.35**	-4.18
TF_{5c}	0.33	0.53	5.83	**5.84**	**5.85**	-5.52
C_T	15.02	9.24	5.83	**16.11**	**10.92**	-9.52
C_{Tc}	4.00	1.87	5.83	**7.07**	**6.12**	-5.01

In Table 5.8 and Table 5.9, the corrected simulation value (S_c) is calculated by $S_c=S-\delta^*_G$, where S is the simulation result. Also, U_c is the corrected uncertainty. For more detailed information on how to calculate these uncertainties, reference can be made to Stern et al. (2006). The notation style of this reference was used in this study, to enable the verification results to be presented clearly.

As can be seen from the results listed in Table 5.8 and Table 5.9, reasonably small levels of uncertainty were estimated for the motion transfer functions. On the other hand, relatively large uncertainties U_G (16.53% and 9.75%) were predicted for C_T, using the CF and GCI methods, respectively. However, these values reduce to 4.37% and 1.95%, respectively, when the corrected uncertainties (U_{Gc}) are estimated. This implies that the total drag force in the resonant case is very sensitive to the grid size resolution. It is expected that the uncertainties for the total resistance coefficient in the other cases are smaller than those in Case 3.

As a result of the convergence studies, corrected and uncorrected verification parameters of the heave and pitch transfer functions and the total resistance coefficients are given in Table 5.10. In the table, the subscript *c* refers to the corrected parameters.

Stern et al. (2006) specify that in order to determine whether a validation has been successful, the comparison error E must be compared to U_V, the validation uncertainty, given by

$$U_V^2 = U_D^2 + U_{SN}^2 \tag{5.18}$$

where U_D is the uncertainty in experimental data, which is 5.83% in Simonsen et al.'s EFD data.

Since the absolute value of the comparison error E is smaller than U_V, the heave and pitch transfer functions, as well as the total resistance coefficient, were validated for both the corrected and uncorrected case. The uncertainty levels were estimated to be 6.12%, 5.84% and 7.07%, respectively, when calculated using the CF method. When the GCI method was used to assess these uncertainties, these values become 5.84%, 5.85% and 6.12%, respectively.

5.4.2 Calm water results

Having validated the CFD model, and having performed the necessary verification study, the reminder of this section addresses the main findings of this work.

The calm water total resistance coefficients (C_T), the dynamic sinkage results non-dimensionalised with the ship length (x_{30}/L_{BP}) and the trim angle (x_{50}) in degrees are presented for two speeds in Table 5.11. The CFD results contained in Table 5.11 for 24 knots are under-predicted by approximately 6.7% compared to the towing tank results of Simonsen et al. (2013). The estimation of the full scale C_T value at 24 knots through the towing tank tests was explained in the previous sub-section. Unfortunately, experimental results for this ship operating at a speed of 19 knots are not available in the literature, and thus could not be included in this study. The quantities listed in the table decrease as the ship speed is reduced to 19 knots, as expected.

Table 5.11 Calm water results.

Speed (kn)		C_T	x_{30}/L_{BP}	x_{50} (deg)
24	EFD (Simonsen et al., 2013)	0.002414	-0.0021	0.1853
	CFD	0.0022945	-0.00196	0.1775
	Error (% of EFD)	**-4.95**	**-6.67**	**-4.21**
19	CFD	0.001923	-0.00112	0.1041

5.4.3 Ship motion responses in head seas

The results obtained using the proposed RANS method were compared to those obtained using the potential theory-based frequency domain code VERES. The method used to calculate ship motions in VERES is based on the two-dimensional, linear, strip theory formulation by Salvesen, Tuck and Faltinsen (1970).

Heave and pitch transfer functions predicted by CFD, EFD and VERES at the two different speeds, listed in Table 5.12, are illustrated graphically in Figure 5.17 and Figure 5.18. This gives a clearer depiction of the responses of the vessel to head waves, enabling a more facile comparison among the different approaches. The comparison errors are also listed in Table 5.12. The EFD data are taken from Simonsen et al. (2013).

Table 5.12 The transfer functions for all cases by three different methods (Error (E) is based on EFD data).

Case no.	Ship speed (kn)	TF_3					TF_5				
		CFD		EFD	VERES		CFD		EFD	VERES	
C	*U*	Result	E (%)		Result	E (%)	Result	E (%)		Result	E (%)
1	24	calm water					calm water				
2		0.738	**-1.35**	0.749	0.580	**-22.46**	0.542	**0.64**	0.539	0.544	**1.02**
3		0.946	**-0.42**	0.950	1.005	**5.74**	0.664	**-4.18**	0.693	0.777	**12.12**
4		1.003	**-9.39**	1.107	1.098	**-0.79**	0.895	**-7.83**	0.971	0.914	**-5.84**
5		0.899	**-4.82**	0.945	1.061	**12.25**	0.985	**-7.32**	1.063	0.976	**-8.18**
6		0.847	**-5.99**	0.901	0.992	**10.15**	1.085	**4.63**	1.037	1.043	**0.55**
7	19	calm water					calm water				
8		0.754	-	-	0.646	-	0.550	-	-	0.598	-
9		0.846	-	-	0.852	-	0.662	-	-	0.778	-
10		0.856	-	-	0.885	-	0.802	-	-	0.894	-
11		0.858	-	-	0.887	-	0.874	-	-	0.952	-
12		0.878	-	-	0.910	-	1.007	-	-	1.023	-

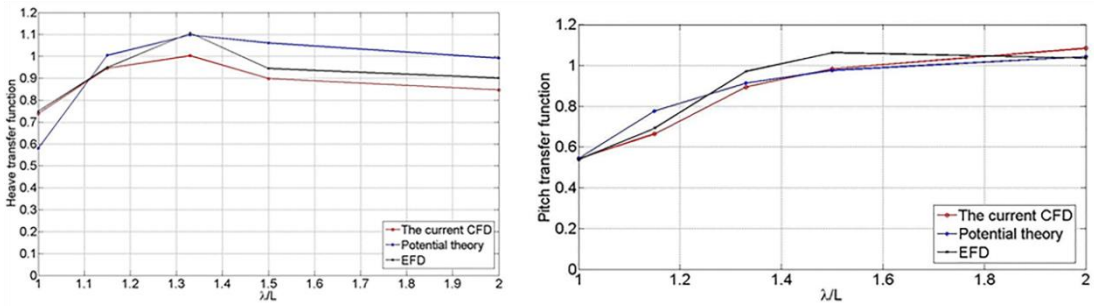

Figure 5.17 A comparison of the ship motions using different methods at a speed of 24 knots (the left- and right-hand sides of the graph show heave and pitch TFs, respectively).

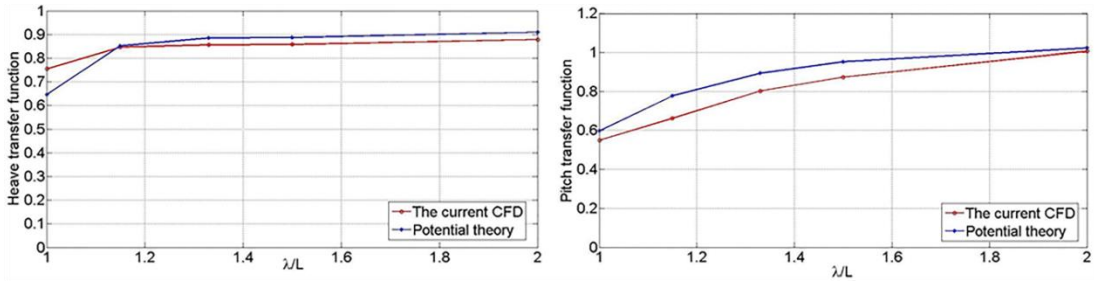

Figure 5.18 A comparison of the ship motions by CFD and potential theory at a speed of 19 knots (the left- and right-hand sides of the graph show heave and pitch TFs, respectively).

As clearly seen from Figure 5.17 and Table 5.12, compared to the EFD, the motions are generally better predicted by the CFD method than by the potential theory-based software package, particularly for heave motion. When Figure 5.17 and Figure 5.18 are compared with each other, the discrepancies between the CFD and VERES are much more pronounced at 24 knots. Generally, VERES seems to over-predict the

motions compared to the CFD method, particularly at 19 knots. Additionally, as can be understood from Table 5.12, the heave and pitch responses of the vessel tend to decrease at 19 knots, compared to those at 24 knots. However, it is predicted that although the vessel decreases its speed when operating in head seas where λ/L=1.0, the heave and pitch responses increase at 19 knots (in Case 8). This is due to the fact that the encounter frequency in that wave condition becomes close to the natural heave and pitch frequency as the speed is reduced to 19 knots.

5.4.4 Resistance coefficients

The resultant added resistance and total resistance coefficients of the vessel in question using the different methods are tabulated in Table 5.13. Also, the comparison errors which are based on EFD data are listed in the table. Since the experimental C_T values are not available, only the results from CFD and potential theory calculations are given for the total resistance coefficients in the table. In addition, the added resistance coefficients at both ship speeds are shown graphically in Figure 5.19.

For the added resistance calculations, the employed potential theory-based software uses the method of Gerritsma and Beukelman (1972), which is based on the determination of the energy of the radiating waves and a strip-theory approximation (Fathi and Hoff, 2013).

As Table 5.13 and Figure 5.19 jointly show, for the added resistance coefficients, CFD agrees much better with the experiments when compared to VERES for the ship speed of 24 knots. Both methods under-predict the added resistance coefficients compared to the EFD data. When the added resistance predictions at the two speeds are compared, it is obvious that the discrepancies between VERES and CFD are much more pronounced at 24 knots, in a similar manner to the ship motion predictions. This is expected, because the results obtained from the linear potential theory are more accurate at moderate speeds than at higher speeds.

Table 5.13 The added resistance and total resistance coefficients for all cases using different methods (Error (E) is based on EFD data).

Case no.	Ship speed (kn)	σ_{aw}					$C_{TS}x10^{-3}$	
		CFD		EFD	VERES			
C	*U*	Result	E (%)		Result	E (%)	CFD	VERES
1	24	calm water					2.295	2.182
2		6.595	**-9.19**	7.263	6.198	**-17.95**	3.726	3.527
3		8.128	**-10.74**	9.106	7.517	**-17.45**	4.644	4.355
4		8.269	**-4.04**	8.617	5.315	**-38.32**	5.481	4.230
5		5.175	**-8.82**	5.676	3.476	**-38.76**	4.822	3.879
6		1.717	**-10.37**	1.916	1.214	**-36.62**	3.794	3.242
7	19	calm water					1.923	1.569
8		5.159	-	-	6.021	-	3.709	3.654
9		5.073	-	-	5.233	-	4.263	3.982
10		3.648	-	-	3.352	-	4.166	3.630
11		2.345	-	-	2.212	-	3.750	3.292
12		1.064	-	-	0.801	-	3.406	2.684

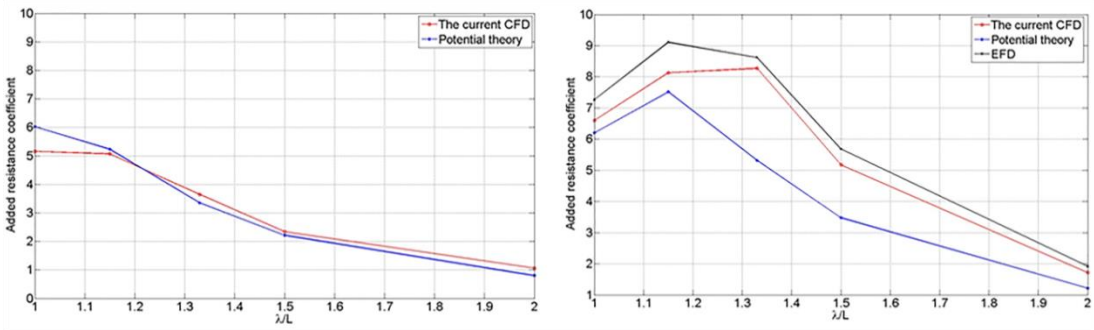

Figure 5.19 A comparison of the added resistance coefficients using different methods at two ship speeds (the left- and right-hand sides of the graph show ship speeds of 19 and 24 knots, respectively).

5.4.5 Increases in the effective power of the vessel due to added wave resistance

The effective power (P_E) is the power required to propel the vessel forward through the water at a constant speed, and is thus calculated as the product of the speed and the total resistance. The effective power can be computed using CFD approaches such as the one which is demonstrated in this chapter; however this is not the case for the fuel consumption. This is due to the very complex interplay of the variables that contribute to fuel consumption, such as engine load, SFOC (Specific Fuel Oil Consumption), propeller efficiency and many others, which depend on a vessel's specifics at different operating conditions. Therefore, in this study, the fuel consumption will not be calculated directly. Instead, the percentage increase in effective power due to the added resistance in waves will be calculated as given by

Equation (5.19). This can be taken as an indication of the implications for fuel consumption, and hence CO_2 emissions, of the vessel in question operating in a seaway, assuming that efficiencies and SFOC remain constant.

$$\%\ \text{Increase in } P_E \text{ due to added resistance} = \frac{\Delta C_T}{C_{T,calm}} x100 = \frac{C_{T,wave} - C_{T,calm}}{C_{T,calm}} x100 \qquad \textbf{(5.19)}$$

Figure 5.20 and Figure 5.21 show the predictions of the percentage increase in the effective power, fuel consumption, and hence CO_2 emissions of the KCS due to induced added resistance at ship speeds of 24 and 19 knots, respectively. The calculations were performed based on the formula given in Equation (5.19). It should be emphasised that when calculating the increase in P_E, the difference in C_T between the wave and calm conditions should be considered at the same speed.

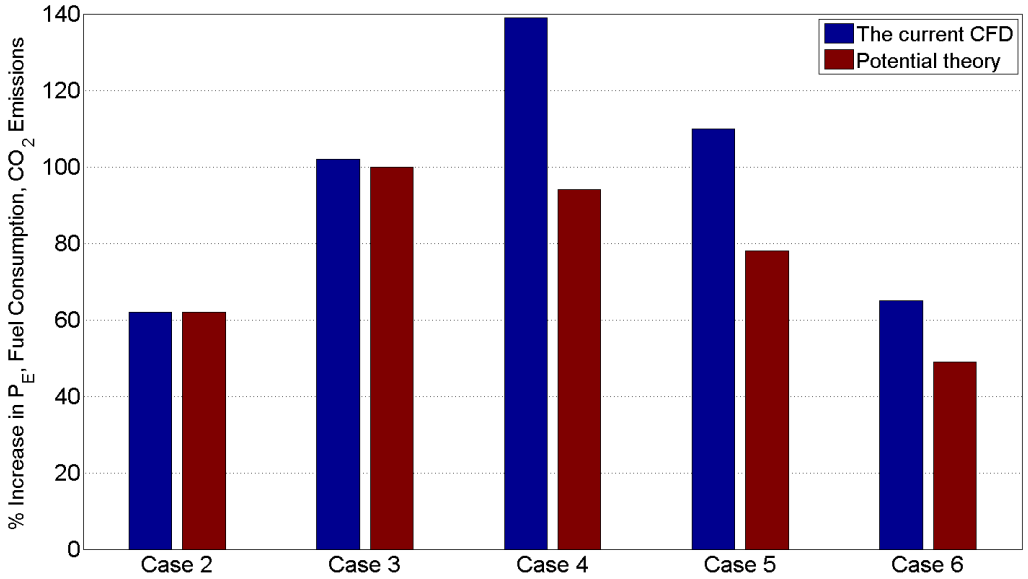

Figure 5.20 Estimation of the percentage increase in the effective power, fuel consumption and CO_2 emissions of the KCS due to operation in head seas at 24 knots.

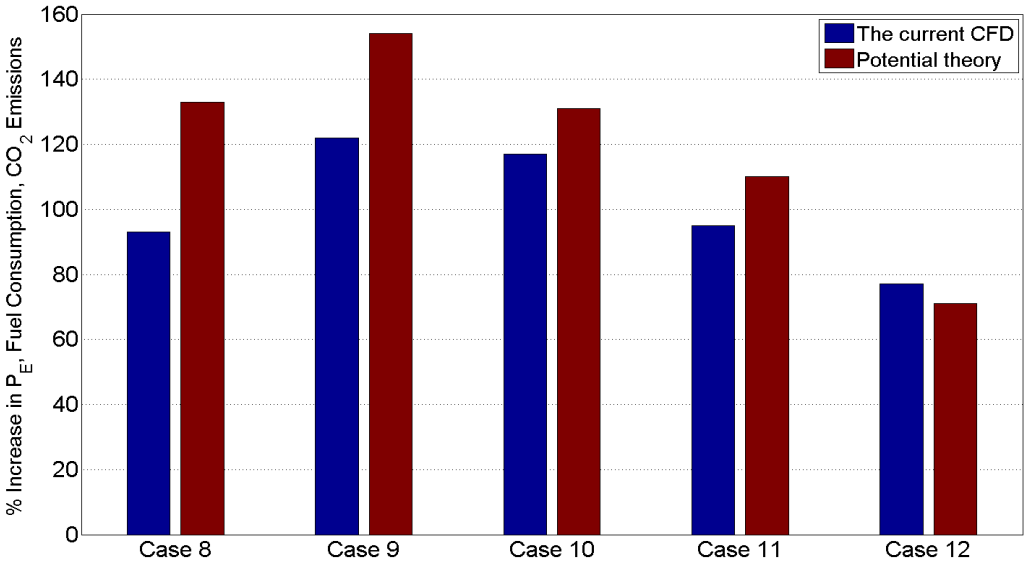

Figure 5.21 Estimation of the percentage increase in the effective power, fuel consumption and CO_2 emissions of the KCS due to operation in head seas at 19 knots.

According to Figure 5.20, CFD calculations imply that the maximum increase in P_E (139%) at a ship speed of 24 knots is observed in Case 4 (λ/L=1.33). On the other hand, potential theory calculations for the same speed predict the maximum increase (100%) in Case 3 (λ/L=1.15). However, the data contained in Figure 5.21 show that the highest increase in the effective power at 19 knots is observed in Case 9 for which λ/L=1.15. This increase is estimated to be around 122% by CFD and 154% by VERES. The minimum increase in the effective power at 24 knots is predicted by CFD as Case 2 (62%) and by VERES as Case 6 (49%). Similarly, both CFD and VERES estimate the minimum increase in P_E at 19 knots in Case 12 with ratios of around 77% and 71%, respectively.

It can be seen from Figure 5.20 and Figure 5.21 that when calculating the increases in the effective power, the largest differences between CFD and potential flow predictions are observed for Cases 4 and 9, under design and slow steaming speeds, respectively. This may be attributed to the fact that Case 4 is the condition in which the maximum excitation force occurs at 24 knots and Case 9 is the condition in which resonance occurs at 19 knots.

In order to reveal the potential benefits of applying the slow steaming approach, for each case the difference in the energy consumed during a voyage under the same wave conditions was calculated between 19 and 24 knots. The metric shown in Equation (5.21) was used to estimate the change in P_E due to slow steaming, which

can be taken as an indication of the fuel consumption, and hence CO_2 emissions, of the ship in question.

$$\% \text{ Change in } P_E \text{ due to slow steaming} = \frac{P_{E(19knots)}.t_{(19knots)} - P_{E(24knots)}.t_{(24knots)}}{P_{E(24knots)}.t_{(24knots)}} x100 \quad \textbf{(5.20)}$$

which can be reduced to:

$$\% \text{ Change in } P_E \text{ due to slow steaming} = \left(\frac{P_{E(19knots)}}{P_{E(24knots)}} . \frac{t_{(19knots)}}{t_{(24knots)}} - 1 \right) x100 \quad \textbf{(5.21)}$$

where '$t_{(19knots)}/t_{(24knots)}$' can be termed the transit time ratio between the durations of the voyages for 19 and 24 knots, respectively.

Figure 5.22 displays the change in the effective power, fuel consumption and CO_2 emissions of the vessel due to its operation under a slow steaming speed condition, with respect to its operation at a more typical service speed. This graph can help to interpret the power reduction or increase for any given case using the CFD and potential theory approaches. For example, when the vessel keeps her course in a head sea condition where $\lambda/L=1.33$ (Case 4) at a speed of 24 knots, if she were to reduce her speed down to 19 knots in the same wave conditions (Case 10), based on this study, it can be estimated that the required effective power will decrease by 52% and 46% using the CFD and potential theory approaches, respectively. Figure 5.22 distinctly shows the advantages of slow steaming operational conditions in terms of fuel consumption and CO_2 emissions.

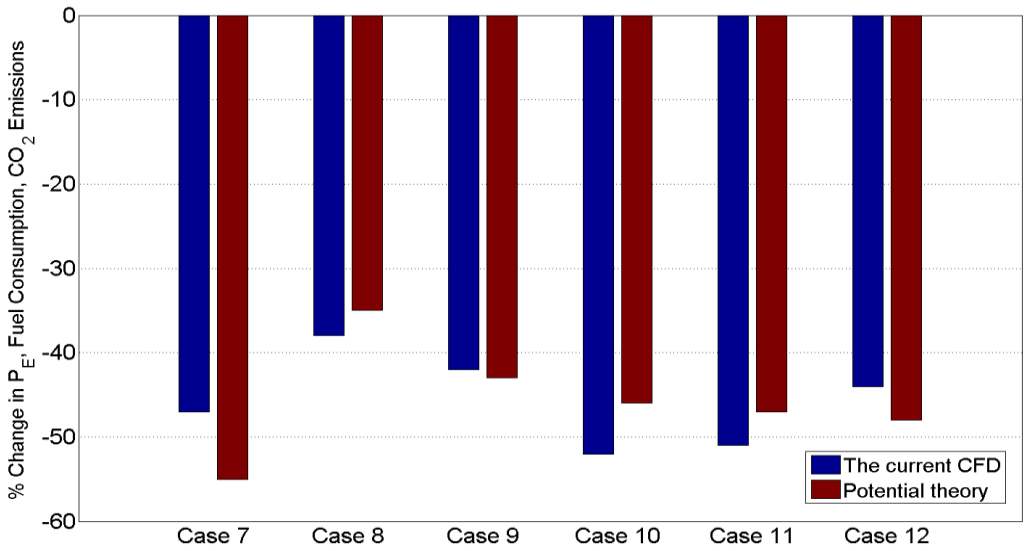

Figure 5.22 Estimation of the percentage change in the effective power, fuel consumption, and CO_2 emissions of the KCS due to operation in head seas at a slow steaming speed (19 knots), compared to a speed of 24 knots.

5.5 Concluding Remarks

In this chapter, fully nonlinear unsteady RANS simulations to predict ship motions and the added resistance of a full scale KCS model were carried out at two speeds, corresponding to service and slow steaming speeds. This enabled the related objectives to be achieved by both revealing the potential benefits of the slow steaming approach, and, by validating the proposed numerical model, to predict heave and pitch motion responses and the added resistance due to waves.

Firstly, it was shown that the total resistance coefficient in calm water at service speed was under-predicted by 4.95% compared to the related towing tank results. For the simulations in the presence of waves, a numerical wave probe was inserted between the inlet and the ship to measure the generated waves. It was then shown that the mean of the first harmonic wave amplitude (for a representative case) was under-predicted by 3.23% compared to the expected wave amplitude. This was deemed to be sufficient for the applied time step and mesh size resolutions. During the verification and validation study it was demonstrated in detail that the heave and pitch transfer functions, as well as the total resistance coefficient, were validated at uncertainty levels of 5.84%, 5.85%, and 6.12%, respectively, when calculated using the grid convergence index method.

In ship motions and resistance predictions, it was demonstrated that the current CFD model predicted the heave and pitch transfer functions within a range of 0.42-9.39% and 4.18-7.83% of the EFD data, respectively. For the total resistance coefficients in waves, the deviations between EFD and CFD varied from 6.19 to 9.52% of the experiments. Similarly, the added resistance coefficients were under-predicted by CFD, falling within circa 10% of those from experiments.

The results obtained using the current CFD model were also compared to those obtained using potential flow theory. VERES was used as a potential theory-based seakeeping code to predict the motion responses and the added resistance of the vessel in question. Comparisons between CFD simulations, potential flow calculations and experiments indicated that CFD, in most cases, predicts motions and added resistance with more accuracy than potential theory. Additionally, it was revealed that the discrepancies between RANS computations and potential theory in both motions and added resistance are greater at 24 knots than at 19 knots. This is due to the fact that linear potential theory is designed for moderate speeds and thus has some deficiencies when applied at high speeds, as noted in Chapter 2. More interestingly, both the CFD and the potential flow calculations generally under-predicted the added resistance coefficients of the vessel when compared to EFD at service speed. It must be recalled that the results obtained using both approaches could only be compared to the experiments at service speed, since the literature does not offer any experimental results conducted at 19 knots.

The increase in effective power due to added resistance was also calculated for each individual wave condition. It was shown in Chapter 5 that this can be taken as an indication of the implications for fuel consumption, and hence CO_2 emissions, of KCS operating in a seaway, assuming that efficiencies and SFOC remain constant. From CFD calculations it was observed that the maximum increases in the effective power due to operation in waves are 122% and 139% at 19 and 24 knots, respectively. VERES, on the other hand, estimates these values for the same speed as 154% and 100%, respectively.

With the current trend towards operation according to the slow steaming principle, vessels are operating in conditions that are significantly different to those for which

they were designed and optimised. It is therefore critical that the impacts of slow steaming upon ship behaviour and performance are well understood. Chapter 5 has shown that slow steaming has beneficial effects on reducing ship motions, power requirements, fuel consumption and hence CO_2 emissions. It was estimated, using the CFD method described in this work, that application of the slow steaming principle can lead to a decrease of up to 52% in effective power and CO_2 emissions, compared to a vessel operating in the same wave conditions at 24 knots.

6. FULL-SCALE UNSTEADY RANS SIMULATIONS OF VERTICAL SHIP MOTIONS IN SHALLOW WATER

6.1 Introduction

Over the last decade, an increasing number of large ships, such as VLCC, have called for a need to understand the performance and behaviour of such ships in shallow water. As indicated by Oortmerssen (1976a), the draft of fully loaded VLCCs is so large that it is often necessary to dredge approach channels around harbours, to enable such ships to enter harbours without grounding. In addition to harbours, even some open sea areas (for instance some areas in the North Sea) can be regarded as shallow water.

These large vessels are loaded and unloaded in exposed areas, where they are moored or secured to buoys or jetties. These designated terminals are located as close to shore as possible, mostly in shallow water. In order to diminish the risk of grounding for these ships, and to design and construct channels appropriately, it is critical to study vertical ship motions (heave and pitch) in shallow water (Oortmerssen, 1976b).

Limited water depth has a perceptible influence on ship motions in waves, in particular when the ratio of water depth to draft of the ship is less than four. According to Oortmerssen (1976b), this effect becomes significant when the water depth is less than twice that of the draft. Beukelman and Gerritsma (1982) later contested this claim, instead suggesting the ratio to be two and a half.

Ship motions in response to incident waves in shallow water are affected in two ways (Oortmerssen, 1976b):

i. Firstly, the incoming waves are affected due to the presence of a finite water depth. The consequential wave forces/moments exerted on the vessel therefore vary from those in deep water conditions.
ii. Secondly, the hydrodynamic coefficients (added mass and damping) of the ship will change, stemming from the effect of the sea bed.

During the literature review presented in Chapter 2.7, it was noted that the majority of the numerical results obtained in shallow water were not actually validated. Although there are several benchmark data sets for researchers to compare their deep water results with, unfortunately no benchmark ship data exists for researchers studying shallow water problems. This shortfall was highlighted in the latest (27^{th}) International Towing Tank Conference and it was concluded that knowledge of the motions of large ships and floating structures in shallow water still remains a challenging issue. The ITTC's Ocean Engineering Committee (2014) has therefore suggested the introduction of benchmark data, to validate numerical methods based on potential theory or CFD.

In addition, to the best of this author's knowledge, no specific study exists which aims to predict the motion responses of a vessel to waves in shallow water, using a CFD-based RANS approach. Therefore, this chapter addresses the gap in the field's current knowledge by calculating the vertical motions of a ship against head seas in shallow water.

Firstly, before starting the real ship motion simulations, the effect of a finite water depth on incoming waves was investigated by conducting a series of simulations in the absence of a ship model. In this part of the study, the intention was to observe the degeneration in the incident wave form due to the sea bottom effect. To do this, nonlinear waves were simulated in three different water depths, and the free surface elevation was measured at various locations within the solution domain.

Then, a 200 kDWT tanker was chosen for this study due to the availability of its geometry and experimental data conducted in shallow water, to validate this study's CFD model. Moreover, this tanker has a very large draft which makes the model of the tanker particularly relevant for this study.

A full-scale tanker model was used for all simulations, to avoid scaling effects. The model was used without any appendages to mimic the real experimental conditions. All CFD simulations were performed in waves at a zero ship speed. The simulations were carried out in three different ratios of water depth to draft (δ=1.2, 3.0 and 4.365). The obtained results for δ=1.2 and 4.365 were compared to those taken from the experimental studies of Oortmerssen (1976a, 1976b) and Pinkster (1980), respectively. During all of the simulations, the heave and pitch time histories of the vessel in question were recorded, free surface wave patterns were obtained and the free surface wave elevations in different locations alongside the ship model were monitored. The results will cover heave and pitch transfer functions (or Response Amplitude Operators, RAOs) of the vessel in question, covering a range of wave frequencies in various water depths.

This chapter is organised as follows: Section 6.2 gives the main ship properties along with its lines plan, and introduces a list of simulation cases applied to the current CFD model. Then, in Section 6.3, the numerical setup of the CFD model is explained, with details provided in the contained sub sections. Following this, all of the results from this work, including validation and verification studies, are shown and discussed in detail in Section 6.4. Finally, in Section 6.5, a summary of the research presented in this chapter is made.

6.2 Ship Geometry and Conditions

The ship motion simulations in shallow water were applied to the full-scale 200 kDWT class large tanker. Taking precedence from the experiments conducted by Oortmerssen (1976a, 1976b) and Pinkster (1980), the rudder, propeller and bilge keels were not appended to the model. The main particulars of the ship are presented in Table 6.1, and its body plan is shown in Figure 6.1 (Oortmerssen, 1976b, Pinkster, 1980). A three-dimensional view of the vessel is illustrated in Figure 6.2.

Table 6.1 Main properties of the 200 kDWT tanker (Oortmerssen, 1976b, Pinkster, 1980).

Length between perpendiculars (L_{BP})	310.00 m
Breadth (B)	47.17 m
Depth (D)	29.70 m
Loaded draft (T)	18.90 m
Displacement (Δ)	234,994 m^3
Block coefficient (C_B)	0.847
Midship section coefficient (C_M)	0.994
Prismatic coefficient (C_P)	0.855
Waterplane coefficient (C_{WP})	0.900
Ship wetted area (S)	22,804 m^2
Longitudinal centre of buoyancy (LCB) from the midship, fwd+	6.61 m
Vertical centre of gravity (KG) from the base line	13.32 m
Metacentric height (GM_t)	5.78 m
Transverse radius of gyration	17.00 m
Longitudinal radius of gyration	77.47 m

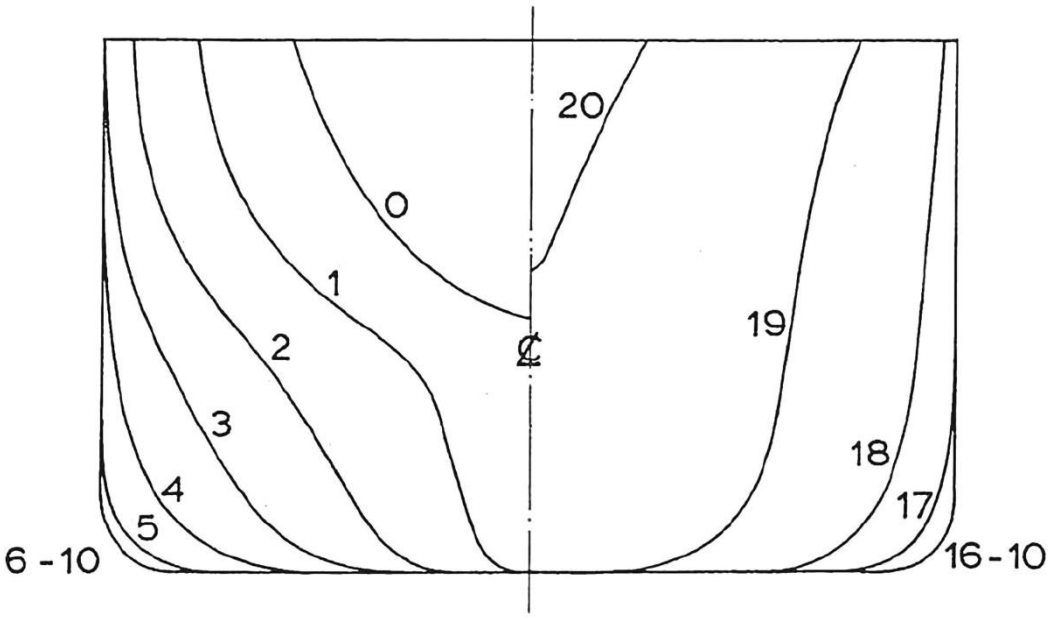

Figure 6.1 Body plan of the tanker, taken from Oortmerssen (1976b).

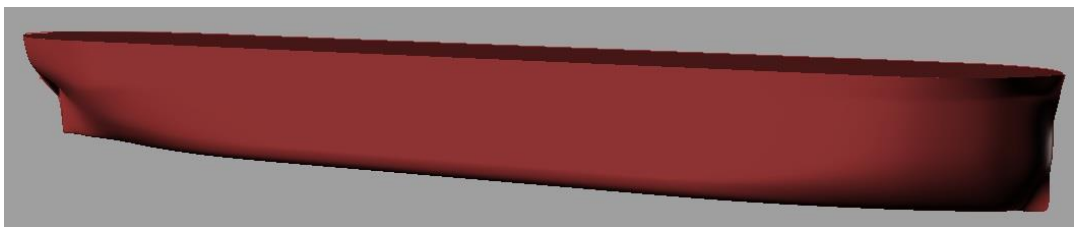

Figure 6.2 A 3-D view of the tanker, modelled using Rhinoceros version 4.0.

As waves approach a shore, they exhibit a reduction in wavelength (λ) and wave celerity (c), whilst the frequency remains the same. For a given wave period (T_w), the

wavelength is predicted according to the dispersion expression, which relates wave period to wavelength, as given in Equation (6.1), below.

$$T = \left[\frac{g}{2\pi\lambda} \tanh\left(\frac{2\pi h}{\lambda} \right) \right]^{-1/2} \quad \textbf{(6.1)}$$

where *h* denotes water depth. Heave and pitch RAO curves will be plotted against the nondimensional frequency numbers, $\omega' = \omega\sqrt{L/g}$ (L: Length between the perpendiculars in metres, ω: wave frequency in rad/s).

The CFD simulations were performed at sixteen different conditions, as listed in Table 6.2, each identified by their case numbers. The characteristics of a wave are determined depending on the relationship between wavelength and water depth. It should be mentioned that in all the cases, the ratios of water depth to wavelength (h/λ) are below the value of 1/2, which corresponds to shallow water waves. The wavelength of each simulation case was calculated using Equation (6.1). However, it should be borne in mind that Equation (6.1) is based on linear wave theory, and therefore the resulting wavelengths in the simulations will be different from those listed in Table 6.2. Having said that, the waves considered in this work are not steep waves, and hence this deviation is not expected to have a significant effect on the results.

The nondimensional period number (τ) shown in the last column of Table 6.2 was calculated by $\tau = T_w(g/h)^{1/2}$. As will be discussed in Section 6.3.2 in this chapter, this number is helpful when deciding which wave model should be used to model regular head waves within the computational domain.

Table 6.2 Cases for which the CFD model is applied.

Case no.	h/T	Wave frequency (rad/s)	Frequency number	Wave-length (m)	Wave-length/L_{BP}	Wave steepness	Period number
C	δ	ω	ω′	λ	λ/L_{BP}	H/ λ	τ
1.1	1.200	0.200	1.12	461.372	1.49	0.0118	20.66
1.2		0.300	1.69	301.539	0.97	0.0210	13.77
1.3		0.400	2.25	219.798	0.71	0.0222	10.33
1.4		0.500	2.81	163.301	0.53	0.0318	8.26
1.5		0.600	3.37	134.491	0.43	0.0333	6.89
2.1	3.000	0.200	1.12	712.292	2.30	0.0098	13.07
2.2		0.300	1.69	450.938	1.45	0.0140	8.71
2.3		0.400	2.25	313.347	1.01	0.0167	6.53
2.4		0.500	2.81	226.259	0.73	0.0199	5.23
2.5		0.600	3.37	166.535	0.54	0.0252	4.36
3.1	4.365	0.178	1.00	959.460	3.10	0.0071	12.17
3.2		0.267	1.50	602.305	1.94	0.0095	8.11
3.3		0.357	2.00	411.543	1.33	0.0139	6.07
3.4		0.443	2.50	295.753	0.95	0.0191	4.89
3.5		0.532	3.00	214.338	0.69	0.0188	4.07
3.6		0.623	3.50	158.342	1.49	0.0118	20.66

6.3 Numerical Modelling Set-Up

Up until this point, this chapter has provided a background to this study and has given an introduction to the work. The following section will provide details of the numerical simulation approaches used in this study and will discuss the numerical methods applied to the current CFD model.

6.3.1 Physics modelling

The same physics modelling, including the DFBI and VOF model, explained in detail in Chapter 5, Section 5.3.1, was used in this specific study. Also, a small time step (1/256 of the wave period) was used over a simulation period.

Figure 6.3 demonstrates how the free surface was represented in this CFD model by displaying the water volume fraction profile on the hull.

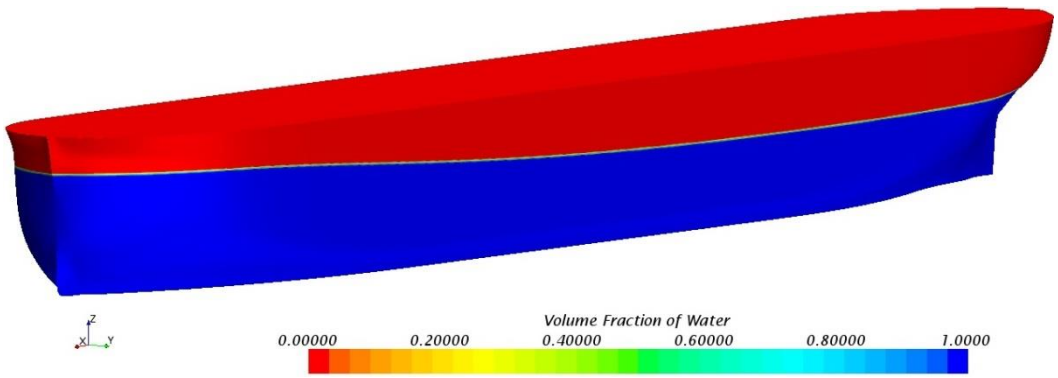

Figure 6.3 Free surface representation.

6.3.2 Wave model

The commercial RANS solver employed in this thesis offers two suitable wave theories to describe regular waves: the fifth-order or the first-order Stokes waves. Fenton (1985) points out that the fifth-order wave theory should not be used for large Ursell numbers (see Equation (6.2)). Det Norske Veritas (DNV) (2007) suggested that the fifth-order Stokes theory should only be applied to Ursell numbers less than 30. In addition, Fenton (1979) concluded in his study that for dimensionless period numbers greater than 8, the fifth-order Stokes wave theory should not be used, and that, instead, the fifth-order cnoidal wave theory should be used. Additionally, Fenton suggests the fifth-order Stokes waves should be used for nondimensional period numbers smaller than 8. Unfortunately, the RANS solver employed in this thesis does not provide the fifth-order 'cnoidal wave theory' to model incident waves and it is not possible to adjust the software package to model any other wave models. Given that linear wave theory can be used for all water depths, we used the first-order Stokes waves inside the solution domain for the cases with τ>8. For the other cases, the fifth-order Stokes waves were used to describe the wave at the inlet.

$$U_R = \frac{H\lambda^2}{h^3} \tag{6.2}$$

6.3.3 Solution domain and boundary conditions

An overset mesh, also known as Chimera or overlapping mesh, was used to facilitate the motions of the full-scale ship model due to the incident waves. As stated previously, when using the overset mesh feature, two different regions were created

to simulate ship responses in waves, namely background and overset regions. A general view of the computation domain with the tanker hull model and the notations of selected boundary conditions are depicted in Figure 6.4.

In order to reduce computational complexity and demand, only half of the hull (the starboard side) is represented. A symmetry plane forms the centreline domain face in order to accurately simulate the other half of the model. It should be noted that in some figures given in this chapter, the mirror image of the ship and domain is reflected on the port side for an improved visualisation.

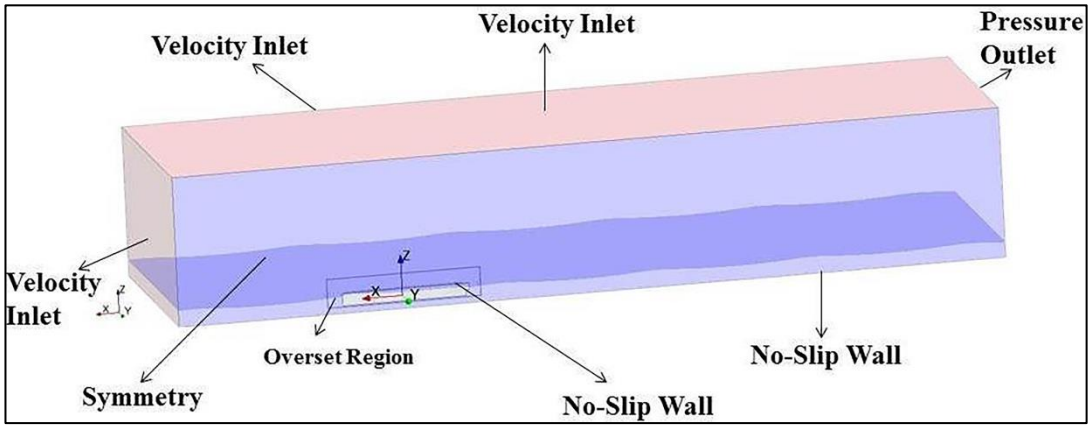

Figure 6.4 A general view of the background and overset regions and the applied boundary conditions.

Figure 6.4 depicts that a velocity inlet boundary condition was set in the positive x-direction, where incident regular waves were generated. The negative x-direction was modelled as a pressure outlet. The top boundary was selected as a velocity inlet, whereas the bottom boundary was selected as no-slip wall boundary condition to account for the presence of the sea floor. The symmetry plane, as the name suggests, has a symmetry condition, and the side of the domain (the negative y-direction) also has a velocity inlet boundary condition.

In this study, the size of the solution domain varied in each simulation case, depending on the wavelength of the incident waves. The locations of the boundaries used are illustrated in Figure 6.5, which gives front and side views of the domain. As shown in the figure, this author suggests that the inlet boundary should be positioned one wavelength or one and a half ship lengths, (whichever is greater), away from the vessel, so that waves can be appropriately generated before encountering the vessel.

Also, it should be highlighted that throughout all the cases, in order to prevent wave reflection from the walls, the VOF wave damping capability of the software package was applied to the background region with a damping length equal to at least one wavelength. This numerical beach model was used in downstream and transverse directions, as depicted in Figure 6.5. For the wave damping modelling, Star-CCM+ adopts the method developed by Choi and Yoon (2009).

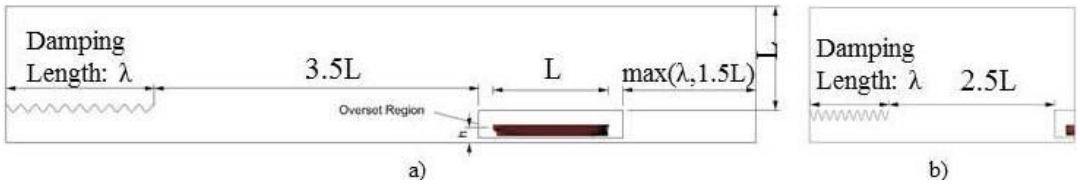

Figure 6.5 The dimensions of the computational domain for the seakeeping simulations a) Front view, b) Side view.

6.3.4 Mesh generation

Mesh generation was performed using the automatic meshing facility in Star-CCM+, resulting in a computation mesh of circa 14 million cells in total. A detailed description about the meshing features of the software package was given in Chapter 5.3.4.

Similar to the mesh generation given in the previous study, the computation mesh had areas of progressively refined mesh size in the area immediately around the hull, as well as the expected free surface. To simulate ship motions in waves, the free surface mesh was generated based on the guidelines for ship CFD applications from ITTC (2011b) and Kim and Lee (2011), which were discussed in detail in Chapter 5.3.4.

Figure 6.6 shows the surface mesh on the ship hull. Figure 6.7 displays the refined mesh area around the free surface regular waves. It should be noted that, for an improved visualisation, Figure 6.7 is scaled by a factor of 10 in the vertical direction.

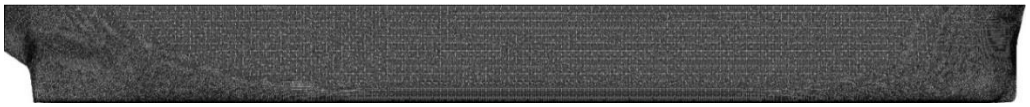

Figure 6.6 Surface mesh generated on the ship hull.

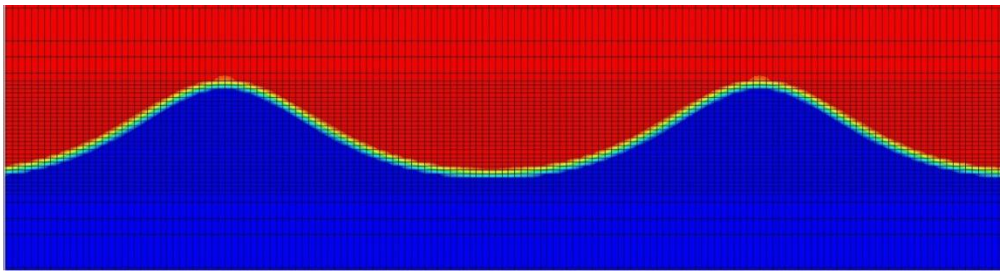

Figure 6.7 A cross-section of the refined mesh area around the free surface waves (scaled by a factor of 10 in the vertical direction).

In viscous fluids, there is a boundary layer on the body due to a no-slip boundary condition. This boundary layer should be meshed more finely, in order to capture the near wall flow accurately. This is crucial in calculating the forces and flow features such as separation. For this reason, a 'prism mesh model' was employed to allow the RANS solver to create orthogonal prismatic cells next to wall boundaries, which ensures a higher degree of accuracy can be achieved for the flow solution. Ideally, the prism layer thickness should be equal to that of the boundary layer. However, this leads to a huge increase in the mesh number, and hence in the computational time. Therefore, a compromise is made, and the prism layer thickness is determined such that the values of the 'non-dimensional wall distance' (y^+) remain below 1, or greater than 30. The reason for this is briefly explained below.

Along with the standard k-ε turbulence model, the 'all y^+ wall treatment' was adopted to resolve mean flow features (such as force, velocity, separation and species concentration) in turbulent boundary layers.

The all y^+ wall treatment is a hybrid model, which provides a more realistic approach than the low-Re or the high-Re treatments. To calculate shear stress, this wall treatment uses blended wall laws, which present a buffer region that suitably blends the laminar and turbulent regions together. The result is similar to the low-Re y^+ treatment as $y^+ \to 0$ and similar to the high-Re y^+ treatment for y^+ values greater than 30 (CD-Adapco, 2014). Since a full-scale ship model was used in the case of

this work, the y^+ values on the ship hull were high, particularly on the wetted surfaces. Figure 6.8, below, demonstrates a wall y^+ distribution on the hull, giving an average value of 32, for a representative simulation case after its run had completed.

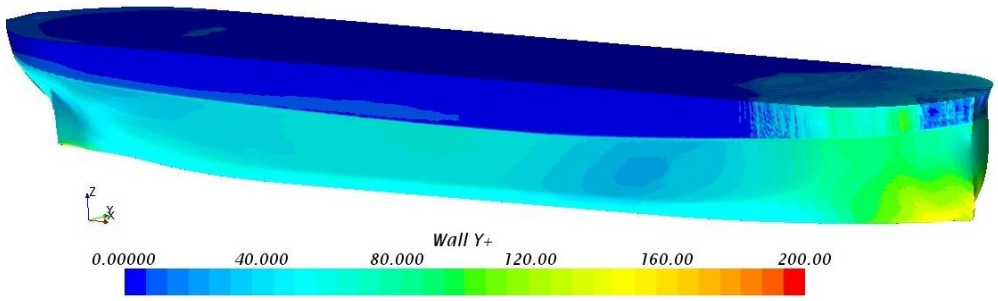

Figure 6.8 Wall y^+ distribution around the hull surface.

6.4 Results and Discussion

This section, consisting of four sub-sections, will first present a verification study. Next, an investigation in understanding the behaviour of waves in shallow water will be provided. Following this, it will outline the simulation results obtained during this study, including wave contours and transfer functions, and will also provide some comparison of the heave and pitch transfer functions with experimental results and the results from 3-D potential flow theory.

Taking precedence from previous numerical and experimental studies, we focused on the 1st order terms for the motion responses, as they are used for the calculation of transfer functions (for example see Troesch and Beck (1974), Oortmerssen (1976a) and Pinkster (1980)).

The heave transfer function was given in Equation (5.7). However, a different transfer function of pitch was used in this Chapter, as follows:

$$TF_5 = \frac{x_{51} L_{BP}}{\zeta_{I1}} \tag{6.3}$$

It must be clarified that in this chapter, the vertical motions were evaluated at the ship's centre of gravity.

6.4.1 Verification study

A verification study was undertaken to estimate the discretisation errors due to grid-size and time-step resolutions for Case 3.2 (h/T=4.364 and ω'=1.5). It is expected that the numerical uncertainties for the other cases are of the same order.

For estimating iterative errors, the procedure derived by Roy and Blottner (2001) was used. The results obtained from these calculations suggest that the iterative errors for the heave and pitch transfer functions were 0.200 and 0.195% of the solution for the finest grid-spacing and smallest time-step, respectively.

Grid-spacing and time-step convergence studies were carried out following the grid convergence index (GCI) method described in Celik et al. (2008). The convergence studies were performed with triple solutions using systematically refined grid-spacing or time-steps.

Detailed information about the four typical convergence conditions was given in Chapter 5, Section 5.4.1.5. For convergence conditions, the generalised Richardson Extrapolation method is applied to predict the error and order-of-accuracy (p_k) for the selected k^{th} input parameter (i.e. grid-size or time-step). For a constant refinement ratio (r_k), p_k can be calculated by:

$$p_k = \frac{\ln(\varepsilon_{k32} / \varepsilon_{k21})}{\ln(r_k)} \tag{6.4}$$

The extrapolated values can be calculated from Celik et al. (2008):

$$\phi_{ext}^{21} = (r_k^p \phi_1 - \phi_2) / (r_k^p - 1) \tag{6.5}$$

The approximate relative error and extrapolated relative error can then be calculated using Equations (6.6) and (6.7), respectively (Celik et al., 2008):

$$e_a^{21} = \left| \frac{\phi_1 - \phi_2}{\phi_1} \right| \tag{6.6}$$

$$e_{ext}^{21} = \left| \frac{\phi_{ext}^{12} - \phi_1}{\phi_{ext}^{12}} \right| \tag{6.7}$$

Finally, the fine-grid convergence index is predicted by:

$$GCI_{fine}^{21} = \frac{1.25e_a^{21}}{r_k^p - 1} \quad \textbf{(6.8)}$$

It should be borne in mind that Equations (6.4)-(6.8) are valid for a constant r_k value. Reference can be made to Celik et al. (2008) for the formulae valid for a non-constant refinement ratio. The notation style of this reference was used in this study in order to enable the verification results to be presented clearly.

For both the mesh-spacing and time-step convergence studies, a constant refinement ratio (r_G) was chosen to be $\sqrt{2}$ in this study. It is of importance to mention that during the mesh convergence study, the refinement ratio was applied only to the overset region, for the same reasons explained in Chapter 5, Section 5.4.1.5. Based on this mesh refinement ratio, the final mesh numbers for each mesh configuration are listed in Table 6.3. Similarly, the time-step convergence study was conducted with triple solutions using systematically lessened time-steps, starting from $\Delta t=T_w/2^8$.

Table 6.3 The final cell numbers for each mesh configuration as a result of the applied refinement ratio to the overset mesh region.

Mesh Configuration	Cell Number (N)		
	Background	Overset	Total
Fine	5,474,918	10,255,979	15,730,897
Medium	5,474,918	6,976,206	12,451,124
Coarse	5,474,918	3,434,465	8,909,383

The verification parameters of the trim, sinkage and the total resistance coefficients for the grid spacing and time-step convergence studies are presented in Table 6.4 and Table 6.5, respectively.

Table 6.4 Grid convergence study for the heave and pitch TFs.

	TF_3 (*with monotonic convergence*)	TF_5 (*with monotonic convergence*)
r	$\sqrt{2}$	$\sqrt{2}$
φ_1	0.683	2.619
φ_2	0.694	2.636
φ_3	0.715	2.658
R	0.524	0.787
p	1.866	0.69
φ_{ext}^{21}	0.671	2.556
e_a^{21}	1.61%	0.649%
e_{ext}^{21}	1.80%	2.46%
GCI_{fine}^{21}	2.21%	3.00%

Table 6.5 Time-step convergence study for the heave and pitch TFs.

	TF_3 (*with monotonic convergence*)	TF_5 (*with monotonic convergence*)
r	$\sqrt{2}$	$\sqrt{2}$
φ_1	0.683	2.619
φ_2	0.692	2.634
φ_3	0.711	2.655
R	0.474	0.714
p	2.156	0.971
φ_{ext}^{21}	0.6749	2.5815
e_a^{21}	1.32%	0.57%
e_{ext}^{21}	1.20%	1.45%
GCI_{fine}^{21}	1.48%	1.79%

As can be seen from Table 6.4 and Table 6.5, reasonably small levels of uncertainty were estimated for the obtained parameters. The numerical uncertainties in the finest-grid solution for TF_3 and TF_5 are predicted as 2.21% and 3.00%, respectively (Table 6.4). These values reduce to 1.48% and 1.78%, respectively, when calculating the numerical uncertainty in the smallest time-step solution (Table 6.5). It can be interpreted that the very small uncertainty results for the time-step convergence study are due to the selection of very small time-step resolutions in the simulations. Also, it is obvious that the pitch transfer function is more sensitive to the grid-spacing compared to the heave transfer function.

It may be interesting to note that these GCI values obtained from both grid-spacing and time-step convergence studies were slightly higher than those obtained in the

previous chapter (see Table 5.8 and Table 5.9). In order words, this explicitly implies that the CFD uncertainties for ship motion simulations in shallow water are slightly higher than ship motion simulations in deep water.

6.4.2 Wave generation

Understanding the behaviour of nonlinear shallow water waves is critical not only for coastal structures, but for CFD standing points as well. From a CFD point of view, the area in the domain where the free surface is expected should be predicted, in order to mesh this area more finely. In this work, a series of simulations was therefore performed to observe the wave form throughout the solution domain, before starting the fundamental ship motion simulations in shallow water. To do this, the overset region, including the ship model, was omitted, leaving only the background domain, which is demonstrated in Figure 6.4. In this specific study, the numerical damping was only applied in the downstream direction in the computational domain. It should also be mentioned that a second-order temporal scheme was applied in order to conduct this study on waves.

Troesch and Beck (1974) also performed such wave analyses experimentally before conducting seakeeping experiments with a ship model in shallow water, concluding that, "*sinusoidal waves in shallow water are unstable and will degenerate fairly rapidly. In order to conduct the ship motion experiments, a knowledge of this process is essential*". Also, many years ago, Korteweg and Vries (1895) theoretically investigated nonlinear shallow water problems. Their study particularly focused on the change of form of long waves advancing in a rectangular canal, by using a perturbation expansion on particle velocities, which has since borne their name in the literature.

Firstly, the degeneration of the shallow water waves as they advance inside the domain was investigated in a similar way to the experiments of Troesch and Beck (1974). For each three water depth conditions (δ=1.2, 3.0 and 4.365), the first harmonic amplitudes of a fifth-order Stokes wave (T_w=12.133 s) as a function of distance down the inlet were calculated, aided by wave probes located at various distances from the inlet. The results obtained are demonstrated graphically in Figure

6.9. In the figure, the harmonic amplitudes were divided by the calculated wave amplitude at the inlet (ζ_o), and the distances (X) were non-dimensionalised with respect to the actual wavelength (λ).

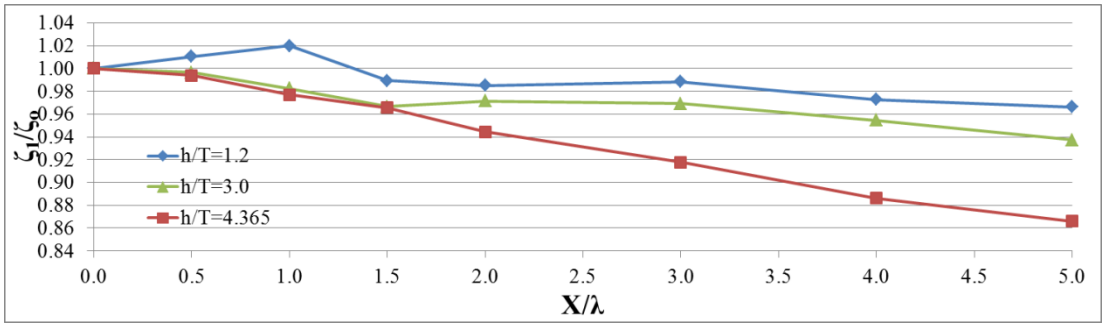

Figure 6.9 Nondimensional 1st FS harmonic amplitudes plotted against nondimensional distance from the inlet at various water depth conditions (T_w=14.183 s).

The results presented in Figure 6.9 show that the first FS harmonic wave amplitudes increase at the beginning, and then decrease as the wave travels through the domain. As can be observed from the figure, the variation in wave amplitudes is most pronounced at Wave 3 (δ=4.365), followed by Wave 2 (δ=3.0). This is because Wave 3 has the longest wavelength amongst the three studied waves. It should be borne in mind that the period number of Wave 1 (δ=1.2) is 7.98, a value where the fifth-order wave theory is still applicable.

As discussed above, the 1st harmonic wave amplitudes varied along the simulation domain length. Therefore, for each simulation case, an average was taken of the wave amplitudes measured at three wave probes, located along the ship's length, to be used in the calculation of the transfer functions (see Equations (5.7) and (6.3)).

Figure 6.10 shows a comparison of the waves generated inside the domain (just after the symmetry plane) at different water depths. This figure also compares the appearances of the first- and fifth-order waves simulated at a water depth of 22.68 m. In addition to this, Figure 6.11 displays the free surface elevations at a distance of one wavelength away from the inlet, obtained using the first- and fifth-order Stokes wave theories. Wave 1 was used to provide the comparison shown in Figure 6.11.

Figure 6.10 and Figure 6.11 jointly confirm that the resulting wave shape, obtained using the first-order wave theory, is different from the sinusoidal wave form. It is obvious that the obtained wave shape is degenerated as it propagates down the inlet.

This result is in agreement with the experimental findings of Troesch and Beck (1974). From the comparison of the first- and fifth-order wave theories provided in Figure 6.10 and Figure 6.11 in the shallowest water, it can be concluded that the simulated waves obtained using the fifth-order theory give more successful results compared to those using the first-order wave theory.

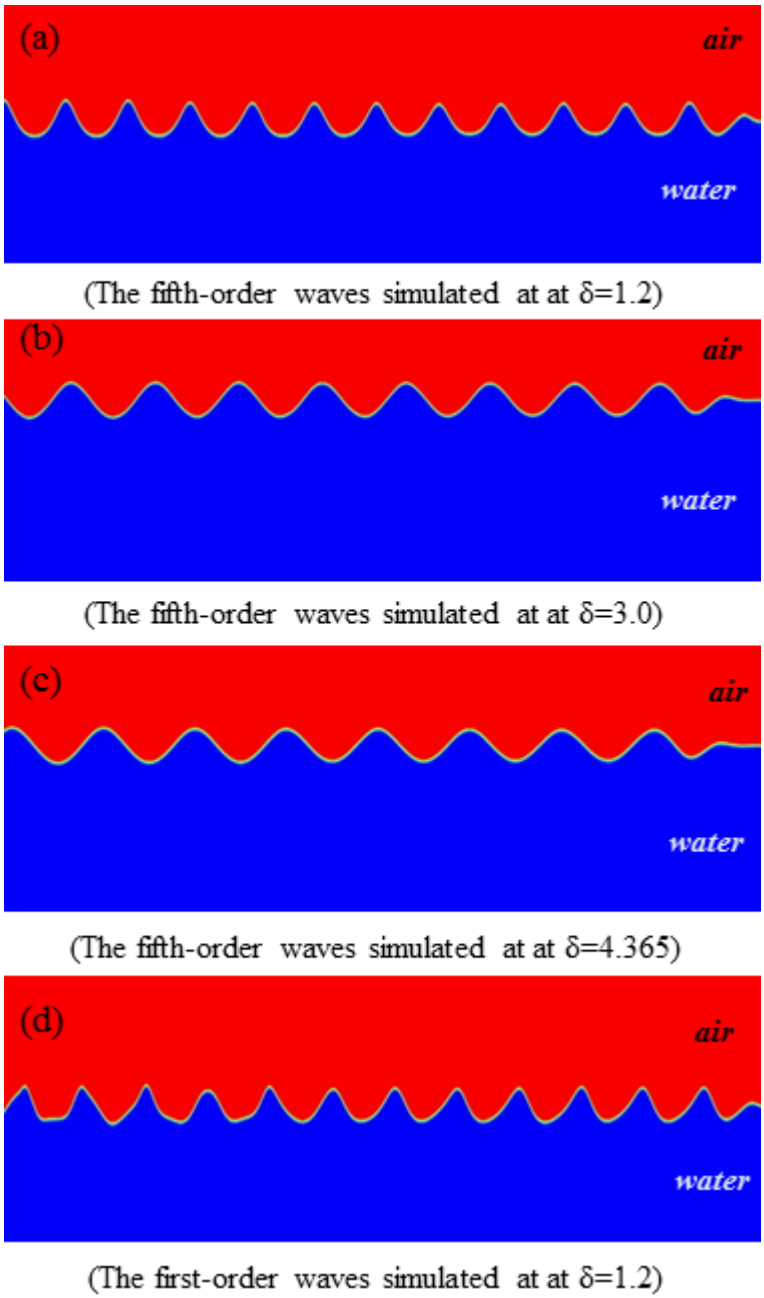

Figure 6.10 A front view of the cross-sections of the simulation domain (just after the symmetry plane) with the waves (T_w=12.133 s, H=5.66 m) generated inside the domain (scaled by a factor of 20 in the vertical direction).

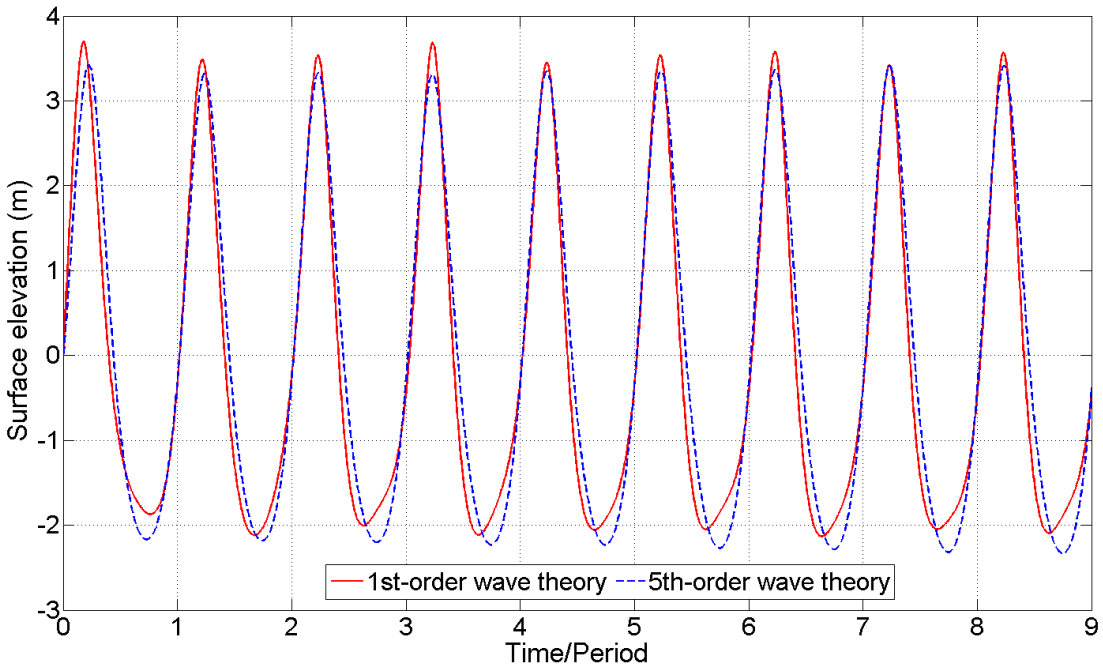

Figure 6.11 Comparison of shallow water waves (T_w=12.133 s, τ=7.98) simulated using the first- and fifth-order Stokes wave theories at a water depth of 22.68 m at one wavelength away from the inlet.

6.4.3 Wave contours

In this sub-section, wave contours generated by the presence of the ship model freely heaving and pitching around a free surface will be presented.

Figure **6.12** illustrates the wave patterns around the tanker in question generated by unit wave amplitude at a water depth of 22.68 m, for various non-dimensional frequencies (ω'=1.12, 1.69 and 2.25). As can be seen from the figure, as the waves become shorter, (in other words as the celerity of waves decrease), the wave contours become densely massed.

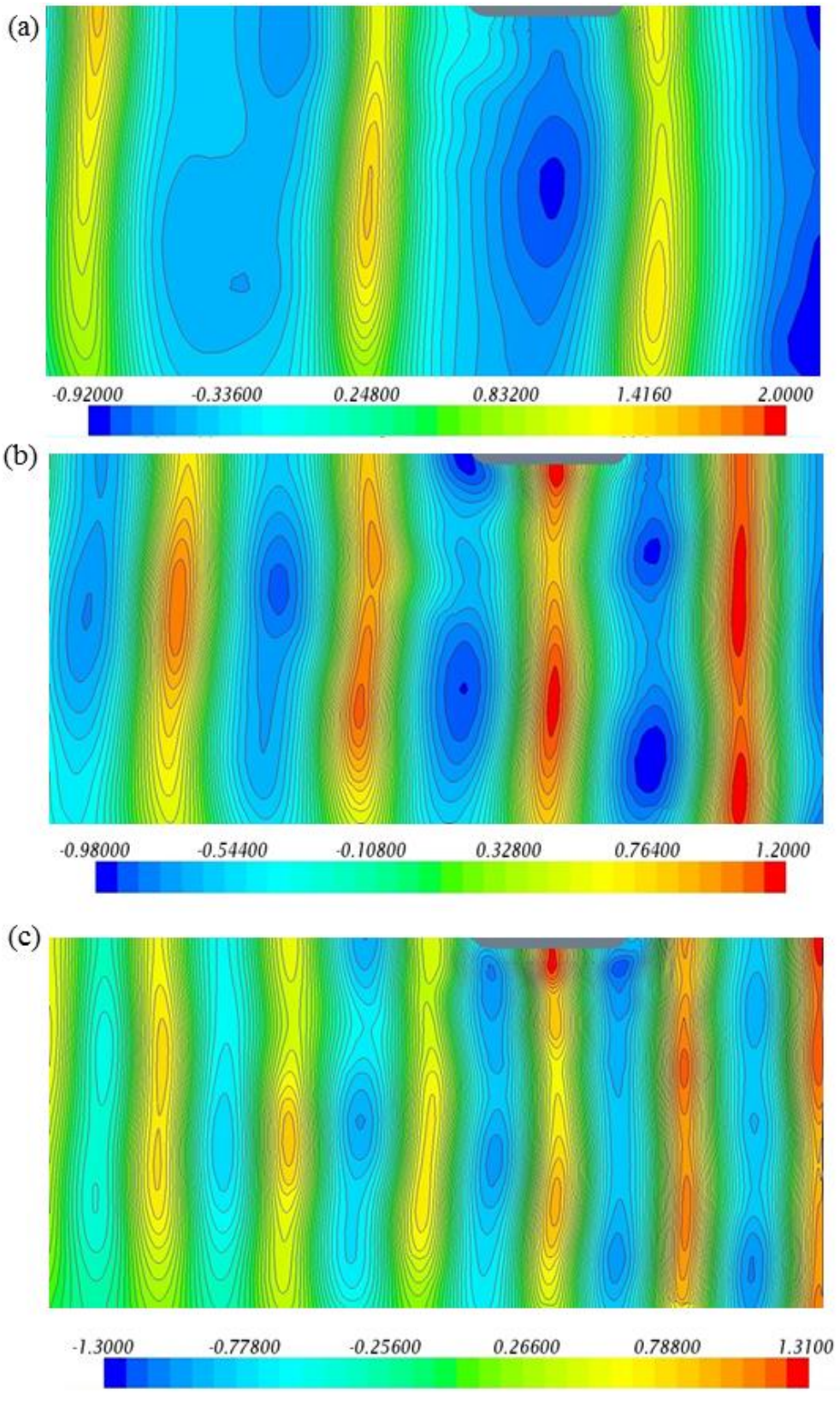

Figure 6.12 Comparison of instantaneous wave patterns generated around the vessel by unit wave amplitude at a water depth of 22.68 m, for various non-dimensional frequencies (a) ω'=1.12, (b) ω'=1.69, (c) ω'=2.25.

6.4.4 Transfer functions

Having performed the necessary verification studies, the transfer functions obtained for all cases will be provided in this sub-section.

The heave and pitch transfer functions obtained by the current CFD model were first validated against the experimental work of Oortmerssen (1976a, 1976b) and Pinkster (1980), and were also compared to those obtained using a potential flow panel method for the two water depth conditions, namely δ=1.2 and 4.365, respectively. The panel methods used in this comparison were developed by the same researchers, who used a 3-D Green function to satisfy free surface and radiation conditions in the frequency domain. The results from the potential flow panel method were adapted from the published studies of the abovementioned researchers. For more details on these numerical methods, reference may be made to Oortmerssen (1976a, 1976b) and Pinkster (1980).

For the two water depth conditions, the heave and pitch transfer functions obtained by all three methods are graphically compared in Figure 6.13 and Figure 6.14, below.

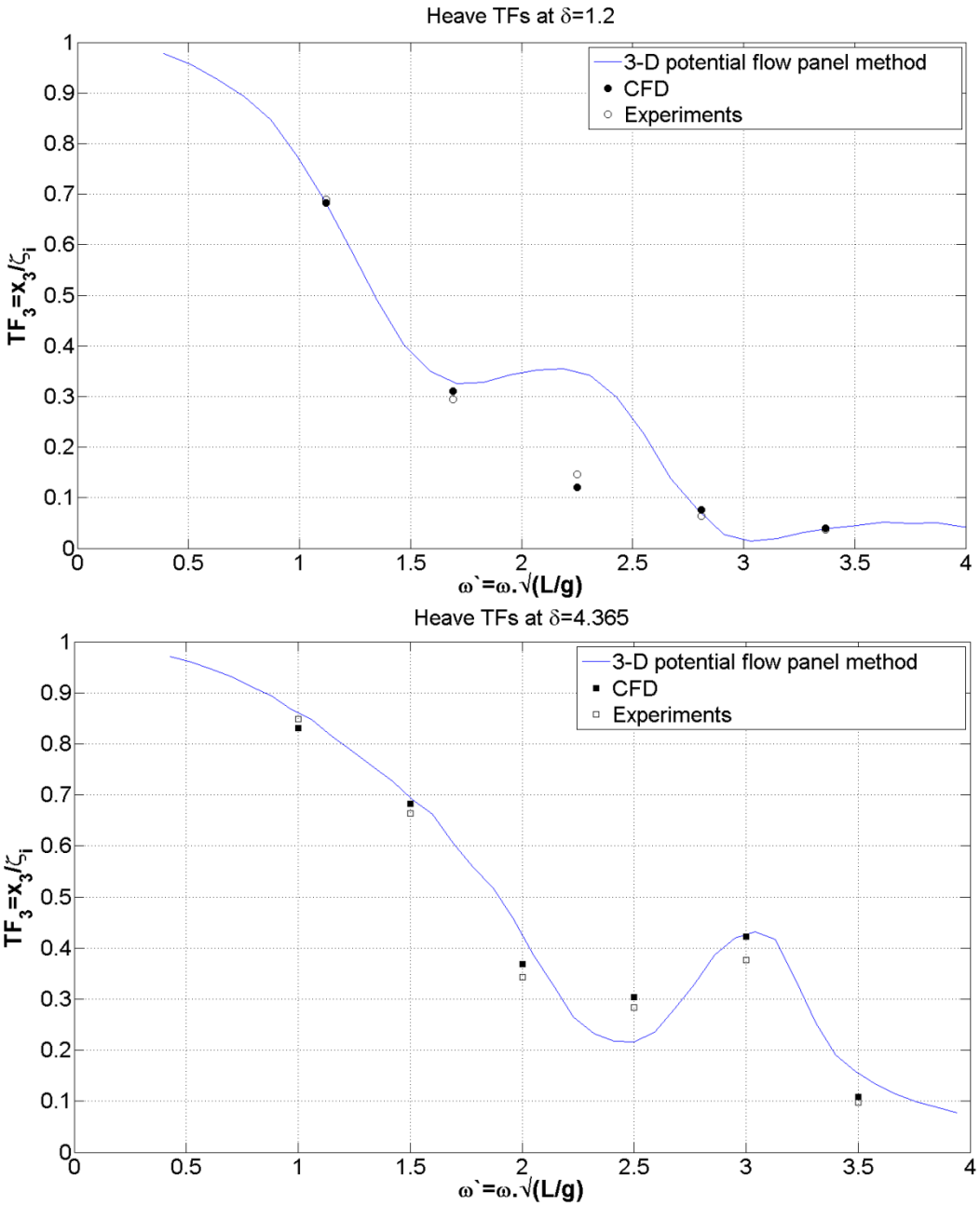

Figure 6.13 Comparisons of the heave transfer functions using different methods in two different shallow water depths at zero speed. The upper half shows the responses at δ=1.2, and the lower half shows the responses at δ=4.365.

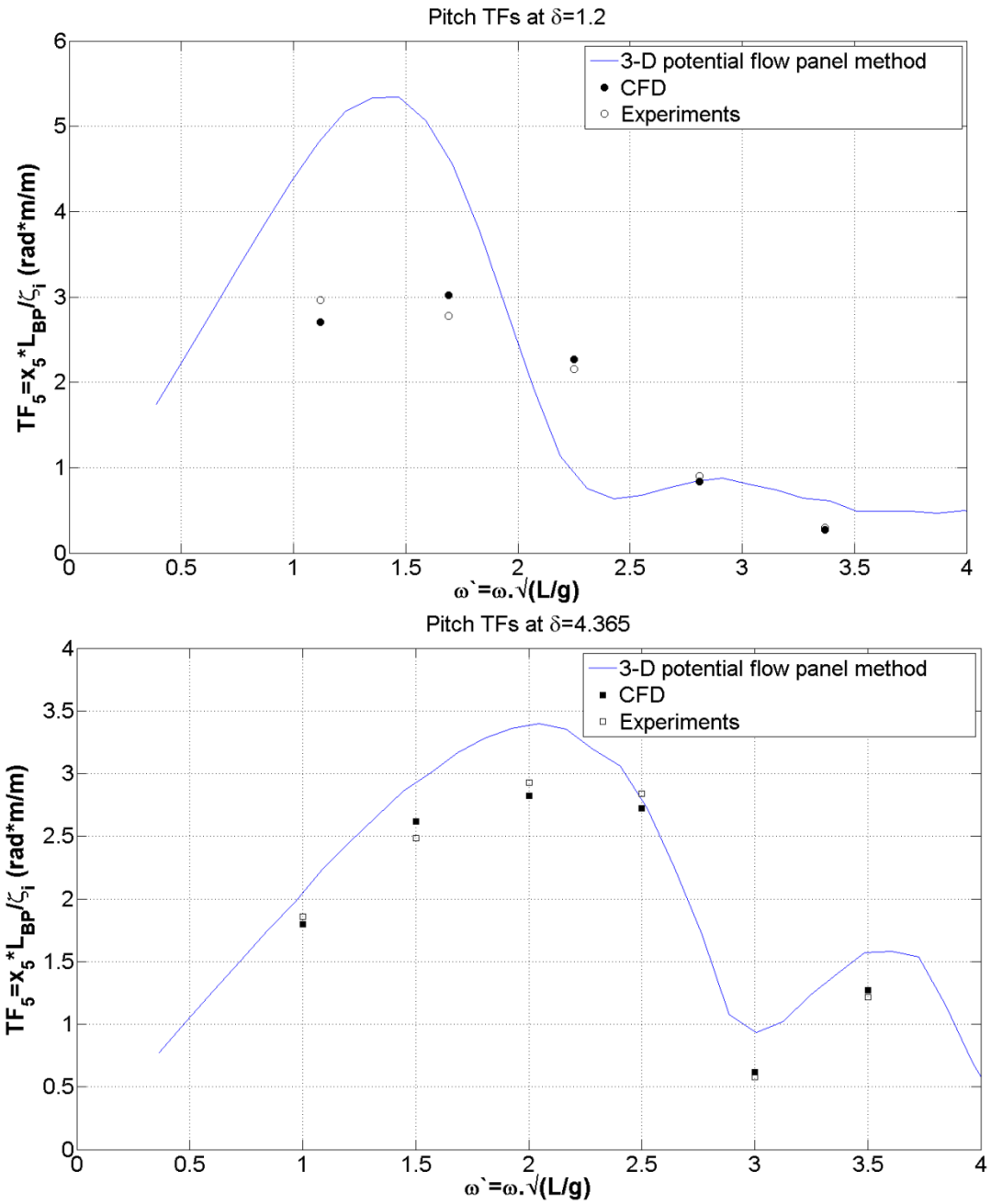

Figure 6.14 Comparison of the pitch transfer functions using different methods in two different shallow water depths at zero speed. The upper half shows the responses at δ=1.2, and the lower half shows the responses at δ=4.365.

As can be seen from Figure 6.13 and Figure 6.14, the transfer functions, obtained using this unsteady RANS approach, are in fairly good agreement with the related experimental results. The discrepancies between this study's numerical results and the experimental results are more pronounced for pitch at δ=1.2, which corresponds to the shallowest water condition. Since the keel is very close to the sea bed in this condition, a much finer mesh may have been needed to better capture the hydrodynamic effects between the keel and the sea floor. Additionally, it is clearly

visible from the figures that in both motion modes the potential flow panel methods over-predict the motion responses compared to the experiments. When the CFD results are compared to those obtained from the panel methods, it can be concluded that the CFD method predicts the motion responses much better than potential flow theory, particularly for pitch motion. It should be mentioned that the differences between the experimental results and the panel methods may stem from the coarse panel generation and the assumptions made in the potential flow theory. It should also be borne in mind that the most recently developed 3-D potential flow theory-based codes, such as the Rankine source panel methods, may give more successful motion predictions than those presented in this chapter.

It may be useful to emphasise that since this chapter's simulations were performed at Fn=0, the problem considered in this study was essentially close to the potential flow problem. It is highly likely that the viscous effects would be much more significant if the vessel had a high forward speed.

Once the current unsteady RANS method was successfully validated, another set of simulations were repeated at δ=3.0, in order to more precisely assess the effect of water depth on ship motions.

For all three water depths, the heave and pitch responses, predicted using this study's CFD model, were compared in Figure 6.15, over the non-dimensional wave frequencies. For each combination of transfer function and water depth, a curve was fitted through the obtained results using a Piecewise Cubic Hermite Interpolating Polynomial, in order to provide a better comparison among the responses.

From the comparison shown in Figure 6.15, it is clear to note that as the water depth becomes shallower, the heave amplitudes tend to decrease, whereas the pitch amplitudes tend to increase at low frequencies (or in long incident waves). However at high frequencies, a slight decrease is recognised in pitch responses as the water depth decreases. It can also be seen that, for this tanker model, the maximum pitch response occurs when the ratio between wavelength and ship length (λ/L) is around 1.0. Therefore, it is observed that when the water depth to the draft ratio decreases, the peak in the pitch transfer functions shifts towards the lower frequencies. It is also

worth noting that the RAO curves in Figure 6.15 show the same trend as those presented by Kim and Kim (2013), who, as explained earlier, carried out similar analyses for a 100-metre Series 60 ship model using the 3-D Rankine panel method.

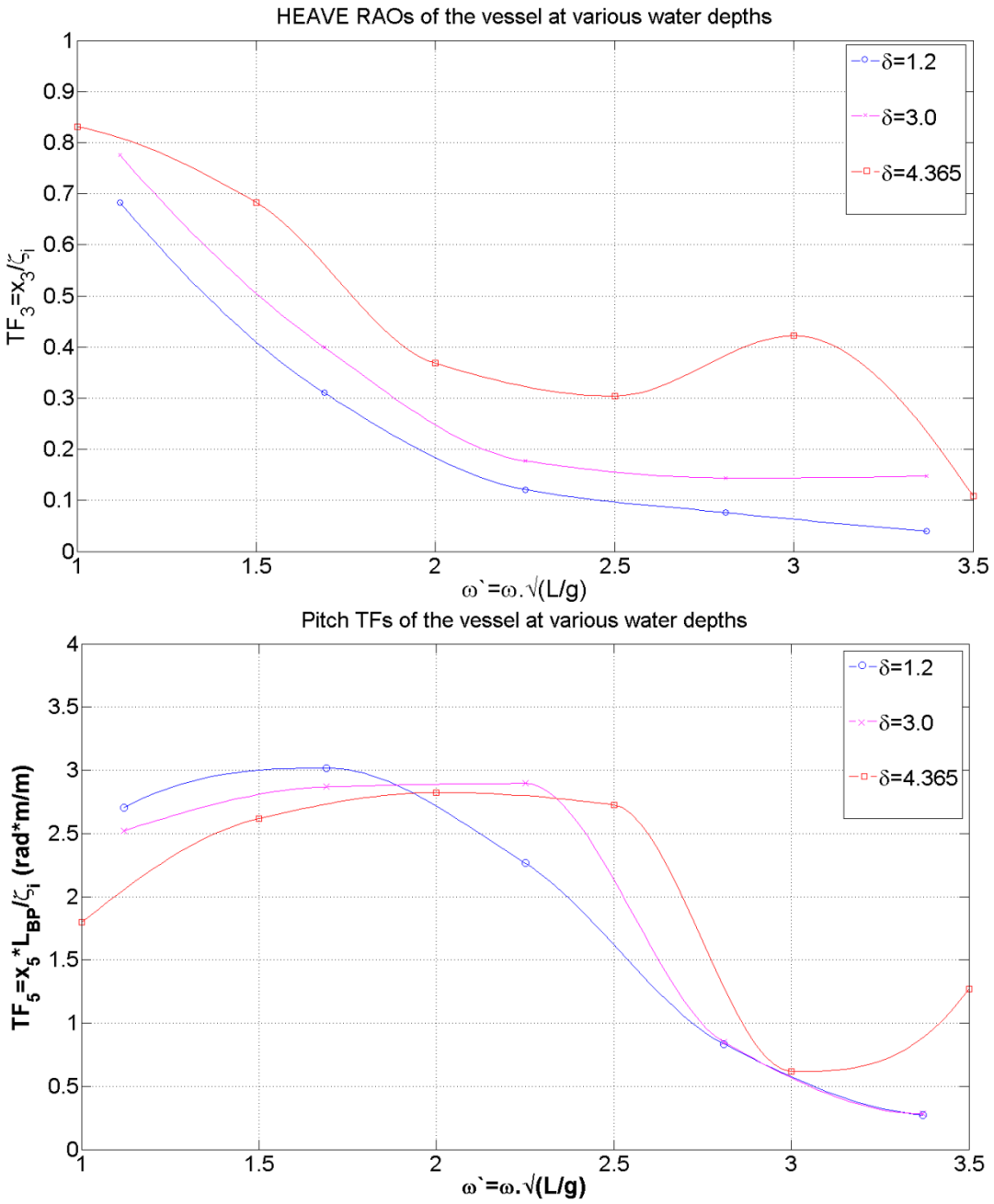

Figure 6.15 A comparison of the ship responses (obtained using CFD) to incident head waves over the nondimensional frequency numbers in the three different shallow waters. The upper and lower halves show the heave and pitch transfer functions of the tanker, respectively.

Aside from presenting the results graphically, the heave and pitch transfer functions predicted by CFD, EFD and potential flow theory at three different h/T ratios are

tabulated in Table 6.6, in order to provide a distinctive comparison among the different methods.

Table 6.6 The transfer functions by three different methods (Error (E) is based on EFD data).

Case No.	h/T	TF_3					TF_5				
		CFD		EFD	Potential Flow Theory		CFD		EFD	Potential Flow Theory	
C	δ	Result	E (%)		Result	E (%)	Result	E (%)		Result	E (%)
1.1	1.2	0.682	**-1.01**	0.689	0.685	**-0.50**	2.705	**-8.72**	2.964	4.845	**63.49**
1.2		0.310	**5.16**	0.294	0.328	**11.44**	3.017	**8.78**	2.774	4.608	**66.12**
1.3		0.121	**-16.97**	0.146	0.352	**140.78**	2.266	**5.18**	2.154	0.925	**-57.05**
1.4		0.076	**19.28**	0.064	0.055	**-14.53**	0.833	**-7.50**	0.901	0.845	**-6.16**
1.5		0.040	**9.21**	0.037	0.033	**-9.23**	0.274	**-7.94**	0.297	0.645	**116.88**
2.1	3	0.775	-	-	-	-	2.521	-	-	-	-
2.2		0.399	-	-	-	-	2.868	-	-	-	-
2.3		0.177	-	-	-	-	2.895	-	-	-	-
2.4		0.144	-	-	-	-	0.849	-	-	-	-
2.5		0.148	-	-	-	-	0.281	-	-	-	-
3.1	4.365	0.831	**-2.20**	0.849	0.857	**0.93**	1.796	**-3.38**	1.859	1.887	**1.52**
3.2		0.683	**2.84**	0.664	0.692	**4.16**	2.619	**5.43**	2.484	2.930	**17.97**
3.3		0.368	**7.25**	0.343	0.408	**19.21**	2.824	**-3.49**	2.926	3.432	**17.32**
3.4		0.304	**7.28**	0.284	0.246	**-13.41**	2.725	**-4.08**	2.841	2.778	**-2.23**
3.5		0.422	**11.88**	0.377	0.432	**14.49**	0.617	**6.17**	0.581	0.932	**60.50**
3.6		0.108	**9.83**	0.098	0.153	**55.25**	1.271	**4.77**	1.214	1.545	**27.33**

As can be seen from Table 6.6, except for a few simulation cases, the current CFD model predicts the heave and pitch responses of the vessel in shallow water within circa 10% of the experiments. As the table agrees, this ratio is much smaller than the potential flow theory-based code's predictions. It should be mentioned that the data under the 'potential flow theory' column in the table were read from the related figures published in Oortmerssen (1976a, 1976b) and Pinkster (1980) using a software package. The potential flow theory's results therefore reflect an approximate set of data.

6.5 Concluding Remarks

Fully nonlinear unsteady RANS simulations, to predict the heave and pitch responses of a full scale very large tanker model to incident head waves, were carried out at a zero forward speed.

Firstly, the numerical modelling set up introduced in Chapter 5 was altered, in order to perform such analyses in shallow water using CFD. All procedures regarding mesh generation, treatment of wall functions, time step selection and wave modelling were presented in detail in this chapter.

Next, a verification study was carried out to assess the uncertainties of the CFD model. The results obtained from this study suggested that the numerical uncertainties in the finest-grid solution for the heave and pitch transfer functions are predicted as 2.21% and 3.00%, respectively. These values become 1.48% and 1.78%, respectively, when the numerical uncertainty in the smallest time-step solution is predicted.

Following this, before beginning the seakeeping analyses, a series of simulations were performed with nonlinear shallow water waves, to observe the change in their form inside the computational domain. It was observed that the wave amplitudes mostly decrease as the waves propagate further down inside the domain. Also, additional simulations with the waves revealed that the waves simulated using the fifth-order theory give more successful results compared to those simulated using the first-order wave theory.

Then, sixteen simulation cases, which were composed of various combinations of water depth and wave frequency, were applied to the tanker model. The results were compared to the experimental data and also to those obtained from potential flow panel methods. The main results drawn from this comparison can be listed as follows:

i. The transfer functions, obtained using the CFD method, predicted the transfer functions of the vessel within approximately 10% of the experimental data, except for a few cases. The differences between the results obtained from this work and the experimental results were slightly more pronounced at δ=1.2, where the keel is closest to the sea bed. Also, it was obvious that the 3-D panel methods over-predict the heave and pitch transfer functions compared to the experimental results. Overall, the unsteady RANS method predicted the

motion responses much more successfully than potential flow theory, particularly for pitch motions.

ii. It was concluded that as water becomes shallower, heave motions decrease, whilst pitch motions increase at low frequencies. On the other hand, at high frequencies, a slight decrease was observed in pitch responses as the water depth decreases.

iii. For the tanker model in question, the maximum pitch response occurred in waves of length equal to, or around, the ship length ($\lambda/L=1.0$). It was observed that when the water depth decreased, the peak in the pitch transfer functions shifted to lower frequencies.

7. A NUMERICAL INVESTIGATION OF THE SQUAT AND RESISTANCE OF SHIPS ADVANCING THROUGH A CANAL USING CFD

7.1 Introduction

As a ship approaches shallow water, a number of changes arise due to the hydrodynamic interaction between the bottom of the ship's hull and the sea bed. The flow velocity between the bottom of the hull and the sea floor increases, which produces a downward vertical force and a moment about the transverse axis. This phenomenon leads to an increase in sinkage, trim and resistance of the vessel. As the ship travels forward, squat of the ship may occur, stemming from this increase in sinkage and trim (Tuck, 1978).

There are three main parameters governing ship squat; namely a ship's speed, its block coefficient and the blockage factor (Briggs, 2006). There is a quadratic relationship between a ship's forward speed and a ship's squat. In other words, the magnitude of a ship's squat is approximately proportional to the square of the ship's speed. As reported in Briggs (2006), squat typically occurs when a ship's forward speed is greater than 6 knots. The block coefficient is another critical parameter which directly affects squat. Full-form ships commonly undergo more squat than fine-form ships. For example, oil tankers undergo more squat compared to fine-form ships, such as passenger ships . The blockage factor (S) is another important factor influencing ship squat. This term can be defined as the ratio of the underwater cross-section of the ship's midship section to the cross-section of the canal or river, as depicted in Figure 7.1. By definition, S can be formulised as given in Equation (7.1).

$$S = \frac{bxT}{Bxh} \tag{7.1}$$

where b is the breadth of the ship, T is the ship's even-keel static draft, B is the breadth of the river or canal and h is the depth of the water, as illustrated in Figure 7.1.

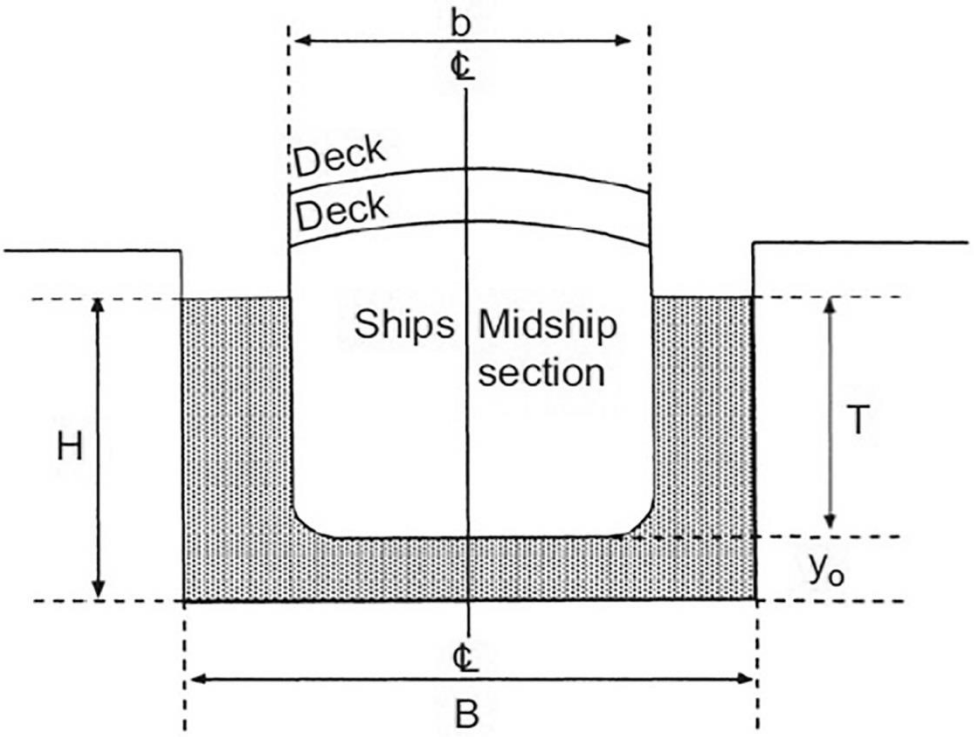

Figure 7.1 Ship in a canal in its static condition, taken from Barrass and Derrett (2012)**.**

Recently, a rapid increase has been seen in the size and number of large ships (such as container ships and tankers) operating worldwide. Owing to this increase, there has been significant interest in the hydrodynamics of these large ships in restricted waters (Beck et al., 1975). Similarly, Barrass and Derrett (2012) claim that ship squat has been an increasing problem for the last 40 years, due to continuing developments in ship size and increases in service speed. For example, super tankers above 350,000 DWT are becoming more commonplace nowadays. When these super tankers visit ports or pass through channels/canals, they have relatively small underkeel clearances of 1.0-1.5 m. A key responsibility of ship masters is therefore to operate the vessel with consideration given to the underkeel clearance. Additionally, as stated in Barrass and Derrett (2012), the speed of container ships has steadily increased in

recent years from 16 knots to 25 knots, which causes an increase in squat, and hence a risk of grounding.

Knowledge of a ship's squat is necessary when navigating vessels through shallow water regions, such as rivers, channels and harbours. Accurate prediction of a ship's squat is therefore essential, to minimise the risk of grounding for ships. Barrass and Derrett (2012) point out that more than 117 ships have recently been reported as grounded, owing to enormous squat and other reasons.

Similarly, predicting a ship's resistance in shallow water is equally important, to be able to calculate its power requirements. As reported in Barrass and Derrett (2012), when a ship has entered shallow water conditions, a reduction in her speed may be observed. This reduction may be as much as 30% if she is travelling in open water. If the vessel travels through a confined channel such as river or a canal, this reduction may rise to 60%. It should be noted that this reduction in speed is not only due to the increase in resistance, but also due to the change in the manoeuvring features of the vessel due to it entering a shallow water area.

The literature offers various approaches to predict the squat and resistance of ships in shallow water. These methods comprise empirical or analytical investigations and experiments. The analytical methods mainly use the assumptions from potential flow theory, presuming the ship to be a slender body. The empirical formulae also have certain constraints and conditions to be satisfied before they can be applied. In addition, conducting towing tank experiments may be costly and time-consuming. On the other hand, CFD techniques are easily capable of predicting the trim, sinkage and resistance of a vessel in shallow water, incorporating both viscous and nonlinear effects in the flow and free surface.

As can be seen from the literature survey presented in Chapter 2, Section 2.8, the theories developed to calculate ship squat in shallow water commonly use linear theory for calculating the flow around a ship. This may be a reasonable approach, as most of the methods are based on the slender-body assumption. Gourlay (2008b) points out the fact that although nonlinearity does not have a major effect on sinkage and trim for slender ships, nonlinearity becomes more significant for larger ships,

such as container ships and bulk carriers. A container ship model was therefore selected as a real case study in this particular study.

The key objective of this study is to perform fully nonlinear unsteady RANS simulations to predict the sinkage and resistance of a model scale Duisburg Test Case (DTC) container ship advancing in a canal. The model was run in calm water conditions free in trim and sinkage. The analyses were carried out in three different ship draughts at various speeds. In each run, sinkage time histories at the ship's centre of gravity, and the frictional and residual drag force time histories acting on the vessel were recorded. The squat results obtained by CFD were then compared with the experimental work of Uliczka (2010).

This chapter describes how to calculate the ship squat and resistance of a vessel advancing through a canal, using a CFD software package. This study aims to predict ship squat with more accuracy than current methods in the literature. An additional purpose of this study is to obtain the frictional and residual resistance coefficients of the vessel, for various draft and speed combinations.

This chapter is organised as follows: Section 7.2 gives the main ship properties and the cross-section of the canal along with its dimensions. Later, a list of the simulation cases which the current CFD model is applied to is presented in detail in Section 7.3. Afterwards, in Section 7.4, the numerical setup of the CFD model is explained, with details provided in the contained sub-sections. Next, all of the results from this work, including the necessary validation and verification studies, are demonstrated and discussed in Section 7.5. Finally, in Section 7.6, a summary of the chapter is provided.

7.2 Ship Geometry and Cross Section of the Canal

The Duisburg Test Case is a typical 14,000 TEU container ship, developed by the Institute of Ship Technology, Ocean Engineering and Transport Systems (ISMT) in Duisburg for benchmarking purposes. There is a wide range of experimental and simulation data available for comparison and validation. Also, its 3-D hull geometry with all of its appendages can be readily found in the public domain (El Moctar et al., 2012). Moreover, in September 2013, a workshop on the numerical prediction of the

squat of ships in shallow and restricted water regions (named PreSquat) was jointly organised by the University of Duisburg-Essen, the Federal Waterways Engineering and Research Institute (BAW) and Germanischer Lloyd (GL) in Mulheim, Germany. The workshop aimed to gauge the efficiency of numerical methods for squat prediction via comparison with the available experimental data (Mucha et al., 2014). The DTC container ship model was therefore used in this work as a case study, owing to its readily available geometric data, and numerical and experimental results.

Table 7.1 Full scale and model scale DTC ship properties (El Moctar et al., 2012).

Property	Ship	Model (1:40)
Length between the perpendiculars (L_{BP})	355 m	8.875 m
Beam at waterline (B_{WL})	51 m	1.275 m
Design draft (T)	14.5 m	0.3525 m
Displacement (Δ)	173,814.762 m^3	2.716 m^3
Block coefficient (C_B)	0.661	0.661
Ship wetted area with rudder and propeller (S)	22352 m^2	13.970 m^2
Longitudinal center of buoyancy (LCB) from the aft peak	174.531 m	4.363 m
Vertical center of gravity (KG) from keel	23.28 m	0.582 m
Metacentric height (GM_t)	1.677 m	0.042 m
Moment of inertia (K_{xx}/B)	0.40	0.40
Moment of inertia (K_{yy}/L_{BP}, K_{zz}/L_{BP})	0.25	0.25

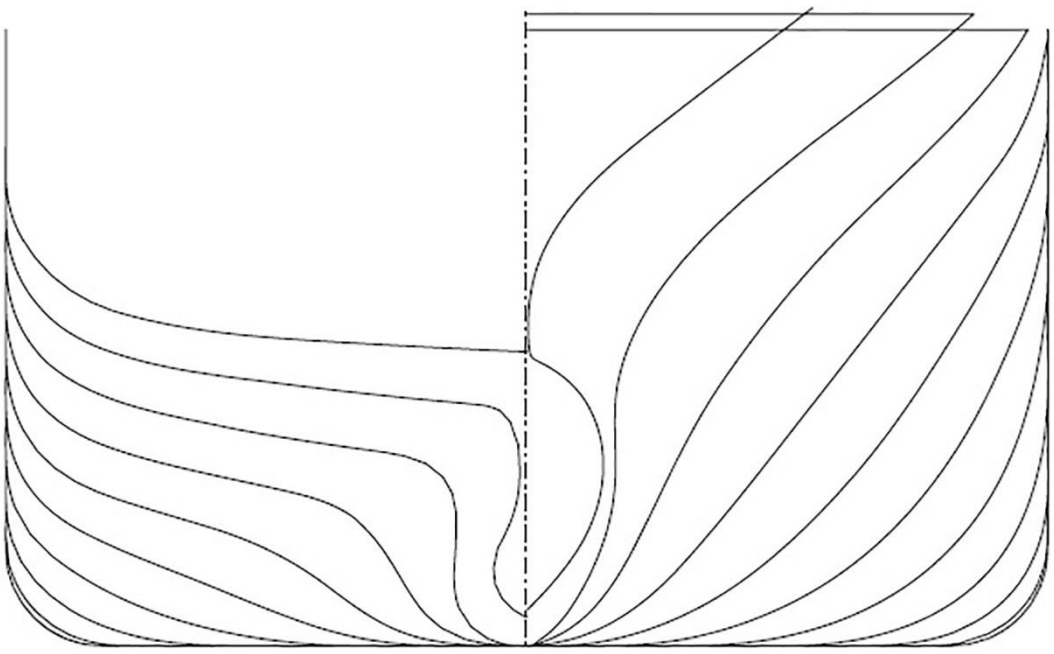

Figure 7.2 Hull sections of DTC container ship, taken from El Moctar et al. (2012).

The applied model was a 1:40 scale model of the DTC appended with rudder and propeller, taking precedence from that used in the towing tank experiments of Uliczka (2010) .The full scale and model scale hull properties are presented in Table 7.1. Figure 7.2 illustrates the hull sections of the ship in question. A three-dimensional view of the vessel is demonstrated in Figure 7.3. The propeller appended to the hull is four-bladed with right rotation and fixed-pitch of the Wageningen B series type. For information about the geometry of the propeller and rudder, reference may be made to El Moctar et al. (2012) and Mucha et al. (2014). Since self-propelled simulations in CFD would dramatically increase the run time, the ship model was instead towed through the canal in this study.

Figure 7.3 A three-dimensional view of the DTC container ship, modelled in Star-CCM+.

As mentioned earlier, the CFD simulations were carried out in an asymmetric canal. The cross section of the canal and the position of the model of the vessel are depicted in Figure 7.4, with its full-scale dimensions presented in Table 7.2 (PreSquat, n.d.).

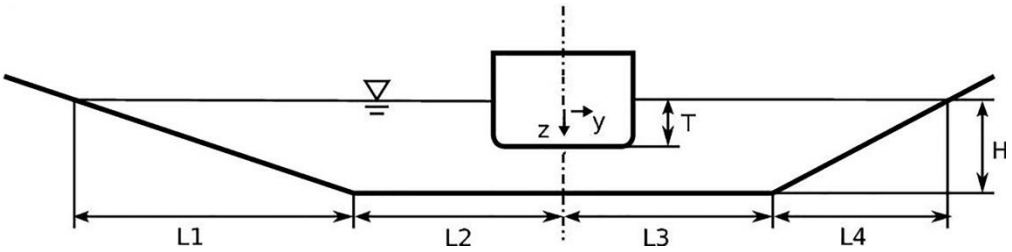

Figure 7.4 Cross-section of the asymmetric canal through which the vessel is advancing, adapted from PreSquat (n.d.).

Table 7.2 Cross-section dimensions of the canal in full scale, taken from PreSquat (n.d.).

Parameters	Value (m)
H	16
L_1	160
L_2	128
L_3	166
L_4	96

7.3 Simulation Cases

The CFD analyses of the vessel in question were performed for three loading conditions corresponding to the actual full-scale static draft midships of 13.0, 14.0 and 14.5 m. In each draft condition, the simulations were carried out for six ship forward speeds, resulting in eighteen different conditions. The simulation cases to which the CFD model was applied are listed in Table 7.3. The ship forward speeds given in the table were chosen in a similar manner to the experiments of Uliczka (2010). It should be highlighted that the depth Froude numbers of all the cases are below 1.0, signifying the subcritical speed region, where squat is expected to be more dominant.

Table 7.3 The cases to which the CFD model is applied.

Case No.	Full-Scale Draft (m)	Ship Speed (U)		Depth Froude Number
		Full Scale (kn)	Model Scale (m/s)	
1	13.0	5.07	0.412	0.208
2		7.35	0.598	0.302
3		10.60	0.862	0.435
4		11.99	0.975	0.492
5		12.92	1.051	0.530
6		13.59	1.105	0.558
7	14.0	4.80	0.390	0.197
8		6.81	0.554	0.280
9		8.34	0.678	0.342
10		11.57	0.941	0.475
11		12.54	1.020	0.515
12		13.25	1.078	0.544
13	14.5	2.42	0.197	0.099
14		6.35	0.516	0.261
15		7.98	0.649	0.328
16		9.71	0.790	0.399
17		11.16	0.908	0.458
18		12.21	0.993	0.501

7.4 Numerical Modelling

7.4.1 Physics modelling

The physics modelling adapted in the current CFD simulations is very similar to that used in the studies presented in Chapters 5 and 6.

As mentioned in the previous chapters, the VOF method was used to model and position the free surface with a flat wave. In order to simulate realistic ship behaviour, a DFBI module was used, with the vessel free in trim and sinkage.

The results from the time-step convergence study conducted to determine the optimum time-step resolution suggested the use of a much smaller time-step ($\Delta t=0.0035L/U$) for this study (see Section 7.5.1 of this chapter). In addition, it is of note that the number of inner iterations within each time-step was limited to ten.

7.4.2 Computational domain and boundary conditions

A general view of the computational domain with the DTC hull model and the notations of selected boundary conditions are depicted in Figure 7.5.

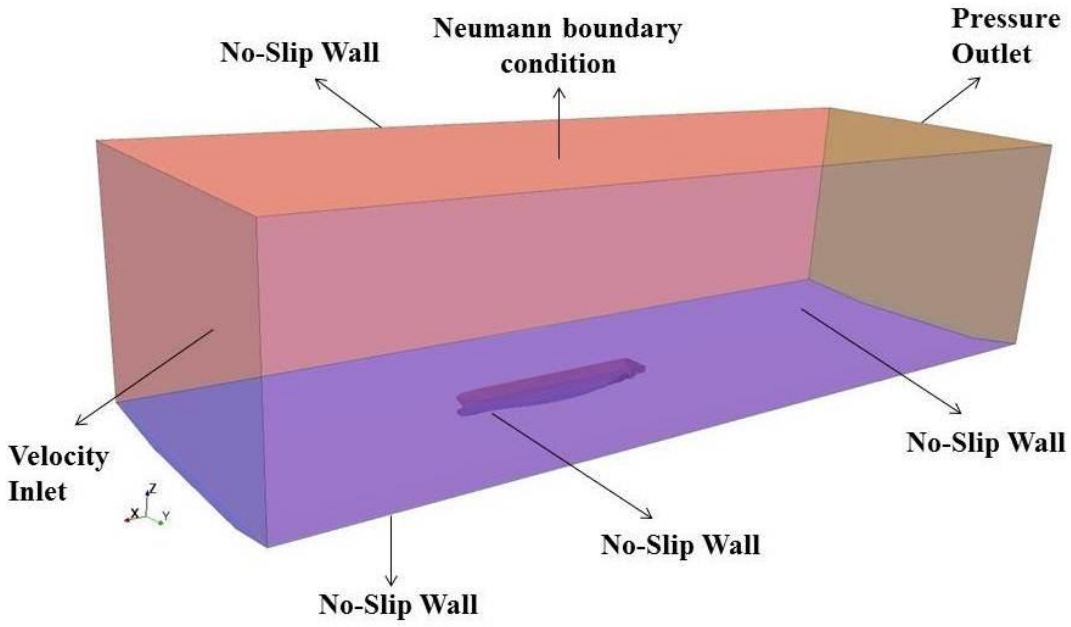

Figure 7.5 A general view of the computational domain and the applied boundary conditions.

Figure 7.5 delineates that a velocity inlet boundary condition was set in the positive x-direction, where flat waves were generated. The initial flow velocity at this inlet

condition was set to the corresponding velocity of the flat waves. Conversely, the negative x-direction was modelled as a pressure outlet. On the top of the domain, a Neumann boundary condition with static pressure equal to the reference pressure (0 Pascal) was applied to mimic the tank conditions. The bottom boundary was selected as a no-slip wall to account for the presence of the tank-floor. Similarly, the two sides of the domain (y-direction) have no-slip wall boundary conditions so that the tangential velocity is explicitly set to zero. Prabhakara and Deshpande (2004) point out that, "*a moving fluid in contact with a solid body will not have any velocity relative to the body at the contact surface. This condition of not slipping over a solid surface has to be satisfied by a moving fluid. This is known as the no-slip conditions*". Also, it is known that for no-slip walls in turbulent flow, only the component of velocity parallel to the wall is of interest (CD-Adapco, 2014).

CD-Adapco (2014) recommends that for trim, sinkage and resistance simulations, the inlet boundary should be located at least $1L_{BP}$ away from the hull, whereas the outlet should be positioned at least $2L_{BP}$ downstream to avoid any wave reflection from the boundary walls. Therefore, in this study, the inlet boundary was positioned $1.22L_{BP}$ away from the hull, and the outlet boundary $2.23L_{BP}$ downstream. It is worth mentioning that throughout all the cases given in this chapter, in order to prevent wave reflection from the walls, the VOF wave damping capability of the software package was applied to the solution domain with a damping length equal to approximately $1.127L_{BP}$ (10 m). This numerical beach model was used in upstream and downstream directions.

7.4.3 Mesh generation

Mesh generation was performed using the automatic meshing facility in Star-CCM+, resulting in a computation mesh of circa 7 million cells in total.

The computation mesh had areas of progressively refined mesh size in the area immediately around the hull, rudder and propeller, as well as the expected free surface and in the wake that was produced by the ship. For any technical details on the mesh generation, reference may be made to Chapter 5, Section 5.3.4.

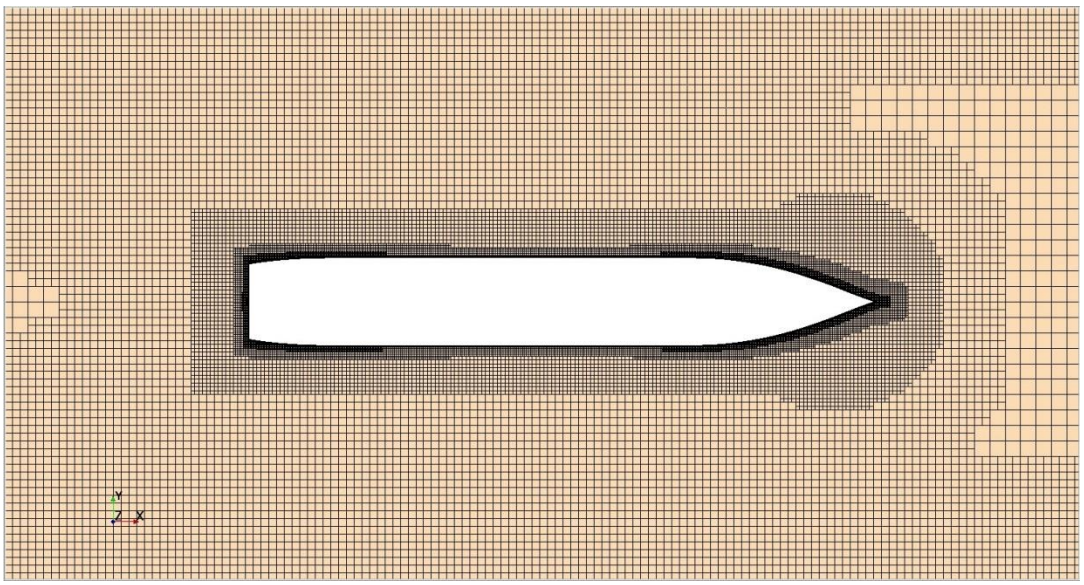

Figure 7.6 A cross-section of the solution domain showing the refined mesh around the hull from above.

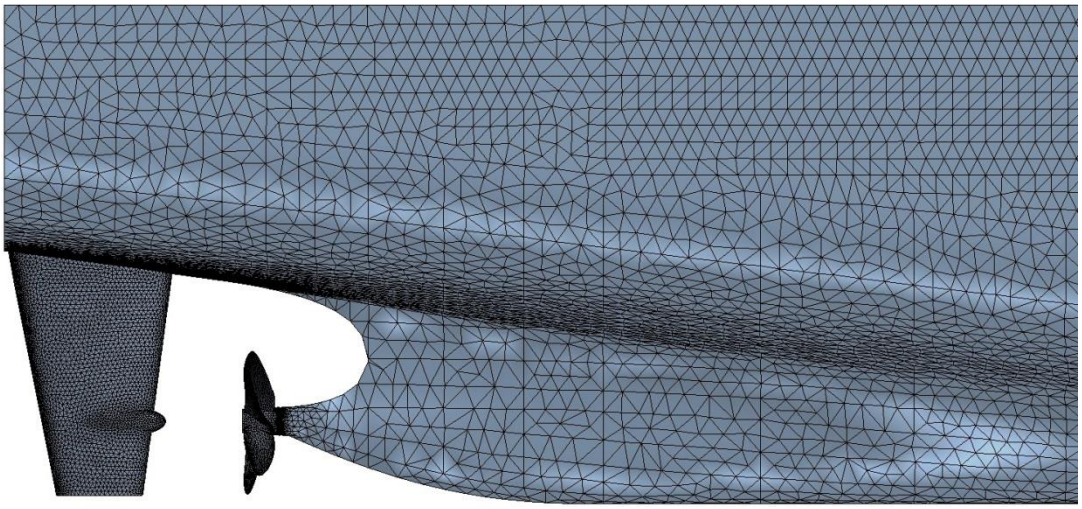

Figure 7.7 Surface mesh on the ship stern with rudder and propeller.

Figure 7.6 shows an overhead view of a cross-section of the computation mesh where the refinement around the hull is clearly visible. Figure 7.7 displays a closer look at the surface mesh on the ship stern with propeller and rudder.

7.5 Results and Discussion

The following section will outline the simulation results achieved during this study, and will also provide some comparison with experimental results. It will then present a discussion on the observation of the results. This section is divided into four main sub-sections, each of which presents different aspects of this work's findings. Before

proceeding to examine the results obtained, it is first necessary to perform a verification study.

7.5.1 Verification study

A verification study was undertaken to estimate the discretisation errors due to grid-size and time-step resolutions for Case 11 (which has a high Fn_h in a moderate draft value). It is expected that the numerical uncertainties for the other cases are of the same order.

For estimating iterative errors, the procedure derived by Roy and Blottner (2001) was used. The results obtained from these calculations suggest that the iterative errors for the squat and the total resistance coefficient are equal to almost zero.

Grid-spacing and time-step convergence studies were carried out following the grid convergence index (GCI) method described in Celik et al. (2008), which was provided in Chapter 6, Section 6.4.1.

In common with the verification study performed in the previous chapter, a constant refinement ratio of $\sqrt{2}$ was chosen in this study, for both the mesh-spacing and time-step convergence studies. It is of importance to mention that during the mesh convergence study, the surface mesh properties on the ship hull with the appendages were kept constant, to model the ship accurately. Based on the mesh refinement ratio which was applied, the final mesh numbers for each mesh configuration are listed in Table 7.4. Similarly, the time-step convergence study was conducted with triple solutions using systematically lessened time-steps, starting from $\Delta t=0.00707L/U$.

Table 7.4 The final cell numbers for each mesh configuration as a result of the mesh convergence study.

Mesh Configuration	Total cell number
Fine	6,963,044
Medium	4,378,144
Coarse	2,549,220

The verification parameters of the squat and the total resistance coefficients for the grid spacing and time-step convergence studies are presented in Table 7.5 and Table 7.6, respectively.

Table 7.5 Grid convergence study for squat and total resistance coefficient.

	Squat at CoG/L_{BP} (*with monotonic convergence*)	C_T (*with monotonic convergence*)
r	√2	√2
φ_1	-0.00279	0.008258
φ_2	-0.00280	0.008085
φ_3	-0.00281	0.007761
R	0.308	0.534
p	3.40	1.81
φ_{ext}^{21}	0.002789	0.0084562
e_a^{21}	0.16%	2.09%
e_{ext}^{21}	0.07%	2.34%
GCI_{fine}^{21}	0.09%	3.00%

Table 7.6 Time-step convergence study for squat and total resistance coefficient.

	Squat at CoG/L_{BP} (*with monotonic convergence*)	C_T (*with monotonic convergence*)
r	√2	√2
φ_1	-0.00279	0.008258
φ_2	-0.00277	0.008257
φ_3	-0.00272	0.008036
R	0.4	0.005
p	2.64	15.58
φ_{ext}^{21}	0.0028033	0.008258
e_a^{21}	0.72%	0.01%
e_{ext}^{21}	0.48%	0.00%
GCI_{fine}^{21}	0.60%	0.00%

As can be seen from Table 7.5 and Table 7.6, reasonably small levels of uncertainty were estimated for the obtained parameters. The numerical uncertainties in the finest-grid solution for squat and C_T are predicted as 0.09% and 3.00%, respectively (Table 7.5). These values change to 0.60% and 0.00%, respectively, when calculating the numerical uncertainty in the smallest time-step solution (Table 7.6). It is obvious that the total resistance coefficient is more sensitive to the grid-spacing compared to the ship squat. As these tables suggest, the uncertainties for squat and C_T are lower than those for TF_3 and TF_5, as predicted in Chapter 6.

7.5.2 Wave pattern

In this sub-section, wave contours generated by the presence of the ship model free to trim and sink around a free surface is presented. Figure 7.8 illustrates the wave

patterns around the container ship model in question, for various depth Froude numbers (Fn_h=0.475, 0.515 and 0.544), for a full-scale draft of 14 m. As can be seen from the figure, as the depth Froude number increases, the length of the transverse waves increases. Another interesting result that can be drawn from the figure is that the wave contours become densely massed along the slope on each side of the canal. Since the canal is asymmetric and has different slope gradients on each side, the length and appearance of the waves generated on the port and starboard sides of the canal are different. In order words, asymmetric wave patterns are obtained by the existence of a ship advancing through an asymmetric canal in calm water.

The pictures given in Figure 7.8 clearly show the trajectories of the waves, firstly generated by the presence of the vessel and then reflected from the side walls of the canal. These reflected waves then dissipate as they propagate towards the mid-canal aft of the vessel.

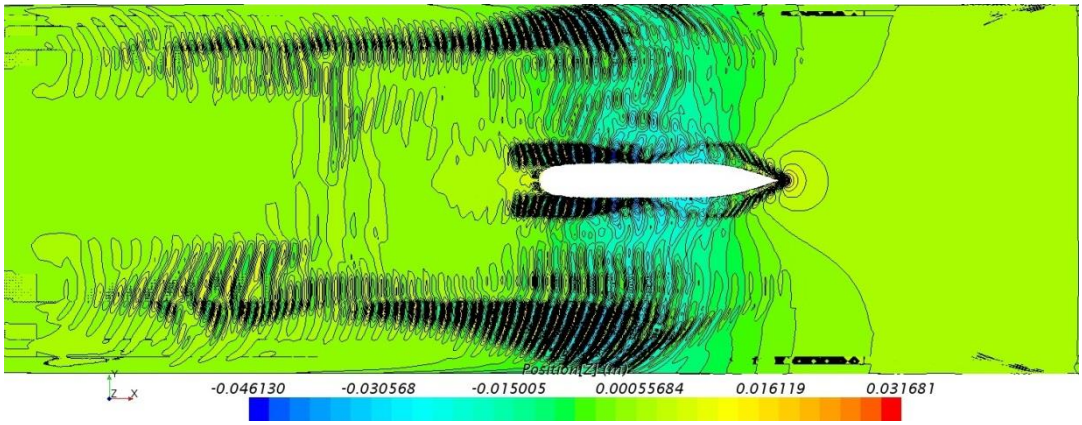

(a)

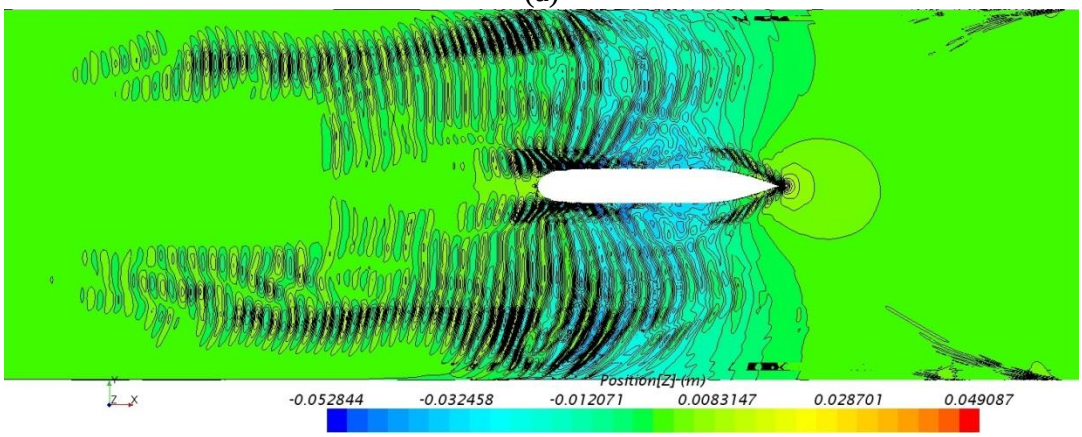

(b)

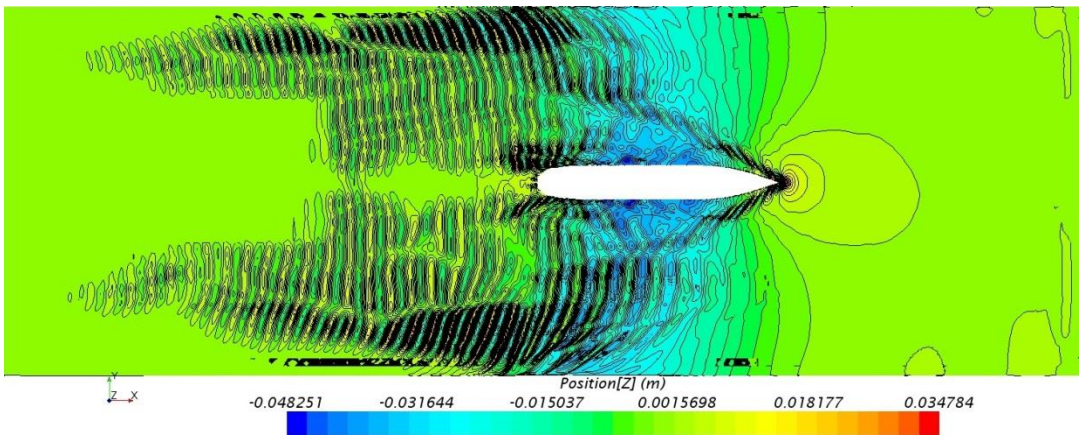

(c)

Figure 7.8 Comparison of wave patterns generated around the model-scale ship, for various depth Froude numbers (a) Fn_h=0.475 (Case 10), (b) Fn_h=0.515 (Case 11), (c) Fn_h=0.544 (Case 12).

7.5.3 Squat results

Having performed the necessary verification study, the remainder of this section addresses the main findings of this work.

The dynamic sinkage results of the DTC container ship model advancing through the canal, non-dimensionalised with the ship length, are presented for three ship drafts in Table 7.7. As mentioned earlier, the squat results obtained using the proposed RANS method were compared to those obtained from the experimental work of Uliczka (2010). The table also covers the comparison errors based on experimental data.

Table 7.7 The squat results for all cases by the current CFD and EFD (Error is based on EFD data).

Case No.	Full Scale Draft (m)	Depth Froude Number	CFD	EFD	Error (%)
			Squat at CoG/L_{BP}	Squat at CoG/L_{BP}	
1	13.0	0.208	-0.000201	-0.000183	9.57
2		0.302	-0.000684	-0.000732	-6.65
3		0.435	-0.001624	-0.001662	-2.30
4		0.492	-0.002193	-0.002338	-6.22
5		0.530	-0.002771	-0.003000	-7.62
6		0.558	-0.003477	-0.003789	-8.22
7	14.0	0.197	-0.000200	-0.000183	9.16
8		0.280	-0.000593	-0.000620	-4.39
9		0.342	-0.001000	-0.001014	-1.35
10		0.475	-0.002175	-0.002296	-5.27
11		0.515	-0.002791	-0.002873	-2.85
12		0.544	-0.003339	-0.003634	-8.13
13	14.5	0.099	-0.000015	-0.000014	7.90
14		0.261	-0.000612	-0.000648	-5.57
15		0.328	-0.000984	-0.001085	-9.26
16		0.399	-0.001586	-0.001577	0.55
17		0.458	-0.002276	-0.002282	-0.26
18		0.501	-0.002828	-0.002986	-5.28

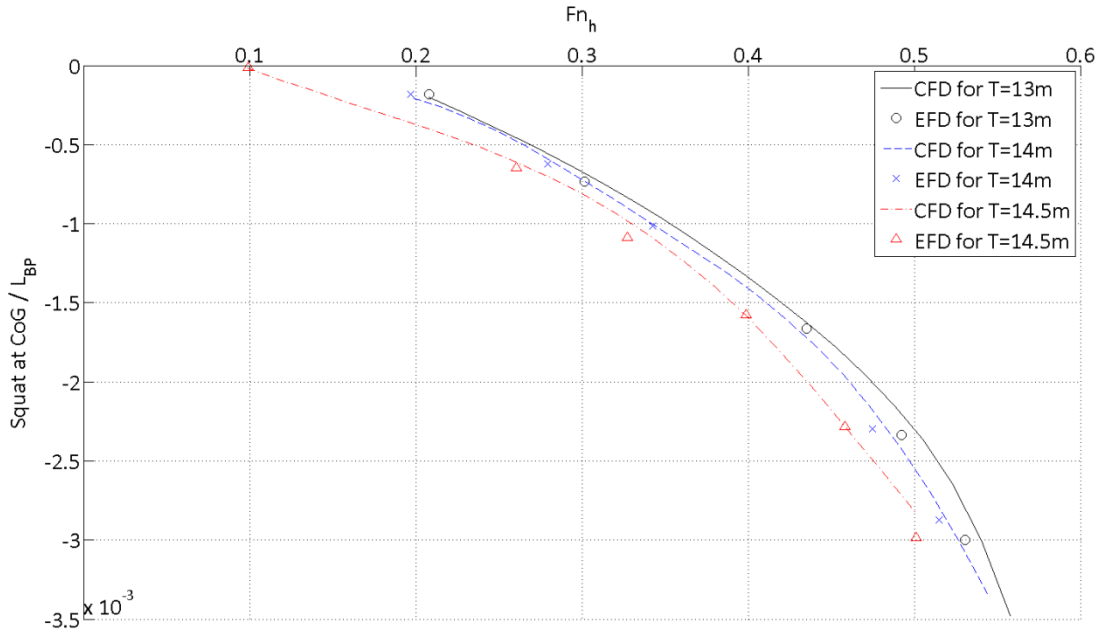

Figure 7.9 Comparison of the non-dimensionalised squat values obtained at ship's CoG, using EFD and CFD methods in three different ship drafts against various depth Froude numbers.

The squat results, listed in Table 7.7, are illustrated graphically in Figure 7.9. This gives a clearer depiction of the ship squat against ship speed for different drafts, enabling a more facile comparison among the CFD and EFD approaches.

As Table 7.7 and Figure 7.9 jointly show, the ship squat increases with increasing depth Froude number, or ship speed. In addition to this, for a constant speed, the vessel demonstrates more squat with a larger draft. Also, it is interesting to note that if the full-scale draft increases in magnitude by 1 m from T=13 m to T=14 m, the squat change only becomes more pronounced at Fn_h values above 0.4 (which roughly corresponds to a full-scale speed of 10 knots). However, as the magnitude of the full-scale draft increases only slightly more to a value of T=14.5 m, then this has a major effect on the squat values across all of the depth Froude numbers involved.

The numerically predicted squat at the ship's CoG agrees well with the model test measurements. Table 7.7 clearly states that the employed CFD model predicts ship squats within 10% of the experimental values. The CFD results tend to underestimate the magnitude of the expected squat, compared to the towing tank experiments. It should be noted that the standard deviations of the experimental squat results are reported to be within the range of 10% (Uliczka, 2010). The discrepancies between the experimental and numerical results may therefore be attributed to high standard deviations of the squat measurement. As explicitly pointed out in Uliczka (2010), during the towing tank experiments conducted for the DTC container ship model, more squat values are observed at the ship's stern compared to those measured at the ship's CoG.

7.5.4 Resistance results

The total resistance (drag) of a ship is mainly composed of two components; the frictional (=shear) resistance (R_F) and residual resistance (=pressure) (R_R) as given by Equation (5.11). The latter component is made up of the wave-making resistance (R_W) and the viscous pressure resistance (R_{VP}). In CFD-based RANS equations, shear and pressure resistances are obtained individually, to provide frictional and residual components of the total resistance.

Equation (5.11) can also be expressed in its more common non-dimensional form. As mentioned in Chapter 5, this is achieved by dividing each term by $0.5\rho V^2 S$. *S* is the mean wetted surface of the vessel, calculated to be 12.931 m^2, 13.619 m^2 and 13.970 m^2 (for a model-scale ship). These values correspond to full-scale drafts of 13 m, 14 m, and 14.5 m, respectively. The total resistance coefficient C_T is therefore composed of the frictional resistance coefficient C_F and the residual resistance coefficient C_R.

The frictional, residual and total resistance coefficients of the model-scale ship obtained using the current CFD model are tabulated in Table 7.8. Unfortunately, the experimental resistance values for the DTC container ship model advancing through the canal are not available in the literature and hence a comparison could not be made.

Table 7.8 The resistance coefficients for the DTC in model scale, obtained using the current CFD model.

Case No.	Full Scale Draft (m)	Depth Froude Number	Froude Number	Resistance Coefficients$\times 10^{-3}$		
				Residual (C_R)	Frictional (C_F)	Total (C_T)
1	13	0.208	0.044	3.714	4.087	7.801
2		0.302	0.064	2.779	3.732	6.511
3		0.435	0.092	3.059	3.618	6.677
4		0.492	0.105	3.170	3.607	6.777
5		0.530	0.113	3.661	3.629	7.290
6		0.558	0.118	4.125	3.688	7.813
7	14	0.197	0.042	4.048	4.049	8.097
8		0.280	0.059	3.357	3.732	7.089
9		0.342	0.073	3.262	3.689	6.952
10		0.475	0.101	4.013	3.634	7.646
11		0.515	0.109	4.568	3.691	8.258
12		0.544	0.115	5.072	3.736	8.808
13	14.5	0.099	0.021	4.567	5.342	9.909
14		0.261	0.055	3.988	3.872	7.860
15		0.328	0.070	4.283	3.775	8.058
16		0.399	0.085	3.934	3.724	7.658
17		0.458	0.097	5.145	3.669	8.814
18		0.501	0.106	5.957	3.759	9.716

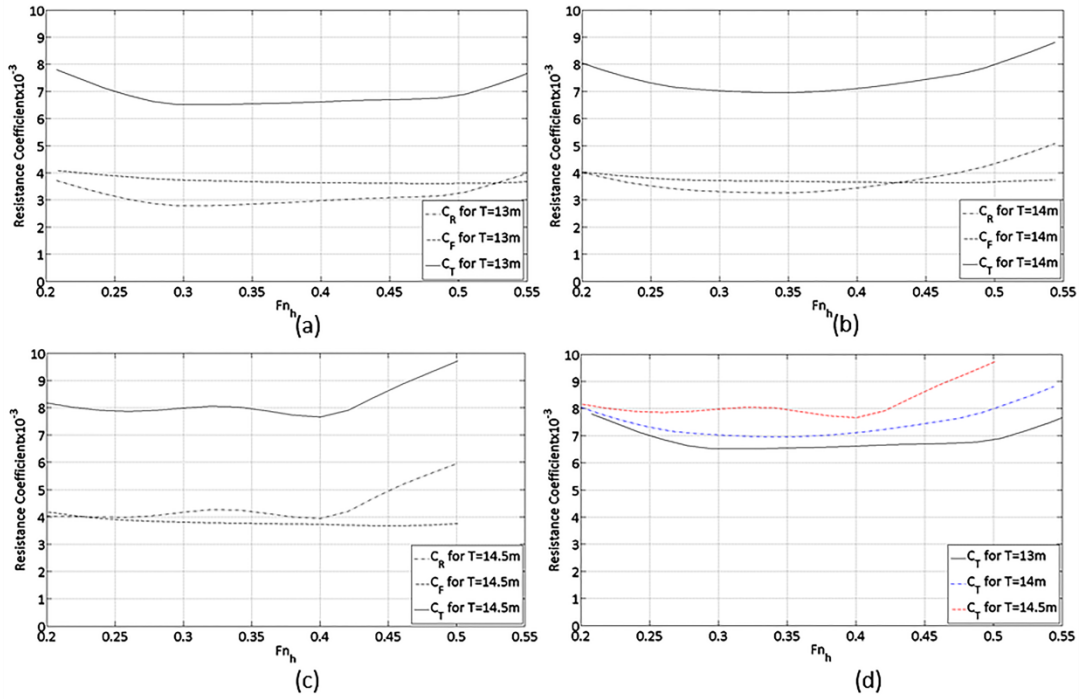

Figure 7.10 Graph of the total resistance coefficient C_T of the model-scale DTC against a range of depth Froude numbers for (a) full-scale draft T=13 m, (b) T=14 m, (c) T=14.5 m. The dashed lines and centre lines show the contributions of the resistance components. (d) shows the comparison of the total resistance coefficients in three different draft conditions.

The data contained in Table 7.8 are graphically shown in Figure 7.10, to enable a clearer comparison among the resistance coefficients obtained for three different loading conditions. As can be seen from both Table 7.8 and Figure 7.10, the resistance coefficients are highly affected by the ship's draft, as expected. For all resistance components, the drag forces increase with larger ship draft. Also, at low speeds, the frictional resistance provides the largest contribution to the total resistance, whereas at higher speeds, the residual resistance becomes dominant. More interestingly, the depth Froude number value, at which the residual resistance starts to become dominant, varies with changing ship draft. Figure 7.10 illustrates that the critical Fn_h values are circa 0.53, 0.42 and 0.22 for full-scale ship drafts of 13 m, 14 m and 14.5 m, respectively. That means the critical Fn_h value decreases as the ship draft increases. This shift in the critical depth Froude number may be attributed to two factors:

i) As the ship draft increases, in other words, as the ship sits deeper in the water, its water plane area as well as the cross-section changes. This in turn affects the wave making resistance of the ship, owing to the hull form.

ii) As the ship draft increases, the ratio of the water depth to the ship draft (h/T) decreases, so the shallow water effects becomes more drastic. As pointed out in many papers (for example Raven (2012), Prakash and Chandra (2013) and Beck et al. (1975)), this ultimately leads to an increase in wave making resistance and hence in residual resistance. Therefore, in the deepest ship draft condition, i.e. in the smallest h/T ratio, the increase in wave making resistance becomes the largest. Consequently, this makes the residual resistance become dominant even at very low ship speeds (or Froude numbers).

In order to reveal the shallow water effect of a ship advancing through a canal on its resistance characteristics, and to eliminate the other factors influencing ship resistance, such as ship form, the same analyses should be repeated in deep water conditions. This is left as a piece of future research as this would require the creation of a further eighteen simulations to be run in deep water conditions.

7.6 Concluding Remarks

In this chapter, fully nonlinear unsteady RANS simulations were performed to predict the squat and resistance of a model-scale DTC container ship passing through a canal, for three different ship drafts at a range of forward speeds. The ship speeds and draft values were selected in analogy to the towing tank experiments available in the literature.

Firstly, a verification study was performed for Case 11. The results showed that reasonably small levels of uncertainty were predicted for the squat and the total resistance coefficient. The numerical uncertainties in the finest-grid solution for sinkage and C_T were calculated to be 0.09% and 3.00%, respectively. These values alter to 0.60% and 0.00%, respectively, for the numerical uncertainty in the smallest time-step solution.

Then, wave patterns generated by the presence of the ship model, free in trim and sinkage, around a free surface were shown for three different depth Froude numbers. During the study it was demonstrated that the length of transverse waves increases with increasing Fn_h values.

Following this, the dynamic sinkage results of the model scale DTC container ship obtained from the CFD simulations were presented at a range of ship forward speeds for three different ship drafts. The numerical squat results were also compared to those from available experiments. A comparison showed that the squat results obtained using CFD were only under-predicted within 10% of the EFD data. However, the standard deviations of the experimental squat results are given to be within the range of 10%.

It was concluded that ship squat increases with increasing ship speeds, as expected. Also, it has been shown that a vessel demonstrates more squat with an increasing draft. Another interesting result drawn from the analyses was that a slight increase in magnitude to a *larger* draft may have more of an effect on ship squat than a much larger increase in magnitude applied to a *smaller* initial draft.

Finally, resistance results were presented for the model-scale DTC container ship. For all simulation cases, the two resistance components (frictional and residual) that contributed to the total resistance were given in standard tabular and graphical formats. As clearly shown in the chapter, the ship resistance was very sensitive to ship draft. A larger ship draft produces higher drag forces. Also, it has been demonstrated that at low depth Froude numbers, the frictional resistance gave the largest contribution to the total resistance. In this work, the depth Froude number where the residual resistance begins to become dominant has been termed the critical depth Froude number. It was interesting to note that as a ship's draft increases, this critical Fn_h value of the ship in question becomes diminished. The reasons for this were attributed to two factors, which were discussed in detail in this chapter.

8. CONCLUSIONS AND FUTURE RESEARCH

8.1 Introduction

This chapter will present a summary of the main outcomes of the studies discussed in this thesis, along with a clear demonstration of how the research aims and objectives have been achieved. Following this, a brief discussion on CFD methods will be given. Finally, recommendations will be presented for relevant fields of future research which are related to the work presented in the main chapters of this thesis.

8.2 Conclusions

The first research objective listed in Chapter 1 was as follows:

- ✓ *To review the available literature on seakeeping of ships and to investigate the differences between various prediction techniques for seakeeping performance of ships*

The 'Critical Review' in Chapter 2 addressed this by presenting a wide-ranging overview of current seakeeping methods, from classical 2-D strip theory to the state-of-the-art fully nonlinear unsteady RANS simulations. A discussion of each theory's strengths and weaknesses was also provided. The chapter also provided a literature survey on specific fields, such as operability assessments of ships, prediction of the hydrodynamic coefficients of ships using a CFD method, CFD applications to seakeeping problems, and the squat and resistance of ships in shallow water regions. Finally, the gaps detected during the literature review were listed in the conclusion of Chapter 2. It was also emphasised that the main chapters of this thesis aimed to fill these gaps.

The following objectives were achieved in Chapter 3.

- ✓ *To describe an operability assessment procedure invoking seakeeping analyses in accordance with reliable seakeeping criteria*
- ✓ *To demonstrate the sensitivity of the adopted seakeeping theories to the vessel's expected operability*
- ✓ *To make a comparison between different methodologies for the calculation of motion induced sickness values for passengers on a catamaran ferry*

A methodology to calculate the seakeeping performance of ships in a specified sea area where a vessel operates was presented in Chapter 3. The methodology depends on the response of the vessel to regular waves, the mission features and the wave climate of the sea site.

Three different methods to generate RAOs of the vessel, to be used in the operability analyses, were chosen and discussed. The limitations and features of each theory were explained in detail in Chapter 2. Following this, an overview methodology of the procedure for operability analysis was presented. A detailed introduction of each individual stage of the methodology was given. Afterwards, a high speed catamaran car/passenger ferry providing service in the west coast of Scotland was used as a case study, and its operability indices were calculated based on predetermined human-comfort seakeeping criteria. The results clearly showed the effect of seasonality on the vessel's expected operability. The particular focus was on the sensitivity of the operability index to the employed seakeeping methods. Figure 3.24 explicitly demonstrated how these theories affect the vessel's operability indices. In addition to this, the motion sickness incidence values of the catamaran were calculated using each theory. It was shown that in the low sea states, the MSI results from the different theories appeared similar to each other, however in the high sea states, the differences became significant.

The next research objective was as follows:

- ✓ *To obtain the hydrodynamic coefficients of heaving twin cylinders in a free surface by employing a CFD-based RANS solver*

In Chapter 4, the proposed method to obtain the hydrodynamic features of a circular section of a 2-D twin cylinder heaving about a calm free surface, utilising a

commercial RANS solver, was presented and compared with the experimental data available in the literature.

The added mass and fluid damping coefficients of the section in question were obtained at fifteen frequencies of oscillation, using the same amplitude of oscillation in each case. At low frequencies of oscillation, the damping coefficients were obtained using the expression given by Equation (4.9). At high frequencies the results were obtained using the Fourier analysis. The resultant damping coefficients were found to be in reasonably good agreement with the experimental results.

The added mass coefficients, on the other hand, agreed well with the experimental data at low frequencies, whereas discrepancies between CFD and the experimental results were detected at relatively higher frequencies. This author believes that the main reason for this lies in the mesh generation. At high frequencies, much finer grid topology around the free surface is required to successfully capture water waves generated by oscillating the section.

This author believes that the proposed strip theory method (depicted in Figure 4.1), which was first proposed by Salui et al. (2000), may not be practical for real ship applications, as it would take a very long time to determine the hydrodynamic coefficients of each individual ship section over various frequencies. Moreover, a similar study presented in Chapter 4 must be extended for sway and roll motions in order to complete the work outlined in Figure 4.1. Instead, it would be much more practical, as well as easier and hence more convenient, to model a 3-D ship geometry to obtain its motion responses to incident regular waves using an unsteady-RANS approach, as shown in Chapters 5 and 6.

Following this, the next two research objectives were addressed.

- ✓ *To gain a better understanding of the effects of operating at a lower speed on the behaviour of a vessel in deep water*
- ✓ *To introduce a CFD-based unsteady RANS simulation model to predict the resistance and motions of a ship operating in head seas*

The research reported in Chapter 5 concerned the numerical investigation of the performance of a full-scale KCS model both in calm water and in head waves. Ship motions, as well as total and added resistance components were estimated under two operational conditions (design speed and a lower speed) with the aim to evaluate the advantages of slow steaming operational conditions, in terms of fuel consumption and CO_2 emissions.

Firstly, the main properties of the KCS were provided, along with a list of the simulation cases applied to the CFD model. Following this, the numerical setup of the CFD model was explained in detail. Before providing the CFD results, validation and verification studies were carried out. Then, the ship motions and resistance results obtained using CFD were compared to those obtained from VERES and the related towing tank experiments. Finally, the advantages of applying the slow steaming approach were revealed using Equation (5.21) and the results were graphically shown in Figure 5.22. Overall, the CFD method has provided very promising results for predicting the motion responses and resistance of a vessel in regular head waves.

The next research objective to be tackled was discussed in Chapter 6.

- ✓ *To test this proposed numerical model for a vessel in shallow water, in order to predict vertical motions of the vessel in different ship drafts at zero speed*

  In Chapter 6, fully nonlinear unsteady RANS simulations to predict the heave and pitch responses of a full scale very large tanker model to incident head waves were carried out at a zero forward speed in three different ratios of water depth to draft of the ship.

  Firstly, the main ship properties along with its geometry were provided. Then, a list of simulation cases, which were applied to the proposed CFD modelling, was given. Following this, the numerical setup of the CFD model was explained, with detailed information about mesh generation, treatment of wall functions and boundary conditions. Also, an explanation on how to generate shallow water waves was provided in the later sub-sections. Next, a verification study to predict the uncertainties of the CFD model for this specific study was performed.

Following this, the results regarding shallow water waves generated through the computational domain were provided. Finally, the transfer functions obtained using the current CFD model were presented in both graphical and tabular format and a comparison between the other methods (EFD and a potential flow theory-based code) was made. The comparison clearly showed that the CFD method predicted the transfer functions of the vessel better than the potential flow theory method.

The final research objective was addressed in Chapter 7.

- ✓ *To predict the squat and resistance of a vessel advancing through a canal using the RANS solver*

In this chapter, fully nonlinear unsteady RANS simulations were performed to predict the squat and resistance of a model-scale DTC container ship for three different ship drafts at a range of forward speeds. The ship speeds and draft values were selected in analogy to the towing tank experiments of Uliczka (2010).

Firstly, the main ship properties and the cross-section of the canal along with its dimensions were provided. Then, a list of the simulation cases applied to the current CFD model was presented. Next, the numerical setup of the CFD model was explained. Following this, a validation study was performed to assess the uncertainties of this work's CFD model. Finally, the squat and the resistance coefficients of the vessel in question were obtained using CFD and a comparison of the squat results with the experimental data was provided. This comparison showed that the CFD model predicted the ship squat values sufficiently well over various ship speeds.

8.3 Discussion

This work was built on two different approaches: potential flow theory and CFD. The particular focus was on the state-of-the-art unsteady RANS approach. The main results drawn from this work were summarised and discussed in detail in the previous section.

This thesis clearly showed that CFD can be used for seakeeping and resistance problems of ships, in order to obtain more accurate results compared to potential flow theory-based numerical methods. When carrying out the CFD work presented in this thesis, a number of problems were encountered. Most of them were experienced when defining the problem in the 'pre-processing' stage of CFD. Every single problem studied in this work required a different combination of numerical models, and the selection of proper boundary and initial conditions. Before conducting the individual studies, exploratory studies were performed, aiming to determine the most feasible numerical modelling set-up. The generation of computational mesh was another challenging issue. Ideally, a very fine grid should be generated, though a compromise was always made between the mesh topology and the run time, in order to avoid overly-long run times. Another important issue was the use of overset mesh. Working with the overset mesh facility greatly increased both the time spent on mesh generation and the subsequent run time of a simulation.

During this work it was seen that, without a doubt, pre-processing is the most important and demanding stage in a typical CFD task. In the pre-processing stage, the physical incident should be defined with great care. In addition to all of these factors to be considered, the time-step resolution is an equally important factor, to be able to obtain results more closely resembling reality. Convergence of the solution was another factor which should be considered in CFD. In some simulations, especially in ship motion simulations in shallow water, the solution did not converge. In this case, the solution was terminated, and the grid-spacing and time-step resolutions were reconsidered. After changing these parameters and regenerating the mesh topology, such simulations were resent to the high performance computers (HPC) to re-run.

In Chapter 1, typical areas of application of CFD in naval architecture and offshore engineering were provided. For the time being, CFD's usage is restricted to existing computational frameworks. Without access to the University of Strathclyde's HPC, the work presented in this thesis could not have been performed. CFD is undoubtedly a very useful tool, though it does take much longer to obtain results compared to potential flow theory.

As stated previously, the pre-processing step is the most demanding stage in a typical CFD task. For example, for a typical CFD simulation of ship motions in deep water, such as that presented in Chapter 5, the pre-processing process can take up to 5 days, including mesh generation (overset and background), defining the physics, boundary conditions, etc. Without a doubt, this length of time may increase or decrease depending on the user's prior experience with CFD. Another time-demanding stage in a CFD task is processing: to give an example, the total CPU time allocated to run a typical case in Chapter 5 is circa 5800 hours. By utilising a 60-core supercomputer, this corresponds to approximately 4 days in real time. It should be pointed out that this applies only to a typical simulation for one speed, and one frequency at a single wave height. On the other hand, potential flow theory can give results in a much shorter time compared to CFD. To give an example from Chapter 5, the ship motions and resistance values of the KCS model can be obtained using VERES in a day, with this timespan including the preparation of the ship model, defining the necessary inputs to run the software and obtaining the results for all speeds and all wave frequencies. One should also take these factors into consideration when determining whether to use CFD.

It should be borne in mind that CFD may offer advantages over conducting experiments, or using the potential flow theory, in some aspects, provided that the Navier-Stokes equations can be solved accurately. This requirement may be incredibly difficult for some engineering applications. For example, high Reynolds number flows make it difficult to obtain an accurate numerical solution of the Navier-Stokes equations. The main reason for this lies in the fact that high Reynolds number flows are highly turbulent flows. High Reynolds number flows therefore require a more accurate numerical treatment than others. Another reason for this is that the viscous sub-layer of a boundary layer is so thin at high Reynolds numbers that it requires much finer grid generation.

It should be noted that CFD-based numerical approaches can only give approximate results. The differences between reality and numerical results stem from the errors which occur in each stage of the numerical modelling process (Ferziger and Peric, 2002). Xiao (2012) states that numerical methods contain at least three forms of

systematic errors, namely; modelling error, discretisation error, and iterative error. Ferziger and Peric (2002) point to the fact that even if the equations are solved exactly, the solution may still not resemble reality. CFD users should therefore validate their results against experiments. CFD is a useful tool at hand, however it may give misleading results if the physical problem is not modelled correctly. This author believes that in order to favour the successful modelling of an incident, it is of critical importance to consider every parameter which may be at play in a given situation.

Having said that, this author believes that in the near future, the use of CFD-based numerical methods will completely outweigh the use of potential flow theory. It is likely that continuous technological revolutions will enable the development of CFD software packages similar to existing ones based on potential flow theory (such as VERES, ShipmoPC and Seakeeper). This will then allow CFD users to operate such software packages more easily and to obtain their desired outcomes in shorter times.

8.4 Recommendations for Future Research

Recommendations for further studies relating to the work presented in this thesis are briefly outlined below.

1. In Chapter 3, the operability analyses were conducted using three different 2-D potential theory-based techniques. As a future piece of work, a vessel's operability could be predicted by employing more sophisticated methods, such as the 3-D Rankine panel method or the CFD based unsteady RANS approach to generate RAOs. The same analyses performed in this work could then be extended by comparing the operability indices obtained using this more advanced theory, to those from other theories. For instance, this particular study could be extended by merging Chapters 3 and 5. It would also be interesting to use experimental RAOs to assess ship operability and observe how the results change.
2. The study presented in Chapter 4 can be extended for sway and roll motions, where strong viscous, and hence nonlinear, effects are expected to be observed.

3. The study performed in Chapter 5 has provided a very useful starting point for investigations into ship behaviour at off-design speeds, specifically at a representative slow steaming speed for container vessels. In addition to this, the impact of variations in vessel trim and draft on ship motions and added resistance should be investigated, specifically for off-design conditions. It has already been observed in simulations and real operations that trim optimisation can be used to reduce the resistance of vessels operating under design conditions. The study should also be extended to incorporate the propeller and appendages, as these will also have a notable effect on ship behaviour and performance. With the propeller present, and a suitable method used to simulate its rotation, further study into the changes in propulsive efficiency due to motions in a seaway could be made. Further, the impact of slower speed operations in different headings should also be investigated, to ensure that no safety issues are likely to arise.
4. Another source of added resistance is hull roughness. The added resistance due to hull roughness can be predicted by employing modified wall functions in CFD software as successfully shown by Demirel et al. (2014). A piece of future work may be the prediction of the added resistance of a ship due to waves and hull fouling, by employing a new wall-function in the CFD software. This may provide a better understanding of the total resistance of a vessel under real operational conditions.
5. The research in Chapter 6 has provided a very useful starting point for further studies on ship behaviour and performance in shallow water. This study should be extended to include simulations in beam or oblique seas, in order to predict roll motions, for which the discrepancies between unsteady RANS methods and potential flow theory are expected to be amplified. However, it should be borne in mind that in this case, the mesh number and the required computational effort will be doubled, as the use of the symmetry boundary condition in the centre line of the ship and the domain will no longer be valid.
6. The study given in Chapter 6 should also be extended to incorporate forward speed effects into the numerical simulations. Using the proposed unsteady RANS method, the added resistance and motion responses of a vessel due to

waves in shallow water should be investigated, as this would be another piece of novel research.

7. The work in Chapter 7 has provided a different aspect for investigations into the resistance of a ship travelling through a canal, from a CFD point of view. The discussion made in Chapter 7 for the change in the critical depth Froude number for varying ship draft should be extended, by running the same simulations in deep water conditions. The study should also be extended to investigate the effect of other parameters, such as channel width, on squat and drag forces. In this thesis, trim values were not assessed as they are not of prominent importance in the sub-critical speed regime. Therefore, a piece of future work may be to incorporate trim behaviour of the vessel under all three speed regimes.

References

Akimoto, H., Omori, T., Saito, H. & Masiur, R. (2010) '*Numerical simulation of KCS container carrier in head wave conditions*'. *Gothenburg 2010-A Workshop on Numerical Ship Hydrodynamics*. Gothenburg.

Alderf, N., Lefrancois, E., Sergent, P. & Debaillon, P. (2011) 'Dynamic ship response integration for numerical prediction of squat in highly restricted waterways'. *International Journal for Numerical Methods in Fluids,* 65 (7), pp.743-763.

Alidadi, M. & Calisal, S. (2011) '*A numerical study on squat of a Wigley hull*'. *Proceedings of the Asme 30th International Conference on Ocean, Offshore and Arctic Engineering, Vol 7: CFD and Viv: Offshore Geotechnics*. Rotterdam, The Netherlands.

Arribas, F.P. (2007) 'Some methods to obtain the added resistance of a ship advancing in waves'. *Ocean Engineering,* 34 (7), pp.946-955.

Bales, S.L. (1983) 'Designing ships to the natural-environment'. *Naval Engineers Journal,* 95 (2), pp.31-40.

Banks, C., Turan, O., Incecik, A., Theotokatos, G., Izkan, S., Shewell, C. & Tian, X. (2013) '*Understanding ship operating profiles with an aim to improve energy efficient ship operations*'. *Low Carbon Shipping Conference*. London, England.

Banks, J.B., Phillips, A.B., Bull, P.W. & Turnock, S.R. (2010) *'RANS simulations of the multiphase flow around the KCS hull form*'. *Gothenburg 2010-A Workshop on Numerical Ship Hydrodynamics*. Gothenburg.

Barras, B. & Derrett, D.R. (2012) *Ship Stability for Masters and Mates*. 7th edn. Elsevier.

Beck, R.F. (1994) 'Time-domain computations for floating bodies'. *Applied Ocean Research,* 16 (5), pp.267-282.

Beck, R.F., Newman, J.N. & Tuck, E.O. (1975) 'Hydrodynamic forces on ships in dredged channels'. *Journal of Ship Research,* 19 (3), pp.166-171.

Beck, R.F. & Reed, A.M. (2001) 'Modern computational methods for ships in a seaway'. *Transactions of the Society of Naval Architects and Marine Engineers,* 109 pp.1-51.

Bertram, V. (1998) '*Numerical investigation of steady flow effects in 3-D seakeeping computations*'. *22nd Symposium on Naval Hydrodynamics*. Washington D.C., USA.

Bertram, V. & Yasukawa, H. (1996) '*Rankine source methods for seakeeping problems'*. *Jahrbuch der Schiffbautechnischen Gesellschaft.* Germany: Springer, pp. 411-425.

Beukelman, W. & Gerritsma, J. (1982) '*The distribution of hydrodynamic mass and damping of an oscillating shipform in shallow water*'. *11th Scientific and Methodological Seminar on Ship Hydrodynamics*. Varna, Bulgaria.

Bhushan, S., Xing, T., Carrica, P. & Stern, F. (2009) 'Model- and full-scale URANS simulations of Athena resistance, powering, seakeeping, and 5415 maneuvering'. *Journal of Ship Research,* 53 (4), pp.179-198.

Boreel, L.J. (1974) '*Wave action on large offshore structures*'. *Conference on Offshore Structures*. London, England: Institute of Civil Engineers.

Brard, R. (1972) 'The representation of a given ship form by singularity distributions when the boundary condition on the free surface is linearized'. *Journal of Ship Research,* 16 (1), pp.76-92.

Briggs, M.J. (2006) *Ship squat predictions for ship/tow simulator*. Available: http://chl.erdc.usace.army.mil/library/publications/chetn/pdf/chetn-i-72.pdf.

Carrica, P.M., Fu, H.P. & Stern, F. (2011) 'Computations of self-propulsion free to sink and trim and of motions in head waves of the KRISO Container Ship (KCS) model'. *Applied Ocean Research,* 33 (4), pp.309-320.

Carrica, P.M., Paik, K.J., Hosseini, H. & Stern, F. (2008) 'URANS analysis of a broaching event in irregular quartering seas'. *Journal of Marine Science and Technology,* 13 (4), pp.395-407.

Carrica, P.M., Wilson, R.V., Noack, R.W. & Stern, F. (2007) 'Ship motions using single-phase level set with dynamic overset grids'. *Computers & Fluids,* 36 (9), pp.1415-1433.

Castiglione, T., He, W., Stern, F. & Bova, S. (2014) 'URANS simulations of catamaran interference in shallow water'. *Journal of Marine Science and Technology,* 19 (1), pp.33-51.

Castiglione, T., Sadat-Hosseini, H., Stern, F. & Bova, S. (2013) '*CFD simulation for sea keeping of Delft catamaran in regular head and oblique waves*'. *12th International Conference on Fast Sea Transportation*. Amsterdam, the Netherlands.

Castiglione, T., Stern, F., Bova, S. & Kandasamy, M. (2011) 'Numerical investigation of the seakeeping behavior of a catamaran advancing in regular head waves'. *Ocean Engineering,* 38 (16), pp.1806-1822.

CD-Adapco (2014) '*User guide Star-CCM+ Version 9.0.2'*.

Celik, I.B., Ghia, U., Roache, P.J. & Freitas, C.J. (2008) 'Procedure for estimation and reporting of uncertainty due to discretization in CFD applications'. *Journal of Fluids Engineering-Transactions of the ASME,* 130 (7), pp.078001.

Chan, H.S. (1990) *A three-dimensional technique for predicting first and second order hydrodynamic forces on a marine vehicle advancing in waves.* PhD. Thesis, University of Glasgow.

Chapman, R.B. (1975) '*Numerical solution for hydrodynamic forces on a surface-piercing plate oscillating in yaw and sway*'. *1st International Symposium on Numerical Hydrodynamics*. Gaithersburg, Maryland.

Choi, J. & Yoon, S.B. (2009) 'Numerical simulations using momentum source wave-maker applied to RANS equation model'. *Coastal Engineering,* 56 (10), pp.1043-1060.

Constantine, T. (1960) 'On the movement of ships in restricted waterways'. *Journal of Fluid Mechanics,* 9 (2), pp.247-256.

Cosner, R.R., Oberkampf, W.L., Rumsey, C.L., Rahaim, C.P. & Shih, T.I.-P. (2006) '*AIAA Committee on standards for computational fluid dynamics: Status and plans*'. *44th Aerospace Sciences Meeting and Exhibit*. Reno, Nevada.

Cummins, W.E. (1956) *The wave resistance of a floating slender body.* PhD. thesis. American University.

Dallinga, R.P., Pinkster, D.J. & Bos., J.E. (2002) '*Human factors in the operational performance of ferries*'. *Human Factors in Ship Design and Operation Conference*. London, England.

Das, S. & Cheung, K.F. (2012) 'Scattered waves and motions of marine vessels advancing in a seaway'. *Wave Motion*, 49 (1), pp.181-197.

Date, J.C. & Turnock, S.R. (1999) *A study into the techniques needed to accurately predict skin friction using RANS solvers with validation against Froude's historical flat plate experimental data*. University of Southampton, Report No. 114.

Daubert, A. (1970) 'Quelques considerations sur les differentes simulations et methodes de calcul du comportement des structures immergees ou flottantes en mer'. *La Houille Blanche*, 2 pp.159-173.

Dawson, C.W. (1977) '*A practical computer method for solving ship-wave problems*'. *2nd International Conference on Numerical Ship Hydrodynamics*. Berkeley, CA, USA.

Demirel, Y.K., Khorasanchi, M., Turan, O., Incecik, A. & Schultz, M.P. (2014) 'A CFD model for the frictional resistance prediction of antifouling coatings'. *Ocean Engineering*, 89 pp.21-31.

Det Norske Veritas (2007) '*Environmental conditions and environmental loads'*. *Recommended Practice.* DNV-RP-C205.

El Moctar, O., Kaufmann, J., Ley, J., Oberhagemann, J., Shigunov, V. & Zorn, T. (2010) '*Prediction of ship resistance and ship motions using RANSE*'. *A Workshop on Numerical Ship Hydrodynamics*. Gothenburg.

El Moctar, O., Shigunov, V.S. & Zorn, T. (2012) 'Duisburg Test Case: Post-Panamax container ship for benchmarking'. *Ship Technology Research*, 59 (3), pp.50-65.

Endo, H. (1987) 'Shallow-water effect on the motions of three-dimensional bodies in waves'. *Journal of Ship Research*, 31 (1), pp.34-40.

Enger, S., Peric, M. & Peric, R. (2010) '*Simulation of flow around KCS-hull*'. *Gothenburg 2010-A Workshop on Numerical Ship Hydrodynamics*. Gothenburg.

Faltinsen, O.M. (1990) *Sea Loads on Ships and Offshore Structures.* Cambridge, UK: Cambridge University Press.

Faltinsen, O.M. (2005) *Hydrodynamics of High-Speed Marine Vehicles.* Cambridge University Press.

Faltinsen, O.M., Helmers, J.B., Minsaas, K.J. & Zhao, R. (1991) '*Speed loss and operability of catamarans and SES in a seaway*'. *First International Conference on Fast Sea Transportation.* Trondheim, Norway: Tapir Publisher.

Faltinsen, O.M., Hoff, J.R., Kvalsvold, J. & Zhao, R. (1992) '*Global loads on high speed catamarans*'. *5th International Symposium on the Practical Design of Ships and Mobile Units*. Newcastle upon Tyne, England: Elsevier Science Pubs Ltd.

Faltinsen, O.M. & Zhao, R. (1991a) '*Flow predictions around high-speed ships in waves'*. In*:* Miloh, T. (ed.) *Mathematical Approaches in Hydrodynamics.* Philadelphia, PA, USA: Society for Industrial and Applied Mathematics, pp. 265-288.

Faltinsen, O.M. & Zhao, R. (1991b) 'Numerical Prediction of Ship Motions at High Forward Speed'. *Philosophical Transactions of the Royal Society of London Series A-Mathematical Physical and Engineering Sciences,* 334 (1634), pp.241-252.

Fathi, D. (2004) '*ShipX Vessel Responses (VERES) Ship Motions and Global Loads Users' Manual'*. Norway: Marintek Report.

Fathi, D. & Hoff, J.R. (2013) '*ShipX Vessel Responses (VERES) Theory Manual'*. Norway: Marintek Report.

Fenton, J.D. (1979) 'A high-order cnoidal wave theory'. *Journal of Fluid Mechanics,* 94 (1), pp.129-161.

Fenton, J.D. (1985) 'A fifth-order Stokes theory for steady waves'. *Journal of Waterway, Port, Coastal, and Ocean Engineering,* 111 (2), pp.216-234.

Ferziger, J.H. & Peric, M. (2002) *Computational Methods for Fluid Dynamics.* 3rd edn. Berlin, Germany: Springer.

Field, P.L. (2013) *Comparison of RANS and potential flow force computations for the ONR Tumblehome hullform in vertical plane radiation and diffraction problems.* MSc. thesis. Virginia Polytechnic Institute and State University.

Finkelstein, A.B. (1957) 'The initial value problem for transient water waves'. *Communications on Pure and Applied Mathematics*, 10 (4), pp.511-522.

Fonseca, N. & Soares, C.G. (2002) '*Sensitivity of the expected ships availability to different seakeeping criteria*'. *21st International Conference on Offshore Mechanics and Artie Engineering*. Oslo, Norway: ASME.

Froude, W. (1861) 'On the rolling of ships'. *Transactions of Institution of Naval Architects*, 2 pp.180-229.

Garisson, C.J. & Chow, P.Y. (1972) 'Wave forces on submerged bodies'. *Journal of the Waterways, Harbors and Coastal Engineering Division*, 98 (3), pp.375-392.

Gentaz, L., Alessandrini, B. & Delhommeau, G. (1997) '*Motion simulation of a two-dimensional body at the surface of a viscous fluid by a fully coupled solver*'. *12th International Workshop on Water Waves and Floating Bodies*. Marseilles, France.

Gentaz, L., Alessandrini, B. & Delhommeau, G. (1999) '*Three-dimensional free-surface viscous flow around a ship in forced motion*'. *7th International Conference on Numerical Ship Hydrodynamics*. Paris, France.

Gerritsma, J. & Beukelman, W. (1972) 'Analysis of the resistance increase in waves of a fast cargo ship'. *International Shipbuilding Progress*, 19 (217), pp.285-293.

Gerritsma, J.W. & Beukelman, W. (1967) 'Analysis of the modified strip theory for the calculation of ship motions and wave bending moments'. *International Shipbuilding Progress*, 14 (156), pp.316-337.

Gillmer, T.C. & Johnson, B. (1982) *Introduction to Naval Architecture.* Annapolis, MD: US Naval Institute.

Giron, J.M., Esteban, S. & Riola, J.M. (2001) '*Experimental study of controlled flaps and t-foil for comfort improvement of a fast ferry*'. *International Federation of Automatic Control Conference on Control Applications in Marine Systems*. Glasgow, UK.

Gourlay, T. (2008a) 'Sinkage and trim of a fast displacement catamaran in shallow water'. *Journal of Ship Research,* 52 (3), pp.175-183.

Gourlay, T. (2008b) 'Slender-body methods for predicting ship squat'. *Ocean Engineering,* 35 (2), pp.191-200.

Graham, R. (1990) 'Motion-induced interruptions as ship operability criteria'. *Naval Engineers Journal,* 102 (2), pp.65-71.

Guevel, P., Vaussy, P. & Kobus, J.M. (1974) 'The distribution of singularities kinematically equivalent to a moving hull in the presence of a free surface'. *International Shipbuilding Progress,* 21 (243), pp.311-324.

Hasselmann, K., T.P., B., Bouws, E., Carlson, H., Cartwright, D.E., Enke, K., Ewing, J.A., Gienapp, H., Hasselmann, D.E., Kruseman, P., Meerburg, A., Muller, P., Olbers, D.J., Richter, K., Sell, W. & Walden, H. (1973) *Measurements of Wind-Wave Growth and Swell Decay During the Joint North Sea Wave Project (JONSWAP).*

Havelock, T.H. (1908) 'The propagation of groups of waves in dispersive media, with application to waves on water produced by a travelling disturbance'. *Proceedings of the Royal Society of London Series A-Containing Papers of a Mathematical and Physical Character,* 81 (549), pp.398-430.

He, W., Castiglione, T., Kandasamy, M. & Stern, F. (2014) 'Numerical analysis of the interference effects on resistance, sinkage and trim of a fast catamaran '. *Journal of Marine Science and Technology,* pp.1-17.

Hermundstad, O.A., Aarsnes, J.V. & Moan, T. (1999) 'Linear hydroelastic analysis of high-speed catamarans and monohulls'. *Journal of Ship Research,* 43 (1), pp.48-63.

Hess, J.L. & Smith, A.M.O. (1964) 'Calculation of nonlifting potential flow about three-dimensional bodies'. *Journal of Ship Research,* 8 (2), pp.22-44.

Hochbaum, C.A. & Vogt, M. (2002) '*Towards the simulation of seakeeping and maneuvering based on the computation of the free surface viscous flow*'. *24th Symposium on Naval Hydrodynamics*. Fukuoka, Japan.

Hochkirch, K. & Mallol, B. (2013) '*On the importance of full-scale CFD simulations for ships*'. *12th International Conference on Computer Applications and Information Technology in the Maritime Industries* Cortona, Italy.

Hoff, J. (2014). *RE: Personal communication.*

Hogben, N., da Cunha, L.F. & Olliver, H.N. (1986) *Global Wave Statistics.* London: Brown Union.

Hsin, C.Y., Kerwin, J.E. & Newman, J.N. (1994) '*A high-order panel method based on B-splines*'. *Sixth International Conference on Numerical Ship Hydrodynamics*. Iowa, USA: National Academy Press.

Hu, C. & Kashiwagi, M. (2007) '*Numerical and experimental studies on three dimensional water on deck with a modified Wigley hull*'. *9th International Conference in Numerical Ship Hydrodynamics*. Ann Arbor, Michigan, US.

Ikeda, Y., Takata, H. & Ishihara, S. (1991) 'A study on evaluation of seakeeping performance for passenger ships'. *Journal of Kansai Society of Naval Architects*, 214 pp.105-112.

International Navigation Association (2003) *Guidelines for managing wave wash from high-speed vessels*. Available: http://www.pianc.us/workinggroups/docs_wg/marcom-wg41.pdf.

International Organization for Standardization (1985) '*Evaluation of Human Exposure to Whole-Body Vibration'. 2631/3, Part 3: Evaluation of Exposure to Whole-Body z-axis Vertical Vibration in the Frequency Range 0.1 to 0.63 Hz.*

International Organization for Standardization (1997) '*2631/1, Mechanical Vibration and Shock-Evaluation of Human Exposure to Whole-Body Vibration'*.

International Towing Tank Conference (1987) *Report of the Seakeeping Committee, 18th ITTC*.

International Towing Tank Conference (2011a) '*ITTC-Recommended Procedures and Guidelines'. Seakeeping Experiment, Revision 04.*

International Towing Tank Conference (2011b) '*Practical guidelines for ship CFD applications*'. *26th ITTC*. Rio de Janeiro – Brazil.Available at: http://ittc.sname.org/CD%202011/pdf%20Procedures%202011/7.5-03-02-03.pdf (Accessed: 1st February 2014).

International Towing Tank Conference (2011c) '*The specialist committee on computational fluid dynamics-Final report and recommendations to the 26th ITTC*'. *26th ITTC,*. Rio de Janeiro – Brazil.

International Towing Tank Conference (2014) '*Ocean Engineering Committee, Final report and recommendation to the 27th ITTC*'. *27th ITTC*. Copenhagen. Available at: http://ittc.info/downloads/Proceedings/27th%20Conference/1-6%20Seakeeping%20Committee.pdf (Accessed: 15th September 2014).

Jachowski, J. (2008) 'Assessment of ship squat in shallow water using CFD'. *Archives of Civil and Mechanical Engineering,* 8 (1), pp.27-36.

Jensen, J.J. (2000) '*Committee VI.1. Extreme hull girder loading*'. *14th International Ship and Offshore Structures Congress*. Nagasaki, Japan.

Jiang, T. (1998) '*Investigation of waves generated by ships in shallow water*'. *22nd Symposium on Naval Hydrodynamics*. Washington DC, USA.

Kashiwagi, M., Mizokami, S., Yasukawa, H. & Fukushima, Y. (2001) '*Prediction of wave pressure and loads on actual ships by the enhanced unified theory*'. *23rd Symposium on Naval Hydrodynamics*. Val de Reuil, France.

Khalid, H., Turan, O. & Kurt, R.E. (2009) '*A simple technique for the operability analysis of an offshore support vessel before deployment at new sites*'. *13th Congress of the International Maritime Association of the Mediterranean*. Istanbul, Turkey.

Kim, C.H. (1968) 'The influence of water depth on the heaving and pitching motions of a ship moving in longitudinal regular head waves'. *Schiffstechnik,* 15 (79), pp.127-132.

Kim, S. (2011) 'CFD as a seakeeping tool for ship design'. *International Journal of Naval Architecture and Ocean Engineering,* 3 (1), pp.65-71.

Kim, S.P. & Lee, H.H. (2011) '*Fully nonlinear seakeeping analysis based on CFD simulations*'. *21st International Offshore and Polar Engineering Conference*. Hawaii, USA.

Kim, T. & Kim, Y. (2013) 'Numerical analysis on floating-body motion responses in arbitrary bathymetry'. *Ocean Engineering,* 62 pp.123-139.

Kim, W.J., Van, S.H. & Kim, D.H. (2001) 'Measurement of flows around modern commercial ship models'. *Experiments in Fluids,* 31 (5), pp.567-578.

Korteweg, D.J. & Vries, G. (1895) 'On the change of form of long waves advancing in a rectangular canal, and on a new type of long stationary waves'. *Philosophical Magazine Series 5,* 39 (240), pp.422-443.

Korvin-Kroukovsky, B.V. (1955) 'Investigation of ship motions in regular waves'. *Transactions of SNAME,* 63 pp.386-435.

Korvin-Kroukovsky, B.V. & Jacobs, W.R. (1957) 'Pitching and heaving motions of a ship in regular waves'. *Transactions of SNAME,* 65 pp.590-632.

Kreitner, J. (1934) '*Uber den Schiffswiderstand auf beschrankter Wasser'*. Werft Reederei Hafen.

Kring, D.C. (1994) *Time domain ship motions by a three-dimensional Rankine panel method.* PhD thesis. Massachusetts Institute of Technology.

Larsson, L., Stern, F. & Visonneau, M. (2011) 'CFD in ship hydrodynamics- Results of the Gothenburg 2010 Workshop'. *Computational Methods in Marine Engineering IV (MARINE 2011),* pp.17-36.

Lee, C.M., Jones, H. & Bedel, J.W. (1971) *Added mass and damping coefficients of heaving twin cylinders in a free surface*. Naval Ship Research and Development Center, Report No. 3695.

Li, L. (2001) *Numerical seakeeping predictions of shallow water effect on two ship interactions in waves.* PhD thesis. Dalhousie University.

Lloyd, A.R.J.M. (1989) *Seakeeping: Ship Behavior in Rough Weather.* Chichester, UK: Ellis Horwood Limited.

Luis, R.M., Teixeira, A.P. & Soares, C.G. (2009) 'Longitudinal strength reliability of a tanker hull accidentally grounded'. *Structural Safety*, 31 (3), pp.224-233.

Maersk (n.d.) *Slow Steaming: The Full Story*. Available: http://www.maersk.com/Innovation/WorkingWithInnovation/Documents/Slow Steaming - the full story.pdf (Accessed: 5th January 2014).

Maniar, H. (1995) *A three dimensional higher order panel method based on B-splines.* Massachusetts Institute of Technology.

Manzke, M. & Rung, T. (2010) '*Resistance prediction and seakeeping analysis with FreSCo+*'. *Gothenburg 2010-A Workshop on Numerical Ship Hydrodynamics*. Gothenburg.

Maruo, H. (1970) 'An improvement of the slender body theory for oscillating ships with zero forward speed'. *Bulletin of the Faculty of Engineering, Yokohama National University,* 19 pp.45-56.

McCauley, M.E., Royal, J.W., Wylie, C.D., O'Hanlon, J.F. & Mackie, R.R. (1976) *Motion sickness incidence: Exploratory studies of habituation, pitch and roll, and the refinement of a mathematical model*. Human Factors Research Inc., Technical Report 1733-2.

McTaggart, K. (1997) *Shipmo7: An updated strip theory program for predicting ship motions and sea loads in waves*. Available: http://oai.dtic.mil/oai/oai?verb=getRecord&metadataPrefix=html&identifier=ADA323840.

Michell, J.H. (1898) 'The wave resistance of a ship'. *Phil. Mag.,* 5 (45), pp.106-123.

Mortola, G., Khalid, H., Judah, S., Incecik, A. & Turan, O. (2012) '*A methodology for rapid selection of a seaworthy vessel for offshore wind turbine construction, operation and maintenance*'. *2nd Marine Operations Specialty Symposium*. Singapore.

Mousaviraad, S.M., Carrica, P.M. & Stern, F. (2010) 'Development and validation of harmonic wave group single-run procedure for RAO with comparison to regular wave and transient wave group procedures using URANS'. *Ocean Engineering,* 37 (8-9), pp.653-666.

Mucha, P., El Moctar, O. & Bottner, C.U. (2014) 'Technical note : PreSquat - Workshop on numerical prediction of ship Squat in restricted waters'. *Ship Technology Research: Schiffstechnik,* 61 (3), pp.162-165.

Munk, M. (1924) *The aerodynamic forces on airship hulls*. Available: http://naca.central.cranfield.ac.uk/reports/1924/naca-report-184.pdf.

Newman, J.N. (1961) 'A linearized theory for the motion of a thin ship in regular waves'. *Journal of Ship Research,* 3 (1), pp.1-19.

Newman, J.N. (1964) 'A slender-body theory for ship oscillations in waves'. *Journal of Fluid Mechanics,* 18 (4), pp.602-618.

Newman, J.N. (1978) 'The theory of ship motions'. *Advances in Applied Mechanics,* 18 pp.221-283.

Ogilvie, T.F. & Tuck, E.O. (1969) *A rational strip theory of ship motions: Part 1*. Department of Naval Architecture and Marine Engineering, College of Engineering, The University of Michigan, Report No. 13.

Ohanlon, J.F. & McCauley, M.E. (1974) 'Motion sickness incidence as a function of the frequency and acceleration of vertical sinusoidal motion'. *Aerospace Medicine,* 45 (4), pp.366-369.

Okan, M. & Umpleby, S. (1985a) 'Free surface flow around arbitrary two-dimensional bodies by B-splines'. *International Shipbuilding Progress,* 32 pp.182-187.

Okan, M. & Umpleby, S. (1985b) 'The use of B-splines for the calculation of two-dimensional potential flow around arbitrary bodies'. *International Shipbuilding Progress,* 32 pp.151-155.

Oortmerssen, G.V. (1972) '*Some aspects of very large offshore structures*'. *9th Symposium on Naval Hydrodynamics*. Paris, France.

Oortmerssen, G.V. (1976a) *The motions of a moored ship in waves*. Netherlands Ship Model Basin, Publication No. 510.

Oortmerssen, G.V. (1976b) 'The motions of a ship on shallow water'. *Ocean Engineering,* 3 pp.221-225.

Orihara, H. & Miyata, H. (2003) 'Evaluation of added resistance in regular incident waves by computational fluid dynamics motion simulation using an overlapping grid system'. *Journal of Marine Science and Technology,* 8 (2), pp.47-60.

Otzen, J.F. & Simonsen, C.D. (2010) *Uncertainty assessment for KCS resistance and propulsion tests in waves*. FORCE Technology, Report No. ONRIII187 01.

Ozdemir, Y.H., Barlas, B., Yilmaz, T. & Bayraktar, S. (2014) 'Numerical and experimental study of turbulent free surface flow for a fast ship model'. *Brodogradnja,* 65 (1), pp.39-54.

Paik, K.J., Carrica, P.M., Lee, D. & Maki, K. (2009) 'Strongly coupled fluid-structure interaction method for structural loads on surface ships'. *Ocean Engineering,* 36 (17-18), pp.1346-1357.

Peters, A.S. & Stoker, J.J. (1957) 'The motion of a ship, as a floating body, in a seaway'. *Communications on Pure and Applied Mathematics,* 10 (3), pp.399-490.

Pinkster, J.A. (1980) *Low frequency second order wave exciting forces on floating structures*. PhD thesis. Delft University of Technology.

Prabhakara, S. & Deshpande, M.D. (2004) 'The no-slip boundary condition in fluid mechanics'. *Resonance,* 9 (4), pp.50-60.

Prakash, S. & Chandra, B. (2013) 'Numerical estimation of shallow water resistance of a river-sea ship using CFD'. *International Journal of Computer Applications,* 71 (5), pp.33-40.

PreSquat (n.d.) *Instructions- Dynamic squat test parameter*. Available: https://www.uni-due.de/IST/ismt_presquat_test.shtml (Accessed: 01/11/2014).

Querard, A.B.G., Temarel, P. & Turnock, S.R. (2008a) '*Hydrodynamics of ship-like sections in heave, sway and roll motions using RANS*'. *12th International Congress of the International-Maritime-Association-of-the-Mediterranean*. Varna, BULGARIA, LONDON: Taylor & Francis Ltd.

Querard, A.B.G., Temarel, P. & Turnock, S.R. (2008b) 'Influence of viscous effects on the hydrodynamics of ship-like sections undergoing symmetric and anti-symmetric motions, using RANS'. *Proceedings of the 27th International Conference on Offshore Mechanics and Arctic Engineering - 2008, Vol 5,* pp.683-692.

Querard, A.B.G., Temarel, P. & Turnock, S.R. (2009) 'The hydrodynamics of ship-like sections in heave, sway, and roll motions predicted using an unsteady Reynolds-Averaged Navier-Stokes method'. *Proceedings of the Institution of Mechanical Engineers Part M-Journal of Engineering for the Maritime Environment,* 223 (M2), pp.227-238.

Raven, H.C. (2012) '*A computational study of shallow-water effects on ship viscous resistance*'. *29th Symposium on Naval Hydrodynamics*. Gothenburg, Sweden.

Richardson, L.F. (1911) 'The approximate arithmetical solution by finite differences of physical problems involving differential equations, with an application to the stresses in a Masonry dam'. *Philosophical Transactions of the Royal Society of London Series A-Containing Papers of a Mathematical or Physical Character,* 210 pp.307-357.

Riola, J.M. & Arboleya, M.G. (2006) 'Habitability and personal space in seakeeping behaviour'. *Journal of Maritime Research,* 36 (1), pp.41-54.

Roache, P.J. (1998) *Verification and Validation in Computational Science and Engineering.* Albuquerque: Hermosa Publishers.

Roddier, D., Liao, S.W. & Yeung, R.W. (2000) 'On freely-floating cylinders fitted with bilge keels'. *10th International Offshore and Polar Engineering Conference (ISOPE-2000)*, Seattle, Wa. CUPERTINO: International Society Offshore& Polar Engineers, pp.377-384.

Ronen, D. (2011) 'The effect of oil price on containership speed and fleet size'. *Journal of the Operational Research Society,* 62 (1), pp.211-216.

Roy, C.J. & Blottner, F.G. (2001) 'Assessment of one- and two-equation turbulence models for hypersonic transitional flows'. *Journal of Spacecraft and Rockets,* 38 (5), pp.699-710.

Sakamoto, N., Wilson, R.V. & Stern, F. (2007) 'Reynolds-Averaged Navier-Stokes simulations for high-speed wigley hull in deep and shallow water'. *Journal of Ship Research,* 51 (3), pp.187-203.

Salui, K.B., Sarkar, T. & Vassalos, D. (2000) 'An improved method for determining hydrodynamic coefficients in roll motion using CFD techniques'. *Journal of Ship Technology Research,* 47 pp.161-174.

Salvesen, N., Tuck, E.O. & Faltinsen, O. (1970) 'Ship motions and sea loads'. *Transactions of the Society of Naval Architects and Marine Engineers,* 78 pp.250-287.

Sarioz, K. & Sarioz, E. (2005) 'Habitability assessment of passenger vessels based on ISO criteria'. *Marine Technology and SNAME News,* 42 (1), pp.43-51.

Sato, Y., Miyata, H. & Sato, T. (1999) 'CFD simulation of 3-dimensional motion of a ship in waves: application to an advancing ship in regular heading waves'. *Journal of Marine Science and Technology,* 4 (3), pp.108-116.

Schmitke, R.T. (1978) 'Ship sway, roll, and yaw motions in oblique seas'. *Transactions of the Society of Naval Architects and Marine Engineers,* 86 pp.26-46.

Schultz, M.P. (2007) 'Effects of coating roughness and biofouling on ship resistance and powering'. *Biofouling,* 23 (5), pp.331-341.

Sclavounos, P.D. (1984) 'The diffraction of free-surface waves by a slender ship'. *Journal of Ship Research,* 28 (1), pp.29-47.

Sclavounos, P.D. (1985) '*The unified slender-body theory: Ship motions in waves*'. *15th Symposium on Naval Hydrodynamics*. Hamburg, Germany.

Sclavounos, P.D. (1990) '*Ship motions by a three-dimensional Rankine panel method*'. *18th Symposium on Naval Hydrodynamics*. Ann Arbor, Michigan.

Sclavounos, P.D. & Nakos, D.E. (1988) '*Stability analysis of panel methods for free surface flows with forward speed*'. *17th Symposium on Naval Hydrodynamics*. DenHague, The Netherlands.

Shen, Z.R. & Wan, D.C. (2013) 'RANS computations of added resistance and motions of a ship in head waves'. *International Journal of Offshore and Polar Engineering,* 23 (4), pp.263-271.

Shin, Y.S., Belenky, V.L., Lin, W.M., Weems, K.M. & Engle, A.H. (2003) 'Nonlinear time domain simulation technology for seakeeping and wave-load analysis for modern ship design'. *Transactions of SNAME,* 111 pp.557-583.

Simonsen, C.D., Otzen, J.F., Joncquez, S. & Stern, F. (2013) 'EFD and CFD for KCS heaving and pitching in regular head waves'. *Journal of Marine Science and Technology,* 18 (4), pp.435-459.

Simonsen, C.D. & Stern, F. (2010) '*CFD simulation of KCS sailing in regular head waves*'. *Gothenburg 2010-A Workshop on Numerical Ship Hydrodynamics*. Gothenburg.

Soares, C.G., Fonseca, N. & Centeno, R. (1995) '*Seakeeping performance of fishing vessels in the Portuguese Economic Zone*'. *International Conference on Seakeeping and Weather*. London, England.

St Denis, M. & Pierson, W. (1953) 'On the motions of ships in confused seas'. *Transactions of the Society of Naval Architects and Marine Engineers,* 61 pp.280-354.

Stern, F., Carrica, P., Kandasamy, M., Ooi, S.K., Gorski, J., O'Dea, J., Fu, T., Hendrix, D., Kennell, C., Hughes, M., Miller, R., Marino, T., Hess, D., Kring, D., Milewski, W., Hoffman, R., Smith, S., Cary, C., Taylor, P., Peterson, B., Harris, D. & Monaco, C. (2008) *Computational hydrodynamic tools for high-speed sealift: phase II final report*. IIHR—Hydroscience & Engineering College of Engineering, The University of Iowa, Report No. 465.

Stern, F., Wilson, R. & Shao, J. (2006) 'Quantitative V&V of CFD simulations and certification of CFD codes'. *International Journal for Numerical Methods in Fluids*, 50 (11), pp.1335-1355.

Stern, F., Wilson, R.V., Coleman, H.W. & Paterson, E.G. (2001) 'Comprehensive approach to verification and validation of CFD simulations - Part 1: Methodology and procedures'. *Journal of Fluids Engineering-Transactions of the Asme*, 123 (4), pp.793-802.

Tezdogan, T., Demirel, Y.K., Incecik, A. & Turan, O. (2014a) '*Predicting the hydrodynamics of heaving twin cylinders in a free surface using an unsteady-RANS method*'. *International Conference on Maritime Technology*. Glasgow, UK.

Tezdogan, T., Demirel, Y.K., Kellett P., Khorsanchi, M., Incecik, A., & Turan, O. (2015) 'Full-scale unsteady RANS CFD simulations of ship behaviour and performance in head seas due to slow steaming'. Ocean Engineering, 97, pp. 186-206. http://10.1016/j.oceaneng.2015.01.011.

Tezdogan, T., Demirel, Y.K., Mortola, G., Incecik, A., Turan, O. & Khalid, H. (2014b) 'Operability analysis of a high speed car/passenger ferry'. *Developments in Maritime Transportation and Exploitation of Sea Resources, Vol 1*, pp.273-281.

Troesch, A. & Beck, R.F. (1974) *Experiments on ship motions in shallow water*. University of Michigan, College of Engineering, Report No. 149.

Tuck, E.O. (1966) 'Shallow-water flows past slender bodies'. *Journal of Fluid Mechanics*, 26 (1), pp.81-95.

Tuck, E.O. (1967) 'Sinkage and trim in shallow water of finite width'. *Schiffstechnik*, 14 (73), pp.92-94.

Tuck, E.O. (1978) 'Hydrodynamic problems of ships in restricted waters'. *Annual Review of Fluid Mechanics*, 10 pp.33-46.

Uliczka, K. (2010) *Fahrdynamisches verhalten eines groben containerschiffs in seiten- und tiefenbegrenztes fahrwasser*. Available: http://www.baw.de/upload/EWisA/FuEVorhaben/documents/A39550270133.pdf.

Varyani, K.S. (2006) 'Squat effects on high speed craft in restricted waterways'. *Ocean Engineering,* 33 (3-4), pp.365-381.

Visonneau, M., Queutey, P. & Deng, G.B. (2006) '*Model and full-scale free-surface viscous flows around fully-appended ships*'. *European Conference on Computational Fluid Dynamics*. Delft, The Netherlands.

Vugts, J.H. (1968) *The hydrodynamic coefficients for swaying, heaving and rolling cylinders in a free surface*. Shipbuilding Laboratory, Delft University of Technology, Publication No. 510.

Wang, S. & Wahab, R. (1971) 'Heaving oscillations of twin cylinders in a free surface'. *Journal of Ship Research,* 15 (1), pp.33-48.

Wang, Z.H. (2000) *Hydroelastic Analysis of High-Speed Ships.* PhD. Technical University of Denmark.

Weymouth, G., Wilson, R. & Stern, F. (2005) 'RANS CFD predictions of pitch and heave ship motions in head seas'. *Journal of Ship Research,* 49 (2), pp.80-97.

Wilson, R., Paterson, E. & Stern, F. (1998) '*Unsteady RANS CFD method for naval combatants in waves*'. *22nd Symposium on Naval Hydrodynamics*. Washington, D.C.

Wilson, R.V., Ji., L., Karman, S.L., Hyams, D.G., Sreenivas, K., Taylor, L.K. & Whitfield, D.L. (2008) '*Simulation of large amplitude ship motions for prediction of fluid-structure interaction*'. *27th Symposium on Naval Hydrodynamics*. Seoul.

Wortley, S. (2013) *CFD analysis of container ship sinkage, trim and resistance*. Curtin University, Department of Mechanical Engineering. B.Eng Mechanical Engineering Project Report 491/493.

Wu, G.X. & Taylor, R.E. (2003) 'The coupled finite element and boundary element analysis of nonlinear interactions between waves and bodies'. *Ocean Engineering,* 30 (3), pp.387-400.

Xiao, Q. (2012) '*Theory and Practice of Marine CFD (Lecture Notes)'*. University of Strathclyde, Department of Naval Architecture, Ocean and Marine Engineering.

Xing, T. & Stern, F. (2010) 'Factors of Safety for Richardson Extrapolation'. *Journal of Fluids Engineering-Transactions of the Asme,* 132 (6), pp.061403.

Yao, J.X. & Zou, Z.J. (2010) 'Calculation of ship squat in restricted waterways by using a 3D panel method'. *Journal of Hydrodynamics,* 22 (5), pp.472-477.

Yasukawa, H. (1993) 'A Rankine panel method to calculate steady wave-making resistance of a ship taking the effect of sinkage and trim into account'. *Transactions of the West Japan Society of Naval Architects,* 86 pp.27-35.

Yasukawa, H. (2003) '*Application of a 3-D time domain panel method to ship seakeeping problems*'. *24th Symposium on Naval Hydrodynamics*. Fukuoka, Japan.

Yeung, R.W., Liao, S.W. & Rodier, D. (1998) *'Hydrodynamic coefficients of rolling rectangular cylinders*'. *International Journal of Offshore and Polar Engineering,* 8 (4), pp.241-250.

Yuan, Z.M., Incecik, A. & Jia, L.B. (2014) 'A new radiation condition for ships travelling with very low forward speed'. *Ocean Engineering,* 88 pp.298-309.

Yueng, R.W. & Kim, S.H. (1985) '*A new development in the theory of oscillating and translating slender ships*'. *15th Symposium on Naval Hydrodynamics*. Hamburg, Germany.

Zou, L. & Larsson, L. (2013) 'Numerical predictions of ship-to-ship interaction in shallow water'. *Ocean Engineering*, 72 pp.386-402.

Publications

The following papers have been either published, or submitted for consideration for publication, in scientific journals and conferences. All of the papers listed below (excepting the first journal paper listed below) have been drawn from this thesis.

Journal papers:

1. Tezdogan, T & Demirel Y.K. (2014) 'An overview of marine corrosion protection with a focus on cathodic protection and coatings'. *Brodogradnja/Shipbuilding*, 65, pp. 49-59. Available: http://hrcak.srce.hr/123461?lang=en.
2. Tezdogan, T., Incecik, A. & Turan, O. (2014) 'Operability assessment of high speed passenger ships based on human comfort criteria'. *Ocean Engineering*, 89, pp. 32-52. http://10.1016/j.oceaneng.2014.07.009.
3. Tezdogan, T., Demirel, Y.K., Kellett P., Khorsanchi, M., Incecik, A., & Turan, O. (2015) 'Full-scale unsteady RANS CFD simulations of ship behaviour and performance in head seas due to slow steaming'. *Ocean Engineering*, 97, pp. 186-206. http://10.1016/j.oceaneng.2015.01.011.
4. Tezdogan, T., Incecik, A. & Turan, O. (2015) 'Full-scale unsteady Reynolds-Averaged Navier-Stokes simulations of vertical ship motions in shallow water'. *Submitted to Applied Ocean Research* (under review).
5. Tezdogan, T., Incecik, A. & Turan, O. (2015) 'A numerical investigation of the squat and resistance of ships advancing through a canal using CFD'. *Submitted to Journal of Marine Science and Technology* (under review).

Conference papers:

1. Tezdogan, T., Demirel, Y.K., Mortola, G., Incecik, A., Turan, O. & Khalid, H. (2014) 'Operability analysis of a high speed car/passenger ferry'. *Developments in Maritime Transportation and Exploitation of Sea Resources*, Vol 1, pp.273-281. http://dx.doi.org/10.1016/j.oceaneng.2014.07.009.

2. Tezdogan, T., Demirel, Y.K., Incecik, A. & Turan, O. (2014) 'Hydrodynamics of heaving twin cylinders in a free surface using an unsteady-RANS method'. *Proceedings of International Conference on Maritime Technology*, Glasgow, United Kingdom, Session 6-21-28.

Abstracts:

1. Tezdogan, T. (2013) 'A nonlinear approach to seakeeping of catamarans'. *Proceedings of 4th United Kingdom Marine Technology Postgraduate Conference*, London, pp. 9-10.